APPLICATIONS OF REMOTE SENSING AND GEOGRAPHIC INFORMATION SYSTEMS IN GEOMORPHOLOGICAL STUDIES: SAFAGA - EL QUSEIR AREA, RED SEA COAST, EGYPT AS AN EXAMPLE.

Dissertation

zur Erlangung des Grades

"Doktor der Naturwissenschaften"

im Promotionsfach Geographie

am Fachbereich Chemie, Pharmazie, Geowissenschaften

der Johannes Gutenberg-Universität Mainz

vorgelegt von

MOAWAD BADAWY MOAWAD BADAWY

Geboren in Kairo, Ägypten

Mainz, 2008

Tag der mündlichen Prüfung: 29/ 02/2008.

Erklärung:

Ich versichere hiermit, die vorliegende Arbeit selbständig und nur unter Verwendung der angegebenen Quellen und Hilfsmittel verfaßt zu haben.

Assertion:

All views and results presented in this thesis are those of the author unless stated otherwise.

TO MY HOMELAND: EGYPT.

AS A CONFESSION OF KINDNESS.

Zusammenfassung

In den letzten drei Jahrzehnten sind Fernerkundung und GIS in den Geowissenschaften zunehmend wichtiger geworden, um die konventionellen Methoden von Datensammlung und zur Herstellung von Landkarten zu verbessern. Die vorliegende Arbeit befasst sich mit der Anwendung von Fernerkundung und geographischen Informationssystemen (GIS) für geomorphologische Untersuchungen. Durch die Kombination beider Techniken ist es vor allem möglich geworden, geomorphologische Formen im Überblick und dennoch detailliert zu erfassen. Als Grundlagen werden in dieser Arbeit topographische und geologische Karten, Satellitenbilder und Klimadaten benutzt.

Die Arbeit besteht aus 6 Kapiteln. Das erste Kapitel gibt einen allgemeinen Überblick über den Untersuchungsraum. Dieser umfasst folgende morphologische Einheiten: Küstenlinie einschließlich flacher Schelfzone und Küstenebene, höher gelegene Ebenen bzw. Terrassen sowie das westlich anschließende stark gegliederte Gebirgsland mit den Wadisystemen. Außerdem werden die klimatischen Verhältnisse, insbesondere die Ariditätsindizes der Küsten- und Gebirgslandschaft sowie das Siedlungsmuster beschrieben.

Kapitel 2 befasst sich mit der regionalen Geologie und Stratigraphie des Untersuchungsraumes. Es wird versucht, die Hauptformationen mit Hilfe von ETM-Satellitenbildern zu identifizieren. Angewandt werden hierzu folgende Methoden: Colour Band Composite, Image Rationing und die sog. überwachte Klassifikation. Letztere ist zwar sehr aufwändig, liefert aber die besten Ergebnisse.

Kapitel 3 enthält eine Beschreibung der strukturell bedingten Oberflächenformen, um die Wechselwirkung zwischen Tektonik und geomorphologischen Prozessen aufzuklären. Es gliedert sich in vier Teile. Der erste Teil stellt eine Einführung dar. In Teil 2 werden die Definition von Lineamenten und ihre Bedeutung für Geologie, Geomorphologie und Fernerkundung diskutiert. In Teil 3 geht es um die vielfältigen Methoden, zum Beispiel das sog. Image Processing, um die im Gebirgskörper vorhandenen Lineamente einwandfrei zu deuten. Spezielle Filtermethoden werden angewandt, um die wichtigsten Lineamente zu kartieren. In Teil 4 werden schließlich die ausgedehnteren Strukturformen, wie etwa Brüche, diapirische Plutone, Dyke-Schwärme und Spalten sowie Verebnungsflächen kartiert. Dies geschieht auf der Grundlage eigens entwickelter Kriterien, die Geländeneigungen und Bruchlinien sowie deren Dichte und Orientierung beinhalten. Das Resultat sind verschiedene geomorphologische und geologische Interpretationskarten des Arbeitsgebietes mit detailliertem Kartierinhalt.

Kapitel 4 stellt den Versuch dar, mit Hilfe von aufbereiteten SRTM-Satellitenbildern eine automatisierte Erfassung des Gewässernetzes bzw. der Wadisysteme durchzuführen. Hierbei geht es um folgende Parameter: Abgrenzung des Einzugsgebietes bzw. Festlegung von Wasserscheiden sowie Quantifizierung der wichtigsten morphologischen Parameter, beispielsweise landförmige und flächige Elemente mit dem Ziel einer Reliefanalyse. Angestrebt wird eine möglichst vollständige Reliefanalyse. Es wird ausführlich diskutiert, inwieweit bei diesen Arbeitsschritten die Qualität kleinmaßstäbiger SRTM-Satellitenbilder mit großmaßstäbigen topographischen Karten 1 : 100 000 und 1 : 50 000 vergleichbar ist. Die Untersuchung kommt zu dem Schluss, dass die SRTM-Satellitenbilder hinsichtlich ihrer Detailgenauigkeit den topographischen Karten 1 : 50 000 durchaus ebenbürtig sind. Weiterhin werden hydrologische Parameter über eine qualitative und quantitative Analyse des Abflussregimes einzelner Wadis erfasst. Der Ursprung von Entwässerungssystemen wird auf der Basis geomorphologischer und geologischer Befunde interpretiert. Ergänzend werden markante Waditerrassen und Deltabildungen von Wadis an der Küste des Roten Meeres untersucht.

Kapitel 5 befasst sich mit der Abschätzung der Gefahr episodischer Wadifluten. Die Wahrscheinlichkeit ihres jährlichen Auftretens bzw. des Auftretens starker Fluten im Abstand mehrerer Jahre wird in einer historischen Betrachtung bis 1921 zurückverfolgt. Die Bedeutung von Regentiefs, die sich über dem Roten Meer entwickeln, und die für eine Abflussbildung in Frage kommen, wird mit Hilfe der IDW-Methode (Inverse Distance Weighted) untersucht. Betrachtet werden außerdem weitere, regenbringende Wetterlagen mit Hilfe von Meteosat Infrarotbildern. Genauer betrachtet wird die Periode 1990-1997, in der kräftige, Wadifluten auslösende Regenfälle auftraten. Flutereignisse und Fluthöhe bzw. Abflussmenge werden anhand von hydrographischen Daten (Pegelmessungen) ermittelt. Auch die Landnutzung und Siedlungsstruktur im Einzugsgebiet eines Wadis wird berücksichtigt.

In Kapitel 6 geht es um die unterschiedlichen Küstenformen auf der Westseite des Roten Meeres. Der erste Teil enthält eine Übersicht über die Erosionsformen, wie etwa Küstenkliffs und Brandungsterrassen; im zweiten Teil geht es um Aufbauformen, beispielsweise Sandstrände, Nebkas und Nehrungsbildungen. In Teil 3 werden untergetauchte Formen entlang der Küste, beispielsweise Wadimündungen, Buchten (Sharms) und Offshore-Inseln mit dem sie umgebenden, intakten Korallenriff beschrieben. Im abschließenden vierten Teil geht es um die Stratigraphie und zeitliche Zuordnung von submarinen Terrassen auf Korallenriffen sowie den Vergleich mit anderen solcher Terrassen an der ägyptischen Rotmeerküste westlich und östlich der Sinai-Halbinsel.

Summary

During the last three decades remote sensing and GIS have become increasingly important tools for improving the conventional methods of data collection and map production in geosciences. The present work represents an endeavour of applying remote sensing and geographic information systems (GIS) in geomorphological studies. Several objectives form the main scope of the study of which assessing the capability of using and integration of remote sensing and geographic information systems to discern the main geomorphologic units is the most important one. To fulfil these objectives, numerous data (e.g. topographic and geologic maps, satellite images, and climatic data) and methods are used.

The thesis consists of six chapters, *chapter one* manifests the general setting of the study area. It illuminates the main morphological units that are: coastal zone and coastal plain, table lands, Red Sea terrain, and drainage basins. It reveals as well the foremost aspects of the area such as climatic conditions, aridity indices, coastal environment, and cultural manifestations.

Chapter two signifies types and ages of the litho-stratigraphy and the regional structure. Several attempts are achieved to discriminate the main rock formations from the ETM+ image such as colour band composite, image ratioing, and supervised classification. The last one gives the most acceptable results for discerning the main rock units.

Chapter three is concerned with structural landforms to clarify the interaction between tectonics and geomorphic processes. It is divided into four sections as follows: The first section is an introduction denoting to scope of the study. Section two discusses the definition of lineaments in view of geology, geomorphology, and remote sensing. Section three presents a variety of advanced methods of image processing for mapping and detecting lineaments. Directional and non-directional spatial filters are widely applied to reveal the main linear features. Finally, section four exhibits the structural forms as faults, warped landforms, peneplanation, diapiric plutons, dyke swarms, and joints. This section points out many criteria and methods for distinguishing faults, dip direction and quantity as well. Numerous geomorphologic and geologic maps are presented within this section for exposing the general outlines of the study area.

Chapter four comes as an attempt to signify a standard method for automation extraction of drainage networks from the processed SRTM images. The model executes stream orders, watershed delineation, and quantifying the most important morphometric parameters such as linear aspects, areal, and relief analysis. The study discusses the validity and competence of extracting drainage networks of different sizes from the SRTM image in comparison with

topographic maps of scale 1:100.000 and 1:50.000. It has been deduced that the SRTM images are to some extent equivalent to the topographic maps 1:50.000. Hydrological significances are also argued via qualitative and quantitative analysis of the drainage systems. Drainage initiation is discussed in regarding to geomorphologic and geologic proofs. Eventually, some fluvial forms are studied such as deltas and terraces.

Chapter five presents an assessment of flash floods and vulnerability analysis. Probability of annual occurrence and return period are computed in a historical framework since 1921. Rain deep over the Red Sea Terrain is extracted using IDW (Inverse Distance Weighted) method and it is involved in estimating probable runoff. On the other hand, the study pointing out the synoptic weather pattern leads to torrential rain based on METEOSAT infrared images for the period 1990-1997. Flood potentiality is assessed using some hydro-morphometric parameters and flood magnitude is weighted as a function of flood potentiality, runoff characteristics, and human interferences.

Chapter six is interested in distinguishing the coastal forms and divided into four parts. The first part tackles erosional forms (i.e. coastal cliffs and wave-cut platforms). Part two deals with depositional forms such as sand beaches, nebka, and sand spits. Part three concerns with submerged forms such as estuaries, lagoons, offshore islands, modern coral reef, and submarine terraces and canyons. Eventually, the fourth part exposes characteristics of the raised coral terraces and their relative ages in comparison with different locations along the Egyptian Red Sea Coast.

Contents:

Introduction …….. 1-8

Chapter One: General aspects of the study area…… 9-31
1. Location…… 9
2. Morphological units……. 9
2.1. Coastal zone and coastal plain…… 9
2.2. Tablelands…….. 11
2.3. Red Sea terrain……... 11
2.4. Drainage basins…….. 12
3. Climatic conditions…….. 16
3.1. Air temperature……... 16
3.1.1. Mean and absolute maximum temperature…….. 16
3.1.2. Mean and absolute minimum temperature……... 16
3.1.3. Mean monthly of temperature…….. 17
3.1.4. Mean and absolute diurnal range of temperature……. 17
3.2. Surface wind……... 17
3.3. Rainfall……... 19
3.4. Evaporation and relative humidity……. 19
4. Aridity index…… 19
5. Coastal environment……. 22
5.1. Waves……. 22
5.2. Tide……. 24
5.3. Longshore currents…… 25
5.3.1. Set of high velocity…….. 26
5.3.2. Set of low velocity……... 26
6. Cultural manifestations…… 27
6.1. Settlements……. 27
6.2. Population……... 27
6.3. Economic activities…… 28
References…… 30

Chapter Two: Geological setting…….. 32-64
1. Litho-Stratigraphy…… 32
1.1. Pre-Cambrian rocks (basement rocks)……... 32
1.1.1. Paragneisses, Migmatites and Geosynclinal Metasediments and Metavolcanics…… 32
1.1.2. Serpentinite…….. 34
1.1.3. Metagabbro-Diorite Complex…….. 34
1.1.4. The Older Granites (Shaitan Granites)……. 34
1.1.5. Dokhan Volcanics…… 34
1.1.6. Hammamat Group…… 34
1.1.7. The Younger Gabbro…… 34
1.1.8. The Younger Granitoids (Gattarian Granites)…….. 34
1.2. Sedimentary rocks…….. 36
1.2.1. Cretaceous and Eocene rocks…….. 36
1.2.2. Miocene and later sediments……... 38

2. Mapping the main rock units using Landsat Enhanced Thematic Mapper Plus (ETM+) imagery……... 41
2.1. Characteristics of the ETM+ imagery data…… 41
2.2. Visual enhancement……... 41
2.2.1. Contrast stretching……... 41
2.2.2. Convolution filtering…… 42
2.3. Elements of image interpretation……... 43
2.4. Data calibration…..... 44
2.5. Digital image processing and interpretation……... 45
2.5.1. Colour band composite (CBC)……. 45
2.5.2. Compound band ratioing (CBR)…….. 45
2.5.3. Multispectral supervised classification (MSC)…… 49
3. Regional structure…… 58
3.1. Faulting……. 58
3.2. Folding…….. 61
References……..... 62

Chapter Three: Structural landforms…… 65-144
1. Introduction…….. 65
2. Definition……. 65
3. Methods of mapping lineaments…….. 66
3.1. Image processing…… 66
3.1.1. Edge detection filters…… 67
3.1.2. Shaded and painted relief maps…… 70
3.2. Data extraction……... 71
3.3. Data comparison and integration…… 72
3.4. Statistical and spatial analysis of lineaments……. 73
4. Features recognitions……... 77
4.1. Faults…….. 77
4.2. Warped landforms…….. 85
4.2.1. Methods of the study…… 88
4.2.2. Terrain analysis…… 93
4.2.3. Structure of the coastal warped forms…….. 95
4.2.4. Structure of the inland depressions…….. 97
4.2.4.1. Mohamed Rabah Basin…….. 97
4.2.4.2. Wasif Basin…… 101
4.2.4.3. Umm al-Hawaytat Basin…… 104
4.2.4.4. an-Nakheil Basin…… 108
4.3. Old erosion surfaces……... 118
4.3.1. Exhumed erosion surface……. 118
4.3.2. Buried erosion surfaces…… 121
4.3.3. Peneplanation phases……... 122
4.4. Diapiric plutons…….. 123
4.4.1. Plutonic of Jabal El Barud…… 124
4.4.2. Jabal Kab Amiri……... 125
4.4.3. Jabal Umm Had…… 125
4.4.4. Jabal Umm Oradah……... 126
4.5. Dyke swarms…….. 131

4.6. Joints ...……... 136
References…… 139

Chapter Four: Modelling and analyzing drainage systems…….. 145-214
1. Introduction. ……... 145
2. Terminology…… 145
3. Methodology…… 146
3.1. Processing digital elevation model……. 146
3.2. Determining flow direction…… 149
3.3. Calculating flow accumulation and delineating watersheds…….. 150
3.4. Extracting stream networks, orders and automatic vectorization……... 151
4. Model validity and competence……... 153
4.1. Variable analysis…… 153
4.2. Variance analysis…… 155
5. Drainage basins…… 158
5.1. El Barud…….. 158
5.2. Abu Asala……... 159
5.3. Naqarah…….. 159
5.4. Umm Iffinah……... 160
5.5. Safaga…… 161
5.6. Gasus…….. 163
5.7. Abu Shiqayli……... 165
5.8. Abu Sebekha……... 166
5.9. Queih…….. 166
5.10. Abu Hamra……... 167
5.11. Hamraween……... 168
5.12. al-Ambagi……. 169
6. Morphometric analysis……. 173
6.1. Linear aspect……... 173
6.1.1. Basin length, width, and perimeter…….. 173
6.1.2. Stream numbers and orders…….. 175
6.1.3. Total stream length……... 176
6.1.4. Average stream length…….. 176
6.2. Spatial analysis……... 176
6.2.1. Drainage area……... 176
6.2.2. Basin shape……... 177
6.2.2.1. Circularity ratio…….. 178
6.2.2.2. Elongation ratio…….. 178
6.2.3. Drainage density……... 179
6.2.4. Stream frequency…… 179
6.2.5. Constant of channel maintenance……. 180
6.3. Relief analysis…… 180
6.3.1. Basin relief……... 180
6.3.2. Slope average……... 180
6.3.3. Relief ratio…… 181
6.3.4. Texture ratio…… 181
6.3.5. Hypsometric analysis……... 182
7. Fluvial landforms……. 186

7.1. Drainage initiation…….. 186
7.2. Deltas and alluvial fans…….. 189
7.3. Wadi terraces…….. 196
7.4. Microforms……. 208
References…… 211

Chapter Five: Flash floods: assessment and vulnerability analysis……. 215-243
1. Data and methods……. 215
2. Runoff prediction and analysis……. 218
2.1. Peak discharge…… 218
2.2. Time of concentration…… 219
3. Historical background…….. 219
3.1. Probability of annual occurrence and return period……... 223
4. The synoptic weather pattern leads to torrential rain……... 225
5. Flash flood potentiality and risk assessment…… 228
6. Human interference…….. 232
7. Flood magnitude and vulnerability…….. 233
Appendix I: runoff coefficients for rational equation…….. 240
Appendix II: conversion factors……... 240
References…… 241

Chapter Six: Coastal landforms……... 244-271
1. Erosion forms……... 244
1.1. Coastal cliffs and wave-cut platform…….. 244
2. Depositional forms……... 244
2.1. Beaches and sand spits……... 244
2.2. Nebka…….. 245
3. Submerged forms…… 246
3.1. Estuaries…… 246
3.2. Offshore islands…….. 247
3.2.1. Safaga island…… 247
3.2.2. Brother islands……. 248
3.3. Modern coral reef……... 248
3.3.1. Physical limiting factors……... 248
3.3.2. Types of coral reef……... 250
3.3.3. Spatial distribution……... 251
3.4. Lagoons……. 255
3.5. Mangrove communities…….. 257
3.6. Submarine topography……... 259
3.6.1. Submarine terraces……... 259
3.6.2. Submarine canyons…….. 262
4. Coral terraces……... 265
References……..... 269

Conclusions ……..……. 272-282

List of figures:

Fig. 1: Investigated locations during the field works…….…….. 7
Fig. 1-1: Morphological units in the study area……. 10
Fig. 1-2: Panoramic view of the eastern escarpment of Jabal Naqarah showing four separated mountainous blocks and rugged relief……. 13
Fig. 1-3: Digital elevation model (DEM) of the study area……... 14
Fig. 1-4: Hydrographic map of the study area…… 15
Fig. 1-5: Percentage frequency of the annual mean of blowing winds…….. 18
Fig. 1-6: Graphical representation of temperature and rainfall after Walter & Lieth (1967)……. 21
Fig. 1-7: Ratio drought index of the study area using band ratio 4/3……. 22
Fig. 1-8: Frequency of wave heights in Hurghada (a) and El Quseir (b)……... 23
Fig. 1-9: The modern coral reefs acting as line of breaker north of El Quseir……... 24
Fig. 1-10: Tidal range in meters……. 25
Fig. 1-11: Influence of local topography and breaking waves on the longshore currents at the outlet of wadi Gasus……. 26
Fig. 1-12: Population growth in the study area during the period 1986-2010……... 28
Fig. 1-13: Changes of the economic activities in the study area during the period 1986-1996…. 29
Fig. 2-1: Geological map of the study area…… 33
Fig. 2-2: Columnar section of Jabal Duwi……. 37
Fig. 2-3: Miocene section in the study area…… 39
Fig. 2-4: Original image and contrast stretching image……. 42
Fig. 2-5: Original image, convolution 3 x 3 edge enhanced image and low pass filter image….. 43
Fig. 2-6: Extracted image of Jabal Barud, effects of tonal differentiation, and spectral curves of granite rocks……. 44
Fig. 2-7: Enhanced ETM+ image of band composite 7, 4 and 2 (R, G, B) showing a high contrast between the main rock units in the study area……. 48
Fig. 2-8: A false colour composite ETM+ image using hydrothermal compound band ratioing 7/5, 3/1, 4/3 (R, G, B) showing high contrast between the main rock units…… 50
Fig. 2-9: Equiprobability contours defined by the maximum-likelihood classifier……... 51
Fig. 2-10: Signature mean plot of the image classes…….. 52
Fig. 2-11: A sample of the output histograms of the selected AOI in band 1 for classes 1. Q, 2. T, 3. K, 4. gy, 5. fel, 6. go, 7. md, 8. sp, 9. ms and 10. coral reefs…….. 53
Fig. 2-12: Classified geological map of the study area…….. 57
Fig. 2-13: Regional geological map of the northern Red Sea and surrounded area in Egypt…… 59
Fig. 2-14: Predominant fault directions in the northern part of the Red Sea…… 60
Fig. 2-15: A normal fault separates the Nubian sandstone and the metavolcanic basement rocks along Qena-El Quseir highway……. 60
Fig. 2-16: Geologic section of Bir Ambagi fold …….. 61

Fig. 3-1: Method used for mapping lineaments……. 67
Fig. 3-2: Comparison between actual data values and ideal model step edge derived using edge detection algorithms……. 68
Fig. 3-3: Types of detectable edges using convolution filter algorithm……. 68
Fig. 3-4: Directionally filtered images……... 69
Fig. 3-5: Original image (left) and the 2ed derivative enhanced image (right)…….. 69
Fig. 3-6: Extract of the shaded relief map covering the southern part of the study area…… 70
Fig. 3-7: Extract of the painted relief map covering the southern part of the study area……... 71
Fig. 3-8: Tonal variations used to manually extract linear features. (a) Lineaments showing darker colour, (b) lineaments showing lighter colour…….. 72
Fig. 3-9: Lineaments map of the study area……... 74
Fig. 3-10: Azimuth frequency diagrams of the lineaments…… 74
Fig. 3-11 a: Spatial concentration map of the lineaments per 5`lat. $_x$ 5`long. unit area and contour interval 10 lineations……. 76
Fig. 3-11 b: Patterns of lineament concentration at Jabal Naqarah (left) and Jabal Umm Oradah (right)……. 76
Fig. 3-12: Regional geological profiles showing the domino-style fault blocks distinguishing the study area…… 78
Fig. 3-13: The coastal fault cliff of Jabal Naqarah……. 80
Fig. 3-14: (A) An inferred E-W offset in Jabal Naqarah. (B) An inferred NW-SE and WNW-ESE faults in Queih area……... 82
Fig. 3-15: DEM overlain by ETM+ image band combination (7, 4, 2) showing fault-controlled forms at Jabal Naqarah……. 83
Fig. 3-16: Zigzag geometry interposed by morphotectonic depressions west of Jabal Duwi…… 83
Fig 3-17: Major faults detaching Jabal Gasus…… 84
Fig. 3-18: Regular NW faults influencing the southern wall of Sodmein gorge…… 84
Fig. 3-19: Spatial distribution of the main warped forms in the study area……... 87
Fig. 3-20: Outcrop identifications of Jabal Duwi……... 89
Fig. 3-21: Dip angle estimation…….. 90
Fig. 3-22: DEM of the inland warped landforms……... 91-92
Fig. 3-23: Subset of ETM+ mosaic images showing the inland depressions……. 94
Fig. 3-24: Geological cross sections along the coastal plain…….. 95
Fig. 3-25: 3D perspective views of some tilted forms along the coastal plain……... 96
Fig. 3-26: Incised gullies detaching a gypsum massif plateau north of wadi Hamraween…… 97
Fig. 3-27: Geomorphological map of Mohamed Rabah Basin……... 99
Fig. 3-28: Panoramic view of the central cuestas of Jabal Mohamed Rabah……. 100
Fig. 3-29: Geomorphological map of Wasif Basin…… 103
Fig. 3-30: Front of the southern cuesta of Wasif…… 104
Fig. 3-31: Geomorphological map of Umm al-Hawaytat Basin……..... 107

Fig. 3-32: Cuesta of Umm al-Hawaytat……. 108
Fig. 3-33: Simplified cross section showing the major structure along Wasif and Umm al-Hawaytat latitude…….. 108
Fig. 3-34: Geological map of Jabal Duwi…….. 109
Fig. 3-35: Geomorphological map of Jabal Duwi…….. 111
Fig. 3-36: Extract of a topographic map 1:50.000 showing right angle junctions of wadi el-Saqia at locations (A) and a sub- basin at location (B)…… 112
Fig. 3-37: Colour level slice 3d view showing a tributary of wadi Sodmein that follows an inferred fault-drag syncline…….. 113
Fig. 3-38: Structural cross sections along Jabal Duwi. 113
Fig. 3-39: (A) east-west panoramic view of southern Jabal Duwi showing microtectonic faults and (B) panoramic view of the western slopes of Jabal Duwi……. 114
Fig. 3-40: Fallen rocks in Sodmein gorge…….. 114
Fig. 3-41: Entrance of Sodmein Cave and the surrounded microtectonics…… 115
Fig. 3-42: Section through Sodmein Cave……. 116
Fig. 3-43: A relatively wide sinkhole in the roof of Sodmein Cave……... 116
Fig. 3-44: Middle Palaeolithic core of limestone flake (Sodmein Cave)……... 117
Fig. 3-45: Geological map and profile showing the exhumed erosion surface…….. 119
Fig. 3-46: Geological map of Jabal Umm Kujurah (upper) and geological profile (lower) showing exhumed and buried erosion surfaces…… 120
Fig. 3-47: An exposure section of the old erosion surface of Jabal Naqarah……. 121
Fig. 3-48: Cross section of wadi an-Nakheil…….. 122
Fig. 3-49: Spatial distribution of the plutons…….. 123
Fig. 3-50: (a) DEM of Jabal El Barud superimposed by the geological map. (b) General view to Jabal El Barud…….. 124
Fig. 3-51: DEM of Jabal Kab Amiri superimposed by the geological information……... 125
Fig. 3-52: (a) Geological map of Jabal Umm Had. (b) DEM of Jabal Umm Had superimposed by ETM+ image band combination 7, 4, 2……... 127
Fig. 3-53: Geological map of Jabal Umm Oradah……. 128
Fig. 3-54: (a) The outer rim of Jabal Umm Oradah looking northwest. (b) Paragneisses and migmatites of Jabal Umm Oradah looking westward…….. 129
Fig. 3-55: Cavities developed in the granite rocks……. 129
Fig. 3-56: (a) Relatively large joint-blocks of older granite gradually rounded into smooth forms by disintegration south of wadi El Barud. (b) Cubic fragments splinting due to thermal weathering. ……. 130
Fig. 3-57: Parallel narrow and nearly straight dykes…….. 132
Fig. 3-58: Dyke recognitions…….. 132
Fig. 3-59: Positive (ridge) and negative (trench) relief formed due to relative resistance of dykes……. 135

Fig. 3-60: Conjugate joint system influencing the younger granite of Jabal Barud…….. 137
Fig. 3-61: Non-orthogonal joint pattern crossing Jabal Umm al-Hawaytat…….. 137
Fig. 3-62: Orthogonal, sheeting, and oblique joint sets affecting granite masses in wadi Safaga. 137
Fig. 4-1: Drainage system components…….. 146
Fig. 4-2: Scheme of the hydrological model…….. 147
Fig. 4-3: (a) DEM contains missing values in the circles and (b) the same DEM after avoiding missing values…….. 148
Fig. 4-4: Grid errors: (a) profile view of a sink before and after filling and (b) profile view of a peak before and after removing…… 149
Fig. 4-5: Determining distances between orthogonal and diagonal cell centers…… 150
Fig. 4-6: Determining flow direction…….. 150
Fig. 4-7: Comparison between original and dissolved features……. 152
Fig. 4-8: Number of streams before and after dissolving…….. 152
Fig. 4-9: Coefficient of variation of the total stream numbers…….. 157
Fig. 4-10: Coefficient of variation of the total stream lengths…….. 157
Fig. 4-11: Wadi El Barud: (a) DEM and linear features and (b) watershed and drainage network…….. 159
Fig. 4-12: Wadi Abu Asala: (a) DEM and linear features and (b) watershed and drainage network…….. 160
Fig. 4-13: Wadi Naqarah: (a) DEM and linear features and (b) watershed and drainage network…….. 161
Fig. 4-14: Wadi Umm Iffinah: (a) DEM and linear features and (b) watershed and drainage network……. 162
Fig. 4-15: Wadi Safaga: (a) DEM and linear features and (b) watershed and drainage network... 163
Fig. 4-16: Wadi Gasus: (a) DEM and linear features and (b) watershed and drainage network ... 164
Fig. 4-17: Wadi Abu Shiqayli: (a) DEM and linear features and (b) watershed and drainage network……. 165
Fig. 4-18: Wadi Abu Sebekha: (a) DEM and linear features and (b) watershed and drainage network……. 166
Fig. 4-19: Wadi Queih: (a) DEM and linear features and (b) watershed and drainage network… 168
Fig. 4-20: Wadi Abu Hamra: (a) DEM and linear features and (b) watershed and drainage network……. 169
Fig. 4-21: Wadi Hamraween: (a) DEM and linear features and (b) watershed and drainage network……. 170
Fig. 4-22: Wadi al Ambagi: (a) DEM and linear features and (b) watershed and drainage network…….. 172
Fig. 4-23: Bifurcation ratio to number of streams and relation of stream lengths to stream orders……... 177
Fig. 4-24: Hypsometric curves and integral of the drainage basins……... 185

Fig. 4-25: Middle Miocene drainage systems in Egypt…….. 188
Fig. 4-26: Late Miocene drainage systems in Egypt. …… 188
Fig. 4-27: Examples of the data model output: a. delta wadi Abu Hamra and b. delta wadi Abagi…… 190
Fig. 4-28: Relation between drainage and deltaic areas……. 190
Fig. 4-29: Extract of a topographic map 1:200.000 showing extension of the deltaic cones below the present-day Red Sea level…… 191
Fig. 4-30: Slope profiles of the deltas along the principal channels…….. 193
Fig. 4-31: Configurations of the deltas under study……... 194
Fig. 4-32: Inverted colour ASTER image showing an example of the inland alluvial fans in wadi el-Saqia, NW Jabal Duwi…… 195
Fig. 4-33: Talus cone of fan-like shape, wadi Umm Taghir…….. 195
Fig. 4-34: White sands filling wadi el-Barud……. 195
Fig. 4-35: Cross profiles showing the alluvial terraces in wadis Abu Hamra, Queih, and al-Ambagi……. 197
Fig. 4-36: Sedimentological section of the 10-12m terrace of wadi al-Ambagi …….…….. 199
Fig. 4-37: Paired wadi terraces at wadi al-Ambagi…… 200
Fig. 4-38: A soil profile of the 20-21 m terrace of wadi al-Ambagi…….. 200
Fig. 4-39: Travertine deposits overlooking a cavernous…… 202
Fig. 4-40: Terrace 12-13 m in wadi Gasus (left) and influences of neotectonics and evaporites (right)…….. 203
Fig. 4-41: Microscopic views showing the heterogeneous materials (left) and the re-worked aeolinaite-like (left)…….. 203
Fig. 4-42: Showing the alluvial deposits overlaying the coastal raised coral reefs at the mouth of wadi Abu Safi……... 204
Fig. 4-43: Side scraper implement found in wadi Hamraween…….. 206
Fig. 4-44: Braided streams in wadi Safaga..... 209
Fig. 4-45: An incised reach of wadi Umm Taghir…….. 210
Fig. 4-46: Gorge of wadi Sodmein……. 210
Fig. 5-1: Extrapolated isohyetal map…….. 217
Fig 5-2: Peak discharge (a) and time of concentration (b)…… 220
Fig. 5-3: Approximate rainfall over the Red Sea Mountains (1925-1997)…… 224
Fig. 5-4: Probability of annual occurrence of the mountainous rainfall……. 224
Fig. 5-5: METEOSAT infrared images covering northern Red Sea showing convection clouds during the major flash flood events for the period 1990-1997……. 227
Fig. 5-6: TRMM image reveals the Red Sea condition on 3rd February 2006…… 229
Fig. 5-7: Flash flood potentiality assessment……. 231
Fig. 5-8: Flash flood potentiality assessment using bifurcation ratio ($\mathcal{R}_b$), stream frequency ($\mathcal{F}_s$), and drainage density ($\mathcal{D}_d$)……. 232

Fig. 5-9: Pattern of land utilization in Safaga city…….. 236
Fig. 5-10: Pattern of land utilization in El Quseir city……... 236
Fig. 5-11: Recent ephemeral channels crossing and bounding Umm al-Hwaytat village in wadi Safaga……... 237
Fig. 5-12: Culverts and bridges used to preserve the coastal highway and railway……... 238
Fig. 5-13: Effects of floods on Umm al-Hwaytat – Wasif road……. 239
Fig. 6-1: Small-scale sand spite northern of wadi Queih mouth…… 245
Fig. 6-2: Sharm wadi Umm Ayish……. 247
Fig. 6-3: Bathymetric profile showing Safaga Island……. 247
Fig. 6-4: The older brother island……... 249
Fig. 6-5: The little brother island…… 249
Fig. 6-6: Spatial locations of the main reefs near Safaga……... 252
Fig. 6-7: Reefs of Shaar, Sbeer, Claude, Handy and Abdallah, south eastern Safaga……... 254
Fig. 6-8: Geomorphology of the non-reef lagoon at wadi Naqarah sharm……. 256
Fig. 6-9: Geomorphology of the reef barrier lagoon at wadi Abu Shiqayli sharm……. 256
Fig. 6-10: Inter-platform lagoons at Shaab Safaga (right) and north of wadi Queih sharm (left).. 257
Fig. 6-11: Mangroves community in the lagoon south east of wadi Abu Hamra…….. 258
Fig. 6-12 a: Shaded relief map showing the main submarine topography……. 260
Fig. 6-12 b: 3d view showing the main submarine topography and the submerged deltas…… 260
Fig. 6-13: Topographic and bathymetric profiles of the nearshore zone…… 261
Fig. 6-14. Correlation between the submarine terraces of 100, 50, and 20 m bsl and the generalized curve of sea level rise since the last ice age…….. 262
Fig. 6-15: Submarine profile of wadi Safaga canyon……. 263
Fig. 6-16: Generalized cross-section showing the stratigraphic relations, major facies, and the suggested age of the post-gypsum sequence of the Red Sea coastal plain, Egypt…….. 266

List of tables:

Table 1: Satellite images involved in the study…….. 3
Table 2: Topographic maps……. 3
Table 3: Geologic maps……... 3
Table 4: Time schedule……... 6
Table 1-1: Aridity index of the studied stations after Emberger…… 20
Table 1-2: Wave height prediction in the study area……... 23
Table 2-1: Classification of the basement complex rocks of the Eastern Desert……... 35
Table 2-2: Correlation matrix of the ETM+ Landsat image……... 42
Table 2-3: Filter Kernel used for edge enhancement……. 43
Table 2-4: Mean and standard deviations of the ETM+ image……... 46
Table 2-5: OIF values and ranked band composites……... 46
Table 2-6: Experimental compound band ratioing (CBR) and assessment……. 49
Table 2-7: Number of AOI for each class name……. 51
Table 2-8: Absolute classification contingency matrix of the assembled AOI……... 55
Table 2-9: Percentage classification contingency matrix of the assembled AOI…… 55
Table 2-10: Producer's and user's accuracies of the assembled AOI…… 56
Table 2-11: Approximately spatial distribution of the main rock types in the study area….. 56
Table 3-1: Experimental kernels used for direction filters…….. 69
Table 3-2: Non-directional Laplacian filter kernel…….. 69
Table 3-3: Statistical analysis of the lineament map……... 73
Table 3-4: Comparison between estimated and field measured dip angles…… 90
Table 3-5: Some morphological parameters of the inland depressions…….. 95
Table 4-1: Percentage of sinks in the involved SRTM images……... 149
Table 4-2: Independent variables analysis…….. 154
Table 4-3: Dependent variables analysis……. 156
Table 4-4: Coefficient of variation of the total stream numbers…… 157
Table 4-5: Coefficient of variation of the total stream lengths……... 158
Table 4-6: Morphometric parameters of drainage basins and networks……. 174
Table 4-7: Average stream lengths versus stream orders…… 176
Table 4-8: Morphometric characteristics of the deltas…… 189
Table 4-9: Heights of the wadi terraces……... 196
Table 5-1: Analysis of rainfall and runoff……... 216
Table 5-2: Extreme rainfall events (1925-1997)…… 221
Table 5-3: Probability of annual occurrence and return period analysis……. 225
Table 5-4: Pattern of human interferences…….. 234
Table 5-5: flood community and magnitudes…….. 234

THIS PAGE IS INTENTIONALLY LEFT BLANK

INTRODUCTION

The present work represents an endeavour of applying remote sensing and geographic information systems (GIS) in geomorphological studies. Since the inception of the Landsat program in the early 1970s, remote sensing in particular has become an increasingly important tool for improving conventional methods of data collection and map production in geosciences. The potential of using remote sensing accompanied by GIS in geology and geomorphology has been long term discussed in the principal literatures e.g. Lillesand & Kieffer 1977-2000, Drury 1987-2001, Avery & Berlin 1992, Campell 1996, Easterbrook & Kovanen 1998, Jensen 2000, Sabins 2000, Janssen et al. 2001, Outtara et al. 2004, and Short 2005. The principal benefits of using remote sensing and GIS are that the automatic extraction of information using automatic classification, band ratioing, quantitative spectral analysis, easy digital integration with auxiliary data, and improving mapping and cartographic skills. Consequently, they are indispensable techniques for geomorphological and geological studies nowadays.

1. Problem Statement.

On one hand, although remote sensing and geographic information systems are recently founded, they have a broad range of applications. During the last three decades, specialists have developed several methods of automatic data extraction from space images integrated with spatial analysis of which one can mention the valuable contributions of More & Waltz (1983), Vaughn R. W. (1983), Clark & Wilson (1994), Akhir & Abdullah (1997), Ait Brahim et al (2000), Briere & Scanlon (2001), Bishta & El-Tarras (2002), Fisher, B. (2004), and Kocal et al. (2004) to lineament extraction and surface curvature. Maidment, D. R. (1993-2002) and Tarabtoon, D. (1991-2000) have contributed several methods of terrain analysis for hydrological purposes. Last but not least, the endeavors of Wood, J (1996), Wang & Yin (1997), and Jordan, G. (2002-2004) to terrain modeling for tectonic geomorphology. The field is still open for more innovations, especially in the light of developing means of image and data acquisition.

On the other hand, the Eastern desert of Egypt received formerly less attention than the western desert and the Nile Valley and it was mysterious for long time. Nowadays, it gains more interest for preserving and developing its natural resources and as

a tourist area along the Red Sea. Lithologic units of the Eastern Desert have undergone multiple stages of deformation and metamorphism associated with the evolution of the Red Sea and divergence of the Arabo-Nubian Shields. Therefore, the terrain is exceptionally rugged and composed of different types of igneous, metamorphic, and sedimentary rocks. Complex structural forms are also abundant. Consequently, the coastal area between Safaga and El Quseir is selected for the present study to reveal the potentiality of discerning and mapping the main geomorphological features using remote sensing and GIS techniques.

2. Objectives.

The main objectives of the study are:

1. To assess capability of using and integrating remote sensing and geographic information systems in the geomorphological study.
2. Discerning and mapping the main rock units relying on training sets, band rationing, and quantitative analyses of the multispectral bands.
3. To reveal structure arrangements and their impacts on the geomorphological setting.
4. Distinguishing the main geomorphological units in the study area accompanied by geomorphological maps, charts, and photographs.
5. Determining potentiality of using digital elevation model for automatically simulating small-scale drainage networks in comparison with conventional manual methods using topographic maps of scales 1:100.000 and 1:50.000.
6. Depicting the hydrological significances of the drainage networks via qualitative and quantitative analysis.
7. Assessment of flood occurrence and determining vulnerable sites and the synoptic weather pattern that leads to such incident torrential rainfall.
8. To accentuate a conceptual view of the geologic-geomorphologic evolution of the study area and climate changes during Pleistocene and Holocene epochs in particular.

3. Available Data.

3.1. Satellite Images.

The remotely sensed data involved within the present study are of TM (Thematic Mapper), ETM+ (Enhanced Thematic Mapper Plus), SRTM (Shuttle Radar Topography Mission) version 2, ASTER (Advanced Spaceborne Thermal Emission and Re-

flection Radiometer), Quickbird images, METEOSAT infrared and TRMM (Tropical Rainfall Measurement Mission) images. The images are either cloud-free or contain the minimal cloud cover with the exception of the METEOSAT and TRMM images. Table 1 showing the most necessary descriptions of each image as follows:

Table 1: *Satellite images involved in the study.*

Image Sensor	*Image Info.*	*Date of acquisition*	*Spatial Resolution*	*Format*	*Source*
TM	Path 174/ Row 042	01.10.1997	30 m	NLAPS	USGS*
ETM+	Path 175/ Row 040	22.12.2000	15, 30, 90 m	GEOTIFF	GLCF**
ETM+	Path 175/ Row 041	19.10.2000	15, 30, 90 m	GEOTIFF	GLCF
ETM+	Path 174/ Row 041	10.09.2000	15, 30, 90 m	GEOTIFF	GLCF
ETM+	Path 175/ Row 042	19.10.2000	15, 30, 90 m	GEOTIFF	GLCF
ETM+	Path 174/ Row 042	23.02.2003	15, 30, 90 m	NLAPS	USGS
ETM+	Path 175/ Row 043	19.10.2000	15, 30, 90 m	GEOTIFF	GLCF
ETM+	Path 174/ Row 043	10.09.2000	15, 30, 90 m	GEOTIFF	GLCF
ETM+	Path 173/ Row 043	05.10.2000	15, 30, 90 m	GEOTIFF	GLCF
ETM+	Path 175/ Row 044	01.09.2000	15, 30, 90 m	GEOTIFF	GLCF
ETM+	Path 174/ Row 044	16.11.2001	15, 30, 90 m	GEOTIFF	GLCF
ETM+	Path 173/ Row 044	06.11.2000	15, 30, 90 m	GEOTIFF	GLCF
SRTM	N26˚ E033˚	12 March 2003	90 m	HGT	GLCF
SRTM	N26˚ E034˚	12 March 2003	90 m	HGT	GLCF
ASTER_L1A	Different images.	2005-2006	15-90 m	HDF	NASA
QuickBird	Different images.	-	2.5, 3 m	JPG	Google Earth Plus v.4.0.0
METEOSAT	Sector 3	Different dates	3 km	JPG and GIF	Internet website
TRMM	-	03.March 2006	-	JPG	Earth observatory

** USGS: United States Geological Survey.*
*** GLCF: Global Land Cover Facility ftp://ftp.glcf.umiacs.umd.edu/*

3.2. Topographic and Geologic Maps.

Topographic and geologic maps of different scales are involved within this study as shown in tables 2 and 3.

Table 2: *Topographic maps.*

Scale	*Date*	*Source*
1:50.000	1989	E.G.S.A*
1:50.000	1970-1973	E.G.S.A
1:100.000	1975	E.G.S.A
1:200.000	N/A	Russian Maps
1:250.000	1976	M.S.A.**

**E.G.S.A. Egyptian General Survey Authority*
***M.S.A. Military Survey Authority*

Table 3: *Geologic maps.*

Label & Scale	*Date*	*Source*
Aswan 1:1000.000	1979	E.G.S.M.A*
Qena 1:500.000	1984	E.G.S.M.A
Safajah 1:100.000	1987	E.G.S.M.A
El Quseir 1:100.000	1987	E.G.S.M.A

**E.G.S.M.A. Egyptian Geological Survey and Mining Authority*

3.3. Climatic Data.

Climatological data of nineteen years (1975-1994) are analyzed to manifest the general climatic conditions in the study area. Rainfall analysis for flood probability estimation is based on unpublished meteorological data for the period 1925-1997 for the coastal stations (Hurghada and El Quseir), which are acquired from the Egyptian Meteorological Authority, Cairo. On the other hand, the METEOSAT infrared images are investigated for showing the synoptic weather pattern that leads to torrential rainfall along the Red Sea coast.

3.4. Field Work.

Although, satellite image interpretation establishes the backbone of the present study, field truth was an indispensable method for revising the interpreted data. Therefore, two field studies were carried out. The first one was done in the period 20-25 November 2004. This expedition designed to explore and compile a comprehensive view for the whole area under study. The second field study was carried out in the period 3-9 March 2007. The main purposes of this study were to verify image interpretation and investigating minor forms, which are too tiny to be detected from satellite images such as wadi terraces, raised beaches, and estuaries. Traverses across the topographic maps were predefined in order to obtain the most complete coverage with systematic intervals, as possible, to assure a greatest level of detail as shown in figure 1. Measurements of dip, lineation, joints, and fractures were recorded in the field with detailed description of lithology. Topographic profiles were measured as well in different locations to reveal the alluvial terraces and raised beaches.

4. Methods.

Different methods of data analysis are applied to fulfill the main purposes of the study and discussed in detail within each chapter. The main methods could be summarized as follows:

- Pre-processing operation includes image rectification and radiometric corrections.
- Computing aridity indices after Köppen (1931), De Martonne (1926), and Thornthwaite (1933). Hyper-arid condition is expressed after Emberger (1955) and Walter & Lieth (1967).
- Using band ratioing for expressing drought index and composite band ratio (CBR) for rock discrimination.

▪ Image enhancement using convolution filter 3x3 for edge enhancement and low pass filter for improving visual image interpretation.

▪ Elements of visual image interpretation are applied for accurate rock discrimination (e.g. colour, shadow, texture, shape, and pattern) and colour band composite is examined as well using the optimum index factor (OIF).

▪ Multispectral supervised classification (MSC) is applied for mapping the main rock formations.

▪ Edge detection filters (i.e. directional and non-directional filters), shaded and painted relief maps are processed for lineament extraction.

▪ Manual digitizing integrated with visual image interpretation is used for mapping lineaments.

▪ DEM analysis for dip estimation and hydrological modelling analysis.

▪ Statistical and mathematical methods are widely used to reveal the morphometric characteristics of drainage basins, drainage runoff, and probability of annual occurrence and return period of flash floods.

▪ Inverse distance weighted (IDW) method is applied to reveal lineament intensity and estimating rain deep over the Red Sea terrain as well.

5. Platforms.

Types of computer systems or software used for image analysis and data processing are:

▪ Erdas Imagine 9, Envi 4.3, Global Mapper 7, 3dem, ER_Mapper 7.4, Ilwis 3.2, and Envi 4.3 for digital image processing.

▪ ARCVIEW 3.2, ARCGIS 9.1 and Surfer 8 for spatial analysis and cartographic skills.

▪ Klimagramm is used to reveal hyper-arid conditions after Walter-Lieth.

▪ WXTide32 version 4.7 for tide predictions.

▪ Photoshop and Jasc Paint Shop Photo Album are used for photo enhancement and creating panoramic views.

▪ Microsoft Office XP package (2003) is widely used for statistical analysis using Excel, typing using Word Processing, and presenting by PowerPoint.

6. Time Schedule.

The study is preceded according to exact sequence stages since July 2004. Table 4 clarifies the main milestones of each stage. Stages 1, 2 and 3 are concerned with collection of the initial data (e.g. satellite images, topographic and geologic maps, literature reviews, and climatic data). These datasets were input by several ways such as manual digitizing, scanning, and editing. Stage of data collection in particular is continued until the end of the thesis parallel to the other stages. The early three stages enabled a community to efficiently complete stage 4. Equally, stage 5 was very important for revising image interpretation and correcting the manuscript of the thesis. Stages 6 and 7 in particular are the fruits harvested from the hard work done in the first five stages.

Table 4: *Time schedule.*

Year	*Months*												*Milestone*
	1	*2*	*3*	*4*	*5*	*6*	*7*	*8*	*9*	*10*	*11*	*12*	
2004							Field work						1. Data Collection
2005													2. Data input & 3. Data Manipulation.
2006													Data Manipulation (cont) & 4. Thesis Writing.
2007	Field work												Thesis writing (cont) & 5. Revising 6. Printing.
2008													7. Reviewing and oral Examination.

7. Structure of the Thesis.

The thesis is organized into six chapters as follows:

Chapter one reveals the general setting of the study area. It illuminates the main morphological units that are: coastal zone and coastal plain, table lands, Red Sea terrain, and drainage basins. It reveals as well the foremost aspects of the study area such as climatic conditions, aridity indices, coastal environment, and cultural manifestations.

Chapter two deals with the geological setting. It signifies types and ages of the lithostratigraphy and the regional structure. Several attempts are achieved to discriminate the main rock formations from the ETM+ image such as colour band composite, image ratioing, and supervised classification.

Chapter three is concerned with structural landforms to clarify the interaction between tectonics and geomorphic processes. It is divided into four sections as follows: The first section is an introduction denoting to the scope of the study. Section two

discusses the definition of lineaments in the view of geology, geomorphology, and remote sensing.

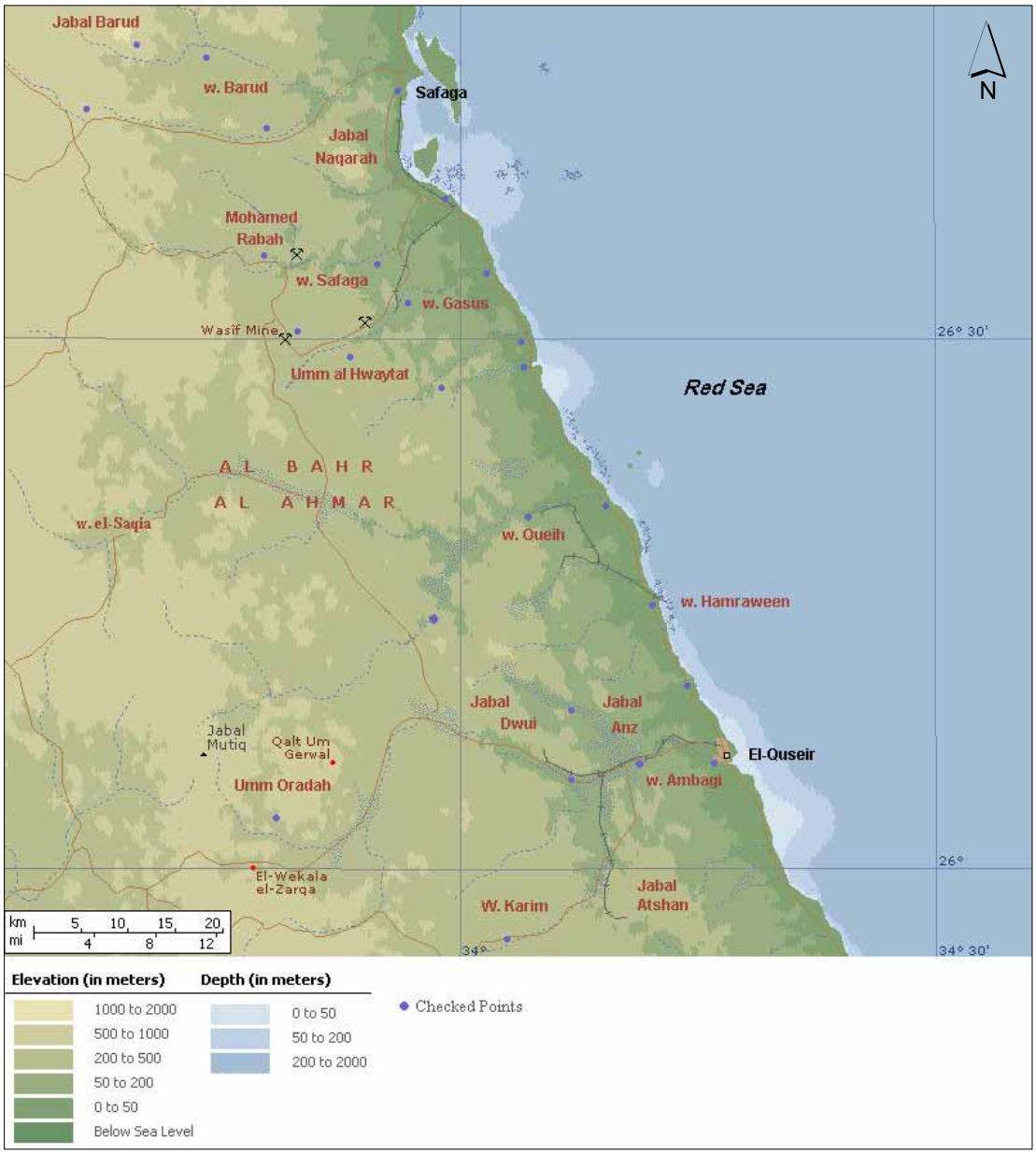

Fig.1: *Investigated locations during the field works.*

Section three presents a variety of advanced methods of image processing for mapping and detecting lineaments. Finally, section four exhibits the structural forms as faults, warped landforms, old erosion surfaces, diapiric plutons, dyke swarms, and joints. This section points out many criteria and methods for distinguishing faults, and dip direction.

Chapter four comes as an attempt to signify a standard method for automation extraction of drainage networks from the processed SRTM images. The model executes stream orders, watershed delineation, and quantifying the most important morphometric parameters such as linear aspects, areal, and relief analysis. The study discusses the validity and competence of extracting small-scale drainage networks from the SRTM image in comparison with topographic maps of scale 1:100.000 and 1:50.000. Hydrological significances are also argued via qualitative and quantitative analysis. Drainage initiation is discussed in regarding to geomorphologic and geologic proofs. Eventually, some fluvial forms are studied such as deltas and terraces, specifically.

Chapter five presents an assessment of flash floods and vulnerability analysis. Probability of annual occurrence and return period are computed in a historical framework since 1921. Rain deep over the Red Sea Terrain is extracted using IDW (Inverse Distance Weighted) method and it is involved in estimating the probable runoff. On the other hand, the study pointing out the synoptic weather pattern leads to torrential rain based on the METEOSAT infrared images for the period 1990-1997. Flood potentiality is assessed using some hydro-morphometric parameters and flood magnitude is weighted as a function of flood potentiality, runoff characteristics, and human interferences.

Chapter six is interested in distinguishing the coastal forms and divided into four parts. The first part tackles the erosional forms (i.e. coastal cliffs and wave-cut platforms). Part two deals with depositional forms such as sand beaches, nebka, and sand spits. Part three concerns with submerged forms such as estuaries, lagoons, offshore islands, the modern coral reef, and the submarine terraces and canyons. Eventually, the fourth part exposes characteristics of the raised coral terraces and their relative ages in comparison with different locations along the Egyptian Red Sea Coast.

1

GENERAL ASPECTS OF THE STUDY AREA

1. Location

The study area locates along the Red Sea coast of Egypt between wadi el Barud (Long. 33º 56`55" E & Lat. 26º 45` 39" N.) about 2.6 kilometers north of Safaga and wadi al Ambagi (Long. 34º 17` 05" E & Lat. 26º 05` 41"N.) south of El Quseir. It extends 88 kilometers approximately along the coastline and covers an area about 5350 square kilometers. Its western border pursues the watershed line that separates between the Red Sea drainage system and the Nile-Mediterranean system, while the Red Sea demarcates its eastern border.

Features of the great African rift geologically characterize the study area. The Pre-Cambrian basement complex rocks form the most widespread rock types (about 78 % of the total area). They leave a narrow longitudinal coastal plain that is formed by laterally coalescing of large deltaic plains and coral reefs. Strike faults gave rise to a remarkable topographical complexity. The Pre-Miocene (Cretaceous-Eocene) strata are preserved forming limestone warped forms of which Jabal Duwi is the most conspicuous one (Said, 1990). Thereby, endogenetic and exogenetic processes associate in evolution of the existing landforms and therefore the relief is considerably rigid and dissected.

2. Morphological Units

The study area could be divided into four major morphological units as follows (Fig. 1-1):

2.1. Coastal Zone and Coastal Plain.

On one hand, the coastal zone is characterized by shallow banks and coral reefs. Depths of hundreds of meters are reached within a few kilometers of the shoreline and there is commonly no effective continental shelf (Braithwaite, 1987).

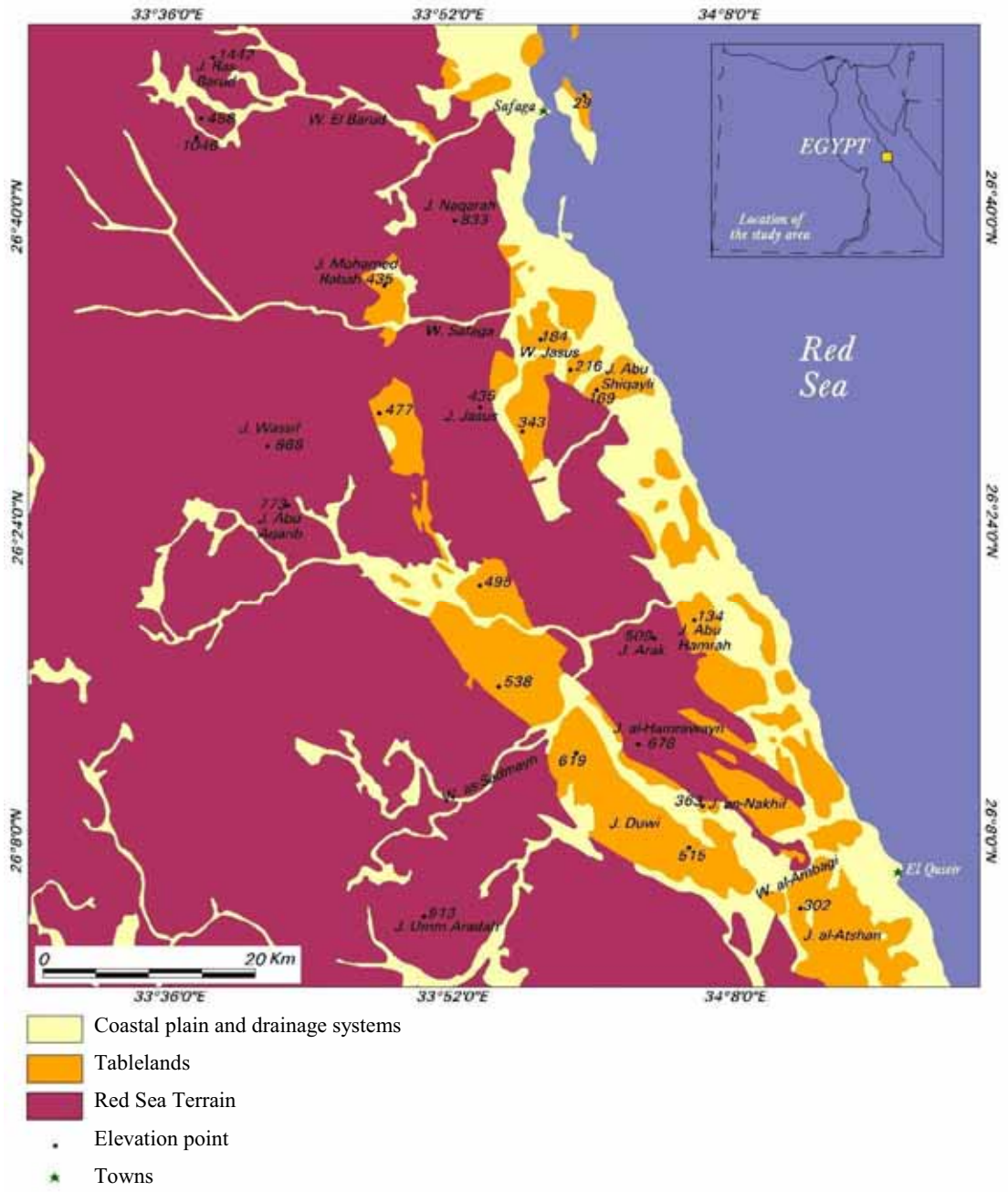

Fig. 1-1: *Morphological units in the study area.*

On the other hand, the costal plain occupies the lowlands parallel to the Red Sea coastline. As formerly mentioned, it is formed by coalescing alluvial fans and coral reefs. The width of the coastal plain varies greatly from place to place depending on the distance between the Red Sea Mountains and the coastline. Therefore, the maximum width is about 6 km north of Safaga where the deltaic fan of wadi el Barud pervades the sea. On the contrary, the width is about 400 meters south of Jabal Abu Shiqayli at latitude 26º 30` N where the Pliocene rocks are quite close to the coastline. Height of the coastal plain varies greatly between 0 near the coastline to 80-100

m asl at the foot-slopes of the Red Sea Mountains. This unit contains different destructional and constructional forms that will be discussed later in detail.

2.2. Tablelands.

Tablelands are located whether on the western border of the coastal plain or inland occupying the intermountain basins. They consist of Cretaceous-Tertiary rocks, which are formed mainly of limestone, sandstone, chalk, and conglomerates constituting low parallel escarpments. The coastal tablelands border the basement rocks from the east and attain an elevation about 155 m asl in Jabal Abu Shiqayli and 162 m asl in Jabal Abu Hamra. The rocks are slightly tilted seawards with general slopes varying between 5°-20° and constituting cuestas, tabular mesas, and inselbergs.

The inland tablelands are preserved within morphotectonic or geosynclinal depressions. So that, they are remnants of the earlier rock covers, which had been existed before the area was prone to the orogenic processes. They can be enumerated from north to south as Jabal Mohamed Rabah (375 m asl), Hills of Wasif (520 m asl), Hills of Umm al-Hawaytat (325 m asl), Jabal Duwi (627 m asl), Jabal an-Nakhil (334 m asl), and Jabal al-Atshan (295 m asl). They situated east of longitude 33º 47`E, while to the west of that longitude most, unless all, of the sedimentary rock cover has been completely eroded and removed. They have the same trend NNW-SSE as well as the same rock formation but, on the contrary of the coastal hills, they are significantly structurally controlled. As a result of that, they comprise distinct long sharp scarps that are a function of dip, thickness, and relative resistances of the rock strata. The form of Jabal Duwi is considered as cuesta owing to moderately dip with a notable difference in steepness as well as length of the front and back slopes. As a whole, the tablelands were experienced intensive faulting and folding that gave rise to distinctive landforms along the coastal plain and within the intermountain depressions.

2.3. Red Sea Terrain.

The Red Sea Mountains composed primarily of the Pre-Cambrian rocks that are crystalline in character (igneous and metamorphic rocks) and extending more or less parallel to the Red Sea at a comparatively short distance inland from the coastline. However, they do not form a continues range, rather a series of mountain blocks, which are more or less adjacent (Fig. 1-2) and dispose linear trend parallel to the coastline

with some detached masses and peaks (Said, 1962). The Red Sea Mountain Ranges themselves are not folded; instead, they have been formed due to a large extent by uplifting the margins of the rift (Braithwaite, 1987). The younger granite represents the dominant rock type within this terrain forming a wild rugged skyline because of its relatively high resistance to weathering processes (Aggour, 1997). The mountains in the study area rise to heights more than 800 m asl (Fig. 1-3). The highest mountains are Jabal Ras Barud (1442 m asl), Jabal Umm Oradah (913 m asl), and Jabal Naqarah (833 m asl) as can be seen in figure 1-1.

Regarding to the erosion cycle, Hamdan (1988) assumed that the physiographic characteristics of the Red Sea Mountains manifest youth stage characters. This is relying on the fact that incised wadis separating broad large blocks and wadi gradients are irregular with waterfalls, rapids, and lakes, which are all formed in response to lithological variations and structural lineaments.

2.4. Drainage Basins.

The Red Sea Mountains are stringency dissected by deeply incised wadis, which are divided into two opposite drainage systems. The first is the Red Sea wadi system characterized by short wadis and relatively small catchment areas, whereas the second system might be called the Nile-Mediterranean system distinguished by relatively long wadis and large basins (Embabi, 2004). The Red Sea system is an exterior discharge one, where all of the wadis debouching into the Red Sea. Most of them cut through the morphotectonic or the geosynclinal depressions, which are oval in shape and filled with alluvial sediments and blown sands. Such depressions are well conspicuous along the longitudinal profiles of wadis el Barud, Safaga, Queih, an-Nakheil, and al Ambagi from north to south successively (Fig. 1-4).

Generally, drainage networks are much intense and convergent owing to geologic structure and rugged relief. Therefore, consequent and obsequent wadis with dendritic and trellised patterns are common.

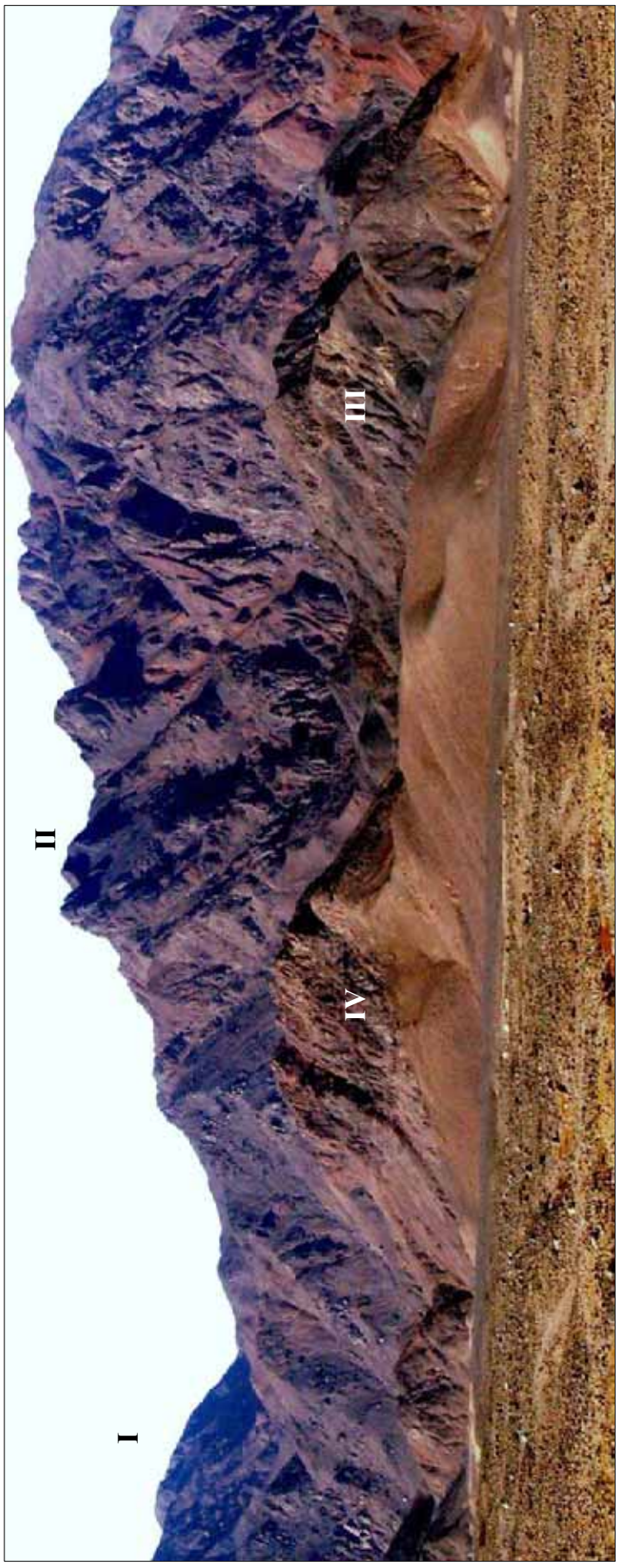

Fig. 1-2: *Panoramic view of the eastern escarpment of Jabal Naqarah showing four separated mountainous blocks and rugged relief.*

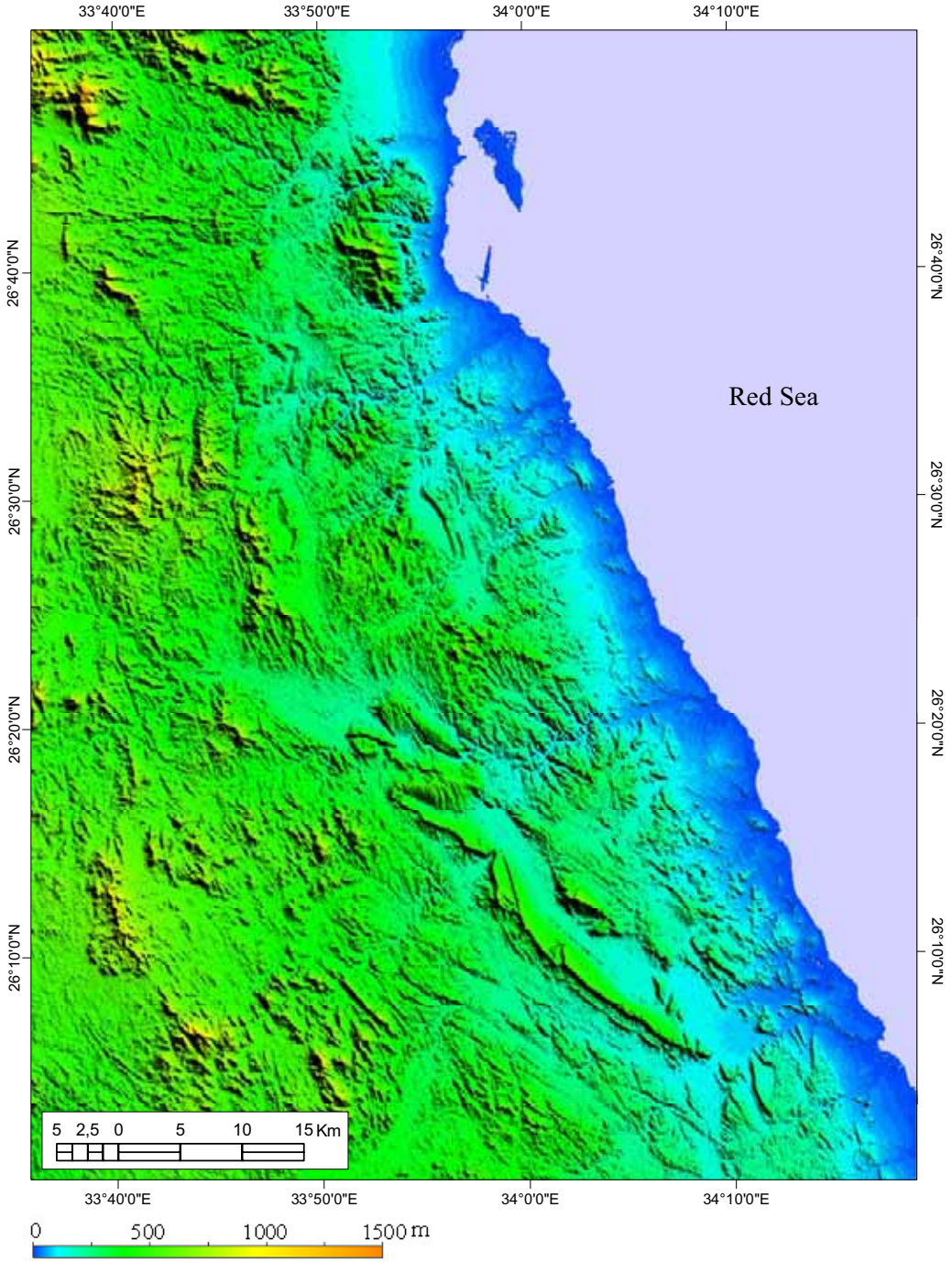

Fig. 1-3: *Digital elevation model (DEM) of the study area.*

(Data assembled using STRM image and calibrated by topographic map of scale 1:250.000)

Equally, features of river capture in the upstream areas, knick points, wadi terraces, and estuaries are common indicating sea level fluctuations and/or climatic changes. Some drainages are of superimposed-like shaped and antecedent such as wadi Sodmein that is down-cutting through Jabal Duwi exhibiting a narrow deep gorge.

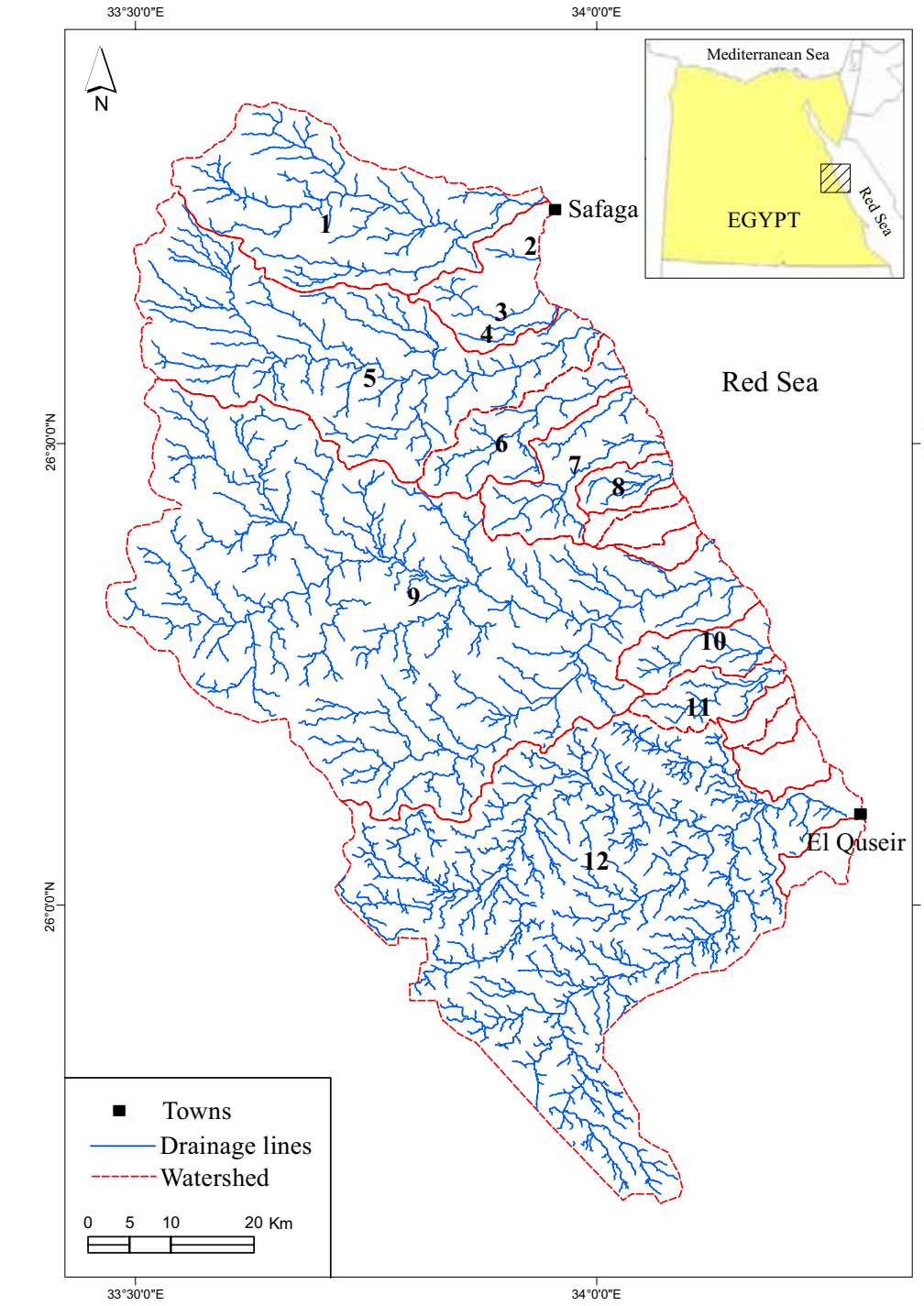

1. Barud 2.Abu Asala 3.Naqarah 4. Umm Iffinah 5. Safaga 6. Gasus
7. Abu Shiqayli 8. Abu Sebekha 9. Quieh 10. Abu Hamra 11. Hamraween 12. Ambagi

Fig. 1-4: *Hydrographic map of the study area.* *(Source: extracted from the DEM)*

Hamdan (1988) assumed that the Red Sea drainage system had been ensued during Pleistocene and Pliocene times, if not in Miocene, as the time when the Eonile was

developed (Said, 1993). Therefore, drainage networks of the study area could be considered as one of the oldest and complex drainage systems in Egypt.

Few wadis of the Eastern Desert ever convey streams of running water at the present day. Normally, it happens only for short periods after exceptionally heavy rainfalls in the mountains and occurs at intervals of several years. However, many wadis contain a certain amount of natural vegetation, which affords grazing for camels, sheep, and goats of the bedawin (Ball, 1939).

3. Climatic Conditions

Unlike the Mediterranean Sea, the Red Sea has much lesser influences on the climate of Egypt. In view of the fact that marine influences of the Red Sea are hampered by the Red Sea Mountains and confined to the coastal plain.

Unfortunately, no adequate climatic stations are available over the Red Sea Mountains. Therefore, two stations along the coastal plain are involved in the present study; they are: Hurghada and El Quseir. Data of these two stations with other two inland stations located in the Nile Valley (Assuit and Qena) are analyzed. Thereafter, meteorological records of nineteen years (1975-1994) of the four weather stations are analyzed as follows:

3.1. Air Temperature.

3.1.1. Mean and Absolute Maximum Temperature.

The highest values of the mean maximum temperature occur in June, July, and August. The mean maximum temperature ranges between 33.4ºC and 40.8ºC in El Quseir and Qena respectively. On the other hand, the absolute maximum temperatures exceed 40º C usually occurred in June and July. It attains 48.4º C in Assuit and 48.8º C in Qena because of their continental location, while it is relatively lower in the coastal stations recorded 43º C and 44.6º C in Hurghada and El Quseir respectively.

3.1.2. Mean and Absolute Minimum Temperature.

Normally, the lowest minimum temperatures take place in winter especially during January and December. The mean minimum temperatures vary greatly between 6.7º

C in Qena and 13.8º C in El Quseir. As well the absolute minimum temperature varies greatly between -0.4º C in Assuit and 4º C in El Quseir.

3.1.3. Mean Monthly of Temperature.

The mean monthly of temperature ranges between 13.2º C in Assuit during January and 32.4º C in Qena during August. During the period from April to November, the diurnal variation of temperature exceeds 20º C in most of the stations under study. According to Soliman (1972) this usually takes place in the coastal stations when the passage of Khamasin depressions causes the cool northerly winds to be replaced by the excessively hot southerly winds and similar values occur in the reverse process after the passage of a cold front. In addition, Edwards (1987) denoted that the hinterlands to all the Red Sea coasts consisting of vast areas of desert or semi-arid that led to a greater annual and diurnal range of temperature throughout the year.

3.1.4. Mean and Absolute Diurnal Range of Temperature.

The mean diurnal range is expressed as the difference between mean maximum and mean minimum temperature during the day, while the absolute diurnal range is expressed as the difference between absolute maximum and minimum temperatures during the day. The later one is very important for determining the exact role of the mechanical weathering in rock disintegration.

Normally, the mean diurnal range exceeds 20º C, where on the other hand, the absolute diurnal range is relatively higher ranges between 25.2º C and 24.2ºC in Hurghada and El Queseir successively. It is extremely higher in Assuit and Qena exceeding 33.8º C and 34.3º C respectively due to sea breeze that leads to soften and decrease the temperature variations along the coastal area. Thereby, shores of the Red Sea experience diurnal wind change usually reaching its maximum strength in early or mid afternoon (Edwards, 1987).

3.2. Surface Wind.

As a whole, the north and north-westerly winds are prevailing throughout the year (Fig. 1-5). In winter the study area is being influenced by disturbances in the Mediterranean because of the troughs of low pressure that move into the Red Sea accompanied by changes in wind, temperature, and humidity (Edwards, 1987). Nevertheless,

Soliman (1972) denoted that the Red Sea area is particularly unaffected by these depressions and most of the time it is influenced by the eastern flank of the sub-tropical high pressure cell. During spring and autumn months the northeasterly wind is prevailing because of the passage of the Khamsin depressions that lead the eastern Mediterranean to become an area of relatively high pressure. As well southeasterly winds may exist because of the extending of the Sudanese trough. During summer the climate is hot, dry, rainless, and the steady Etesian winds (north or northwest) blow persistently. These winds are part of the circulation around the huge Asiatic low centered over northwestern India (Soliman, 1972).

The mean annual wind speed is relatively high along the coastline about 12.3 (22.14 km/h) and 8.9 (16.04 km/h) knots in Hurghada and El Quseir respectively. The inland region is notably less windy because of the topographic obstructions. Although, gales may occur during summer due to the strong northwesterly winds that are produced by local topography and the shallow small centers of low pressure dominates the northern Red Sea (Soliman, 1972). Actually, the wind has a minor influence on the physical landscape of the study area, which is restricted to dispersed patches of nebkas and sand sheets along the coastal plain.

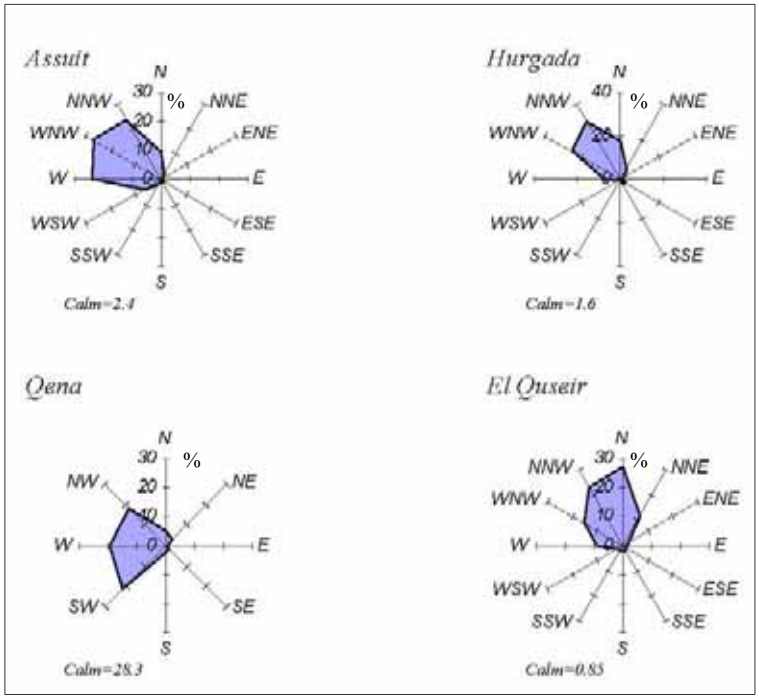

Fig. 1-5: *Percentage frequency of the annual mean of blowing winds.*

3.3. Rainfall.

Scarcity and irregularity of rainfall are the most significant characteristics of the study area, where the total amount of rainfall is usually less than 5 mm/yr. Analysis of the rainfall records revealed that one rain may equal or exceed the mean annual rainfall. Therefore, the maximum amount is considerably high reached 42 mm in Hurghada (1939), while the station has an annual mean of only 3.6 mm. Likewise, the maximum amount in El Quseir reached 60 mm (1965), where it receives only 3.2 mm/yr, 55.3 mm in Qena (1942), and 37 mm in Assuit (1994). Such heavy rain is of a torrential type that may stem flash floods. It is usually produced from violent thunderstorms and gales that frequently occur in the southern part of Egypt. Soliman (1972) denoted that increasing of the rain in the Red Sea stations (30-40 mm) owing to the orographic effects.

3.4. Evaporation and Relative Humidity.

The amount of evaporation is relatively large and intensive in the study area due to effects of the relatively high wind speed and low humidity (Soliman, 1972). The mean daily evaporation varies greatly from winter to summer between 9.6 mm in January for El Quseir and 22.3 mm in June for Assuit.

In contrast, relative humidity is higher in winter than in summer. It is inversely proportional to air temperature and evaporation. The mean annual values are relatively high along the coast in Hurghada and El Quseir (49%), whereas it attains 38% in Assuit and 36.6% in Qena. However, the mean monthly values reveal that the highest values occur during the period from October to January (i.e. Hurghada 55%, El Quseir 54%, Assuit 50%, Qena 63%), while the lowest values take place during May and/or June (i.e. 43%, 45%, 24%, 30% respectively).

4. Aridity Indices

Although the climate involves several parameters, temperature and rainfall are the most utilized parameters for expressing the aridity index. Implementation of aridity indices after Köppen (1931), De Martonne (1926), and Thornthwaite (1933) revealed that the study area is considerably arid. However, verifying extreme aridity is expressed by implementation of Emberger's equation (1955) as follows:

$$Q = P_{mm} / ((T_{max} + T_{min})(T_{max} - T_{min})) 1000$$

Where:

Q is the aridity index, P_{mm} is the average annual precipitation (mm), T_{max} is the mean maximum temperature of the hottest months (ºC), and T_{min} is the mean minimum temperature of the coldest month (ºC). Accordingly, the study area is considerably hyper-arid since the aridity index is exceptionally lower than 20 (Table 1-1).

Table 1-1: *Aridity index of the studied stations after Emberger.*

Station	***P*** $_{mm.}$	***T*** $_{max.}$ ***(ºc)***	***T*** $_{min.}$ ***(ºc)***	Q	***State***
Hurghada	3.6	33.3	9.7	3.5	Hyper-arid
El Quseir	3.2	33.4	13.8	3.4	Hyper-arid
Qena	3.7	40.8	6.7	2.2	Hyper-arid
Assuit	0.7	38	7	0.5	Hyper-arid

The same conclusion is acquired using the graphical representation of the aridity index after Walter & Lieth (1967), which reads as (Domrös & Gongbing, 1988):

$$n = 2t$$

Where: n represents the mean monthly precipitation (mm), and t is the mean monthly temperature (ºC). Thus, precipitation and temperature on the two vertical axes of the climate diagram are in the ratio of 2 to 1. As can be seen in figure (1-6), precipitation curves (blue lines) are very low throughout the year comparatively than temperature curves (red lines) indicating extreme arid conditions generally.

Extreme aridity was also expressed in the study area using vegetation indices that are a well significance to climatic conditions and soil moisture. The vegetation index is determined using image processing because the active terrestrial vegetation strongly absorbing red light and reflecting the near-infrared (NIR) energy. There is no other material at the Earth's surface have the same spectral signature (Aber, 2002). Accordingly, Pinder & Mc Leod (1999) demonstrated the ratio drought index RDI as:

$$RDI = MIR / NIR$$

Where: MIR is mid-infrared band and NIR is near-infrared band. Counterpart of that the RDI can be expressed using ETM+ Landsat image as:

$$band\ 7 / band\ 4$$

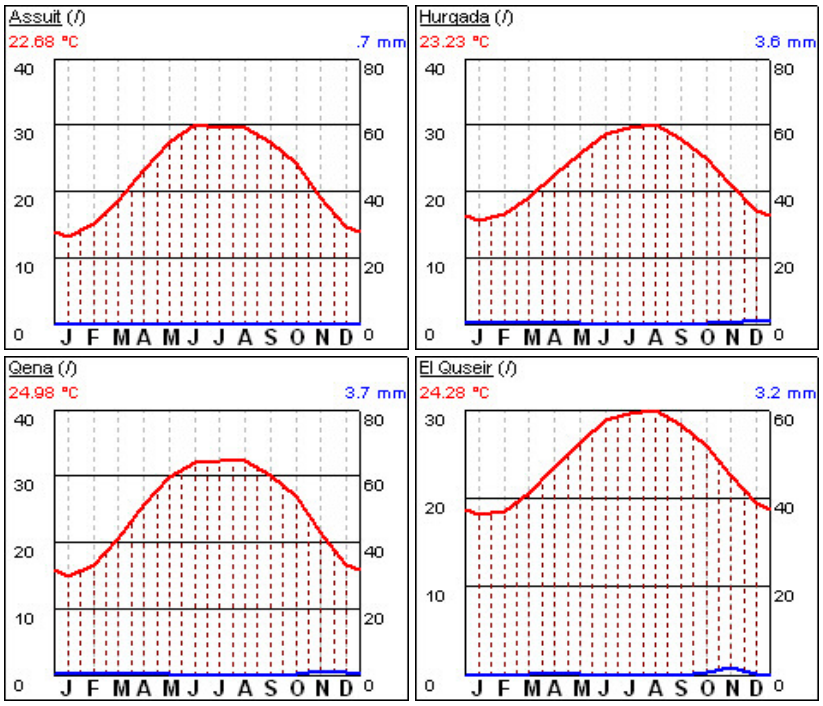

Fig. 1-6: *Graphical representation of temperature and rainfall after Walter & Lieth (1967).*

Where: band 7 is the *MIR* ranging between 2.09-2.35 *µm-wavelength* and band 4 is the *NIR* band ranging between 0.750-0.900 *µm-wavelength* (Lillesand & Kiefer, 2000). The vegetation index can be also expressed as (Leica Geosystems, 2003):

$$IR/R$$

Where: *IR* is the infrared band and *R* is the red band. Accordingly, the vegetation index is expressed using ETM+ Landsat image as:

$$band\ 4\ /\ band\ 3$$

Where band 3 is the red band ranging between 0.630-0.690 *µm-wavelength* and band 4 is the near-infrared band as previously mentioned. Applying the last band ratio revealed that vegetation cover in the study area is almost absent and confined to some Mangrove patches along the coast where the brackish water exist (Fig. 1-7). Terrestrial vegetation is confined to a very small area as well at Ain el Ghazal in wadi al Ambagi west of El Quseir.

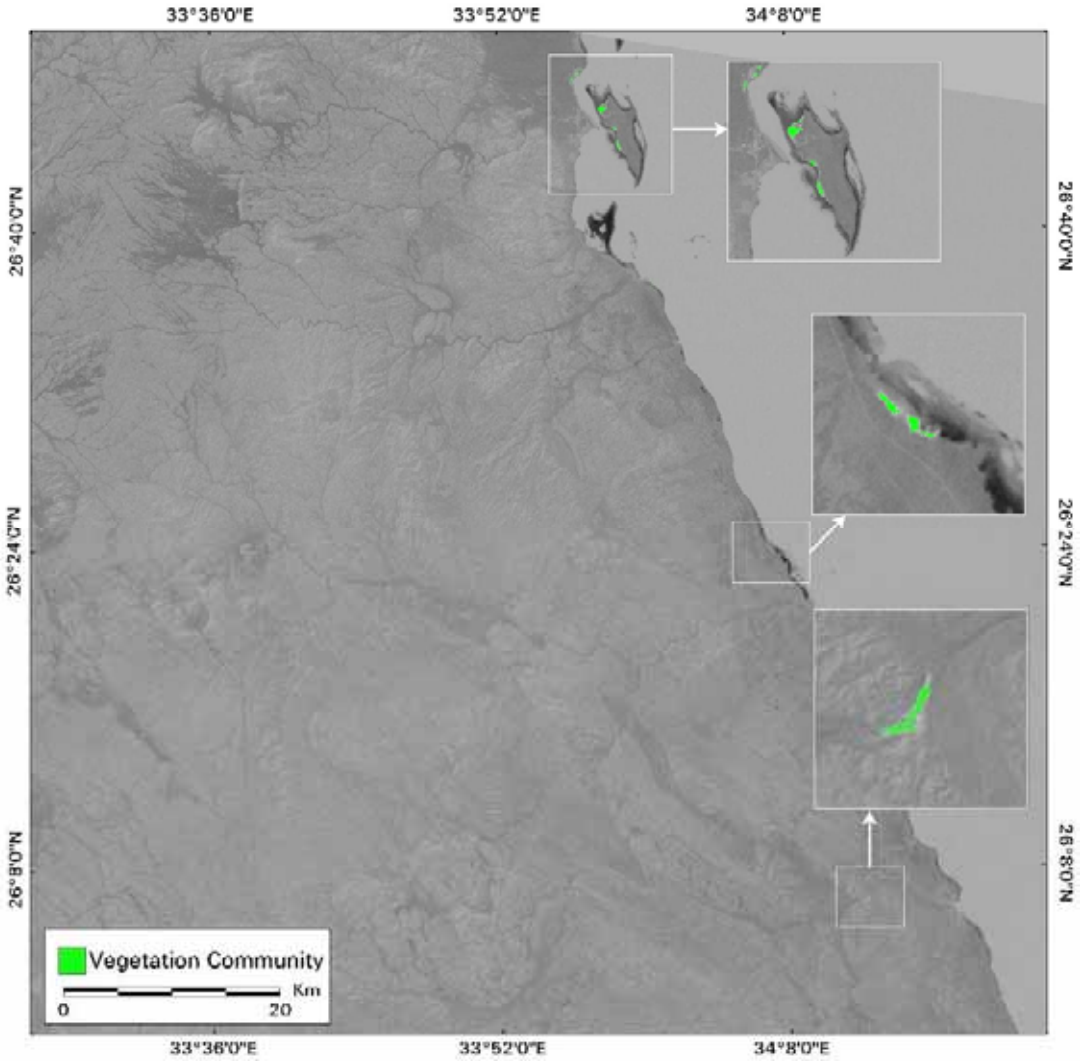

Fig. 1-7: *Ratio drought index of the study area using band ratio 4/3.*

5. Coastal Environment

No much data are available for the coastal environment of the Red Sea and accurate data are given only for a few locations and covering very limited periods (Edwards, 1987). In consequence of that, the present study depends on different data sources such as previous works, reports, field-survey, and data modeling to demonstrate the role of the coastal processes in the study area as follows.

5.1. Waves.

By using Beaufort wind scale and the climatic data of the two coastal weather stations, some wave parameters are estimated. In the regard of that, it has been estimated that probable wave height ranges between 0.6-1.5 m in El Quseir and Hurghada re-

spectively throughout the year (Table 1-2) and the mean annual percentage of the wave height revealed that capillary waves (≤ 0.6 m) representing 38.1 % in Hurghada and 64.3 % in El Quseir (Fig. 1-8).

Table 1-2: *Wave height prediction in the study area.*

Station	Winter		Summer	
	Mean wind speed (knots)	Probable wave height (m)	Mean wind speed (knots)	Probable wave height (m)
Hurghada	11.4	1-1.5	13.3	1-1.5
El Quseir	9.3	0.6	8.06	0.6

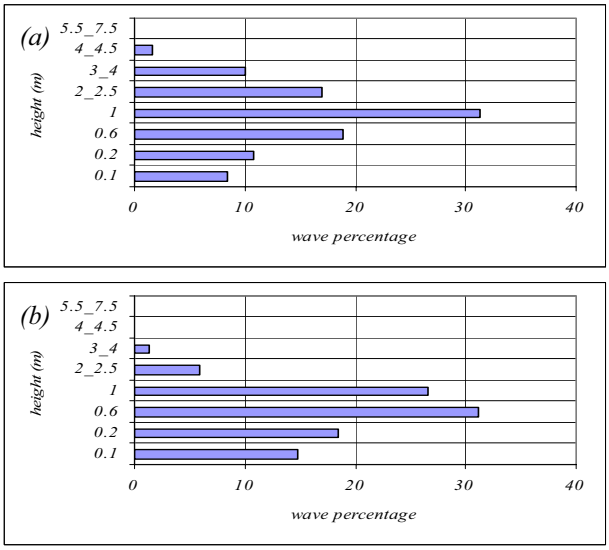

Fig. 1-8: *Frequency of wave heights in Hurghada (a) and El Quseir (b).*

Furthermore, height of the wave infrequently exceeds 3 meters when the wind speed increases than the normal average, and hardly exceeds 5 m during the gale wind, where the wind speed is higher than 34 knots. This usually occurs during winter and spring months for about 6 days in Hurghada and 1 day in El Quseir. During the gale winds, usually harbours of Hurghada and Safaga would be closed for several days such as on 25 February 2006; 08 March 2006; and 04 February 2007 (Aljazeera News).

On the other hand, wave length varies between 47-93 m and wave period is about 3.9-7.7 seconds. Length of the fetch is estimated to vary from 24 to 65 km (Lud's wave prediction FAQ).

Wave direction varies according to the wind direction; therefore, the NW-SE direction is the predominant one during winter and the NE-SW direction is prevailing during summer. In any case, the waves incline where approaching the coastline because of the coral reefs that act as line of breaker and lie in the vicinity of the coastline at about 300-500 m at Safaga, 100-150 m at Hamraween, and 100-250 m at EL Quseir (Fig. 1-9) with a depth varies between -0.5 and -1 m bsl. Briefly, Wave action is usually moderate in the absence of oceanic fetch (Jones et al. 1987).

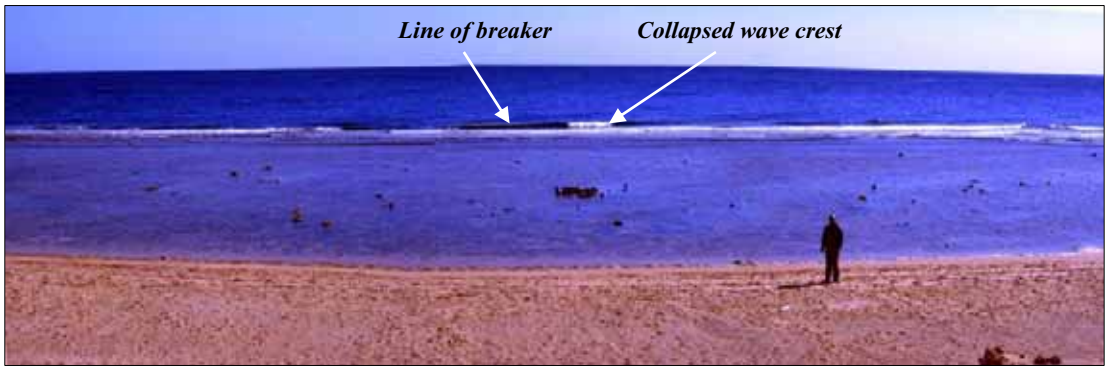

Fig. 1-9: *The modern coral reefs acting as line of breaker north of El Quseir.*

Wave celerity in the shallow water was estimated as:

$$C = \sqrt{gh}$$

Where: C is celerity of the wave, g acceleration due to gravity (9.8 ms-^{2}), and h is the water depth (Viles & Spencer, 1995, Tomczak, 1996-2000). Consequently, the wave celerity varies between 2.21-3.1 m/sec where the depth of the shallow water varies between -0.5 and -1 m behind the line of breaker respectively.

5.2. Tide.

It is well known that the Red Sea is one of the micro-tidal environments since the spring tidal range is smaller than 2 meters (Davies, 1980). Likewise, tides are semi-diurnal where time difference between successive high waters or low waters is approximately 12 hours with amplitude about 0.6 m (Edwards, 1987). Tide records along the coast of Hurghada revealed that spring tide varies between 1.04-0.81 m in winter and summer respectively, while in contrast, neap tide ranges between 0.83 m in winter and 0.68 m in summer. On the other hand, the average ebb tide varies between 0.31 m in winter and 0.17 m in summer and the maximum ebb tide varies between 0.58 m in winter and 0.33 m in summer (Minabary, 1991). Thereby, tidal am-

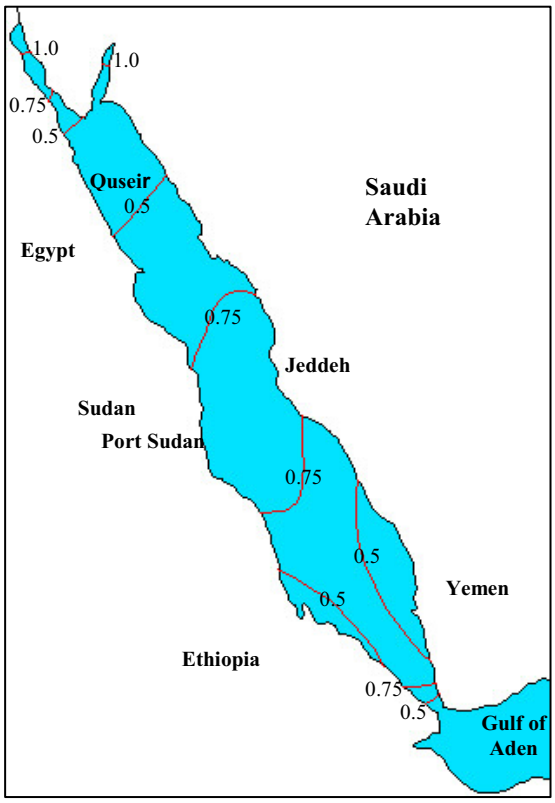

Fig. 1-10: *Tidal range in meters. (After: Marcos (1970); Murty & El-Sabh (1985)*

plitude varies between 0.46-0.48 m in winter and summer respectively and the maximum amplitude is about 0.5 m (Fig. 1-10). As tides are small, tidal currents are very weak ranging in speed between 3-6 cm/sec (Soliman & Gerges, 1983).

5.3. Longshore Currents.

Where the northerly winds are dominant, a set of surface water moves in a south-southeasterly direction. Edwards (1987) estimated that the average velocity of the longshore currents is about 12 cm/sec. Process of waves approaching the coastline, shoaling, breaking, and running up the beach face is relentless and has the ability to generate longshore velocities between the breaker zone and the swash zone, which eventually feed rip currents (Andrew, 2001). Velocity of the longshore current was measured in the field behind the line of breaker using the following equation:

$$\mathcal{V} = \mathcal{D}/\mathcal{T}$$

Where:

$\mathcal{V}$ is the velocity of the longshore current, $\mathcal{D}$ is the distance between two definite points, and $\mathcal{T}$ is the time required for a floating object to pass between the two definite points. By this mean, the study concluded that the longshore current is running from NW to SE direction parallel and closer to the shoreline. It has been also observed that local topography influences the velocity of the currents (Fig. 1-11) that may be associated with tidal and wind-generated currents producing complex distributions of the current across the shore (Larson & Kraus, 2000). Thereby, the study distinguished two sets of current velocities; they are:

5.3.1. Set of High Velocity.

This set of currents exists where the cliffs overlook the sea. At such places, the velocity of the longshore current is relatively higher ranging between 50-60 cm/sec. This may give a well explanation why there are no destructive materials on the foot of such cliffs because this current set drifts most of the beach materials into the low angle slope beach profiles.

5.3.2. Set of Low Velocity.

Once low angles characterize the beach profile (2º-4º), velocity of the longshore current decreases between 20-30 cm/sec. Accordingly, the beach materials accumulate constituting shingle and/or sandy beaches of low angles.

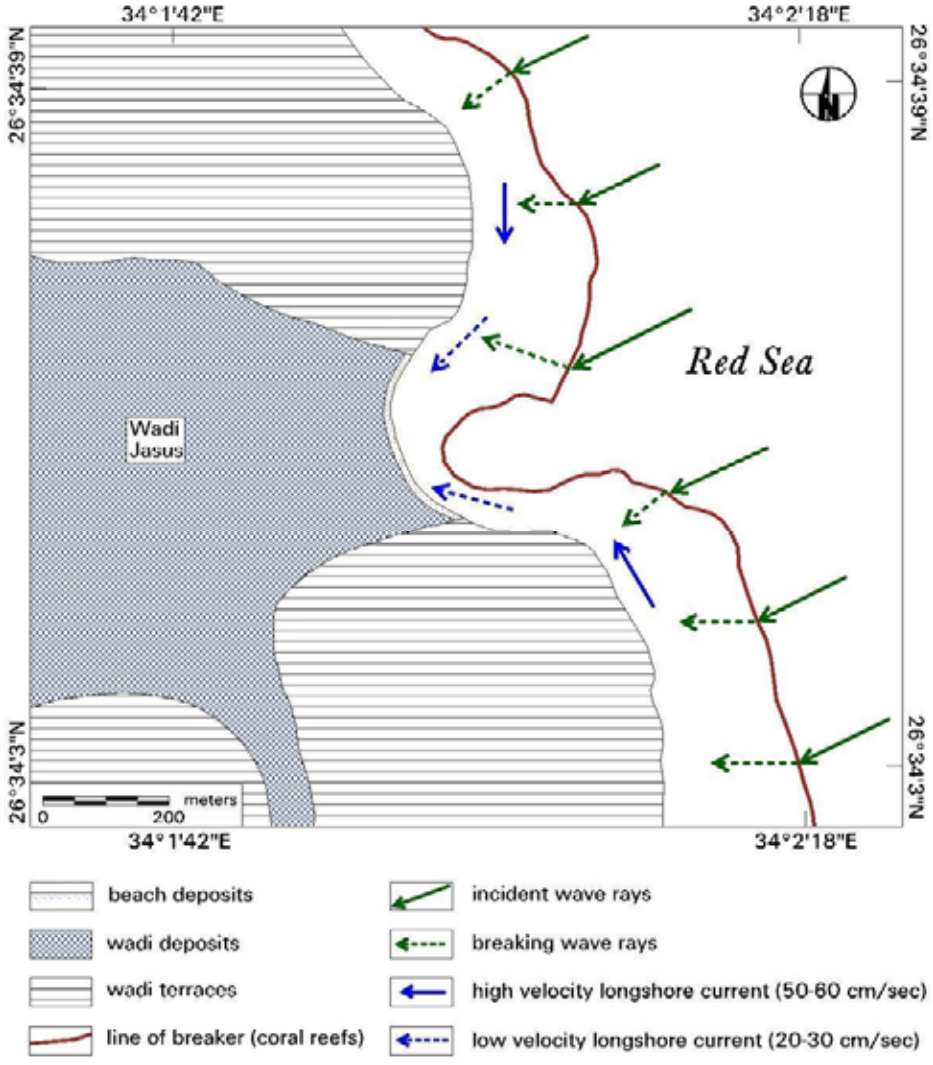

Fig. 1-11: *Influence of local topography and breaking waves on the longshore currents at the outlet of wadi Gasus.* *(Source: field work study, topographic maps & ETM image)*

6. Cultural Manifestations

A Comprehensive view of human manifestations in the study area could be exposed as the following:

6.1. Settlements.

The settled population is mainly confined to few places along or near the coastline where phosphates are mined as well as where the modern tourist centres are constructed. Three relatively main residential centers are located, in the study area, along the coastline; they are from north to south: Safaga, Port of El Hamraween and El Quseir.

Safaga city is located about 53 km south of Hurghada. The port of Safaga has been constructed for exporting phosphates and transporting Hajjis to Mecca. The city is under development; so that, several modern tourist resorts and hotels specializing in diving holidays and windsurfing have been constructed. Port of El Hamraween is located about 63 km south of Safaga and 21 km north of El Quseir. The port has been recently constructed in a peri-urban area for exporting phosphates. El Quseir is located about 84 km south of Safaga. It was known during Ptolemaic times as the white harbour that has a long history as one of the major ports of the Red Sea. From El Quseir, Queen Hatshepsut launched her expedition to the land of Punt (Somalia), as depicted in the sculptures in Deir el-Bahari temple at Luxor. During the 16^{th} century, fortress of Sultan Selim (Ottoman's occupation) was constructed and still standing in the center of the town showing the former strategic importance of El Quseir. Nowadays, it is a quiet resort with its clear water and coral reefs. An ancient caravan trail to Qift in the Nile Valley leads from El Quseir through the mountains passing through several Pharaonic and Roman sites (Tour Egypt, 1999-2004).

6.2. Population.

Since the Red Sea coast is under development, several projects and resorts have been established contributing urban expansion and population growth by natural increase and/or immigration during the period 1986-1996. Moreover, a projection of the period 1996-2010 was calculated using the following equation:

$$p2010 = p1996 \times e^{rt}$$

Where:

$P1996$ is the total population in 1996, e is a constant, r is the annual growth rate of population in the period 1986-1996, and t is the period between the dates of the projection (1996-2010). The annual growth rate of population r was calculated as follows:

$$r = \ln p1996 / p1986 / t$$

Thereby, the annual growth rate of population during the period 1986-1996 varies between 7.9 % in Safaga, 0.7 % in El Hamraween and 0.07 % in El Quseir. Accordingly, the population would grow up at the same rate, if all demographic and geographic factors are constant. Figure (1-12) reveals the population growth in the cities under study during the years 1986, 1996 and 2010.

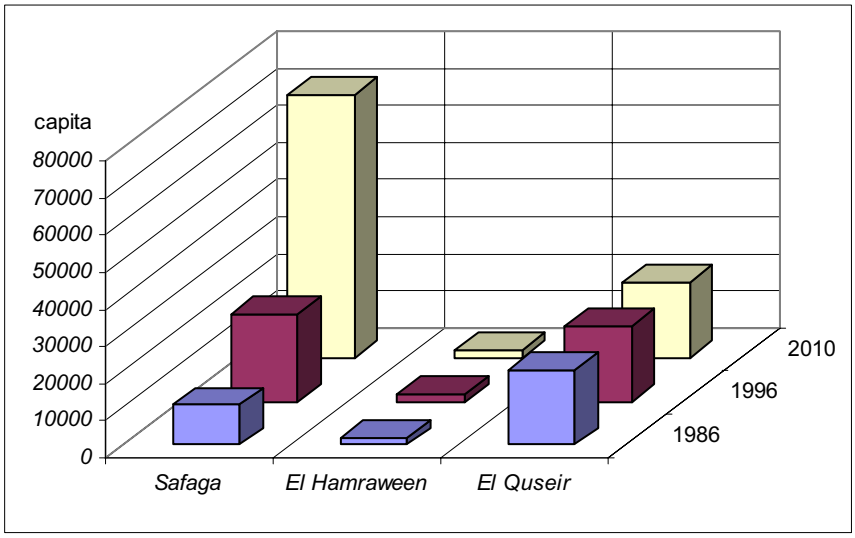

Fig. 1-12: *Population growth in the study area during the period 1986-2010.*

6.3. Economic Activities.

Changes of human activities are significant to the vast development that has been occurred during the last two decades. Such activities can be summarized into four major sectors; they are: mining, manufacturing, tourism & trade, and other activities. Figure 1-13 depicting the greatly changes from mining to tourism and trade activities within the last few years. It can be said that the tourism sector constitutes the backbone of the economic activities in both Safaga and El Quseir nowadays. Such development required much investments and well planed infrastructure such as roads,

transport, fresh water, and electricity especially after exhausting large amounts of the phosphate.

Eventually, it could be concluded that the study area has distinctive landforms that have attracted and fascinated the earlier geologists and geomorphologists during the last few decades. On the other hand, the coast of the Red Sea receives a special interest of development and investments as a tourist environment for its fascinating fauna and flora, clear water, warm weather, physical landscape, and coral reefs. Therefore, the present study may be helpful for the decision maker and giving new lights on the evolution of the physical landforms.

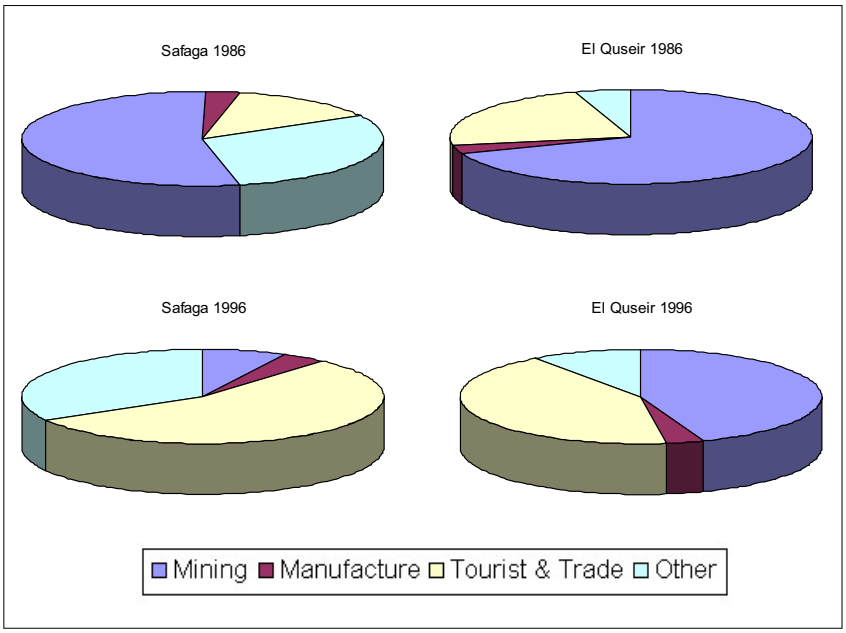

Fig. 1-13: *Changes of the economic activities in the study area during the period 1986-1996.* *(Establishments census for the years 1986 - 1996)*

References:

Aber, J. S. (2002) Landsat Image Processing. *http://academic.emporia.edu/aberjame/-remote/landsat_proc.htm (Accessed on 10 March 2005).*

Aggour, T. A. (1997) Impact of Geomorphological and Geological Setting on Groundwater in Qena-Safaga District- Central Eastern Desert- Egypt. *Unpublished M. Sc. Department of geology, Faculty of Science, Ain Shams University, Cairo, 328 p.*

Aljazeera News: *http://www.aljazeera.net/News/Archive. (Accessed on 08. February 2007).*

Andrew, C. J. F. (2001) Reviewing Nearshore Current, Turbidity and Morphology Models. *DSTO Aeronautical and Maritime Research Laboratory, Victoria, Australia, 55 p.*

Ball, J. (1939) Contribution to the Geography of Egypt. *Survey & Mines Department, Government Press, Cairo, 308p.*

Braithwaite, C. J. R. (1987) Geology and Paleogeography of the Red Sea Region. In: Edwards, A. J. & Head, S. M. (eds.) Red Sea. pp. 22-44, *Pergamon Press, Oxford.*

CAPMAS (1986-1996) The population census and establishments census for the years 1986 and 1996. *Central Agency for Public Mobilization and Statistic, Cairo.*

Davies, J. L. (1980) Geographical variation in coastline development. *2ed edition, Longman, London, 212 p.*

Domrös, M. & Gongbing, P. (1988) The climate of China. *Springer-Verlag GmbH. Berlin, 361 p.*

Edwards, A. J. & Head, S. M. (eds.) (1987) Red Sea. *Pergamon Press, Oxford, 441 p.*

Embabi, N. S. (2004) The Geomorphology of Egypt: Landforms and Evolution. *Vol. 1, The Egyptian Geographical Society, Cairo, 447p.*

Embarger, L. (1955) Afrique du Nord-Ouest. *In: Plant ecology: reviews of research (ed. UNESCO), pp. 219-249. Paris, France: UNESCO.*

Hamdan, G. (1980) The Personality of Egypt (in Arabic). *Vol. 1, Aalam El-Kotob, Cairo, 841 p.*

Jones, D. A., Ghamrawy, M. & Wahbeh, M. I. (1987) Littoral and shallow subtidal environments. In: Edwards, A. J. & Head, S. M. (ed.) Red Sea. pp. 169-193, *Pergamon Press, Oxford.*

Khaled, M. A. (1995) Geological and Geophysical Investigation for Groundwater in El Quseir-Abu Ghusun area, south of the Eastern Desert – Egypt. *Unpublished M. Sc. Thesis, Dept. of Geology, Faculty of Science, Cairo University, 192 p.*

Larson, M. & Kraus, N.C. (2000) Enhancements of the numerical model of the longshore current NMLONG to include interaction between currents and waves (NMLong-CW). *Coastal Engineering Technical Note CETN-IV-25, U.S. Army Engineer Research and*

Development Center, Vicksburg, MS, http://chl.wes.army.mil/ library/pub-lications/cetn/ (Accessed on 27 February 2005).

Leica Geosystems (2003) Erdas field guide. 7th edition, *Leica Geosystems GIS & Mapping, LLC, Georgia. 627 p.*

Lillesand, T. M. & Kiefer, R. W. (2000) Remote sensing and image interpretation. *4th edition, John Wiley & Sons, Inc. New York, 724 p.*

Lud's wave prediction, FAQ. *http:// facs.scripps.edu/surf/luds.html (Accessed on 27 February 2005).*

Marcos (1970); Murty & El-Sabh (1985) Tidal range of the Red Sea. *http://loki.ssc.erc-.msstate.edu/Tides2D/red_sea.html (Accessed on 25 February 2005).*

Minabary, N. Y. (1991) Some geomorphological features along the Red Sea Coast, south of Suez Gulf- Egypt. *Unpub. Ph.D Thesis (in Arabic), Dept .of Geography, Faculty of Arts, Ain Shams University, Cairo, 454 p.*

Office of Naval Research, Ocean in Motion: Waves- Beaufort wind Scale. *http://www. onr.navy.mil/focus/ocean-/motion/waves4.htm (Accessed on 27 February 2005).*

Pinder, J. E. & McLeod, K.W. (1999) Indications of relative drought stress in long leaf pine from Thematic Mapper data. *Photogrammetric Engineering and Remote Sensing, 65; 495-501.*

Said, R. (1962) The geology of Egypt. *Elsevier Publishing Co. Amsterdam, 377p.*

Said, R. (ed.) (1990) The geology of Egypt. *A. A. Balkema Rotterdam, 734p.*

Said, R. (1993) The River Nile: Geology, Hydrology and Utilization *(in Arabic) Dar El Helal, Cairo, 342 p.*

Soliman, K. H. (1972) The climate of the United Arab Republic. In: Griffiths, J. *F. (ed), World Survey of Climatology, Climate of Africa, Vol. 10. Elsevier Publ. Co. Amsterdam, pp. 79-92.*

Soliman, G. F. & Gerges, M. A. (1983) Effect of bottom topography on the tide in the Red Sea. *Bull. Instit. Oceanography and Fish, Cairo, vol. 9. pp. 42-47.*

Tomczak, M. (1996-2000) Description of Waves. *http//www.es. flinders .edu. au/ ~mattom/ Intro Oc/ lecture09. html (Accessed on 25 February 2005).*

Tour Egypt (1999-2004) The Red Sea Coast: al-Quseir. *http//www.touregypt-.net/al-Quseir.htm (Accessed on 16 March 2005)*

Viles, H. & Spencer, T. (1995) Coastal Problems. *Edward Arnold, London, 350 p.*

2

GEOLOGICAL SETTING

1. Litho-Stratigraphy

The Litho-Stratigraphy of the study area could be divided as follows:

1.1. Pre-Cambrian Rocks (Basement Rocks).

The Pre-Cambrian rocks constitute about 78 % of the study area (Fig. 2-1). They are mainly crystalline in character forming a complex of igneous and metamorphic rocks totally devoid of recognisable fossils. Some of the metamorphic rocks that enter into the complex, such as gneisses and schists, were originally sedimentary rocks (Ball, 1939).

The Pre-Cambrian basement rocks of the eastern desert of Egypt have been distinguished and classified by Hume (1935), Ibrahim (1941), Schürmann (1949-1953), Akaad & El-Ramly (1960b) and El-Ramly (1972). Schürmann (1953) adapted the classification of Hume with more addition of a new subdivision as shown in table 2-1. The following paragraphs denote the main basement rocks in the study area.

1.1.1. Paragneisses, Migmatites and Geosynclinal Metasediments and Metavolcanics. They are the most widespread rock types in the study are. The paragneisses and migmatites are the oldest rock types. They are composed of psammitic, hornblende and biotite gneisses and migmatites. The geosynclinal metasediments are distributed in the lower part of the study area. They include biotite, hornblende, chlorite schists, metagreywacks, metamudstones, phyllites, slates and occasionally conglomerates (EL-Ramly, 1972). They were subjected to low grade metamorphism (green schist faces) and occasionally pass in the vicinity of big intrusions such as Umm Oradah. The metavolcanics are associated with the metasediments. They are eruptions of surface or submarine effusive, represented by regionally metamorphosed rhyolites, dacites, andesites, basalts, and pyroclastics (El-Ramly, 1972). Normally, this rock group manifests dark colours and rugged relief.

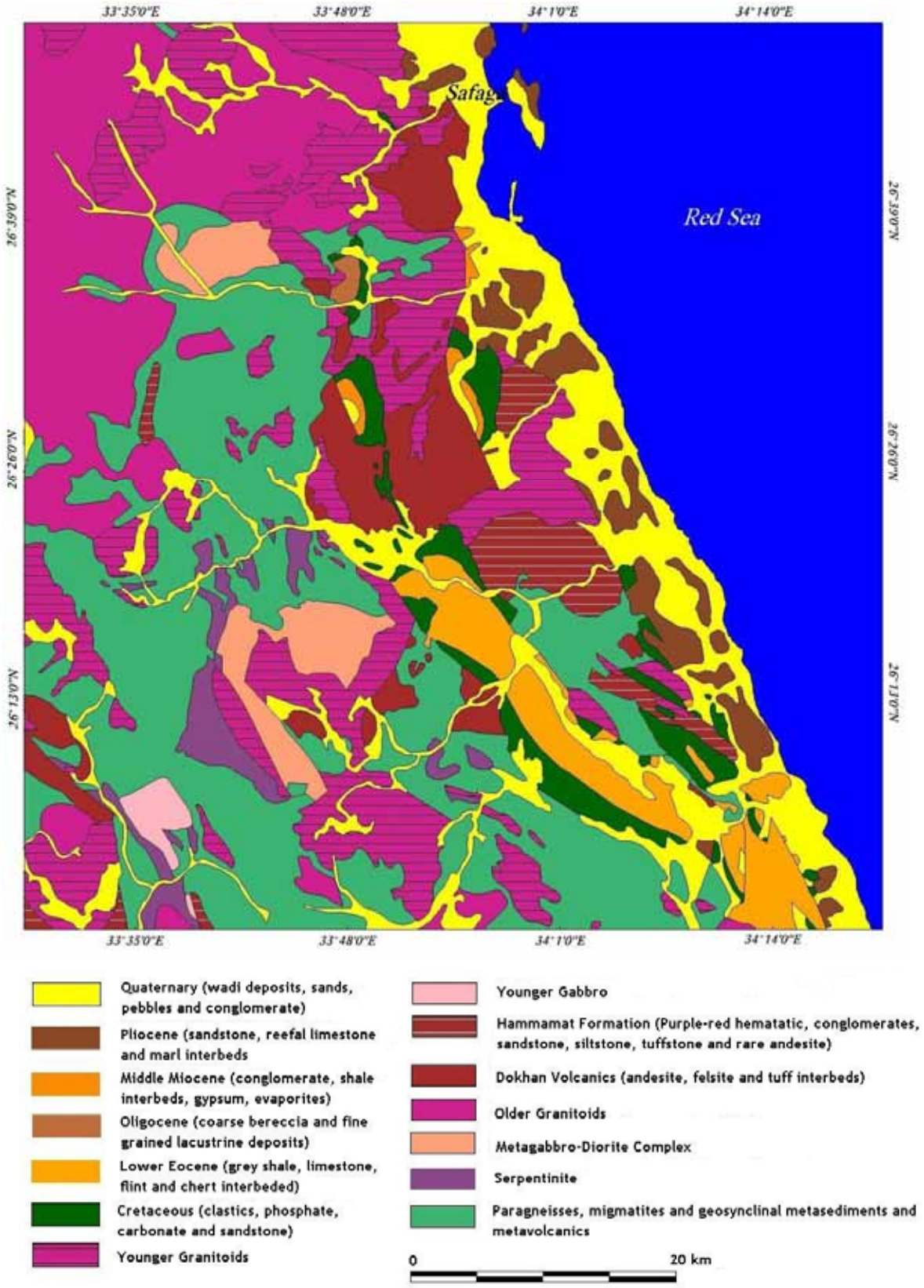

Fig. 2-1: *Geological map of the study area.*

(Source: Geological map of Qena 1:500,000)

1.1.2. Serpentinite occurs as relatively scattered masses or belts associated with the geosynclinal metasediments and metavolcanics.

1.1.3. Metagabbro-Diorite Complex forms the older gabbros. It includes a group of gabbroid and doleritic masses, which were structurally affected by the older granites.

1.1.4. The Older Granites (Shaitan Granites) cover substantial area characterised by an increase in the amount of plagioclase over the potashfeldspars. They form typical orogenic belts that are believed by Hunting (1967) to be of the syn-tectonic to late tectonic phase of orogenic cycle, which created and destroyed the geosynclinal troughs (El-Ramly, 1972). The older granites are experienced long-term of erosion and exhibiting a worn surface.

1.1.5. Dokhan Volcanics are post-tectonic rocks mostly nonmetamorphosed volcanics that are well known as purple coloured imperial porphyry. They represented mainly by andesites, felsites and tuff interbeds. They are well presented in the study area in Jabal Naqarah (west of Safaga) and Jabal Umm al-Hawaytat. The Dokhan volcanics are dated at 607 ±8 Ma (Reischmann, 2000, after, Stern and Hedge, 1985).

1.1.6. Hammamat Group is essentially unmetamorphosed conglomerates, greywackes, sandstone, siltstone, tuffstone and rare andesites. The group is post-geosynclinal sediments resting unconformably over the older basement rocks (EL-Ramly, 1972).

1.1.7. The younger Gabbro is restricted to small mass east of Jabal Umm Had.

1.1.8. The Younger Granitoids (Gattarian Granites) form relatively small masses usually with round or oval shapes such as Jabals Barud and Umm Oradah. They are composed of medium grained biotite hornblende granites showing pink to reddish colours.

Interpretation of the basement rock map of Safaga District (1:100,000), and the geological map of Qena (1: 500,000) revealed that two orogenic phases were occurred during the Pre-Cambrian time. At the late orogenic phase, the older granites became exposed and a period of great volcanic activity took place during the upper Protero-

zoic producing andesites and porphyrites such as the Dokhan Purple Imperial Porphyry (Said, 1962).

Table 2-1: *Classification of the basement complex rocks of the Eastern Desert.*

Gattarian ***(Younger Granitoids)***	*Granite of second Series and Dykes*	*Mons Claudianus granite*	*Normal igneous, calc-alkali and alkali magmas, no metamorphism, sometimes marginally gneissic.*
Eparchaean	*Epeirogenesis Hammamat Series*	*Breccia verde antico*	*Sandstones, breccias and conglomerates with interbedded quartz-dioritic flows.*
	Unconformity Dokhan series and Shadli Series	*Imperial porphyry*	*Quartz-diorite flows. Gabbro and serpentine, schist (red, black, and green), some breccia, tuffs. No Regional metamorphism*
	Unconformity series of old Paraschists	*Red breccia*	*Metamorphic sediments, marble, andesitic flows, red aplite-breccia. Regional metamorphism.*
Shaitian ***(Older Granite)***	*Unconformity granite of first series*	*Shait granite*	*Normal igneous, calc-alkali magma indicating intensive metamorphism.*
Metarchaean	*Atalla Series*	*Steatite*	*Quartzite, red jasper, rhyolitic flows, also some andesitie flows.*
	Mitiq Series	*Gneisses*	*Highly metamorphic schists, marble, paragneisses and orthogneisses of calc-alkali magma.*
Protarchaean	*Fundamental Gneiss*		*Migmatites of Wadi Feiran (S. Sinai)*

(Simplified after: Akaad & El –Ramly. 1960 b, after Shürmann, 1953).

Along the troughs, which were produced in this late orogenic phase, a great thickness of red beds, conglomerates, subgreywackes, and mudstones was deposited. Such sediments are widely distributed and well developed in Hammamat area to the east of Qena. Thereafter, a great period of plutonic activity followed the deposition of the Hammamat beds, which extended from the upper Proterozoic (Early Gattarian Complex) to the lower Paleozoic (Late Gattarian Rare-Metal Complex) and producing the so-called Gattarian granites or younger granitoids *(type locality Jabal Gattar, about 45 km south-west of Hurghada)*. Those are widespread forming many of the pinna-

cles of this range, such as Jabal Shayeb at about 40 km north-west of Safaga. A number of acidic to basic dykes cut the older basement rocks and the Gattarian granites as well indicating a period of volcanicity in post–Gattarian time. Recent absolute age determination of Gattarian granites shows that these may be of lower Paleozoic age. A period of erosion followed and the mass of basement rocks, particularly the older granite, became peneplain and relatively rugged (Said, 1962).

1.2. Sedimentary Rocks.

Said (1990) divided the sedimentary rocks in the study area into two major successions as follows:

1.2.1. Cretaceous and Eocene Rocks.

This is the older division of rocks that is exposed in the isolated outcrops of Jabal Duwi and its continuations at Jabal Atshan and Hamadat (Fig.2-2). The succession is from bottom to top as follows:

1.2.1.1. Nubia Group.

The Nubia group represents the oldest sedimentary beds rest uncomfortably over the basement complex rocks. The beds occupy many of the topographic depressions in the study area. They are divided into two units; the lower unit is about 200 m thick built up by seemingly non-fossiliferous sandstone beds with interbeds of mudstones. The upper unit is about 70 m thick in Jabal Atshan that is built up by poorly fossiliferous variegated shales of El Quseir formation.

1.2.1.2. Duwi Formation.

El Quseir variegated shales are overlain by Duwi formation, which is built up by three phosphate horizons separated by beds of marl, shale, and oyster limestone with flint. The lower horizon of phosphate is known as Hamadat or Abu Shigeila horizon was followed by a section of variegated shales of non-marine to marginal marine origin. The middle horizon is the best developed one and most consistent of the phosphate horizons that are exploited in Duwi and Hamadat mines. The phosphatic rock is dark in colour and has silicified phosphatic nodules. The upper phosphate horizon named Atshan horizon is exploited in the Atshan and an-Nakhil mines in the Quseir area that is varying in thickness between 4-10 meters.

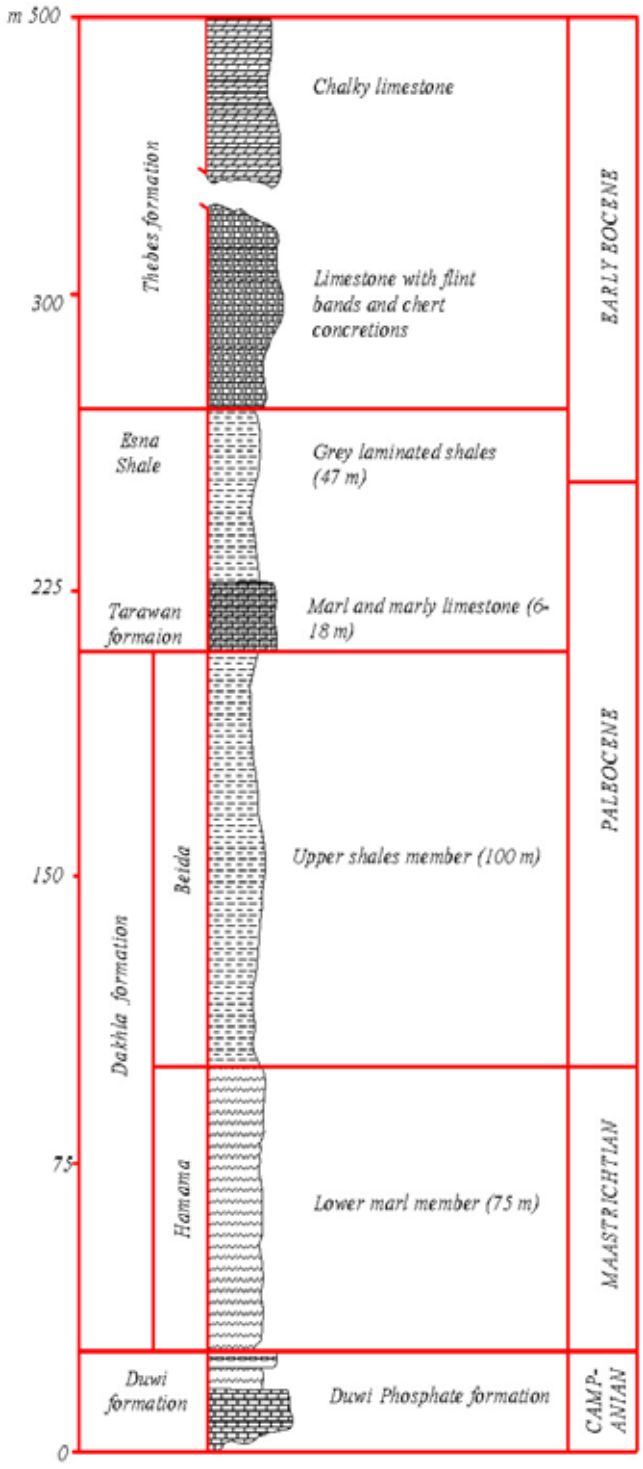

Fig. 2-2: *Columnar section of Jabal Duwi (Simplified after Said, 1990).*

1.2.1.3. Dakhla Formation.

Duwi formation is overlain by a series of marls and shales of about 75 m thick in Jabal Duwi. The marl member, which is known as Hamama member, overlies the Atshan phosphate but its lower boundary extends to the top of the Duwi member.

The upper shale member known as Beida is about 100 m thick and its age is early Paleocene. At Jabal Anz west-north of El Quseir, Dakhla formation attains about 90 m thick and it is made up only of the lower Maastrichtian marly member. In Safaga, Dakhla shale is relatively thin ranges between 23-30 m and belongs to Maastrichtian.

1.2.1.4. Tarawan Formation.

The formation is made up of marl and marly limestone, ranges in thickness from 6 to 18 m. It is postdated at late Paleocene age.

1.2.1.5. Esna Formation.

Esna formation is made up of grey laminated shales of about 47-50 m thick in Jabal Duwi and Safaga consequently. The formation ranges in age from late Paleocene to early Eocene times.

1.2.1.6. Thebes Formation.

Thebes formation unconformably overlays Esna Shale. The formation is made up of limestone with flint bands or nodels and chert concretion interbed, which forms the important topographical features of Jabals Duwi (about 285m thick), Atshan, Anz (about 166 m thick), and Hamadat (about 250 m thick). It is forming old white cliffs running sharply to ground level with a dip slope of 15 to 20 degrees. A thinly bedded chalky limestone overlies the limestone with flint indicating a deep-water phase of predominantly pelagic[1] deposition. The age of the formation might be of early to middle Eocene.

1.2.1.7. an-Nakheil Formation.

This formation is built up of very coarse brecciate beds and fine-grained lacustrine deposits. The coarse-grained breccia beds include no Pre-Cambrian fragments. The thickness of the formation may exceed 60 m. The formation occupies the slopes of the Thebes formation. Most authorities give the formation an Oligocene age.

1.2.2. Miocene and Later Sediments.

The Miocene and later sediments form a very narrow strip along the coast. They are essentially littoral in character exhibiting marked lithological changes laterally and vertically. They rest unconformably with a distinctively dip on the older rocks. They fall into the following formations (Fig.2-3):

1.2.2.1. Ranga Formation.

Ranga formation overlays the older sediments unconformably. The lowermost bed is made up of conglomerate derived from the basement with rounded to angular clasts that range in size from granular to boulders. The conglomerate is embedded in a red-brown sandy matrix and the basal conglomerate bed ranges in thickness between 8-16 m followed upward by a long series of fine to medium grained sandstone of varying colours and minor shale beds.

---

[1] *Pelagic: term used to describe the mode of life of sea floor animals which live in the open sea, including forms which are free-swimming (nektonic), e.g. fish, and forms which float passively in the surface waters (planktonic), such as jellyfish (Whitten & Brooks, 1972).*

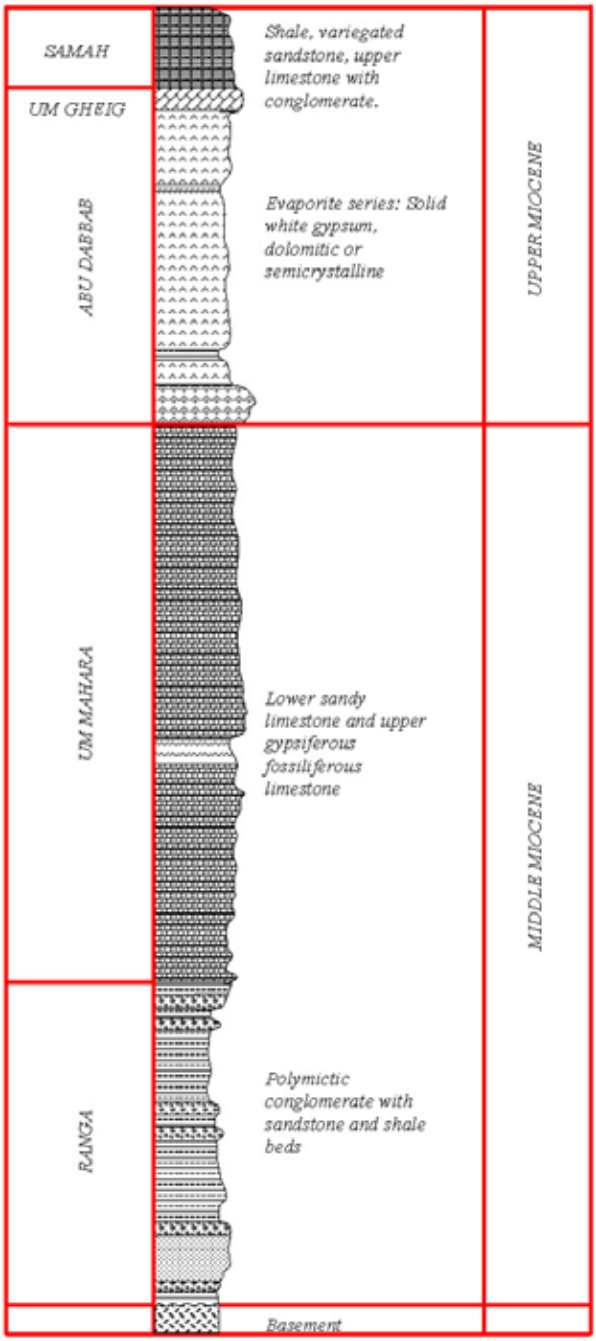

Fig. 2-3: *Miocene section in the study area (simplified after Said, 1990).*

In wadi Gasus the formation exceeds 123 m thick. Generally, it is non-fossiliferous and seems to be deposited sub-aerially by rivers that drained the elevated un-covered basement complex.

1.2.2.2. Umm Mahara Formation.

The Umm Mahara formation rests unconformably over Ranga formation. The formation attains about 181 m thick and it is made up of a lower sandy limestone member and upper gypsiferous fossiliferous limestone member. The beds are massive, partly dolomitic, and mostly coralline reefs. The unit is shallow marine origin and the fossils are of Mediterranean aspect. The formation is assigned to middle Miocene.

1.2.2.3. Abu Dabbab Formation.

The formation is formed of evaporite (gypsum) deposits and extending for hundreds of kilometres along the coastal plain. The gypsum is patchy distributed and ranging in thickness between 90 - 400 m in the onshore areas. It is quite solid white and weathered showing yellowish brown colour. Locally, it is interbedded with hard compact and sometimes dolomitic or semi-crystalline limestone. Abu Dabbab formation is dated to late Miocene.

1.2.2.4. Umm Gheig Formation.

Formation of Umm Gheig varies in thickness between 8-10 m. It consists of hard dolomite bed that seems to be deposited in shallow water above the wave base.

1.2.2.5. Samah Formation.

This formation overlays unconformably Abu Dabbab formation or Umm Gheig formation. It is built up mainly by limestone of about 15-20 m thick that is recrystallized in character. The formation is dated to late Miocene and seemingly deposited in intertidal to super-tidal flats.

1.2.2.6. Pleistocene Reefs, Raised Beaches, and Wadi Terraces.

The Pleistocene reefs, wadi terraces and raised beaches have been described in the study area by Issawi et al. (1971) and from wadi Shagra south of El Quseir by Akkad & Dardir (1966). The section is about 34 m thick and built up by a succession of four organic reefs separated by conglomerate and gravel beds. These latter beds are interpreted as representing pluvial episodes, which interrupted an otherwise dry climate. Several raised beaches skirt the coast; three levels are recorded by Said (1990). They are: 1 m beach is dated at 2500 to 6500 years BP, 7 and 11 m beaches are dated 81 to 141,000 years BP (Said, 1990).

2. Mapping the Main Rock Units Using Landsat Enhanced Thematic Mapper Plus (ETM+) Imagery

2.1. Characteristics of the ETM+ Imagery Data.

The available ETM+ imagery was acquired by Landsat 7 on 23rd Feb. 2003 (path 174/ row 042), provided in NLAPS *(National Land Archive Processing System)* data format that is radiometrically and geometrically corrected (Level-1G systematically corrected[1]). The image contains 8 bands, 1-5, and 7 at resolution of 28.5 m, band 6 at resolution of 60 m, and band 8 at resolution of 14.25 m. The image contains no cloud cover. The study area covers a window of 3294 x 3256 pixels, which was subset from the original image. Using of multivariate statistic correlation of 7 bands clarified that the original DN (Digital Numbers) values of bands 1-5 and 7 are highly correlated to each other with the exception of band 6. Consequently, their DN values are redundant (Table 2-2). The correlation coefficient indicates a direct relationship between each two pair of bands where it is close to +1. This suggests that if reflectance (DN) of a pixel in one band is known, reflectance of the same pixel in the other bands can be derived or estimated. On the other hand, the coefficient indicates an inverse relationship between the reflectance values of the two bands where it is close to -1. The high correlation between bands 1 and 2, for example, suggests the removal of one of them in a colour composite using band 1 or 2 (ITC, 2001). Thus, image processing was essential to expand the original image data for better visual image interpretation.

2.2. Visual Enhancement.

2.2.1. Contrast Stretching.

The image data is assigned over a range of 0-256 grey levels and the DN values rarely extend over this entire range. Therefore, the intent of applying contrast stretching is to expand the narrow range of brightness of the original image over a wider range of grey values. The result is an image that is designed to accentuate the contrast between features of interest (Lillesand & Kiefer, 2000). Figure 2-4 showing the effect of the contrast stretching over Jabal Naqarah west of Safaga.

---

[1] *Systematic Correction (Level 1G) includes both radiometric and geometric corrections. Image data is assigned to 8-bit (DN) values. The scene is being rotated, aligned, and georeferenced to user-define map projection.*

Table 2-2: *Correlation matrix of the ETM+ Landsat Image.*

Image Bands	*B1*	*B2*	*B3*	*B4*	*B5*	*B6*	*B7*
B1	1						
B2	0.97	1					
B3	0.94	0.99	1				
B4	0.91	0.98	0.99	1			
B5	0.88	0.95	0.97	0.98	1		
B6	0.72	0.58	0.52	0.5	0.48	1	
B7	0.89	0.95	0.97	0.98	0.99	0.49	1

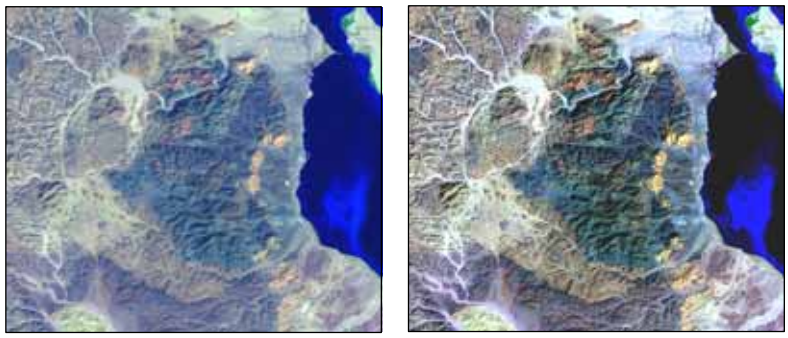

Fig. 2-4: *Original image (left) and contrast stretching image (right).*

2.2.2. Convolution Filtering.

Convolution filtering is the process of averaging small sets of pixels across an image in order to change the spatial frequency characteristics of the image (Lecia Geosystems, 2003). A matrix or kernel of 3 x 3 pixels is used to the stretched image to average the image value and enhance edges between image features. Equally, a low pass filter is applied to clarify the larger homogenous areas of similar tone and reduce the smaller details in the image (Canada Center for Remote Sensing, 2002). In such matrix, one cell always lies at the center and each cell in the matrix has a weighting or coefficient C, and the whole matrix can be expressed by the function $C(k, l)$, where k and l being the cell coordinates within the matrix (Drury, 1993). The kernel moves throughout the original image and the DN at the center of the kernel in the output image is obtained by multiplying each coefficient in the kernel by the corresponding DN in the original image (Lillesand & Kiefer, 2000). Thereafter, the total is divided by the sum of the values in the kernel (Lecia Geosystems, 2003). The kernel of edge enhancement is implemented using negative values for the non-central kernel coefficients (-1) (table 2-3). The output is calculated as follows: 1/ (16-8) = 1/8 = 0.125.

-1	-1	-1
-1	16	-1
-1	-1	-1

Table 2-3: *Filter Kernel used for edge enhancement. (Janssen et al. 2001).*

The sharpening effect can be made stronger by using smaller value for the center pixel with a minimum of 9 (Janssen et al. 2001). Figure 2-5 is an example of using 3 x 3 edge enhancements and low pass filter in comparison with the original image of Jabal Naqarah.

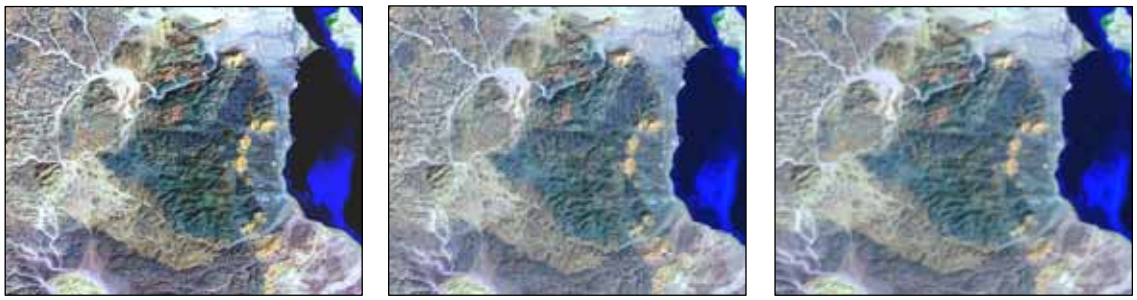

Fig. 2-5: *Original image (middle), convolution 3 x 3 edge enhanced image (left) and low pass filter image (right).*

In other words, using 3 x 3 edge enhancement exaggerates the local contrast of the original image for portraying linear features or edges in the image data (Lillesand & Kiefer, 2000). Eventually, a detailed geological map can be obtained using convolution filter 3 x 3 edge enhancements, while regional or generalized geological map can be obtained using low pass filter.

2.3. Elements of Image Interpretation.

Image interpretation for geologic purposes involves knowledge of some basic elements that are valuable for image interpretation. These elements can be defined as: image tone or colour, shadow, image texture, shape, pattern, and spectral analysis. Image ***tone*** refers to the relative brightness or colour of an object in the image. Although tonal differentiation is a good indicator to distinct between the main rock units and mineral compositions, one rock type may reflect several tonal degrees due to effects of the ***shadow***. Therefore, the illuminated side reflects light tone whereas sheltered side reflects relatively dark colour. Figure 2-6 showing an example of such effects of tonal differentiation and shadow in Jabal Barud, which lead the spectral curves of the younger granite to vary greatly from place to place.

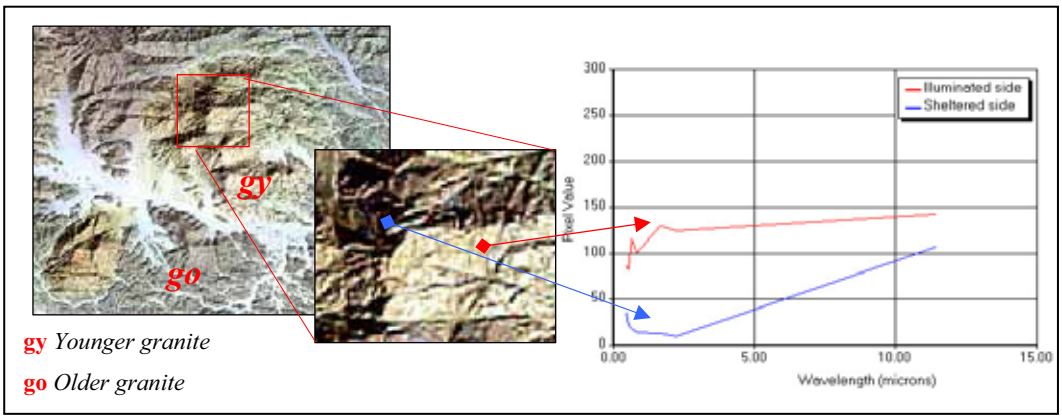

Fig. 2-6: *Extracted image of Jabal Barud (left), effects of tonal differentiation (middle), and spectral curves of granite rocks (right).*

Image ***texture*** has been also taken into account, which is defined as a continuous area in which feature changes and/or frequency of tonal changes are not detected (Janssen et al. 2001). Image texture is often related to terrain roughness and rock types. By this mean, different rock types could be simply distinguished. To give only one example, the sedimentary rocks in the study area often reflect finer texture than the basement rocks that reflect coarse and very coarse textures due to their resistance against erosion processes. However, texture may give a good indicator to the geomorphologic stage of physiographic features. In figure 2-6 one can observe the very coarse texture of the younger granite that built up Jabal Barud, whereas the surrounded older granite is relatively less coarse.

Object ***shape*** refers to the morphology of an image phenomena. For example: dykes that cut through the basement rocks are often linear and diapiric plutons have oval shapes as can be deduced from figure 2-6.

Pattern refers to the spatial arrangement of a specific object and implies the characteristic repetition and/or relationship of a certain object (Janssen et al. 2001). Typical examples of pattern recognition can be derived from drainage networks that will be discussed later.

2.4. Data Calibration.

Interpreted data have been calibrated from the basement rock map of Safaga district (scale 1:100.000), and the geological map of Qena (scale 1: 500.000). As well several

geological reports were reviewed in order to distinguish and discriminate the main rock units i.e. Hume (1935), Said (1962, 1990), El-Akkad & Dardir (1966a), and El-Ramly (1972). Furthermore, field truth is carried out at several points of Jabal Barud, Jabal Naqarah, Jabal Duwi, and Jabal Umm Oradah for data verification.

2.5. Digital Image Processing and Interpretation.

2.5.1. Colour Band Composite (CBC).

Optimum band selection was firstly used to colour synthesizing for visual interpretation. So, three-band selection was carried out using the Optimum Index Factor (OIF) that reads as:

$$OIF = \frac{Std_i + Std_j + Std_k}{|Corr_{i,j}| + |Corr_{i,k}| + |Corr_{j,k}|}$$

Where:

Std_i standard deviation of band i

Std_j standard deviation of band j

Std_k standard deviation of band k

$Corr_{ij}$ correlation coefficient of band i and band j

$Corr_{ik}$ correlation coefficient of band i and band k

$Corr_{jk}$ correlation coefficient of band j and band k

The optimum combination of all possible 3 bands is that one with the highest sum of standard deviation and the least amount of duplication (lowest correlation among band pairs)[1]. Number of the possible band combinations of the ETM+ image is determined as:

$$\binom{N}{3} = \frac{N!}{(3! * (N-3)!)}$$

Where N is the total number of bands and N! is factorial operation[2]. Accordingly, there are 20 available combinations for the ETM imagery after excluding the thermal infrared and panchromatic bands. However, the Optimum Index Factor (OIF) of 10 probable band combinations is calculated depending on table 2-4, which represents the mean and the standard deviations of bands 1-5 and 7.

---

[1] *For details see: Ilwis 3.21 Help, Optimum Index Factor, Functionality/Algorithm.*

[2] *The expression n! means the product of the integers from 1 to n, for example 4! Reads four factorial is 4x3x2x1= 24.*

Table 2-4: *Mean and standard deviations of the ETM+ image.*

	b1	*b2*	*b3*	*b4*	*b5*	*b7*
Mean	60.52683	54.62863	65.4358	48.54024	61.36517	53.98886
St. Dev.	15.61644	22.63698	34.58263	27.88549	39.17382	33.56441

Accordingly, band combination 5 (red), 4 (green) and 3 (blue) gives the maximum variance in the image because the different wavelengths often pick out different features (Jensen, 1986) (table 2-5). Nevertheless, band combination is highly dependent upon the nature of application of the data set (Jasrotia et al. without date) and it is not implied that it creates the best colour composite because this greatly depends on the purpose of the study. Therefore, it has been observed that band combination 7 (red), 4 (green), and 2(blue) is being the best band combination among all for discriminating the main rock units and clarifying intrusive dykes (Fig. 2-7). In that manner, band combination 1 (red), 2 (green), and 7 (blue) is well clarifying shallow water and it is useful for coral reef studies.

Table 2-5: *OIF values and ranked band composites.*

Rank	*Band Combination (red, green, blue)*	*OIF Value*	*Rank*	*Band Combination (red, green, blue)*	*OIF Value*
1	5,4,3	55.84	6	7,4,2	46.45
2	7,4,3	53.05	7	5,4,1	45.17
3	7,5,4	52.95	8	7,4,1	42.34
4	5,3,2	52.96	9	3,2,1	39.8
5	5,4,2	49.28	10	1,2,7	39.46

2.5.2. Compound Band Ratioing (CBR).

The major target of applying band ratioing is to enhance the spectral differences between the image bands and reduce the effects of topography (R.S.I. 2003). Band ratioing convey the spectral or colour characteristics of the image features regardless of variations in scene illuminations. It is often useful for discriminating spectral variations in a scene that are masked by the brightness variations (Lillesand & Kiefer, 2000).

Band ratioing is produced by dividing one spectral band by another; producing an image that provides relative band intensities. Three pairs of ratio images can be co-registered and projected as colour composites and; therefore, certain ground features tend to be highlighted based on unusual or anomalous ratio values (Nicholas & Short,

2004). Number of possible ratios that can be developed from *n* bands of data is expressed as (Lillesand & Kiefer, 2000):

$$n\,(n\text{-}1)$$

Thus, for Landsat ETM+ image there are *6(6-1)* or 30 possible combinations after excluding the thermal infrared and panchromatic bands. Since the image bands are highly correlated and bands 2, 3 and 8 currently saturate in low gain (Markham, 2000), these bands giving poor results if used together in band ratioing. On the contrary, bands 4, 5 and 7 reveal great deviations in responses and trends between detectors.

Accordingly, different compound band ratioing (CBR) are examined. Table 2-6 showing the experimental compound band ratioing of which the hydrothermal band ratioing 7/5, 3/1, 4/3 (red, green, blue) gives the best output for determining and separating the main rock units in the study area (Fig. 2-8). It is because the Fe-O charge-transfer transition is characterized by a broad absorption band at wavelength less than 0.55 μm. It is responsible for the strong red colouration of rocks rich in iron oxides and hydroxides. Occasionally, this colouration is masked by the mixture of iron minerals with large amounts of minerals such as quartz, which is reflected strongly at all wavelengths. The ratio of red to blue reflectance (b3/b1) would enhance the small contribution of iron minerals, giving pixels of iron-bearing rocks a higher value than those composed of pure quartz. Iron also produces an absorption band between 0.85 and 0.92 μm owing to crystal-field effects. This feature falls within the range of band 4, while high reflectance for all minerals is found in band 5. The ratio of band 5 to band 4; therefore, shows higher values for oxidized iron-rich rocks than for other types. Eventually, the Al-OH and Mg-OH rational effects associated with clays and other hydroxylated minerals result in absorptions within band 7. By ratioing this band against band 5, clay-rich rocks manifest dark areas (Drury, 1993).

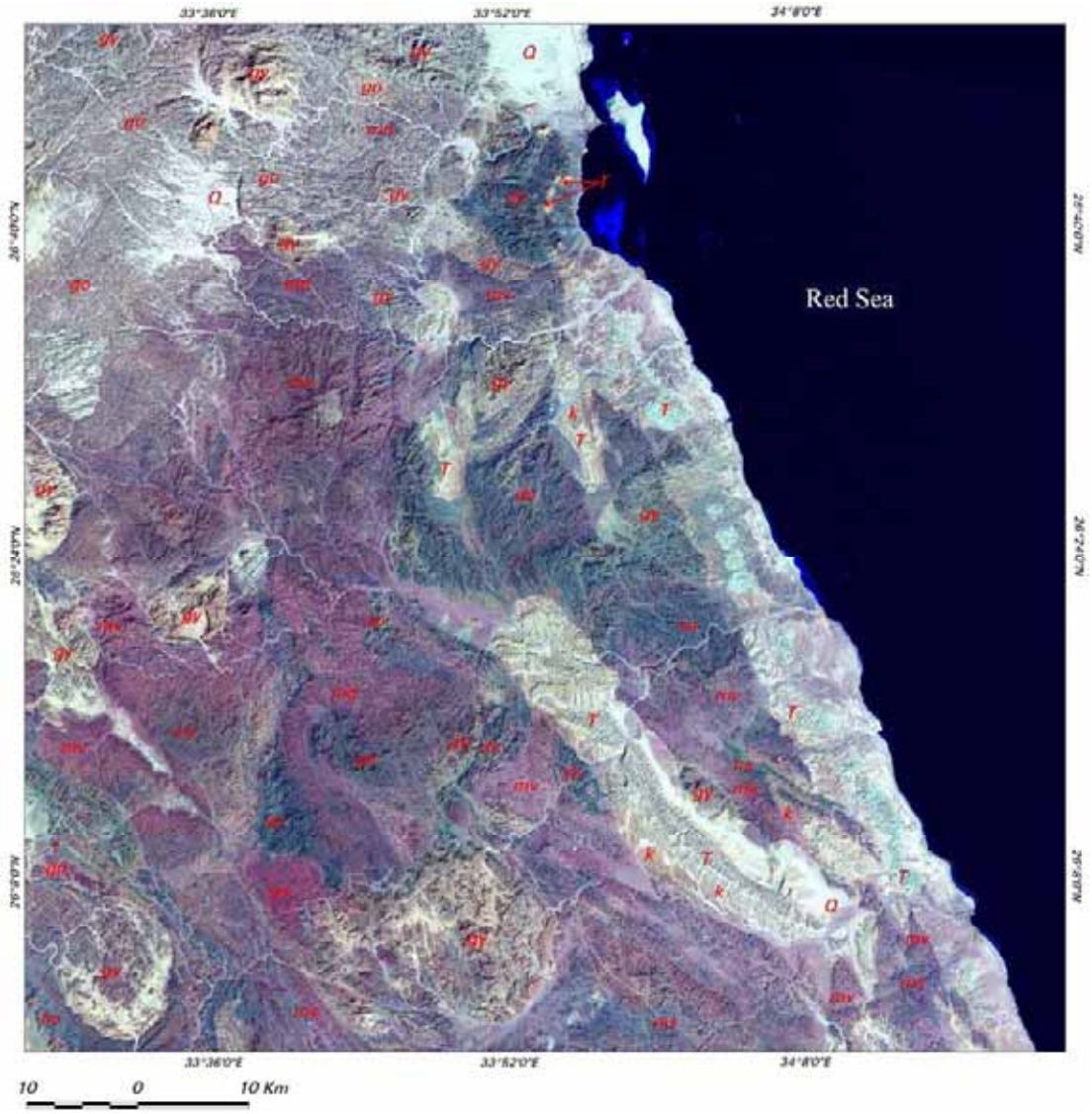

Q	*Quaternary (Alluvial deposits, sand, pebbles and conglomerate)*
T	*Undifferntiated Tertiary Rocks (Chalk, limestone, conglomerate, gypsum)*
K	*Undifferntiated Cretaceous Rocks (Nubian sandstone, phosphate)*
gy	*Younger Granitoids*
ga	*Gabbro*
f	*Felsite*
ha	*Hammamat Group (Hematitic, conglomerate, sandstone, siltstone, tuffstone and rare andesite)*
dv	*Dokhan Volcanics (Andesite, porphyry, felsite and tuff interbeds)*
go	*Older Granitoids*
md	*Metagabbro-Diorite complex*
sp	*Serpentinite*
mv	*Metavolcanics*
ms	*Geosynclinal Metasediments*
gn	*Paragneisses and Migmatites*

Fig. 2-7: *Enhanced ETM+ image of band composite 7, 4 and 2 (R, G, B) showing high contrast between the main rock units in the study area.*

Table 2-6: *Experimental compound band ratioing (CBR) and assessment.*

Band Ratioing (R, G, B)	*Source*	*Assessment*
7/5, 3/1, 4/3	Hydrothermal band ratio	Excellent
5/7, 5/4, 3/1	Mineral composite band ratio	Good
5/7, 5/1, 4/3 4/3, 3/1, 5/7	Ramadan (2003)	Good
4/3, 5/4, 5/7	Jasrotia & Das	Fair
4/5, 5/6, 7/6	El Rakaiby (1988)	Poor
5/7, 5/1, 5/4 x 4/3 1/4/2/5, 3/4/5/7, 4/5/1/3 5/7, 5/1, 4/5 x 3/4	Yousif (1999)	Poor

As can be deduced from figure 2-8, several rock formations are recognized according to their tonal and textural characteristics. On the contrary, distinguishing and separation of gabbro, felsite and andesite rocks depends on data compilation using the available geological maps due to the great similarity of their mineral components that have the same characteristics.

2.5.3. Multispectral Supervised Classification (MSC).

Multispectral supervised classification is the process of sorting pixels into a finite number of individual classes or categories of data based on their data file value (Lecia Geosystems, 2003). The classification process is carried out using the maximum likelihood algorithm based on the assumption that the histogram of the image has normal distribution. The algorithm defines the probability that a pixel belongs to a particular class and these probabilities are equal for all classes. Accordingly, the algorithm delineates ellipsoidal “equiprobability contours” in a scatter diagram (Fig. 2-9). Shape of the equiprobability contours expresses sensitivity of the likelihood classifier to covariance (Lillesand & Kiefer, 2000). The likelihood algorithm is the most accurate classification rules in ERDAS IMAGINE software because it takes the most variables into consideration by using covariance matrix (Lecia Geosystems, 2003). As well as, the algorithm consider not only the cluster center, but also its shape, size, and orientation (Janssen et al. 2001). On the other hand, Lillesand & Kiefer (2000) clarified that the maximum likelihood classifier would only be required for those land cover categories where residual ambiguity exists between over-lapping classes. The multispectral supervised classification is applied according to the following steps:

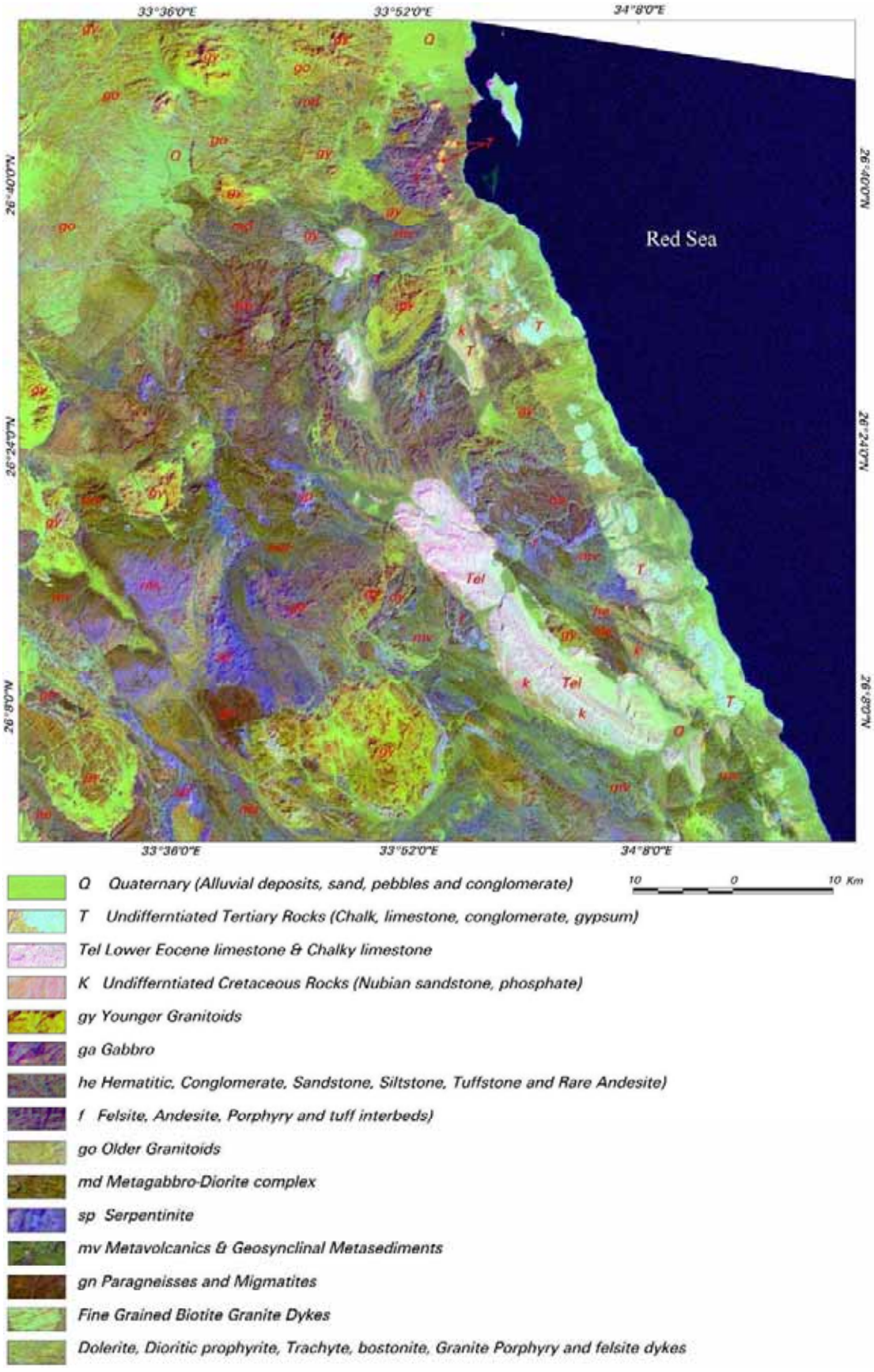

Fig. 2-8: *False colour composite ETM+ image using hydrothermal compound band ratioing 7/5, 3/1, 4/3 (R, G, B) showing high contrast between the main rock units.*

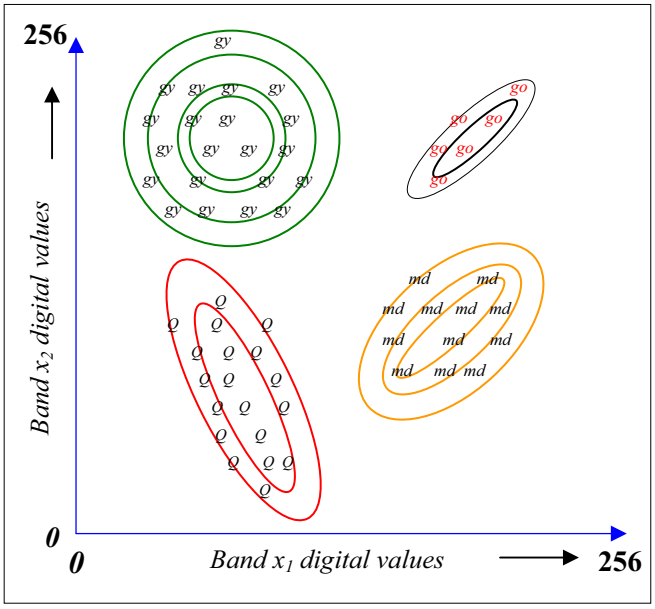

Fig. 2-9: *Equiprobability contours defined by the maximum-likelihood classifier.*

2.5.3.1. Assembling Areas of Interests and Spectral Signatures.

All categories are associated with known features using the available geological maps. Therefore, 303 supervised training or areas of interests (AOIs) are selected and controlled to represent 12 categories in order to assemble a set of statistics that describe the spectral response pattern of each rock unit (table 2-7). Number of the AOIs of each class is convenient to include tonal, texture, shadow, and pattern differentiations for each class.

Table 2-7: *Number of AOIs for each class name.*

Class_ID	*Class_Name*	*No. AOIs*	*Class_ID*	*Class_Name*	*No. AOIs*
1	Q	36	7	md	5
2	T	84	8	Sp	5
3	K	23	9	ms	21
4	gy	66	10	Modern coral reefs	5
5	fel	29	11	Sea Water	5
6	go	17	12	Vegetation	7
Total					303

Spectral Signatures of the selected AOIs are examined and statistical parameters are calculated for the seven spectral bands with the exception of the panchromatic band. The signature mean plot of 10 assembled classes clarifies that chalk, limestone, and

carbonate rocks have relatively high spectral values in general (Fig. 2-10). On the contrary, coral reefs have the lowest reflections in bands 3-7, the basement and sandstone showing intermediate response. It can be revealed that band 1 as a whole has the lowest mean values because of iron absorption and reflection. Nearly all minerals are highly reflected in the shorter-wavelength middle infrared band 5. Sabins (1996) assumed that different materials commonly have greater spectral variations in the thermal IR region than the visible region; nevertheless, the thermal IR (band 6) of the ETM+ image reveals the lowest spectral variations and it is less or poorly correlated with other bands.

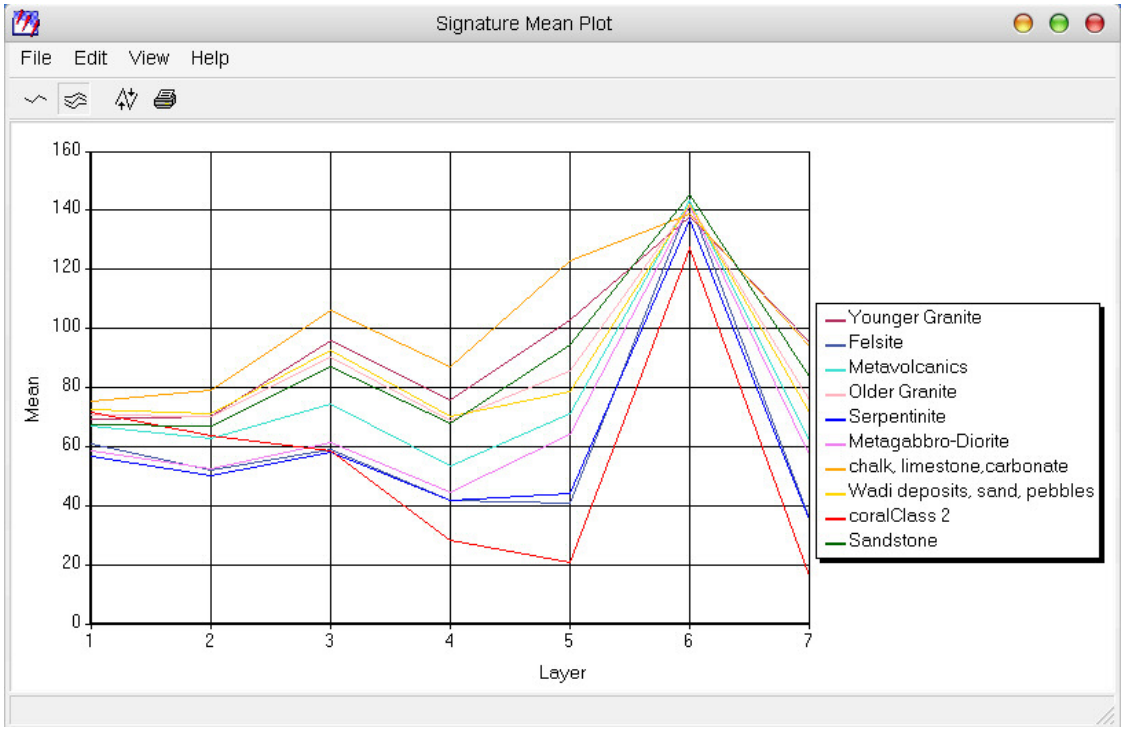

Fig. 2-10: *Signature mean plot of the image classes.*

2.5.3.2. Visual Verification.

Samples of the spectral response patterns of the selected AOIs are visually verified through the output histograms. Figure 2-11 showing a sample of the output histograms in band 1. The histograms from 2 to 9 are of normal distribution and histograms 1 and 10 are of bimodal because of the intervention in other classes[1].

[1] *For details see: Lillesand & Kiefer, 2000, p. 547.*

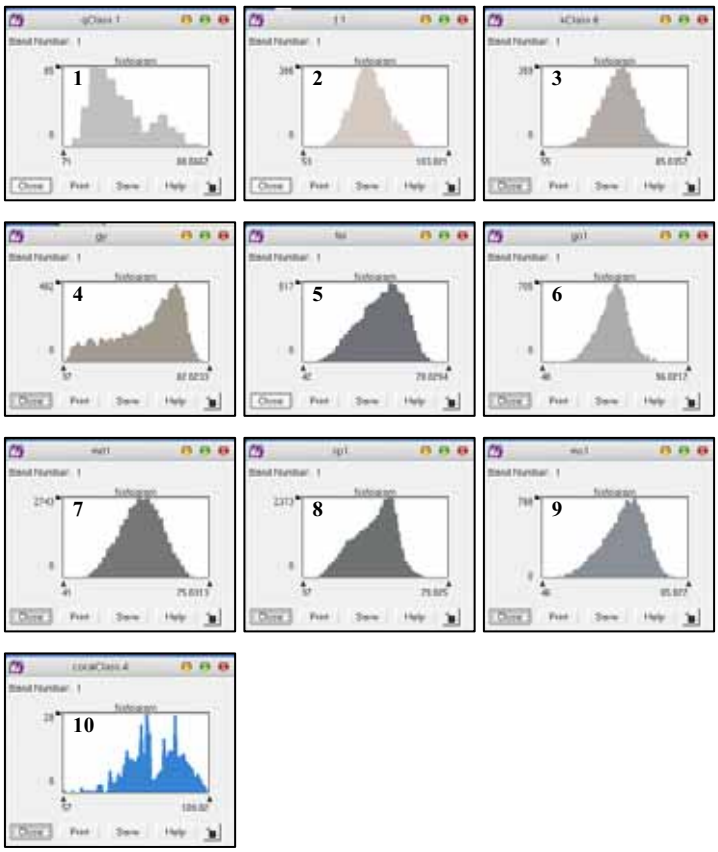

Fig. 2-11: *Histograms of some selected AOIs in band 1 representing classes 1.* ***Q****, 2.* ***T****, 3.* ***K****, 4.* ***gy****, 5.* ***fel****, 6.* ***go****, 7.* ***md****, 8.* ***sp****, 9.* ***ms*** *and 10.* ***coral reefs.***

2.5.3.3. Classification Contingency Matrix.

Pixels of each training sample are not so homogeneous that every pixel is actually classified into its corresponding class. Each sample pixel only weights the statistics that determine the classes. Then, the contingency matrix (usually known as a confusion matrix or error matrix) is calculated. The matrix contains numbers and percentages of pixels that are classified as expected (Lecia Geosystems, 2003). It allows comparison, on a category-by-category basis, of the relationship between known reference data and the corresponding results of an automated classification. The matrix contains number of rows and columns equal to the number of the assessed categories. Table 2-8 showing the contingency matrix that determines how well classification has categorized the assembled AOIs. The table clarifies the number of pixels representing each class and the total number of both rows and columns. On the other hand, table 2-9 showing the percentage contingency matrix and clarifies that the accuracy assess-

ment is ranging between 89.56% for ms class, and 99.96% for sea water class. The overall accuracy was obtained from table 2-8 by the following equation:

$$X1 + X2 + \ldots X_n \,/\, total\ number\ of\ reference\ pixels\ x100$$

Where: $X1, X2 \ldots X_n$ are the absolute number of pixels of each class within the contingency matrix, and the *total number of reference pixels* is the row and/or column total in the contingency matrix. Accordingly, the overall accuracy of the classification is about 93.26%. In the same manner, producer's accuracy and user's accuracy were calculated. Producer's accuracy indicates how well training set pixels of a given cover type would be classified, where user's accuracy indicates the probability that a pixel has been classified into a given category actually (Lillesand & Kiefer, 2000). Producer's Accuracy and user's accuracy are expressed as:

$$Producer's\ Accuracy = X\ /col.\ Total\ x\ 100$$
$$User's\ Accuracy = X/Row\ total\ x\ 100$$

Where: X is as mentioned above, *col. and Row Total* represent the total columns and rows of each class within the matrix. Therefore, producer's and user's accuracies are generally high indicating high credibility of the classification process (table 2-10).

Finally, it can be concluded that multispectral supervised classification is one of the best image processing methods for distinguishing between the main rock units within the study area. The classified geological map (Fig. 2-12) represents a well base map within the present study that is helpful for further analysis. The map contains 12 classes, of which 10 classes represent the main rock units in the study area. Table 2-11 shows the approximately spatial distribution of each class and the related rock type.

Table 2-8: *Absolute classification contingency matrix of the assembled AOI.*

Classes	gy	fel	ms	go	sp	md	T	Q	Coral reefs	Sea water	Vegetation	K	Row total
gy	7989	3	0	84	83	100	24	0	0	0	0	6	8289
fel	0	6591	303	16	1426	75	0	0	0	1	0	0	8412
ms	0	149	9060	66	574	2399	2	0	0	0	0	0	12250
go	93	57	102	7305	366	217	165	11	1	0	0	0	8317
sp	82	291	171	23	29670	216	1	0	0	1	0	0	30455
md	14	36	473	83	381	31080	15	0	0	0	0	3	32085
T	76	4	5	39	44	6	5639	0	0	0	1	13	5827
Q	0	0	0	309	0	0	0	540	0	0	0	0	849
Coral reefs	5	0	2	1	92	0	4	0	117	8	0	0	229
sea water	0	0	0	0	0	0	0	0	1	25754	0	0	25755
Vegetation	0	0	0	0	0	0	0	0	0	0	84	0	84
k	136	2	0	1	1	105	8	0	0	0	0	548	801
Col. Total	8395	7133	10116	7927	32637	34198	5858	551	119	25764	85	570	133353

Table 2-9: *Percentage classification contingency matrix of the assembled AOI.*

Classes	gy	fel	ms	go	sp	md	T	Q	Coral reefs	Sea water	Vegetation	K
gy	95.16	0.04	0	1.06	0.25	0.29	0.41	0	0	0	0	1.05
fel	0	92.4	3	0.2	4.37	0.22	0	0	0	0	0	0
ms	0	2.09	89.56	0.83	1.76	7.02	0.03	0	0	0	0	0
go	1.11	0.8	1.01	92.15	1.12	0.63	2.82	2	0.84	0	0	0
sp	0.98	4.08	1.69	0.29	90.91	0.63	0.02	0	0	0	0	0
md	0.17	0.5	4.68	1.05	1.17	90.88	0.26	0	0	0	0	0.53
T	0.91	0.06	0.05	0.49	0.13	0.02	96.26	0	0	0	1.18	2.28
Q	0	0	0	3.9	0	0	0	98	0	0	0	0
Coral reefs	0.06	0	0.02	0.01	0.28	0	0.07	0	98.32	0.03	0	0
sea water	0	0	0	0	0	0	0	0	0.84	99.96	0	0
Vegetation	0	0	0	0	0	0	0	0	0	0	98.82	0
k	1.62	0.03	0	0.01	0	0.31	0.14	0	0	0	0	96.14

Table 2-10: *Producer's and user's accuracies of the assembled AOIs.*

Classes	*Producer's Accuracy*	*User's Accuracy*
Q	98	63.6
T	96.26	96.77
K	96.14	68.41
Gy	95.16	96.38
fel	92.4	78.35
go	92.15	87.83
md	90.88	96.86
sp	90.91	97.42
ms	89.56	73.95
coral reefs	98.32	51.09
sea water	99.96	99.99
Vegetation	98.82	100

Table 2-11: *Approximately spatial distribution of the main rock types in the study area.*

Class Name	*Rock Type*	*Appr. Area (Km^2)*	*Area (%)*
Q	Quaternary & wadi deposits	628.52	15.41767
T	Tertiary rocks	399.5008	9.799803
k	Cretaceous sandstone & Phosphate	148.8592	3.651534
gy	Younger granitoids	923.5888	22.65574
fel	Felsite & Andesite	387.112	9.495904
go	Older granitoids	323.0432	7.924289
md	Metagabbro-Diorite	256.248	6.285794
sp	Serpentinite	188.7232	4.629403
ms	Metavolcanics, metasediments, Parag-neisses and migmatites	751.696	18.43919
Coral reefs	Recent coral reefs	69.3296	1.700663
total		4076.621	100 %

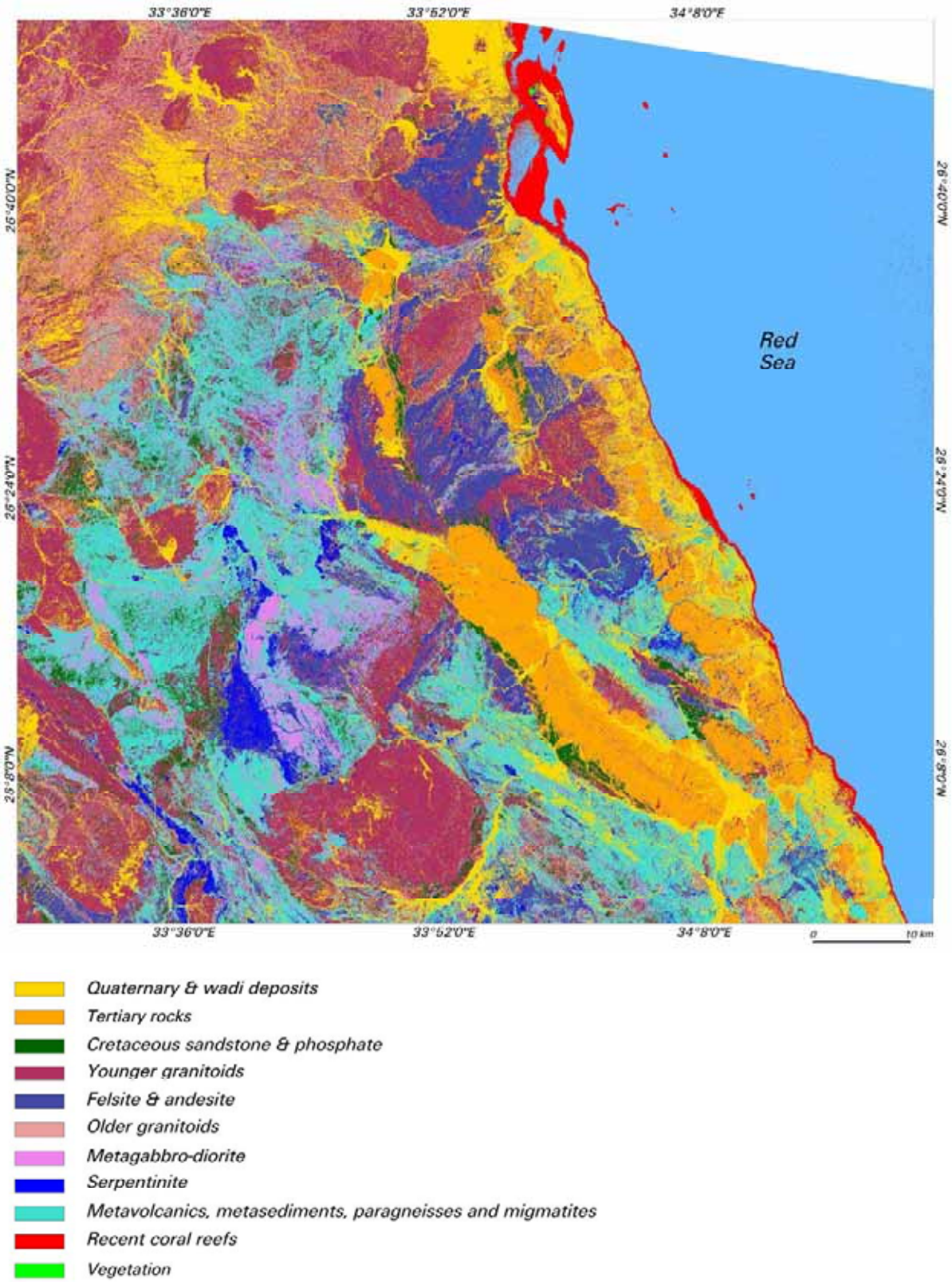

Fig. 2-12: *Classified geological map of the study area.*

3. Regional Structure

Structure of the study area should be studied in a more realistic manner with regards of the regional structure. It is well known that the Red Sea is one of the largest and most astonishing cracks in the Earth's surface. It extends about 7000 km from Lake Malawi (formerly Lake Nyasa) at Lat. 23°30`S. up to the Anatolian fault in Asia Minor at approximately Lat. 37°N. It includes the Great African Rift Valley, the Red Sea and Gulf of Aqaba, the Dead Sea, and the Levant. Therefore, it is obvious that the major structures along the Red Sea are a large number of NW-SE faults with general downthrows towards the E and NE (Akaad & Abu El Ela. 2002).

Actually, it is not proposed in this work to deal with the origin of the Red Sea and the Great African Rift Valley. The mechanisms of their origin have been long-term discussed in details within many publications. To give only a few of the more prominent pioneer works, the following should be mentioned: Walter (1888), Blanckenhorn (1893), Hume (1901), Ball (1909, 1920), Gregory (1920, 1921, and 1923), Bogolepov (1930), Willis (1936), Shalem (1954), Swartz & Arden (1960), Summerfield (1991). Therefore, study of the regional structures constitutes only of regional major faulting and folding as follows:

3.1. Faulting.

Investigation of the regional geological map of the northern part of the Red Sea and surrounded area in Egypt revealed two main directions of the major faults; they are: NW-SE and NE-SW (Figs. 2-13, 14). The first direction is the most widespread one that is adhering to the main direction of the Red Sea graben *(known as Erythrean or African faulting*). It is bounding the east scarp of the Red Sea Mountains. The second direction corresponds with the Gulf of Aqaba direction *(known as Aualitic faults)*. Both of them influenced the basement rocks as well as the Tertiary rocks lying between the Red Sea and the Nile Valley. It is deduced that these faults were formed in the late Tertiary time as a response of the formation of the Red Sea and the Gulf of Aqaba.

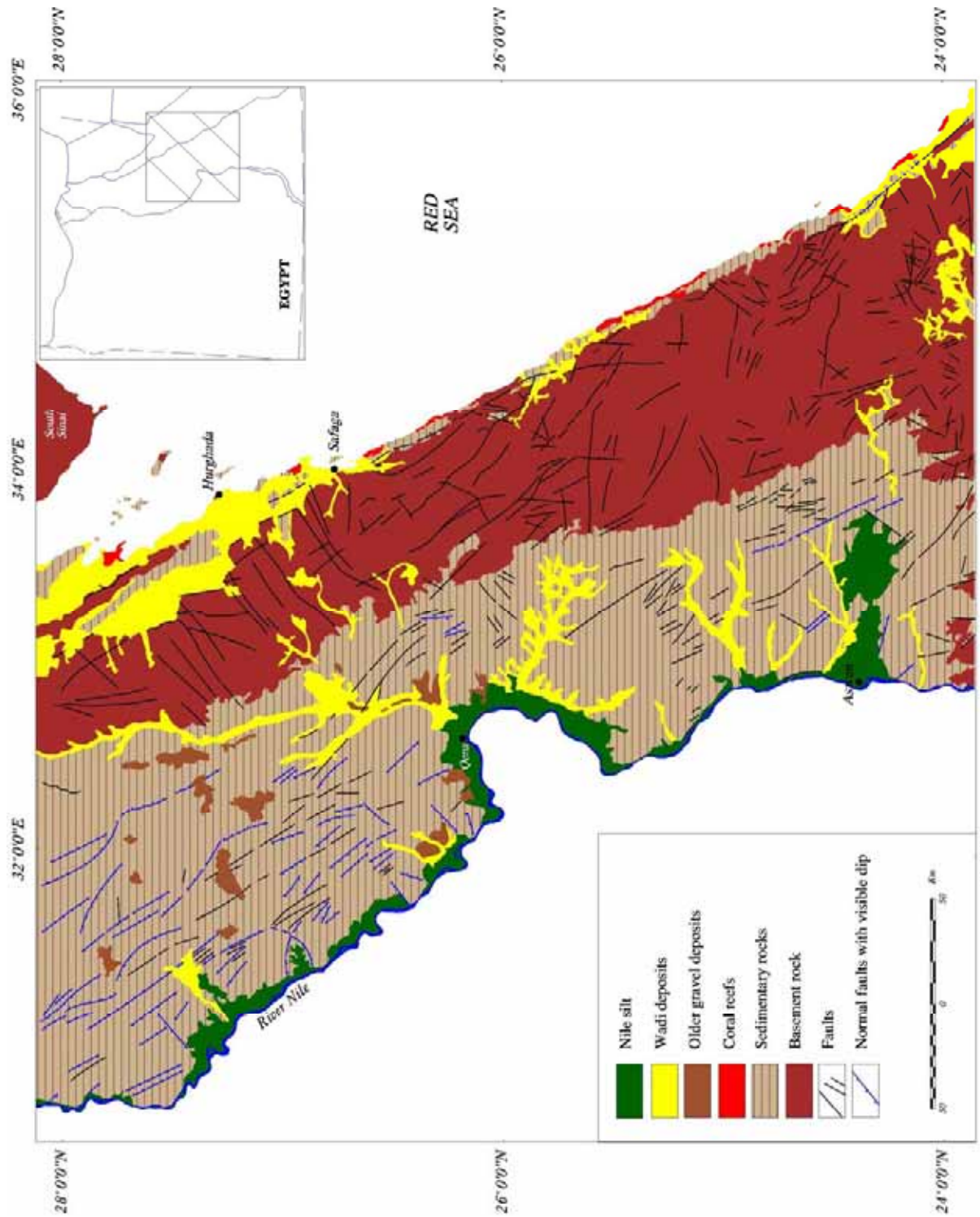

Fig. 2-13: *Regional geological map of the northern Red Sea and surrounded area in Egypt.*
(Geological map 1:1000.000)

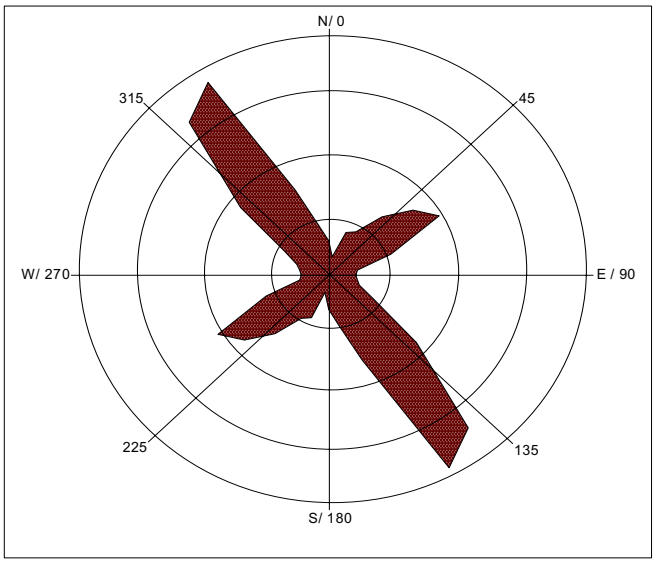

Fig. 2-14: *Predominant fault directions in the northern part of the Red Sea.*

Regardless of the mechanism that originated the Red Sea, Said (1962) argued that the normal faults control almost the entirety of the Red Sea coast. Step faults are common affecting different rock formations, a phenomenon which may suggest that the formation of the graben must have continued for a long time after their inception in lower Tertiary. Akaad & Abu El Ela (2000) denoted that the step faults are being most conspicuous along Qena-El Quseir highway where the basement rocks are faulted against the Nubian Sandstone (Fig. 2-15) that is in turn faulted against the Eocene strata of Jabal Duwi along NW-SE direction.

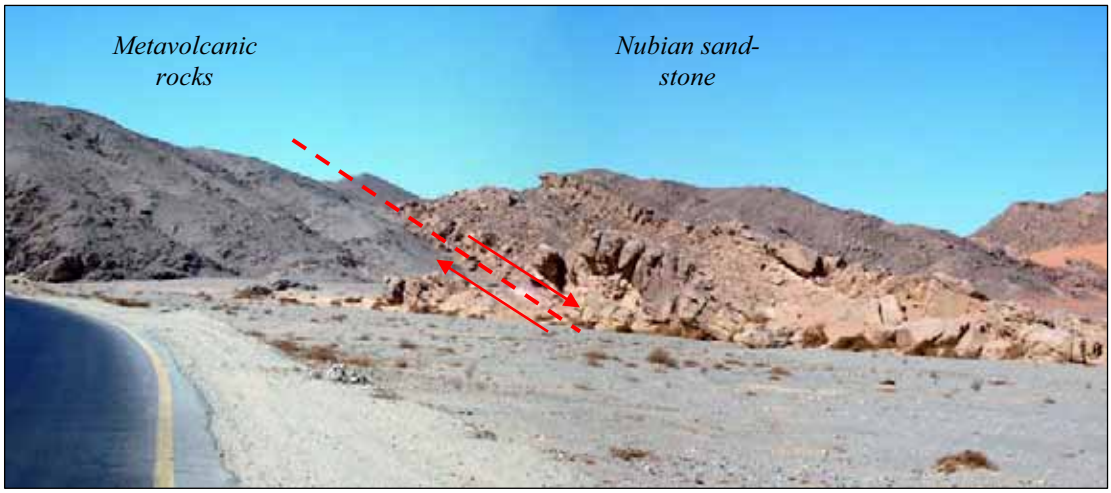

Fig. 2-15*: A normal fault separating the Nubian sandstone and the metavolcanic basement rocks along Qena-El Quseir highway.*

3.2. Folding.

The sedimentary rocks along the Red Sea coast were subjected to folding processes. The dominant folds are trending NNW-SSE and NW-SE into which the Cretaceous–Eocene series were involved during upper Eocene and Oligocene times. Beadnell (1924) enumerated several anticlines encountered the post-Eocene strata in the area between El Quseir and wadi Ranga. Two anticlines of which are located within the study area; they are: Bir Ambagi and Jabal Duwi.

Jabal Duwi is shown by Barron and Hume to terminate at a point ten kilometers south-west of El Quseir where the Eocene and Cretaceous rocks abut against schists along a nearly north - south fault (Beadnell, 1924). On the other hand, Bir El Ambagi fold lies between Jabal Duwi and El Quseir with a general dip 18 º to the east (Fig. 2-16). It is another remnant of Eocene-Cretaceous rocks. At other points, there are indications of a reversal dip, so that the beds as a whole might be regarded as a synclinal fold. As a whole, the folded rocks have been subjected to intense erosion except some remnant isolated hills along the coastal strip and within the morphotectonic depressions.

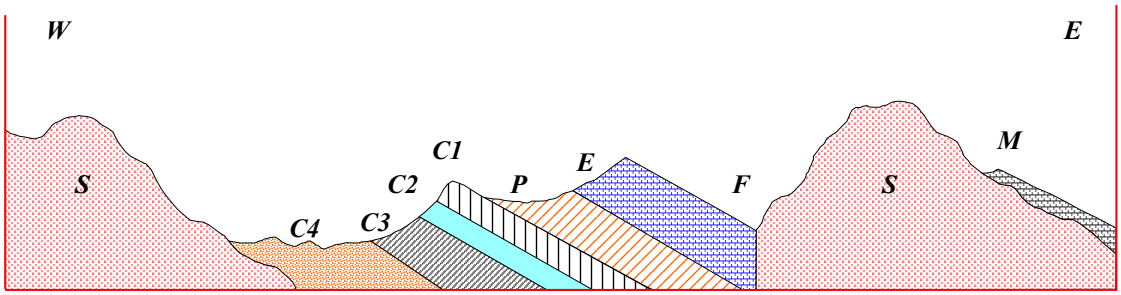

M. Miocene
E. Eocene limestone
P. Passage beds and Danian series
S. Schists
F. Fault and fold

C1. Cretaceous Ostrea Villei beds
C2. Cretaceous Phosphate series
C3. Cretaceous Shales
C4 Nubian Sandstone

(After: Beadnell, 1924)

Fig. 2-16: *Geologic section of Bir Ambagi fold.*

References:

Akaad, M. K. & El-Ramly, M. F. (1960a) The basement complex in the Central- Eastern Desert of Egypt between latitudes 24º 30` and 25º 40` N. *Geological Survey of Egypt, Cairo, papers no. 8, 35 p.*

Akaad, M. K. & El-Ramly, M. F. (1960b) Geological history and classification of the-basement rocks of the Central-Eastern Desert of Egypt. *Geological Survey of Egypt, Cairo, Paper No. 9, 24 p.*

Akaad, M. K. & Abu El Ela, A. M. (2002) Geology of the basement rocks in the eastern half of the belt between latitudes 25º 30` and 26º 30` N. Central Eastern Desert, Egypt. *Geological Survey of Egypt, Cairo. Paper No. 78, 118 p.*

Amin, M. S. (1955b) Some regional features of the Pre-Cambrian in the central Eastern De-sert, Egypt. *Bull.Inst. Desert, Egypt, 5(1): pp.193-208.*

Ball, J. (1913) A brief note on the phosphate deposits of Egypt. *Egypt Survey Dept., Cairo, 6 p.*

Ball, J. (1939) Contributions to the geography of Egypt. *Egypt Survey Dept., Cairo, 300 p.*

Barron, T. & Hume, W. F. (1902) Topography and geology of the Eastern Desert of Egypt (Central Portion). *Egypt Survey Dept. Cairo, 331 p.*

Beadnell, H. J. L. (1924) Report on the geology of the Red Sea Coast between Quseir and Wadi Ranga. *Petrol. Res. Bull. 13, Govern-ment Press, Cairo, 37 p.*

Canada Center for Remote Sensing (2002) Fundamentals of remote sensing. *http:// www.ccrs.nrcan.gc.ca (Accessed on 30 March 2005).*

Drury, S. A. (1993) Image interpretation in geology. *2ed edition, Chapman & Hall, London, 283p.*

El-Akkad , S. & Dardir , A. A. (1966a) Geology of the Red Sea Coast between Ras Shagra and Mersa Alam with short note on results of exploratory work at Gabal El- Rusas lead zink deposits. *Geological Survey of Egypt, Cairo. Paper No. 35, 67 p.*

El Rakaiby, M. L., Yehia, M. A. & Ayoub, A. S. (1988) Discrimination of lithologies in South-western Sinai Peninsula, Egypt, using Landsat Thematic Mapper Enhanced Data. *Middle East Research Center (M.E,R.C),Ain Shams University, Earth Sc. Ser., Vol. 2, pp. 104-115.*

El-Ramly, M. F. (1972) A new geological map for the basement rocks in the Eastern Desert and South Western parts of Egypt, scale 1: 1000 000. *Annals of the Geological Survey of Egypt, vol. II, pp. 1-18.*

Gregory, J. W. (1920) The African Rift Valleys. *Geographical Journal, 56: 13-47; 327-328.*

Hume, W. F. (1907) A preliminary report on the geology of the Eastern Desert of Egypt, between latitudes 22º N and 25º N. *Egypt Survey Dept., Cairo, 72 p.*

Hume, W. F. & Little, O. H. (1928) Raised beaches and terraces of Egypt. *Union Geograph. Intern., Paris, (Rept. Comm. Plio-and Pleistocene Terraces), pp. 9-15.*

Issawi, B., Francis, M., El-Hinnawy, M., Mehanna, A. & El-Deftar , T. (1971) Geology of Safaga-Quseir coastal plain and of Mohamed Rabah area. *Ann. Geol. Surv. Egypt. Vol 1, 19 p.*

ITC (2001) ILWIS 3.0 academic user's guide. *Unit Geo software Development Sector Remote sensing & GIS IT department, ITC, Enschede, The Netherlands, 530 p.*

Janssen, L. L. F. (ed.) (2001) Principles of remote sensing: an introductory text-book. *ITC, Enschede, the Netherlands, 170 p.*

Jasrotia, A. S. & Das, I. C. (without date) Spectral characterisation for base metal minerals and its probable extension in Udaipur area, Rajasthan. *http:// www. Geo-spatialtoday.com/ articles /article_31a.asp (Accessed on 04 April 2005).*

Jensen, J. R. (1986) Introductory digital image processing. *Prentice Hall, New Jersey, 384 p.*

Jensen, J. R. (2000) Remote sensing of the environment: an earth resource perspective. *Upper Saddle River, NJ: Prentice Hall, 544 p.*

Lecia Geosystems & GIS Mapping Division (2003) Erdas field guide. *7th ed. Erdas LLC., Atlanta, Georgia, USA, 698 p.*

Lillesand, T. M. & Kiefer, R. W. (2000) Remote sensing and image interpretation. *4th edition, John Wiley & Sons, Inc. New York, 724 p.*

Markham, B. (2000) Landsat-7 ETM+ radiometric calibration. *CSIRO Millennium Workshop, NASA/ GSFC/ LPSO/ 923, 48 p.*

Nicholas, M. & Short, Sr. (2004) The remote sensing tutorial. *http: // rst. gsfc. nasa. gov/Front/tofc.html (Accessed on 07 April 2005).*

Press, F. & Saviers, R. (1994) Understanding earth. *Freeman and Company, New York, 593 p.*

R.S.I (2003) ENVI user's guide. *Research System, Inc. Colourado, U.S.A. 1078 p.*

Ramadan, T. M., El Mongy, A. S. & Salah El Dein, S. (2003) Exploration for Uranium and Thorium mineralizations at Wadi Um Laseifa area, Central eastern Desert, Egypt: using remote sensing technique. *Jour. Remote Sensing and Space Sci., Cairo.*

Reischmann, T. (2000) Ophiolites and island arcs in the late Proterozoic Nubian Shield. *Ofioliti, Vol. 25 (1), pp.1-3.*

Sabins, F. F. Jr. (1996) Remote sensing, principles and interpretations. *3rd ed. W. H. Freeman & Co., New York, 494 p.*

Said, R. (1962) The geology of Egypt. *Elsevier Pub. Co. New Amsterdam, 377p.*

Said, R. (ed.) (1990) The geology of Egypt. *A.A. Balkema Rotterdam, Netherlands, 734p.*

Schürmann, H. M. E. (1949) The basement rocks of the northern part of the Eastern Desert of Egypt. *Bull. Soc. Geograph. Egypt, 23: pp. 35-61.*

Short, N. M. (2006) Remote sensing tutorial: lineaments and fractures. *http://rsd.gsfc-.nasa.gov/rsd/RemoteSensing.html (Accessed on 10 March 2006).*

Summerfield, M. (1991) Global geomorphology: an introduction to the study of landforms. *John Wiley & Sons Inc. New York, 537 p.*

USGS EROS Data Center (2004) Enhanced Thematic Mapper Plus (ETM+). *http:// edc. usgs.gov/products/satellite/landsat7.html. (Accessed on 02 August 2005).*

Whitten, D. G. & Brooks, J. R. (1972) The Penguin dictionary of geology. *Penguin Books, Great Britain, 514 p.*

Yousif, M. S. M. & Shedid, G. A. (1999) Remote sensing signature of some selected basement rock units from the Central Eastern Desert of Egypt. *Egypt. J. Remote Sensing & Space Sci., Vol. 1, Cairo.*

3

STRUCTURAL LANDFORMS

1. Introduction

Recall from chapter two, the study area has been long-term subjected to tectonic processes that contributed distinctive landforms not only within the study area, but also within the surrounding areas along the Red Sea and the Gulf of Aqaba. The proceeded landforms are much conspicuous particularly where the basement rocks dominantly characterize the ground surface. Therefore, the main purpose of this chapter is to clarify the interaction between tectonics and geomorphic processes.

2. Definition

"Structural landforms" is a wide spread term refers to landforms that have been originated primarily by geological structure and they gain considerably attention nowadays as a cornerstone of the tectonic geomorphology. Application and integration of remote sensing and geographic information systems (GIS) for studying these features involve firstly determination of structural lineaments. The early usage of structural lineament as a term was prior to the availability of aerial photographs. It was originally used by Hobbs (1904) for describing the significance lines of landscape that reveal the hidden architecture of the basement rocks (Campbell, 1996). Seventy-two years later, O'Leary et al. (1976) defined lineament as a mappable, simple or composite linear feature of a surface whose parts are aligned in a rectilinear or slightly curvilinear relationship. It differs from the pattern of adjacent features and presumably reflects some subsurface phenomenon. The definition given by O'Leary et al. is widely accepted and applied by Akhir & Abdullah (1997), Briere & Scanlon (2001) and Miyatake (2002). On the other hand, Ramsay & Huber (1987) defined such features as narrow linear fracture zones of regional scale, which give rise to marked topographic features easily recognizable on air photographs and satellite images. Peters & Shea (1988) derived such linear features from aerial photos and satellite images as guides to probable geologic structure that are assumed to represent faults and other fractures. Lineaments are determined by Drury (1993) as long line-like character often subtle, linear arrangements of various topographic, tonal, geologic, geophysical

and geochemical features. In that manner, Clark et al. (1994) defined lineaments as straight linear elements visible at the earth's surface and are the representations of geologic and/or geomorphologic phenomena. According to Campbell (1996), lineament as a name was given by geologists to lines or edges, which presume geologic origin and visible on remotely sensed images. Such features have also referred to as linears or lineations, which are applied to specific geologic or geomorphic features as topographic features, lithologic contacts and/or zone of fracture. Lillesand & Kiffer (2000) referred to lineaments as regional linear features that are caused by linear alignment of regional morphological features such as: streams, escarpments and mountain ranges and tonal features that are the surface expressions of fractures or fault zones. Short (2006) in his online book entitled ″Remote Sensing Tutorial″ determines lineaments as any linear features that could be picked out as lines (appearing as such or evident because of contrasts in terrain or ground cover on either side) in aerial or space imagery. If geological, these are usually faults, joints, or boundaries between stratigraphic formations. Other causes of lineaments include roads and railways, contrast-emphasized contacts between natural or man-made geographic features (e.g. fence lines). Short's definition is applied by Kocal et al. (2004).

Eventually, there is unanimity between the mentioned definitions to identify structural lineaments as linear features, probably evident geologic and/or geomorphologic structures. Regarding to characteristics of the remotely sensed data, a lineament can be defined as a series of pixels that have similar digital values, whatever they express. The present study concerns primarily in determining lineaments presuming geologic and geomorphologic origin (i.e. faults, folds, dykes, joints), while the man-made features will be avoid.

It is worthy mentioning that study of lineaments is not only to define the geologic influences on the physical landscape, but also it is valuable for further purposes such as groundwater, mineral, and hydrocarbon explorations.

3. Methods of Mapping Lineaments

3.1. Image Processing.

Nowadays, satellite images are widely used for determining lineaments. Different methods of image processing required for delineating lineaments are presented by

several workers (e.g. Berlin et al. 1976, Moore & Waltz, 1983, Vaughn, 1983, Drury, 1993, Akhir & Abdullah, 1997, Legely-Padovani & Mering, 1997, Briere & Scanlon, 2001, Bishta & El-Tarras, 2002, Miyatake, 2002, Kocal et al. 2004, Akman & Tüfekci, 2004, Jordan et al. 2005).

The present study involves various procedures of image processing applied on the ETM+ Landsat and STRM[1] images as follows (Fig. 3-1):

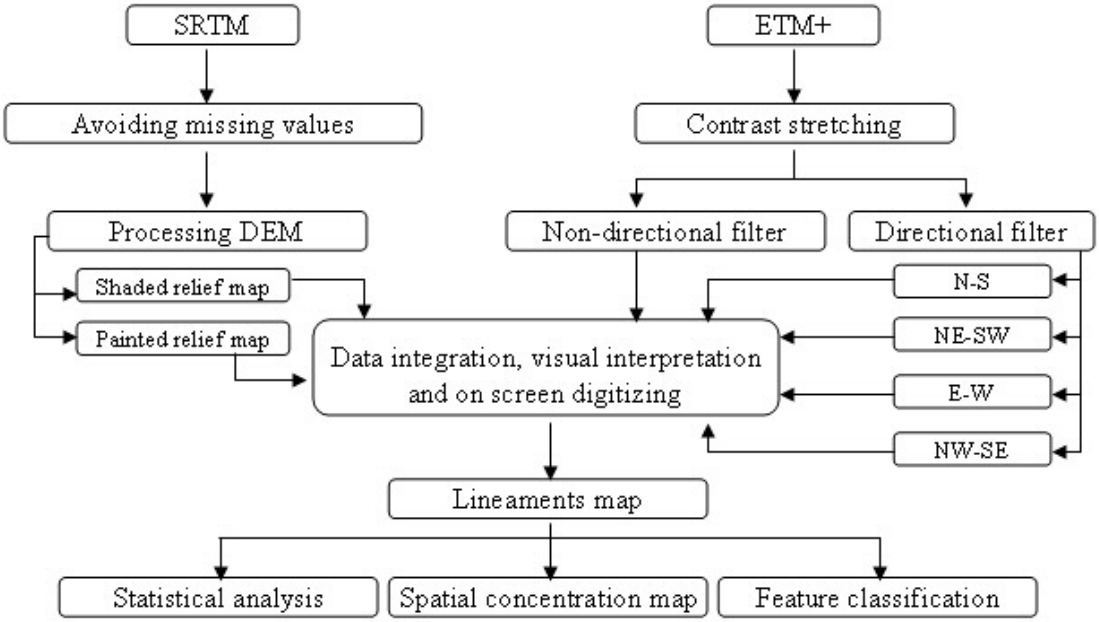

Fig. 3-1: *Method used for mapping lineaments.*

3.1.1. Edge Detection Filters.

According to Akhir& Abdullah (1997), all bands of the ETM+ image are visually compared in terms of contrast and definition of geological features (lineaments). It has been observed that linear features are clearly shown using band 4 more than other image bands. Accordingly, several convolution filters are applied to this band for reducing and modifying data distortions produced from sensor noise or vibration and edge detection enhancement (Fig. 3-2). Four types of edges are detectable by using convolution filter they are (Fig. 3-3):

[1] *SRTM: Shuttle Radar Topography Mission is an international project spearheaded by the National Geospatial-Intelligence Agency (NGA) and NASA that consisted of a specially modified radar system. The project is designed to obtain a high-resolution digital topographic database.*

- *Ramp edge:* where the DN (digital numbers) values increasing from low to a high level and distinguished by DN changes, slope, and slope midpoint.
- *Step edge:* a ramp edge with a slope angle of 90°.
- *Line or spike edge:* a region bounded on each end by an edge.
- *Roof edge:* a line with a width near zero.

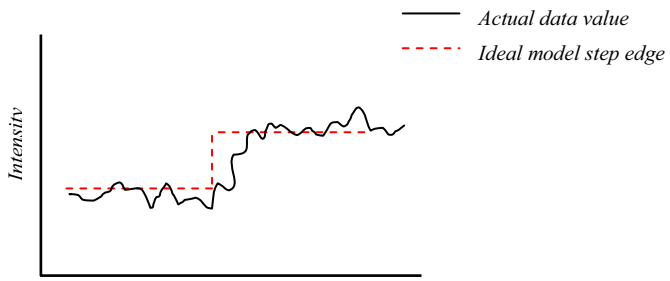

Fig. 3-2: *Comparison between actual data values and ideal model step edge derived using edge detection algorithms. (Leica Geosystems, 2003)*

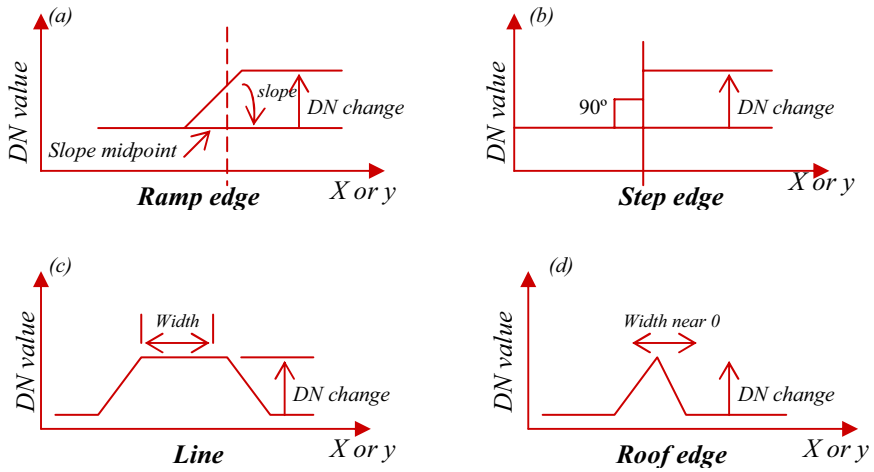

Fig. 3-3: *Types of detectable edges using convolution filter algorithm. (Leica Geosystems, 2003)*

The convolution filter algorithm is used in two ways:

- **Directional Filters.**

Directional filter is the 1st derivative edge enhancement filter that selectively enhances image features having specific direction components (gradients). The sum of the directional filter kernel elements is zero (Table 3-1). The results are areas with uniform pixel values that are zeroed in the output image, while those that are variable are presented as bright edges. Therefore, the image is directionally filtered from different directions as can be seen in figure 3-4.

Table 3-1: *Experimental kernels used for direction filters.*

N-S		
-1	0	1
-1	0	1
-1	0	1

NE-SW		
-1.4	-0.7	0
-0.7	0	-0.7
0	-0.7	-1.4

East-West		
-1	-1	-1
0	0	0
1	1	1

NW-SE		
0	-0.7	1.4
-0.7	0	-0.7
1.4	-0.7	0

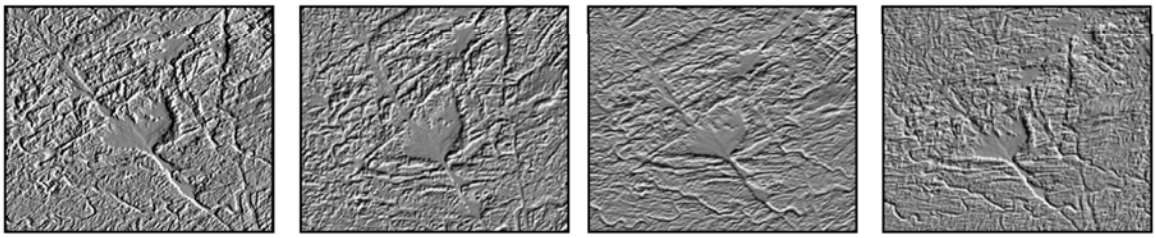

Fig. 3-4: *Directionally filtered images.*

▪ **Non-Directional (Laplacian) Filter.**

Laplacian filter is the 2nd derivative edge enhancement used to enhance edges regardless of edge direction (RSI, 2003). It is considered as the best operators for line detection within ERDAS IMAGINE software (Leica Geosystems, 2003). The operator is applied in the present study according to Akhir & Abdullah (1997) in their study for mapping and analysis of lineaments in NW peninsula Malaysia using LANDSAT TM imagery. The kernel composed of a high center value surrounded by negative weights in north, south and east directions. However, it is surrounded by positive values from the west and the coroners are of zero values (Table 3-2). The output is a panchromatic enhanced image where the linear features are more obvious and could be simply distinguished (Fig 3-5).

0	-1	0
1	5	-1
0	-1	0

Table 3-2: *Non-directional Laplacian Filter Kernel.*

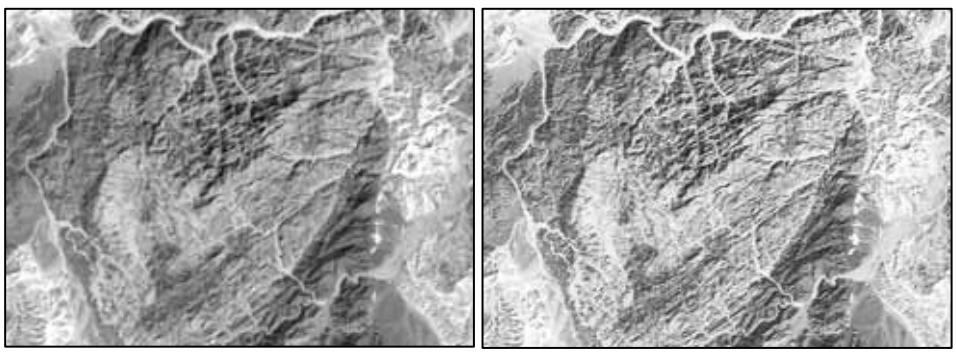

Fig. 3-5: *Original image (left) and the 2ed derivative enhanced image (right).*

3.1.2. Shaded and Painted Relief Maps.

Shaded and painted relief maps are processed from the DEM mentioned in chapter one, of 90 meters resolution, by vertically exaggerating the topography (DEM scale) 2.5 times. The shaded relief map artificially illuminates the relief by a light source positioned 45 degrees above the horizon from an azimuth[1] of 225° and topographic features are enhanced by strong illumination on the southwest direction facing slopes. However, the painted relief map is illuminated from the north-western direction of 345°.

On the one hand, shaded relief map depicts small features that could not be effectively shown using original image data. It improves the topography showing areas to be hilly or flat as well as the steepness of slopes. Areas that are flat or have few features are smooth on the map; on the contrary areas with steep slopes and mountains appear more rough (Fig. 3-6). Shaded relief map could be considered as one of the most appropriate terrain models for recognition and interpretation of complex morphological features (Jordan et al. 2005) such as surface fractures, faults, folds, and drainages.

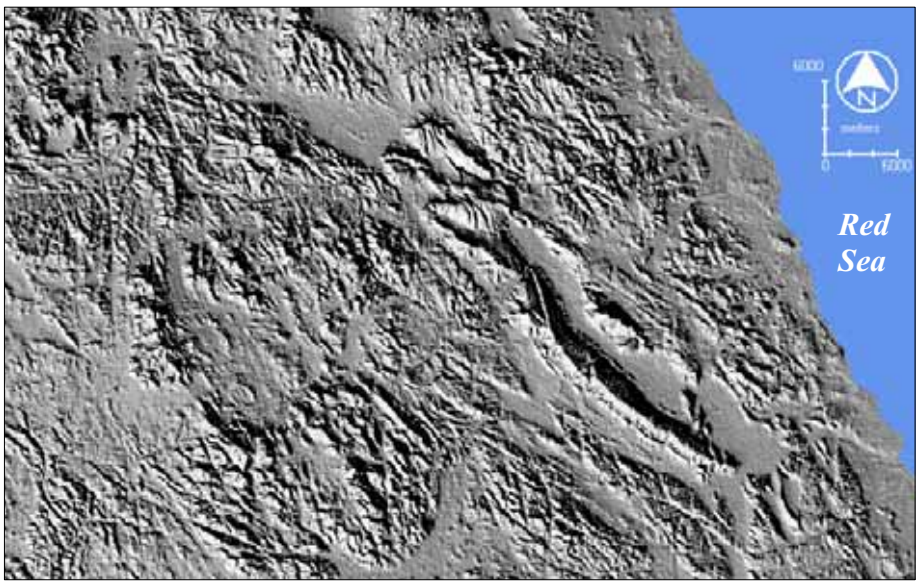

Fig. 3-6: *Extract of the shaded relief map covering the southern part of the study area.*

[1] *The azimuth is the angular of the sun. It is varies from 0 to 360, similar to compass direction. If the azimuth is 90 the sun is located to the east. Altitude is the angle of elevation of the sun above the horizon. It varies from 0 to 90 degree, which would be directly overhead.*

On the other hand, painted relief map is a colour topographical representation that is created using actual minimum and maximum ranges of the DEM (0-3000 m) with 25 colour levels. It provides a quick visual understanding to the terrain. Using different colours permits better identification of slope angles and changes in elevation (Fig. 3-7).

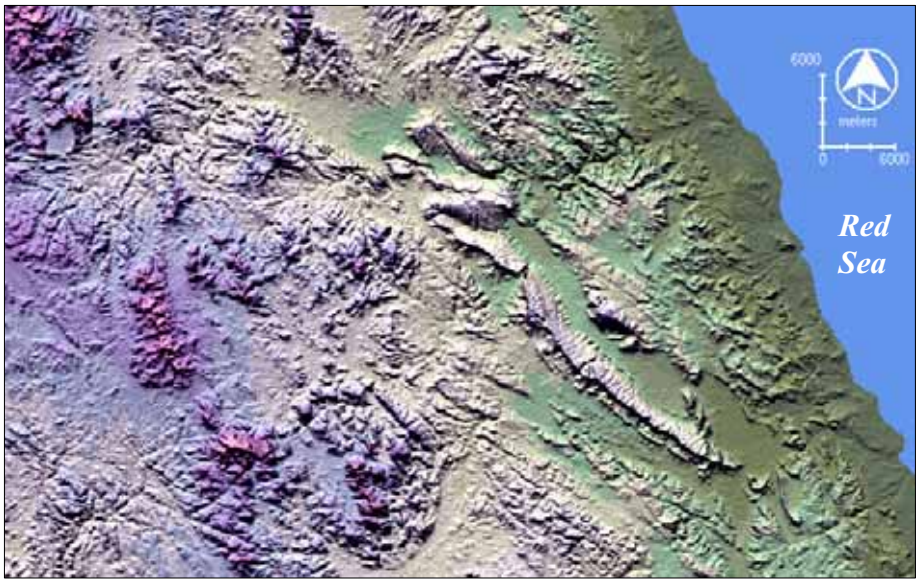

Fig. 3-7: *Extract of the painted relief map covering the southern part of the study area.*

3.2. Data Extraction.

Because some lineaments are only seen in a certain direction, lineaments are manually digitized based on visual image interpretation from the directional filtered images *(N-S, NE-SW, E-W, NW-SE)*, non-directional laplacian filtered image, and shaded and painted relief maps. The principal parameters used in the digitizing process are linear tonal variations, linear features separation, geological units of different texture, ridges, and the main wadi channels (El-Etr & Abdel Rahman. 1974).

Contrary to Kocal et al. (2004), most of the extracted lineaments show either darker pixels in the middle and relatively lighter grey on both sides in the directional filtered images (Fig. 3-8a). In some cases, such as the coastline, they clarify lighter colour in the middle and relatively darker colour on the both sides (Fig. 3-8b). At any case, lineaments could be distinguished and simply digitized due to their linear shape and lengthening. Application of manual digitizing permits detection of the non-geologic lineaments such as roads.

3.3. Data Comparison and Integration.

Integration of image data with "non-image" or ancillary data set is applied according to Lillesand & Kiefer (2000). Major faults, folds, and dykes are digitized from the geologic maps[1] and reports as well. Thereafter, the vector data are merged together for yielding the final lineament map (Fig. 3-9). The features are cleaned and topologically related to each other as line shapes to compute counts and lengths of the lineaments.

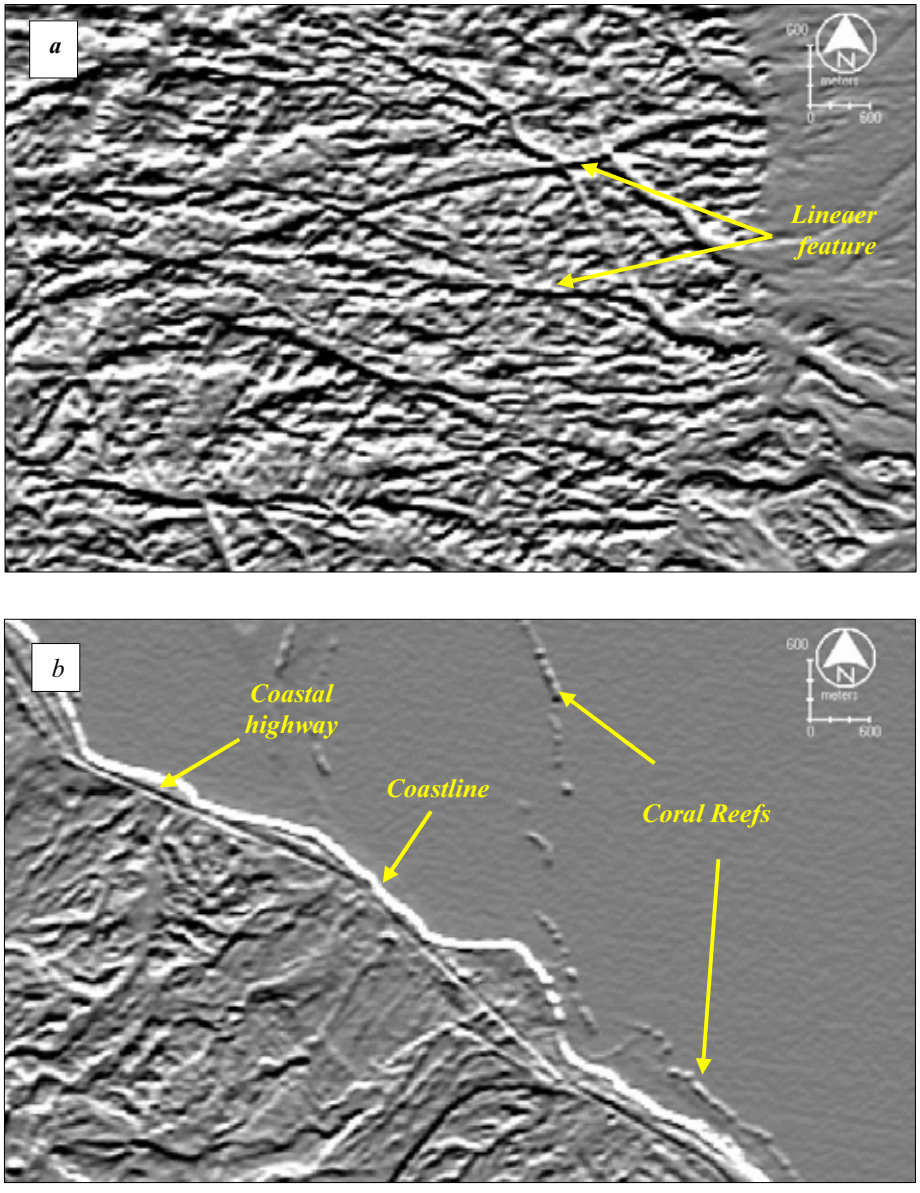

Fig. 3-8: *Tonal variations used to manually extract linear features. (a) Lineaments showing darker colour, (b) lineaments showing lighter colour.*

[1] *Basement Rocks of Safäjah Quadrangle, Egypt. Scale 1:100,000, E.G.S.M.A. 1987 and Metallogenic map of the Qena Quadrangle, Egypt. Scale 1:500,000, E.G.S.M.A. 1984.*

3.4. Statistical and Spatial Analysis of Lineaments.

The lineament map contains a total of 7329 linear features of a total length 5212 kilometers. Azimuth frequency diagrams of 10 degrees bin size are automatically extracted from the vector lineament map using ER_Mapper lineament module for representing total counts and lengths per direction (Fig. 3-10). The diagrams clarify three conspicuous trends or peaks of lineaments, they are: N-S, NE-SW, NW-SE. These peaks represent 9.59 %, 7.6%, 7.5% of the total count and 10.85%, 8.46%, 8.26% of the total length consequently (Table 3-3). Peaks more than 7% of the total length are considered as anomalies that might reflect significant regional and/or local trends (Hammad & Eweida, 1989 and Shabana, 1998). Some other directions, e.g. E-W, NNE-SSW, NNW-SSW are also noticeable but they are of a lesser significant.

Table 3-3: *Statistical analysis of the lineament map.*

Direction	*Counts*	*Counts %*	*Length Km*	*Length %*	**T.L./T.N.*
-80	432	5.89	289.89	4.95	0.67
-70	326	4.45	238.89	4.72	0.73
-60	493	6.73	407.95	8.27	0.83
-50	550	7.50	418.09	8.26	0.76
-40	524	7.15	416.54	7.35	0.79
-30	399	5.44	291.92	4.35	0.73
-20	314	4.28	185.10	2.71	0.59
-10	393	5.36	250.44	4.88	0.64
0	703	9.59	506.73	10.85	0.72
10	263	3.59	163.21	3.29	0.62
20	149	2.03	97.93	1.77	0.66
30	207	2.82	127.92	2.46	0.62
40	402	5.49	273.71	5.76	0.68
50	557	7.60	405.62	8.46	0.73
60	504	6.88	392.99	8.24	0.78
70	397	5.42	264.30	4.91	0.67
80	240	3.27	155.93	2.58	0.65
90	476	6.49	324.87	6.21	0.68
Total	7329	100%	5212.03	100%	0.71

* ***T.L. /T.N.*** = *ratio of total length to total numbers of lines.*

It is deduced that the total length of lineaments is proportional to the total count within each direction and; therefore, the T.L./T.N. ratio is considerably low ranging between 0.59-0.83.

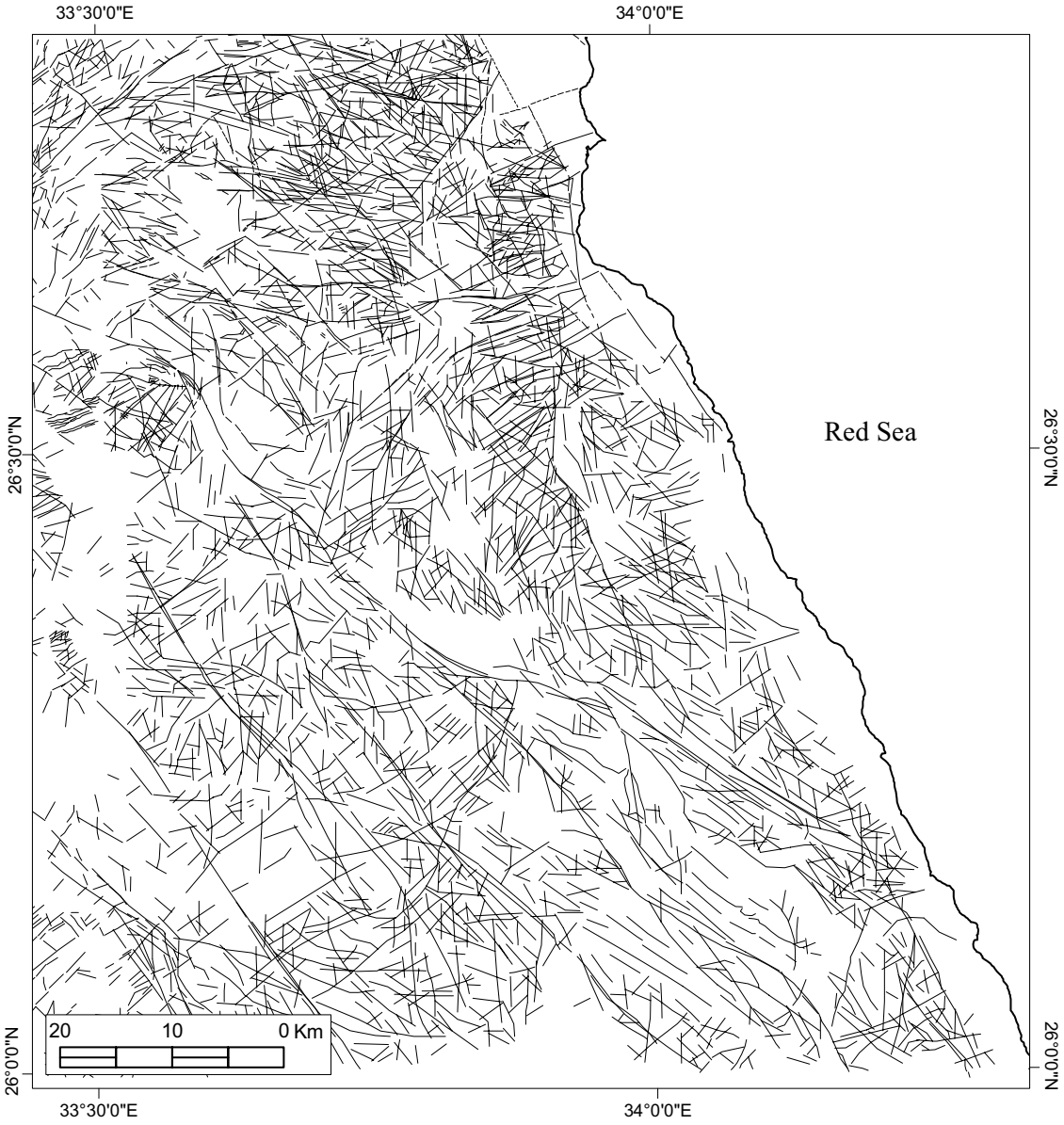

Fig. 3-9: *Lineaments map of the study area.*

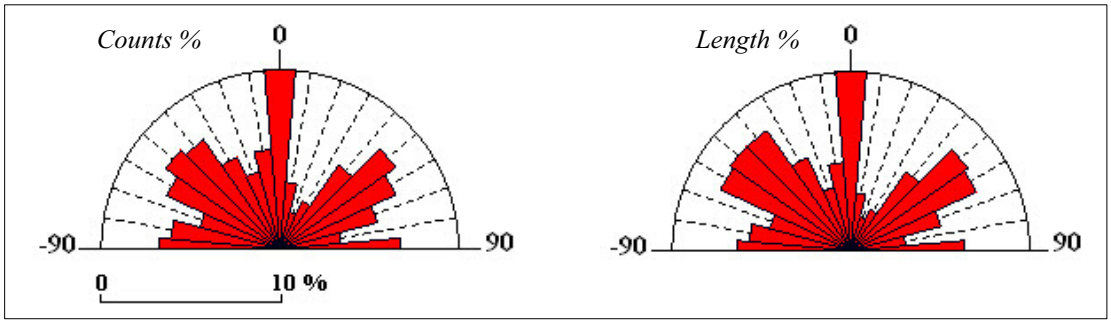

Fig. 3-10: *Azimuth frequency diagrams of the lineaments.* *(Bin Size: 10 degrees)*

It is worthy mentioning that the same major orientations are shown by Said (1962) and El Rakaiby (1984) in south central Sinai, Abdel-Rahman (1995) in the northeastern Egypt and Shabana (1998) along the Gulf of Aqaba. Furthermore, the NE-SW and NW-SE trends are mentioned by Foweler (2001) in Jabal Umm Had in the southwestern corner of the study area and Korrat et al. (2005) in his seismo-tectonic study of the northern Egypt.

In order to spatially analyse the lineament map, a grid of 5̀ lat. x 5̀ long. is used to divide the map into 85 squares. Each square is weighted by a point to represent the total number of lineaments within it. Thereafter, isolines are created using inverse distance weighted (IDW) method with line interval 10 lineations to clarify the spatial concentration of lineaments (Fig. 3-11 a). The resulting map shows different epicenters of lineament concentration.

The lineaments are more concentrated along the coastal plain where the mountain ranges are in the vicinity of the coastline and the isolines are being more approach to each other. By turning away from the sea, the isolines become less intense and divergent relative to each other because of the older granite, which forms a subdued surface. The epicenters are spatially dispersed and confined to plutonic intrusions of the younger granite and Dokhan volcanics such as at Jabals Barud and Naqarah successively. On the other hand, the Tertiary rocks manifest lower concentrations and equally the concentration is being very low where the lineations are concealed beneath the recent coastal plain and alluvial deposits.

Finally, it could be concluded that lineaments in the study area are controlled lithologically since the Tertiary rocks and the older granite manifest relatively lower concentration than Dokhan volcanic and younger granite dominating Jabal Naqarah and Jabal Umm Oradah respectively (Fig. 3-11 b). In spite of that, no particular orientation can be given to distinguish specific rock units.

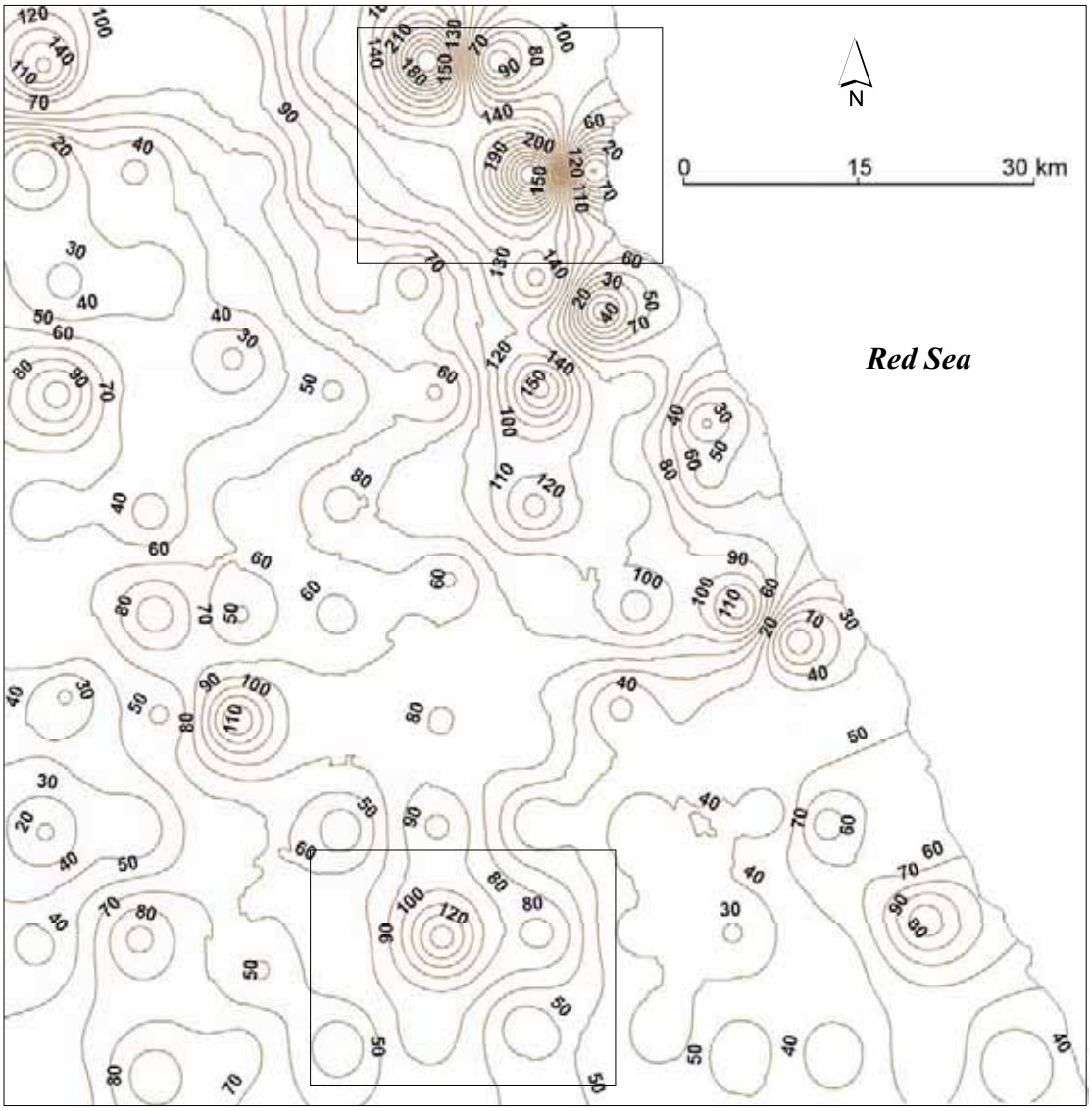

Fig. 3-11 a: *Spatial concentration map of the lineaments per 5`lat.* $_X$ *5`long. unit area and contour interval 10 lineations.* *(Boxed areas referring to the figures below)*

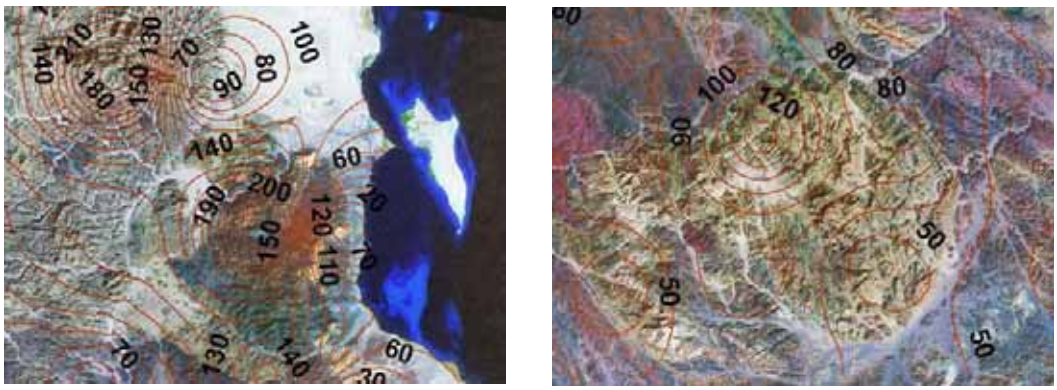

Fig. 3-11 b: *Patterns of lineament concentration at Jabal Naqarah (left) and Jabal Umm Oradah (right).*

4. Features Recognitions

Lineaments in the study area exhibit various structural landforms, which can be specified as follows:

4.1. Faults.

The basement complexes in the Central Eastern Desert of Egypt occur in the northwestern trending zone parallel to the general trend of the orogeny of the Red Sea (Beniamin et al. 2005). They comprise a mountainous range, which is well known as uplifted and/or fault-block mountains owing to crustal extension and manifesting horsts and graben. Normal and step faults constitute the most widespread fault systems as well as strike-slip[1] faults. Accordingly, the area extends between Safaga and El Quseir comprises a half graben[2], which is separated by Sodmein accommodation zone[3]. Rift-parallel (Clysmic) faults are oriented NNW and joined by transfer faults oriented NNE and WNW and by relay ramps as well (Moustafa, 2001).

The Clysmic faulting are the major structures consisting of a large number of NW-SE faults (Akaad & Abu El Ela, 2002). Consequently, the basement rocks are faulted against the Nubian sandstone that is faulted against the Eocene strata of Jabal Duwi. Akaad & Abu El Ela (2002) denoted that most of the exposure rock units are bounded by faults and the rock contacts are actually fault contacts.

According to Khalil & McClay (2002), the study area is dominated by two large linked normal fault systems, they are: the coastal fault system and the border fault system inducing domino-style fault blocks (Fig. 3-12).

---

[1] Strike-slip faults are usually known as wrench faults that involve motion parallel to the strike of the fault-frequently described as side-by-side motion. Normally they are steeply dipping with horizontal displacement and they are of sinistral (left) lateral or dextral (right) lateral faults depending if the block opposite the viewer moved to the right or left respectively.

[2] A half-graben is a down-dropped block bounded by a normal fault on only one side. Graben as a term is used as both singular and plural.

[3] The term accommodation refers to a complex zone of faulting that accommodates an along – strike change in both the fault dips and in sub-basin polarity within a rift system (Khalil & McClay, 2002).

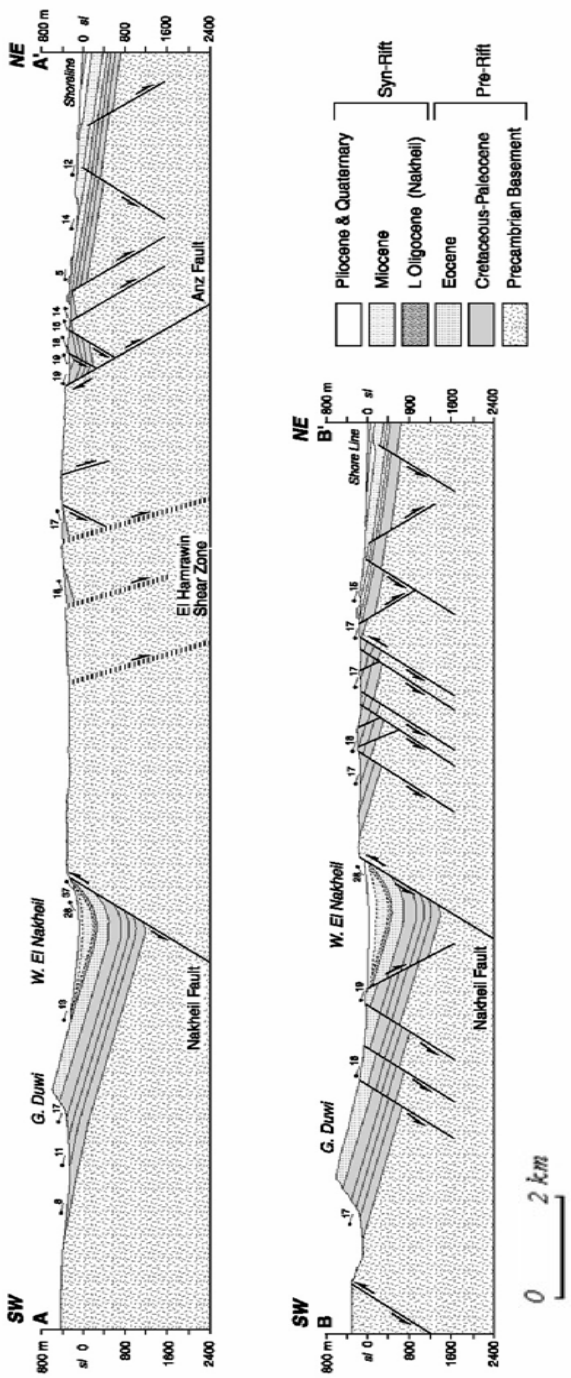

Fig. 3-12: *Regional geological profiles showing the domino-style fault blocks distinguishing the study area. (Khalil & McClay, 2002)*

The coastal fault system dominantly trends NW and delineates the main exposure syn-rift strata along the Red Sea. It induces abrupt topographic discontinuities of landforms and producing a major steep coastal fault scarp that is less or more modified by erosion (Fig. 3-13). Drainage lines flow on the top of the scarp and cut down forming deeply-incised **V**-shaped wadis yielding and cutting the scarp into a series of triangular facets.

Morphology of the coastal fault system between Safaga and El Quseir is considerably controlled by two NW oriented Queih and Hamraween shear zones. The intersection of the coastal fault with these zones divides the coastal fault into three segments, each with a characteristic hanging wall and footwall style. The southernmost segment consists of zigzag NS and WNW fault segments that extending from Zog el-Bahar block and terminating at Jabal al-Anz. Fault displacement along this segment increases towards the NW until the fault disappears underneath the Anz block northwest El Quseir (Younes & McClay, 1998).

The central fault segment is nearly continuous and extending from the northern side of the Anz block until wadi Queih. This segment exposes several fault blocks that juxtapose the pre-rift sequence next to the basement. The pre- and syn- rift strata in the hanging wall of this fault segment generally dip to the NE parallel to the fault dip direction. The hanging wall, pre-rift strata, is cut by NW and NE faults. The northern side of the fault block is separated from the northern segment by WNW faults that are parallel to the Hamraween and Queih shear zones. They juxtapose the pre-rift sequence next to the Miocene clastics (Younes & McClay, 1998).

The third coastal fault segment consists of a series of en-echelon giving an overall orientation parallels to the rift faults. The zone extends from wadi Queih to Jabal Gasus and encloses three relay ramps and several smaller ones between the fault segments (Younes & McClay, 1998).

On the other hand, the border fault system is more complex bounding a series of WNW and NW half graben whose average width is about 8 km and average bed dip is 15˚ towards the northeast. The half graben are cut by smaller faults dip 55˚-65˚ and have stratigraphic throw ranges from tens to few hundreds of meters (Khalil & McClay, 2002).

Fig. 3-13: *The coastal fault cliff of Jabal Naqarah.*

Normally, fault identification using satellite images is often more reliable than their detection in the field because of the following reasons (Drury, 1993):

- They are usually weaknesses and fault surfaces are rarely seen at outcrops.
- Changes in vegetation and surface texture related to faults are difficult to see when the geologist is close to them.

In the course of image interpretation, faults are recognized in the present study as surfaces across which blocks of crust have moved relative to one another. It is deduced that major faults are established in various directions i.e. N-S, NW-SE and NE-SW and exhibiting different phenomena, which are beneficial for fault identification as follows:

- Different types and ages of rock units juxtapose to each other because of the vertical or strike-slip displacements. Accordingly, it has been inferred that Jabal Naqarah is latterly faulted from E to W along the lower segment of wadi Abu Asala that is debouching about 6.5 km south of Safaga. The displacement is measured between two definite points along the fault line and it is estimated that the Tertiary rocks have been displaced 1.7 km approximately (Fig. 3-14a). Equally, the post-Hammamat felsite *(fbh)* comprises narrow strip intrudes the Hammamat group *(ha)* and depicts NW-SE and WNW-ESE normal faults bounding and sometimes crossing wadi Queih (Fig. 3-14b). They are of that type of sinistral strike-slip faults (Abdeen & Greiling, 2005).

▪ Sudden changes in elevation and slopes (topographic abruption) are ensued due to the major faults producing distinctive fault-controlled forms such as fault scarps, intermountain basins, and straight wadi channels (Fig. 3-15).
▪ Tracing fault-controlled wadis that are defined by fault systems. They might be a result of differential erosion of weakened rock or the juxtaposition of two different rock types. Normally, the fault-controlled wadi tends to be sharp straight like the lower segment of wadi El Barud that lies between two bends before reaching the coastal plain (Fig. 3-15). Such wadis might be suffered shifting and bending around the topographic obstacles to maintain their watercourses.
▪ Occasionally, the ground surface is dominantly characterized by zigzag geometry due to the intersection of two fault trends such as the Clysmic and transfer fault systems. Usually, they are interposed by the morphotectonic depressions, which are often filled with alluvial deposits and loose materials (Fig. 3-16).

Moreover, vertical displacements were investigated in the field in different locations. Faults of the basement rocks are incised detaching the mountainous range into several blocks (Fig. 3-17). They filled occasionally with dykes or occupied by short wadis. Vertical faults are more systematic in the sedimentary rocks exhibiting regular spaces and offsets. For example: walls of Sodmein gorge expose perpendicular NW-SE faults varying in displacement between few centimetres and 2.5 m (Fig. 3-18).

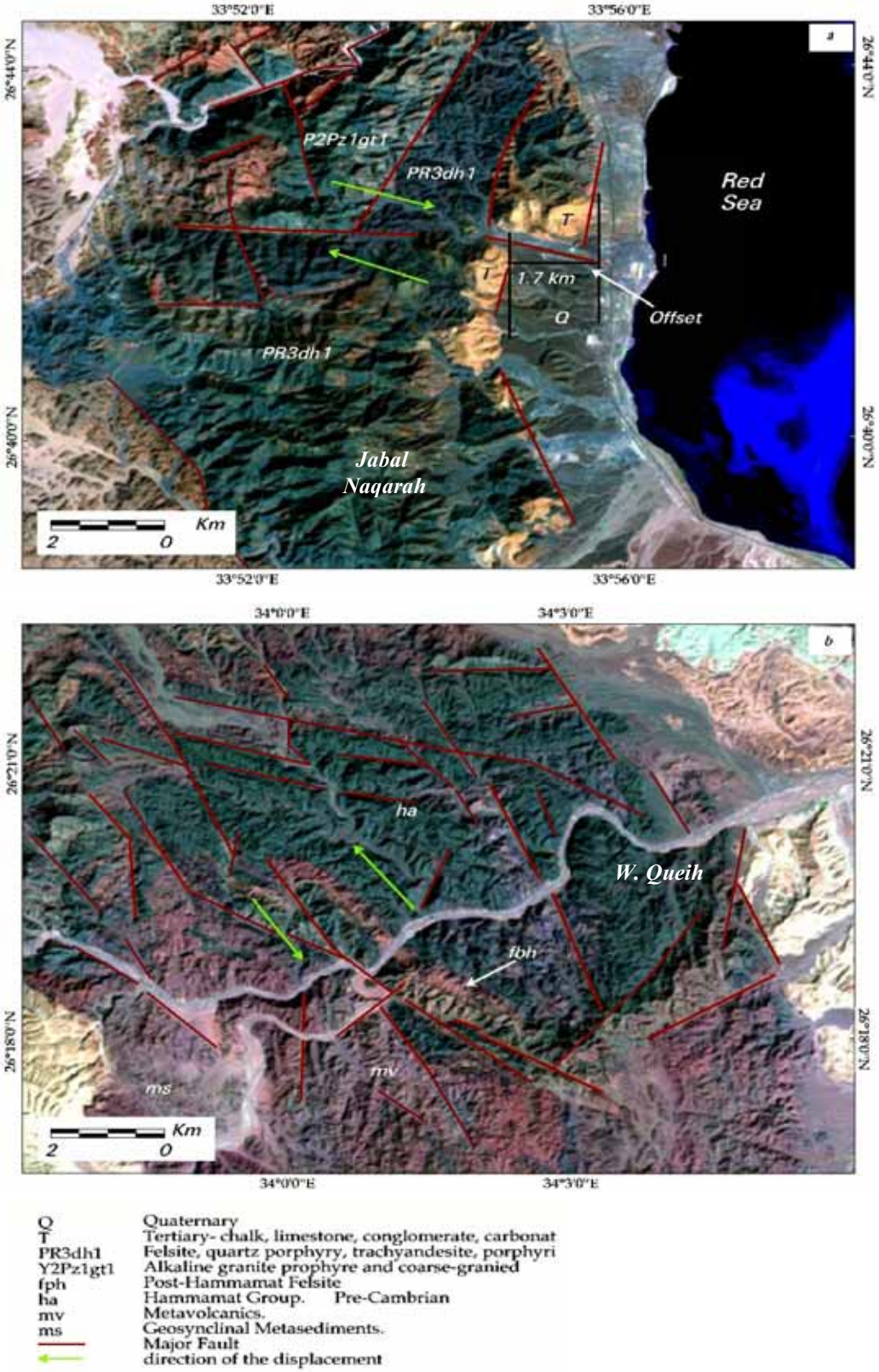

Fig. 3-14: *(A) An inferred E-W offset in Jabal Naqarah. (B) An inferred NW-SE and WNW-ESE faults in Queih area.* *(Extract from the ETM+ image and the lineaments map).*

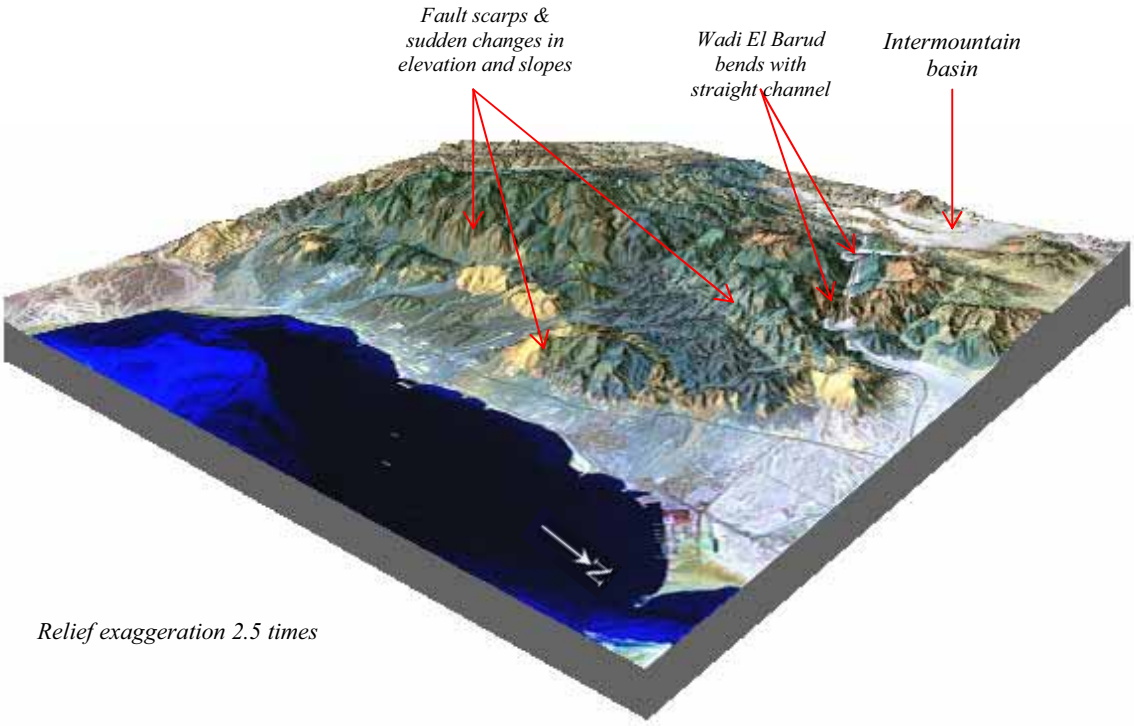

Fig. 3-15: *DEM overlain by ETM+ image band combination (7, 4, 2) showing fault-controlled forms at Jabal Naqarah.*

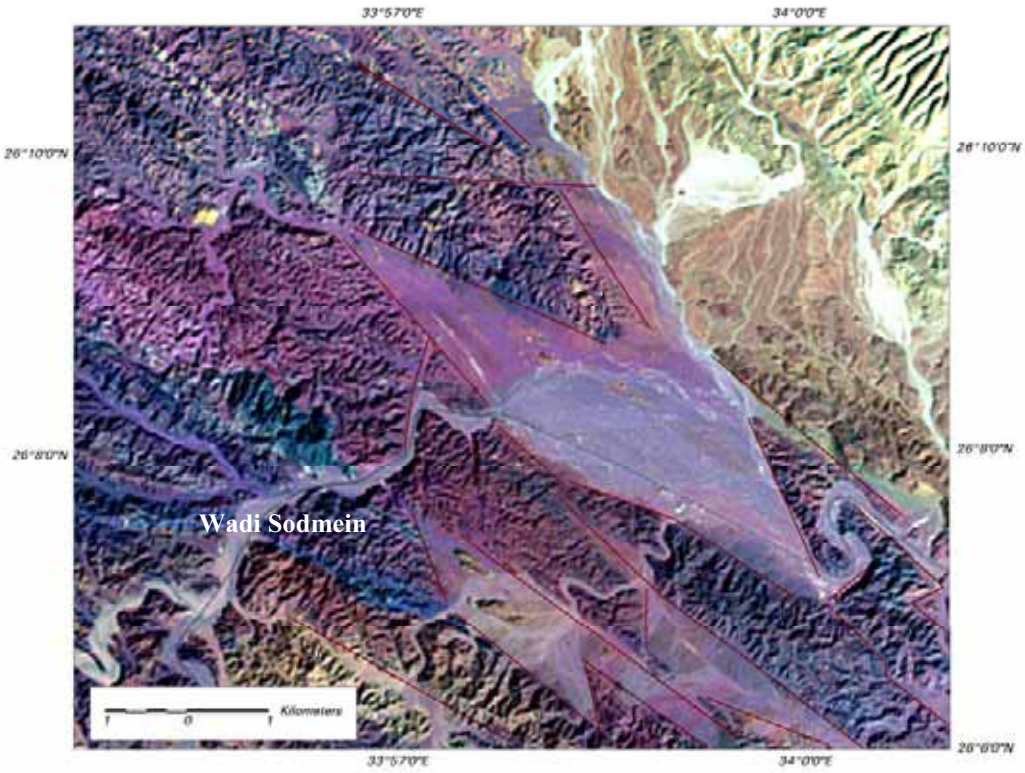

Fig. 3-16: *Zigzag geometry interposed by morphotectonic depressions west of Jabal Duwi.*

Fig 3-17: *Major faults detaching Jabal Gasus.* *(Looking southwest)*

Fig. 3-18: *Regular NW faults influencing the southern wall of Sodmein gorge.* *(Looking southeast)*

4.2. Warped Landforms.

In view of the fact that the study area underwent intensive tectonic events, sedimentary rocks have been wrenched and yielding warped or tilted landforms. These features are recognized in the study area by using satellite imagery and the digital elevation model (DEM) depends on their upward (anticline) or downward (syncline) forms. Their outcrops are often obvious in many localities owing to dip, curvature, and/or displacement that stand out in relation to neighbouring features (Short, 2006). They are much or less preserved in elongated inland depressions and along the coastal plain due to the action of the great faults. It is believed that they do not stand out individually; instead they comprise parts of continuous fold systems, which extend from Halaib in the southeastern Egypt to the Gulf of Suez. They are more or less parallel to the main direction of the Red Sea and probably comprise remnants of larger and longer plateaus, which have been detached by widening of the drainage systems and underwent severe deformation.

Warped landforms in the study area are built of Cretaceous-Tertiary rocks and generally varying in dip from 12˚ to 25˚. As well as they vary greatly in elevation from 100 to 150 m asl along the coastal plain and 350-620 m asl inland. Said (1990) demonstrated the NW-SE trend as the main structural fault set distinguishes such folds and it is affected by another cross perpendicular east-west fault system. According to him, these faults extending eastward into the main Red Sea depression showing the Red Sea margins as homocline dips gently eastward from the shore and is made of many horsts and fault blocks. Sometimes, the main structural axe (NW-SE) is shifted laterally probably as a result of east-west cross faults.

On the other hand, Beadnell (1924) assumed that the general parallelism between Cretaceous-Eocene folds, crystalline ranges, coastline, and the Red Sea itself seems to indicate that the present topography had been determined to a very important extent by pre-Miocene or pre-middle Miocene events. In that manner, Said (1962) argued that it does not preclude the possibility that the area may have been affected by latter movements, the fact that the Miocene and latter sediments are raised and domed up in place may be taken as an indication that faulting continued in post-Miocene times.

Wunderlich (1983) invoked the Paleozoic, Mesozoic and Tertiary maps after Said (1962) and pretended that there was a huge sedimentological basin (größeres Sedi-

mentbecken) separated from a bay (Bucht) called Urgolf of the Paleozoic Sea that had comprised half graben, in which the Nubian Sandstone is interposed. According to him, the basin was enduring until the Eocene time and had extended to the latitude of El Quseir. Accordingly, the elongated depression, where the warped rocks are preserved, might be inherited?!

Zaky (1999) indicated that the area was subjected to the following movements:

- NW compression movements, which are probably related to the late Cretaceous-Early Tertiary oblique convergence between Africa and Eurasia and the closure of the Tethys Sea.
- NE extension that is resulted from divergent movement between Africa and Arabia since Oligocene-Early Miocene phase. This extension caused right-lateral displacement along NE trend.
- Post-Early Miocene movement 'Mid-Clysmic event'. This event represents approximately one third to one half of the extension in the Red Sea-Gulf of Suez rift.

Interpretation of satellite images, topographic and geologic maps revealed that warped forms in the study area take place along the coastal plain and in the inland depressions (Fig. 3-19). The inland forms are most conspicuous for their distinctive features, of which Jabal Duwi (+595 m asl) and its continuations in Jabal Umm Hammad (the western flanks of Jabal Duwi), Jabal Al Atshan in the south (+353 m asl) and Jabal an-Nakheil in the east (+362 m asl) are the most conspicuous. Further to the north, three other obvious folded and faulted blocks are recognized as Jabal Mohamed Rabah (+392 m asl), hills of Wasif basin (+481 m asl), and hills of Umm al-Hawaytat (+370 m asl).

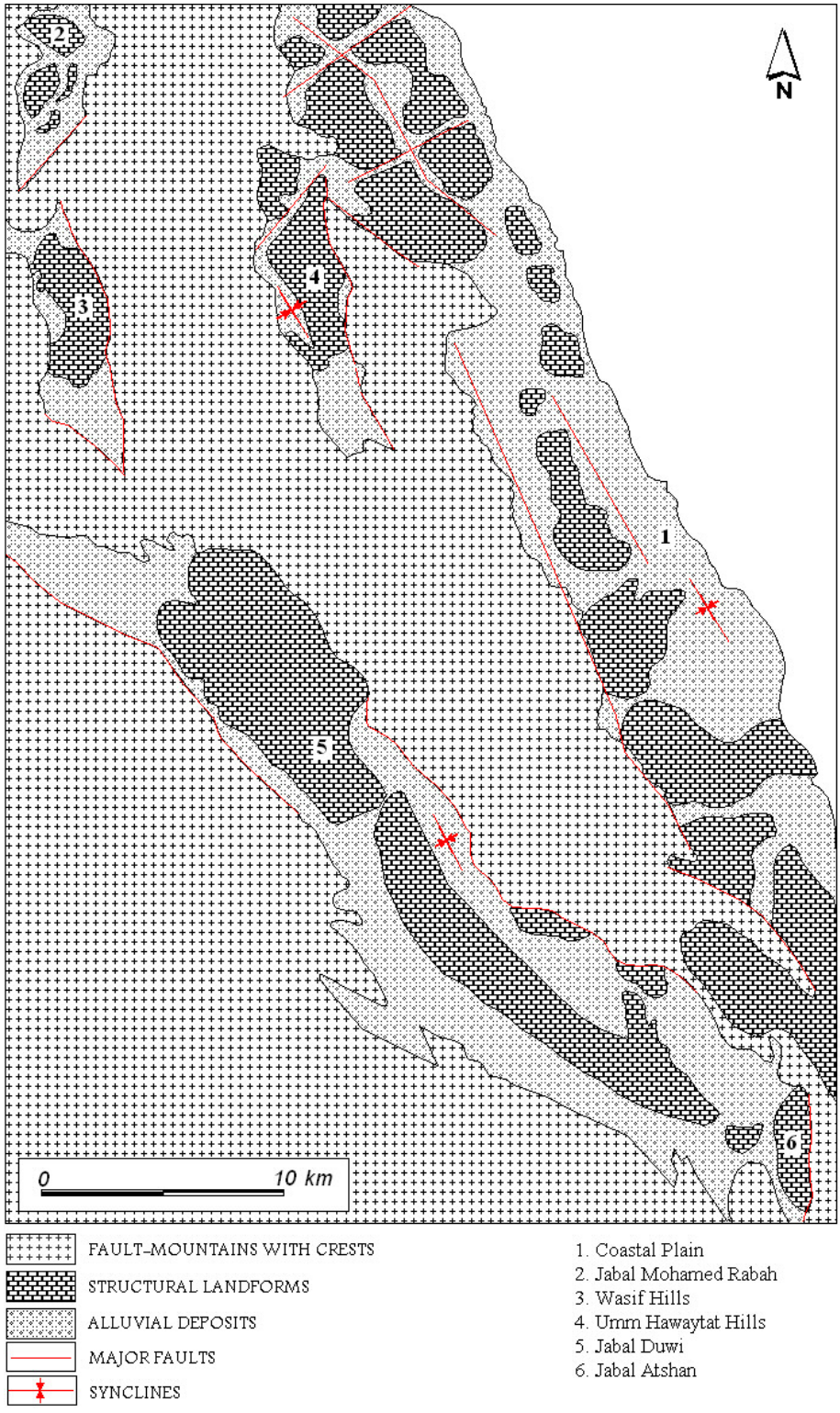

Fig. 3-19: *Spatial distribution of the main warped forms in the study area.*

(Source: ETM+ image, topographic maps 1:100.000, Field Study)

4.2.1. Methods of the Study.

The present study depends on the integration of different data layers of various sources (i.e. ETM+ image, DEM, geological data, slope map and lineaments map). The data are combined together or individually investigated. The main objectives of data integration are to find out an optimal qualitative and quantitative method for studying warped forms using remote sensing as follows:

4.2.1.1. Outcrops.

Outcrop refers to a portion of rock strata that is exposed above the surface. Analysis of the processed data revealed that the inland warped landforms are relatively tilted more than the coastal landforms showing upward forms with distinctive scarps. Therefore, one limb is often higher showing free face slope such as the western scarp of Jabal Duwi. As a result, the outcrops are obvious and could be stripped simply (Fig. 3-20). They could be also identified from the wadi sides where a wadi system crosses through the anticline. Identification of outcrops is beneficial for identifying dip direction and verifying rock resistance.

4.2.1.2. Dip Identification.

Dip of the rock was firstly identified from the satellite images according to the following criteria (Drury, 1993):

- In valleys the boundaries assume **V** shape that is pointing to the direction of the dip. The **V**-shaped notches would be ensued where streams incise homoclinal ridges perpendicular to strike due to the head-ward erosion and cutting through the scarp face. Law of **V**s, in the case of a **V**-shaped notch, could be formulated as the apex of the **V** point down dip in the direction of the dip.
- Stripping of layers and their boundaries.
- Examining drainage patterns: In the case where dips are less than about 45˚ consequent and resequent streams tend to be longer than obsequent streams, and they can reveal a crude direction of dip.

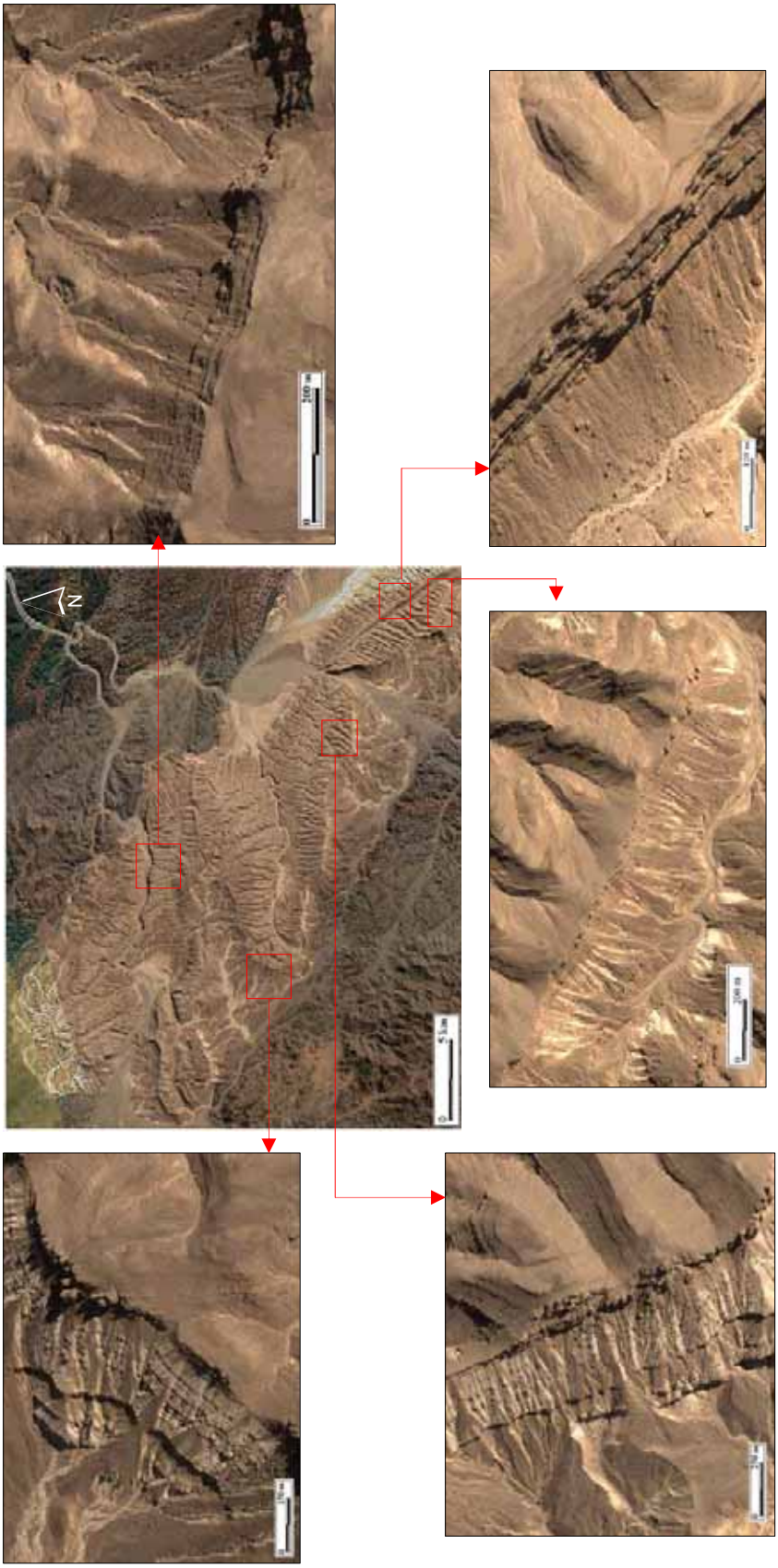

Fig. 3-20: *Outcrop identifications of Jabal Duwi. (Source: Google Earth Plus)*

Dip angle θ of the tilted topography (e.g. homoclinal ridges, cuesta, and hogback) is assumed to be equivalent to slope angle that is expressed as *[rise /run]* or *[vertical relief (h) /horizontal distance (d)]* as shown in figure (3-21) and; therefore, dip angle is equal to *[Inv. Tan (h/d)]*. Table 3-4 showing the estimated dip angles from the DEM (Fig. 3-21) in comparison with field measured dips.

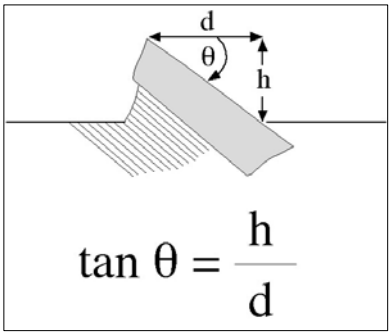

Fig. 3-21: *Dip angle estimation. (After Jensen, 2000)*

Table 3-4: *Comparison between estimated and field measured dip angles.*

Location	*h (m)*	*d (m)*	*tan θ*	*Estimated Mean Dip deg.*	*Field Measure-ments*			*Dip dir.*
Mohamed Rabah	335	780	0. 42	23	18	19	22	West
Hills of Wasif	455	1150	0.39	21.5	18	19	21	West & SW
Umm al-Hawaytat	330	820	0.40	22	14	15	20	West & SW
Northern J. Duwi	440	2072	0.21	12	11	14	15	West & SW
Mid. J. Duwi	410	1127	0.36	20	14	15	18	East
Southern J. Duwi	460	1214	0.38	21	18	19	23	East
Jabal Atshan	225	439	0.51	27	19	22	24	East

As can be deduced from table 3-4, the estimated dip angles vary greatly from 12º at the northern of Jabal Duwi to 27º at Jabal Atshan. At the same time, field measured angles vary from 11º at the northern of Jabal Duwi to 24º at Jabal Atshan. It could be concluded that there is a great similarity between the estimated dips and field measured dips. On the other hand, dip direction differs from place to place. For instance, Jabal Mohamed Rabah, hills of Wasif and hills of Umm al-Hawaytat incline westward opposite to the Red Sea (Fig. 3-22 a, b, c).

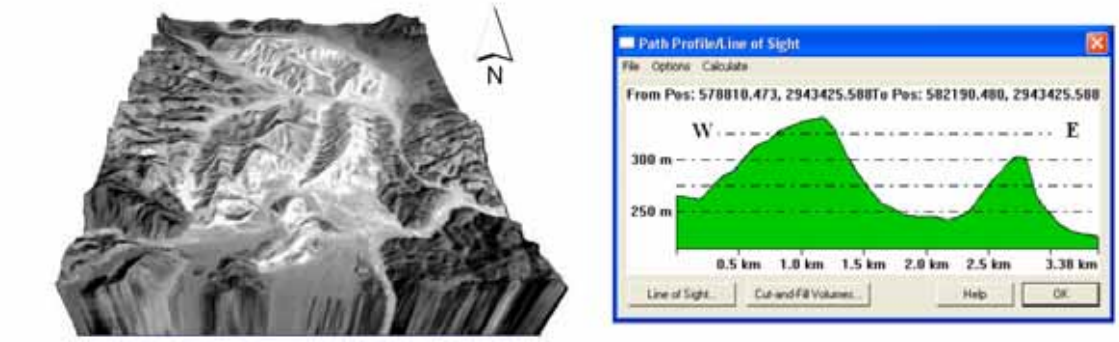

a) DEM and slope profile of Jabal Mohamed Rabah.

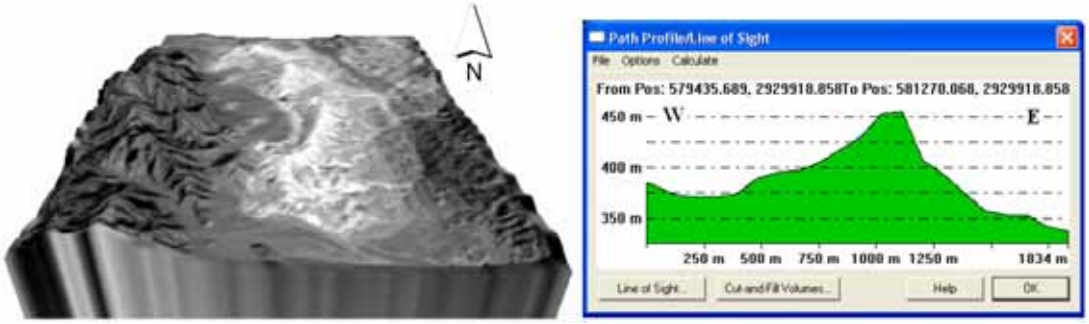

b) DEM and slope profile of Wasif hills.

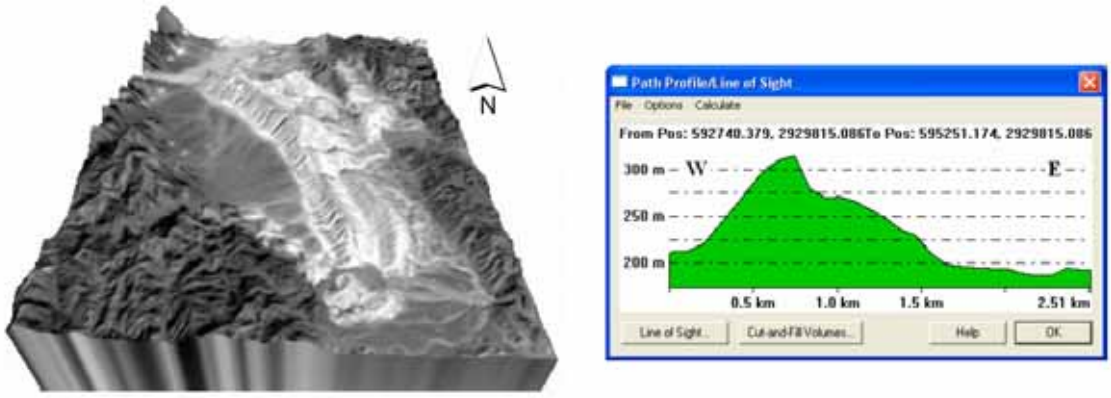

c) DEM and slope profile of Umm al-Hawaytat hills.

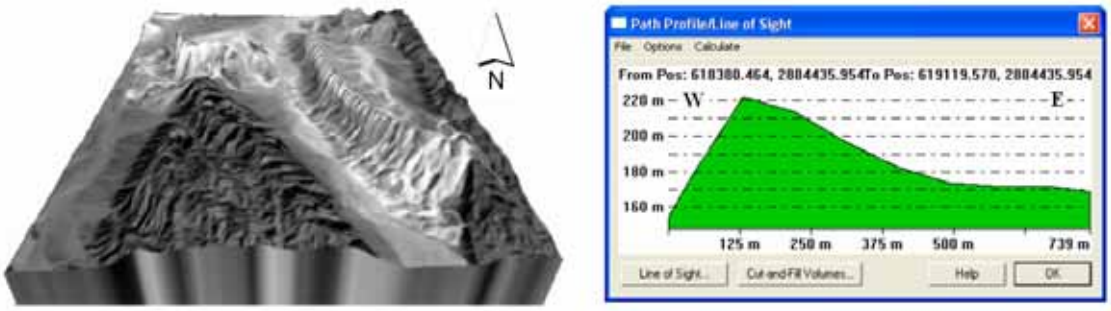

d) DEM and slope profile of Jabal Atshan.

Fig. 3-22: *DEM of the inland warped landforms.*

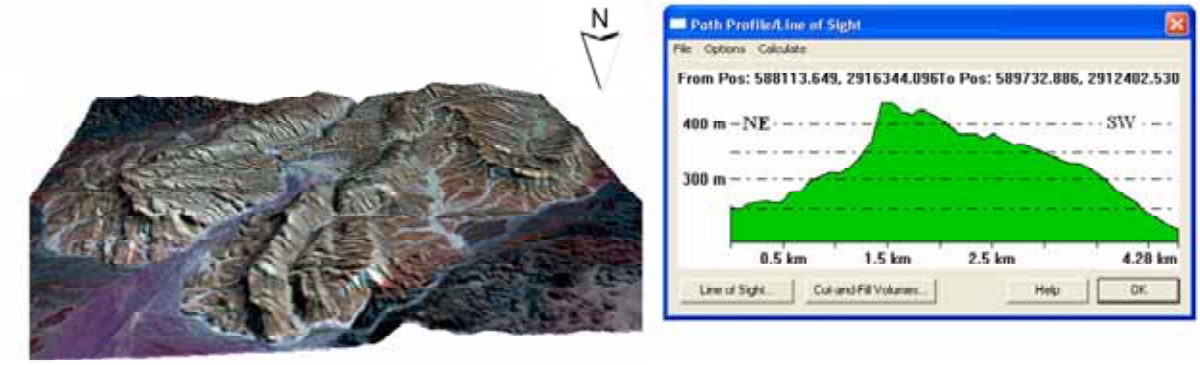

e) DEM and slope profile of northern Jabal Duwi.

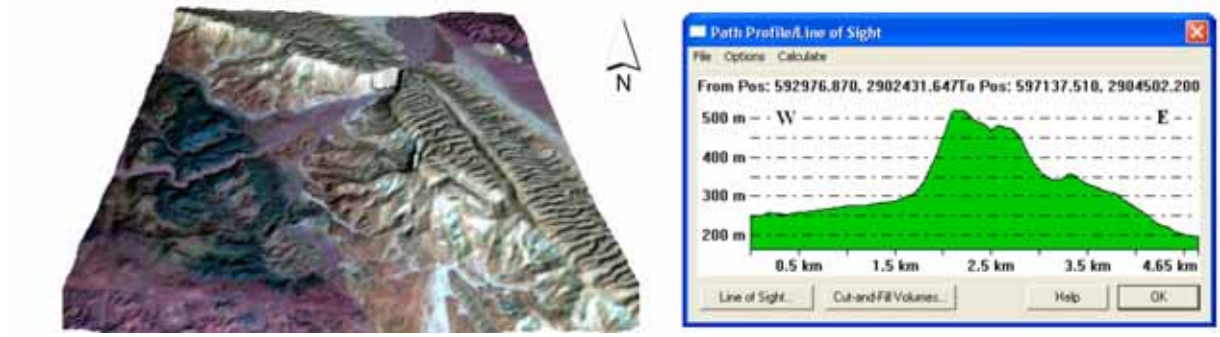

f) DEM and slope profile of central Jabal Duwi.

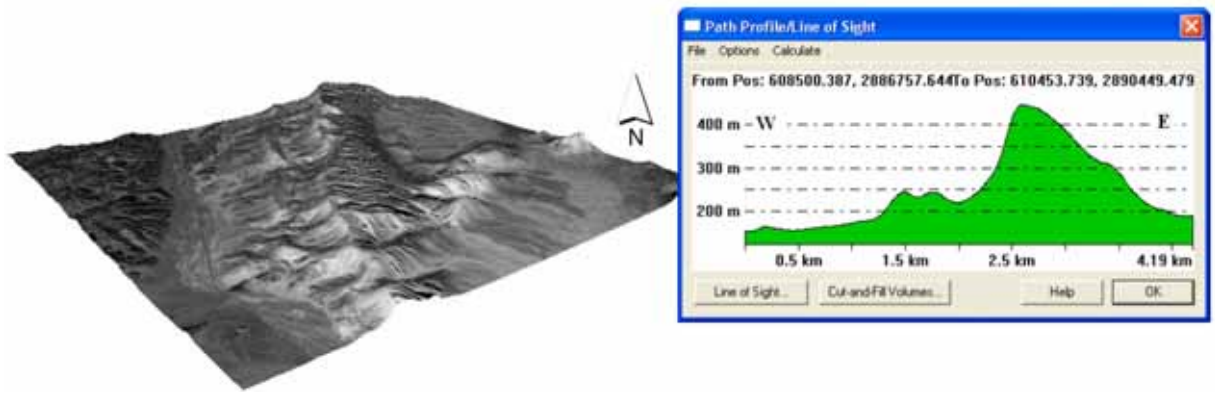

g) DEM and slope profile of southern Jabal Duwi.

Fig. 3-22: *Continue.*

The northern part of Jabal Duwi inclines towards the west and southwest directions in reverse to the main fold axe of Jabal Duwi, which trends NW-SE generally. Therefore, the northern part of Jabal Duwi manifests an overturned fold (Fig. 3-21 e). At the same time, the middle and southern parts of Jabal Duwi and Jabal Atshan incline eastwards or seawards (Fig. 3-22 d, f, g).

4.2.2. Terrain Analysis.

Quite satisfying regards to figure 3-22 reveal that the inland tilted landforms occupy the intermountain or morphotectonic depressions. The general terrain comprises half graben separating between two huge uplifted faulted mountain blocks (horsts). Interpretation of 11 ETM+ images covering the Eastern Desert of Egypt revealed two main distinctive depressions; they are: the coastal depression and the inland depression. The coastal depression is faulted downward against the basement rocks along its western border in accordance with major normal faults that trending NW-SE parallel to the Red Sea trench. It is believed that its eastern margins comprise an upward fault against the Red Sea trench as well. The depression attains its maximum wideness north of Halaib near the Egyptian-Sudanese border and extends northward to the south of Zafrana at the Gulf of Suez.

On the other hand, the inland depression comprises elongated depression trends NW-SE generally. It is restricted by Mohamed Rabah basin in the north (Lat. 26 º 35̀ N - Long. 33 º 48̀ E) and extending about 115 km southward to Lat. 25º 41̀ N- Long. 33 º 48̀ E. The depression neither extends north nor south of these limits. It could be concluded that it is a distinctive figure characterizes the Central Eastern Desert of Egypt for preserving the Cretaceous-Tertiary rocks.

The inland depression does not perform a continuous depression; instead it is divided into five semi-closed depressions. These depressions are more or less connected to each other and extending outside of the study area. They could be nominated from north to south as follows (Fig. 3-23):

- *Mohamed Rabah Basin.*
- *Wasif Basin.*
- *Umm al-Hawaytat.*
- *an-Nakheil Basin.*

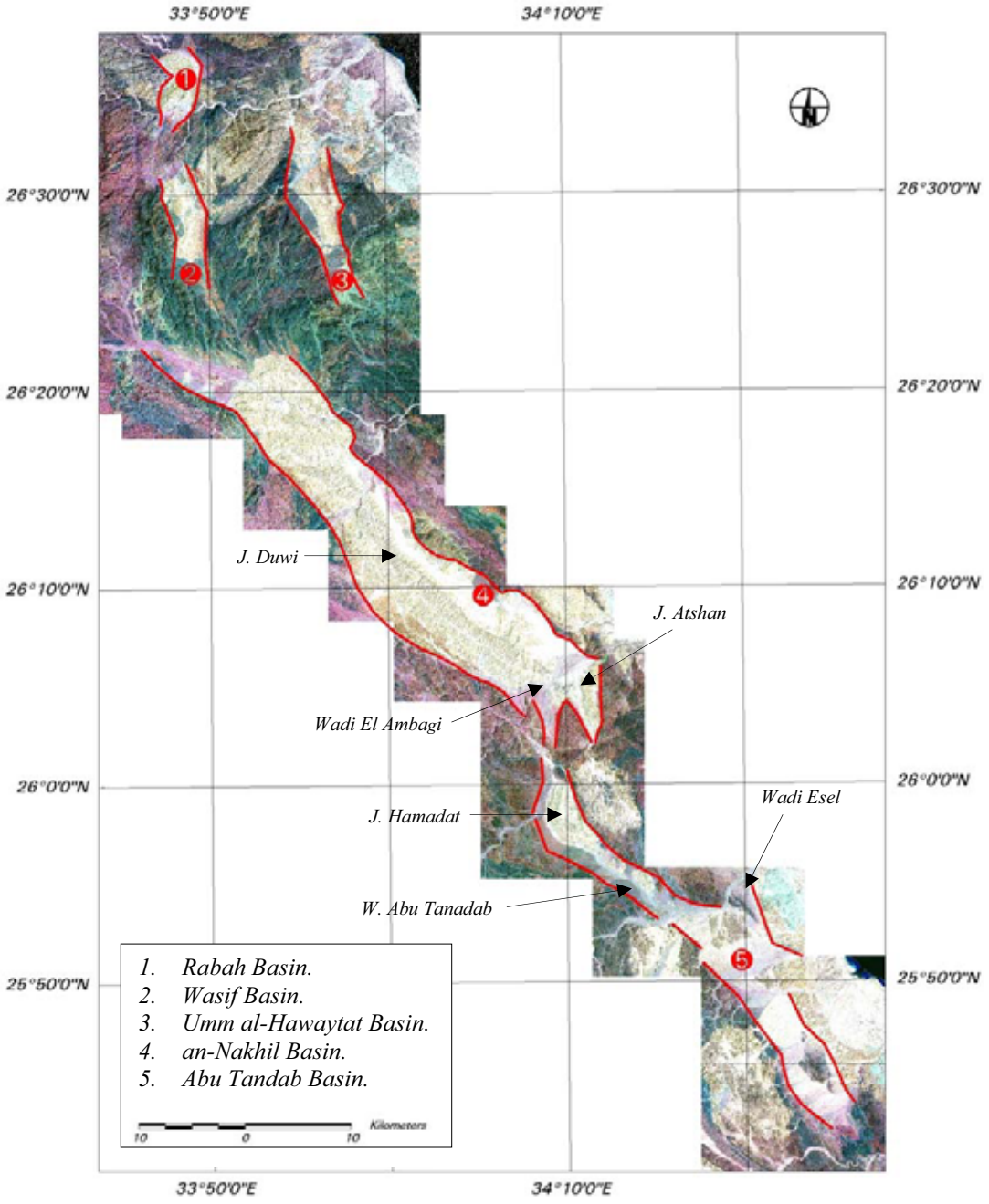

Fig. 3-23: *Subset of ETM+ mosaic images showing the inland depressions.*

▪ *Abu Tandab Basin:* the name is imputed to wadi Abu Tandab that is a major tributary of wadi Esel that stands outside of the study area. The depression begins from the junction between wadi Karim and wadi Ambagi. It adheres to N-S major faults and turning NW-SE along the main direction of wadi Abu Tandeb. This depression is distinctive because the preservation of Jabal Hamadat that is the most southern limit of the inland preserved Cretaceous-Tertiary rocks in the Central Eastern Desert.

Table 3-5 showing some morphological parameters of the inland depressions extracted from the ETM+ images.

Table 3-5: *Some morphological parameters of the inland depressions.*

Depression	*Mean Length km*	*Mean width km*	*Area km2*	*Orientation*
Mohamad Rabah	11.2	3.7	27.4	NNE-SSW
Wasif Basin	15.4	3.0	43.6	NNW-SSE
Umm al-Hawaytat	17.8	3.5	41.4	NNW-SSE
an-Nakheil Basin	54.7	10	348.8	NW-SE
Abu Tandab Basin	47.3	4	161.8	NW-SE

Although the forces that induced these depressions are still ambiguous, there is unanimously that they might have been resulted because of lateral compression since the depressions and the preserved tilted massif rocks as well are displaced laterally by strike-slip faults (Zaky, 1999).

4.2.3. Structure of the Coastal Warped Forms.

The general structure of the upward rocks (Miocene-Pliocene rocks) along the coastal plain reveals a simple monocline or flexure dipping uniformly eastwards with dip angles varying from 5˚ to 20˚ and ranging in elevation between 100 - 400 m asl (Fig. 3-24). They constitute a series of cuestas, tabular mesas, and outliers (Fig. 3-25), which are probably remnants of a larger plateau that has been subjected to severe erosion.

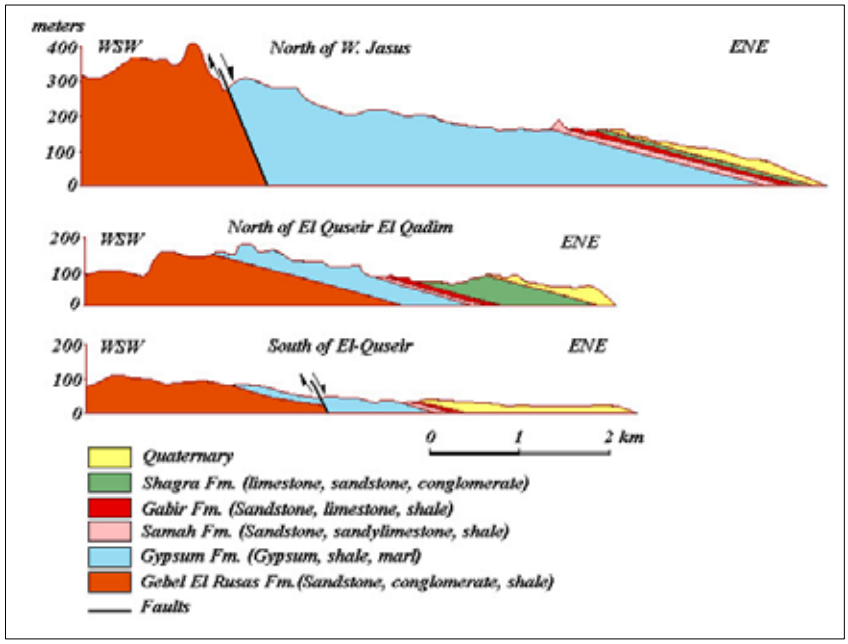

Fig. 3-24: *Geological cross sections along the coastal plain.* *(After: Issawi et al. 1971)*

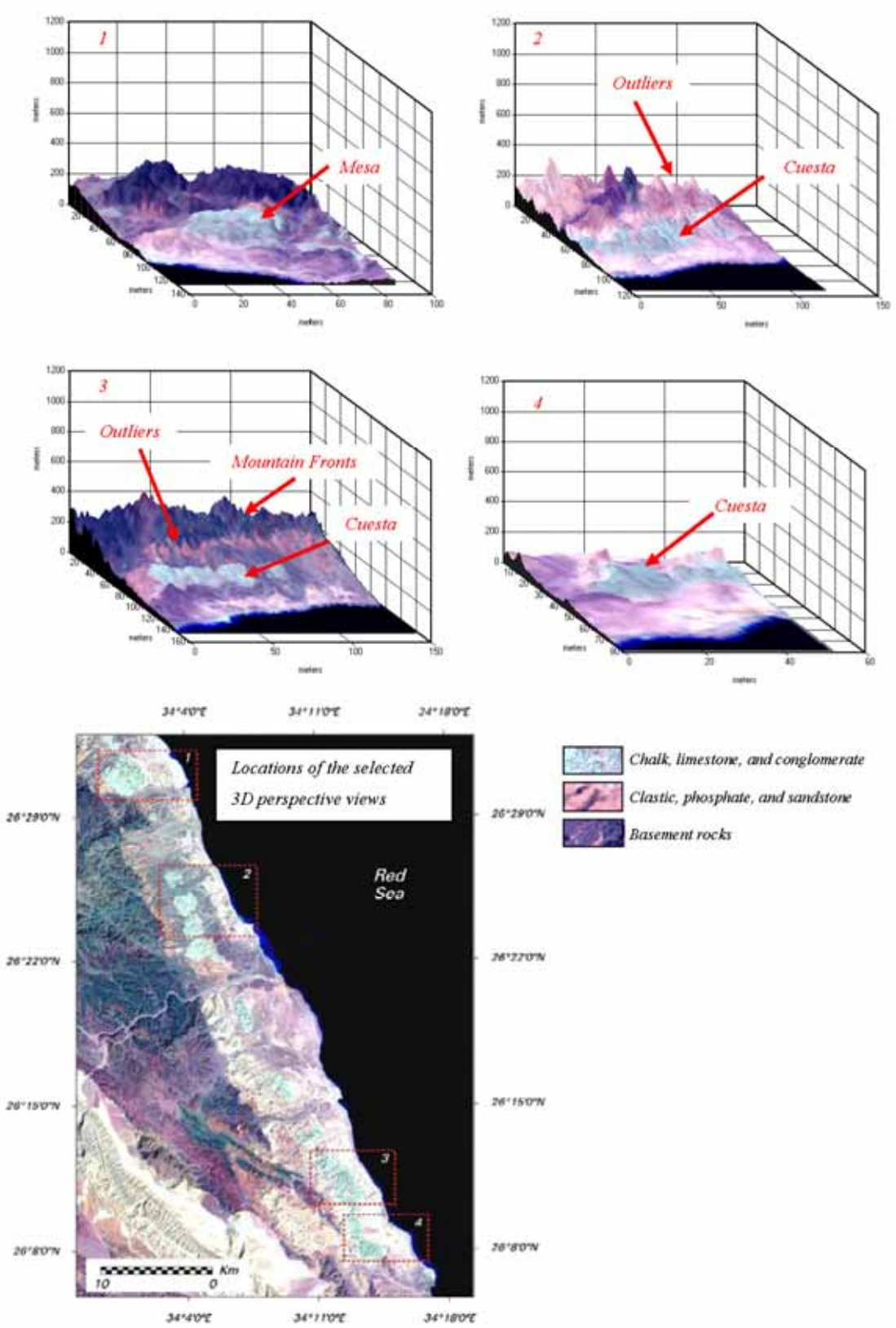

Fig. 3-25: *3D perspective views of some tilted forms along the coastal plain.*

The coastal strip is subjected to northwest-southeast step faults intersected by E-W fault system and varying in length from few meters at the minor faults up to 100 meters at the major faults. Fault planes are steep varying from 60˚ to 80˚ (Issawi et al. 1971). Due to the intersection of these two fault systems, the Miocene-Pliocene rocks along the coastal plain are widely dissected and flat topped and/or slightly tilted isolated outliers are formed on the foot slopes of the Red Sea Mountains.

Furthermore, El-Akkad & Dardir (1966 b) denoted doming effect due to gypsum flows that are well manifested in the area and resulting in tilting beds up to 15˚. Issawi et al. (1971) assumed that the doming is due to a recent movement that might have taken place during Quaternary because some Quaternary benches are tilted with angles up to 10˚ and are away from the affects of the gypsum flow such as in wadi Ambagi. However, gypsum sediments ranging between 100-300 m asl along the coastal plain and exhibiting pinkish-red colours. Gypsum masses are impressed by countless short gullies, which incised into the bedrock and showing the massif block as badlands (Fig. 3-26).

Fig. 3-26: *Incised gullies detaching a gypsum massif plateau north of wadi Hamraween.* *(Looking to westward)*

4.2.4. Structure of the Inland Depressions.

4.2.4.1. Mohamed Rabah Basin.

Mohamed Rabah basin is an oval shaped hollow occupied by relatively low hills, which comprise Jabal Mohamed Rabah. The basin is semi-closed since it is connected with the other basins through incised narrow wadis. The area is highly rugged and attains about 375 m height asl. The main stratigraphic successions of Jabal Mohamad Rabah range from Upper Cretaceous to Oligocene. They are from top to bottom as follows (Issawi et al. 1971):

- *Nakheil formation: sandstone, limestone, marl, shale and conglomerates comprise the top of Jabal Mohamed Rabah.*
- *Thebes formation: limestone with flint, forming a steep scarp.*
- *Esna shale.*
- *Tarawan formation: marl, marly limestone beds (chalk).*
- *Dakhla formation: marl, marly limestone, shale.*
- *Duwi formation: phosphate, shale, marl and chert intercalation.*
- *Quseir variegated shale: shale beds with sandstone intercalation.*
- *Nubian sandstone.*

The general structure demonstrates markedly normal faults of different trends (i.e. NW-SE, NE-SW, and E-W). Some of them adhere to strikes, whereas others possess oblique trends. These faults vary greatly in length from few hundreds of meters to 2.5 km with downthrows of 10 m in average. The most important structural feature is the occurrence of two thrust faults at the eastern part of the central block. These faults run in an approximately N-S direction (Isawi et al. 1971).

As a whole, the area establishes faulted basin (graben) flanked by the basement rocks. Jabal Mohamed Rabah is preserved in the basin constituting subdued and dissected cuestas, which vary in dips from 18˚ to 22˚ westwards. The cuestas are detached by major west-east wadi persists in strike-slip fault. Three massif blocks could be distinguished from north to south as the following (Fig. 3-27):

- The northern block is generally oval shaped covers an area about 4.8 km^2. It extends along northwest direction about 29 km and attains about 2 km width. This block is bounded completely by wadi Mohamed Rabah that drains Jabal Abu Furad (1032 m asl) (Lat. 26 º 40̀ N - Long. 33 º 39̀ E) about 10 km northwest of Mohamed Rabah basin and pierces the basin from its northwestern margins. The wadi is branched into two effluents bounding the northern block. The northern branch pursues the rock contacts, whereas the southern branch follows the NW-SE normal fault and W-E strike-slip faults (Zaky, 1999). The later fault trend separates the northern block of Jabal Mohamed Rabah from the central block.

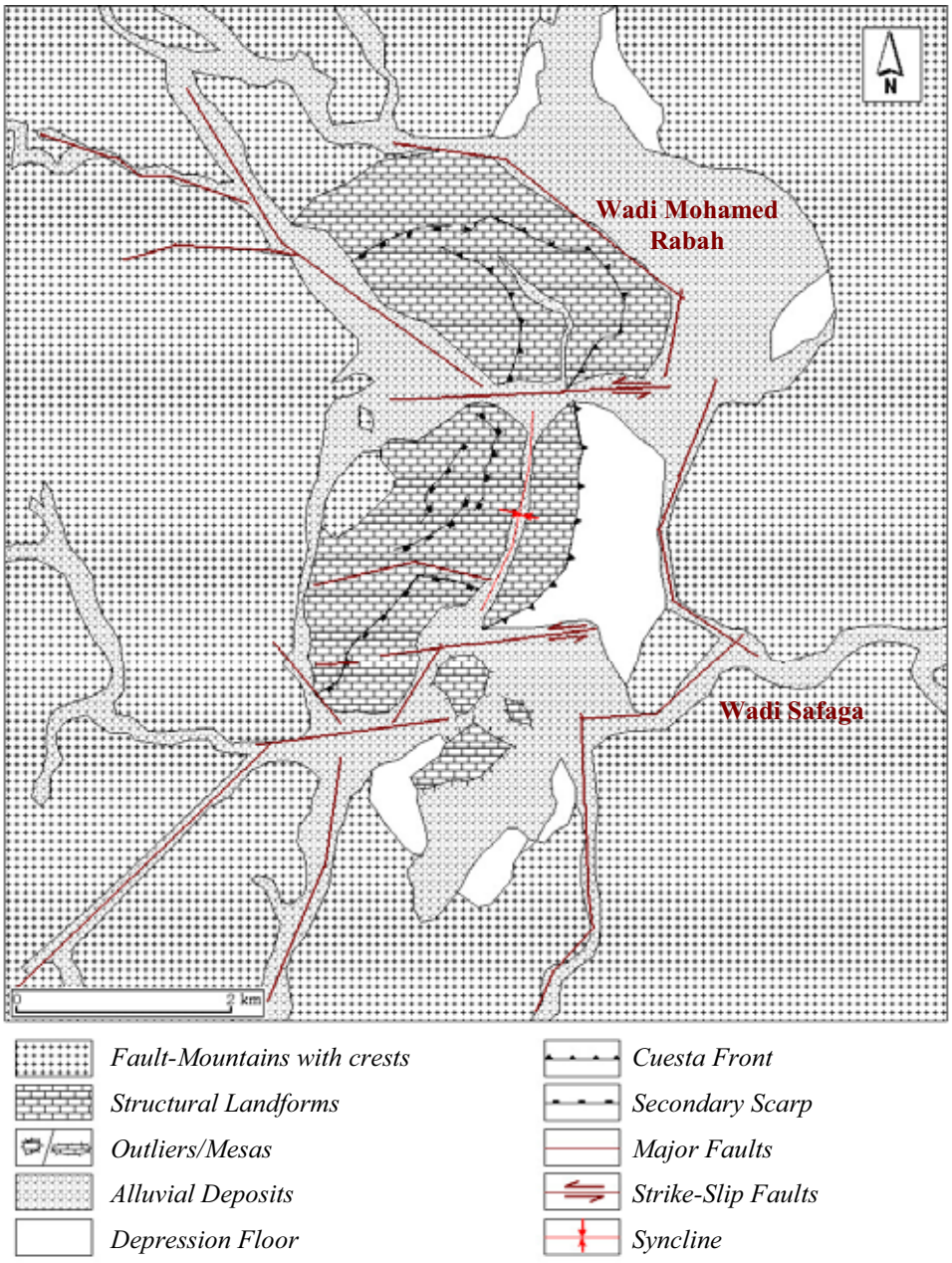

Fig. 3-27: *Geomorphological map of Mohamed Rabah Basin.*

(Sources: ETM+ Image, topographic maps 1:100.000, field work, Issawi et al. 1971 and Zaky, 1999).

The outer slopes of this block are demarcated by relatively short wadis, which debouching into wadi Mohamed Rabah where the main direction of the basin is being N-S generally before wadi Mohamed Rabah debouching into wadi Safaga.

On the other hand, the center of the block is detached by a subsequent annular dendritic wadi adhering to a fault-drag syncline. Therefore, the block is divided into two subdued overlapping cuestas. The eastern cuesta is relatively lower varies in elevation from 318 to 332 m asl and the western cuesta attains 435 m height asl.

▪ The central block extends generally NNE-SSW for about 3.2 km and covers an area of 6.7 km^2. It is bounded from the east by wadi Mohamed Rabah and from the west by a tributary pursues the contact line between the basement and the sedimentary rocks and proceeds after arcuate fault line. From the south, the block is experienced intensive erosion due to debouching of wadi Mohamed Rabah into wadi Safaga.

Likewise the northern block, the center of the block is impressed by subsequent annular wadi pursues a fault-drag syncline that is dividing the block into two cuestas. The eastern cuesta is much symmetrical one attains about 362 m height asl, while on the contrary, the western cuesta is asymmetrical because of intensive erosion and varies in elevation from 366 to 392 m asl (Fig. 3-28).

Fig. 3-28: *Panoramic view of the central cuestas of Jabal Mohamed Rabah. (Looking northward)*

▪ The southern blocks constitute semi-tabular remnants covering about 0.98 km^2. They are mostly separated from the central block because of the E-W Strike-slip faults, which are followed by wadi Safaga.

As can be deduced from the geomorphological map, wadi Mohamed Rabah incises down in the neighbouring basement mountains before debouching into the basin. It could be then inferred as an antecedent wadi that maintained its watercourse across the uplifted hills of Mohamed Rabah. The wadi might have been prior to the orogenic processes of the hills and the rate of erosion should have been equivalent to the uplift rate.

4.2.4.2. Wasif Basin.

Wasif basin comprises an elongated semi-closed depression occupied by relatively low sedimentary hills and filled with alluvial deposits. The basin is surrounded by basement mountains that are much higher on the west (Jabal Wasif 868 m asl) than those on the east (499 m asl). The basin reveals graben-like since it is restricted by two major normal faults trending NNW-SSE generally from the east and west.

The eastern fault of the graben spreads about 15 km and caused the Nubian sandstone to be faulted against the recent successions in the northern part of the basin. The western fault is more irregular in shape adhering to the fault scarp of Jabal Wasif on the west and exposing zigzag outline.

The exposure rocks in the basin were classified by El-Akkad & Dardir (1966 b) under the following successions from top to bottom:

- *Wadi alluvium.*
- *Nakheil formation: sandstone, limestone, marl, shale and conglomerates.*
- *Thebes formation: limestone with flint*
- *Esna shale.*
- *Dakhla formation: marl, marly limestone, shale.*
- *Duwi formation: phosphate, shale, marl and chert intercalation.*
- *Quseir variegated shale: shale beds with sandstone intercalation.*
- *Nubian sandstone.*

Commonly, the hills are dissected by effluents of wadis Gasus and Wasif causing separation of the area into three units, which are dislocated in relation to each other (Akkad & Dardir, 1966 b). They comprise dissected cuestas, which are tilted towards the west and southwest directions with angles varying from 14º to 21º. They increase in area and altitude progressively from north to south up to 440 m and 520 m asl successively. These units are distinguished as follows (Fig.3-29):

- The northern hill is elliptical in shape, covering an area about 1.9 km^2 and extending NE-SW about 2.3 km. It varies in elevation from 432 to 441 m asl and bounded by alluvial deposits and the basement rocks from its northern and western sides that are the steeper sides of the hill.

▪ The central hill is in form of a long sharp ridge extends about 3.6 km and gently sloping to the west. It covers about 3.4 km^2 and attains an elevation varies from 400-500 m asl. The structure of this hill is much simple than the other two hills (Akkad & Dardir, 1966 b). The sedimentary beds forming this hill strike north-south and the dip increases dip-ward to attain 25º. Landslips are common in the eastern side of this area, bringing down at the foot slopes of the hill blocks of Duwi phosphate with over-laying beds (Akkad & Dardir, 1966 b).

▪ The southern hill is relatively small covers about 2.5 km^2 and extending NNE-SSW for 4.2 km. Its western scarp constitutes an arcuate low ridge inclines from 10º -20º westward. Dip of the rocks generally increases southwards up to 30º (Akkad & Dardir, 1966b). The eastern ridge is the primary one revealing cuesta front and its foot slopes exposing undulated low rock bench covered with glacis (Fig. 3-30). This hill is impressed by parallel and/or sub-parallel anti-dip or obsequent streams on its eastern flank. The streams are of a dendritic pattern due to the homogeneity of the Nubian sandstone, which forms the depression floor. Most of the streams assembled together to form the primary feeders of wadi Abu Gawa that is a main tributary of wadi Gasus. On the other hand, the hill is significantly eroded from south and the basin becomes wider because of widening of wadi Abu Aqarib that drains Jabal Wasif and flows into southwest direction.

▪ Furthermore, there are two outliers or inselbergs attending on the western side of the depression that are separated from the main hills. As well, the sandstone outcrops in the southern part of the depression comprising low tabular remnants, which are faulted along NNW-SSE and NW-SE axes.

Hills of Wasif basin are described by Akkad & Dardir (1966b) and Zaky (1999) as tilted fault blocks whose steep slope forms the fronts of the blocks, while the gentle side is the back slope. In that manner, the hills could be topographically expressed according to the dip that does not exceed 30º and in regarding to their erosional states as subdued cuestas. Their fronts are retreated westwards from the original fault plane owing to erosion forces.

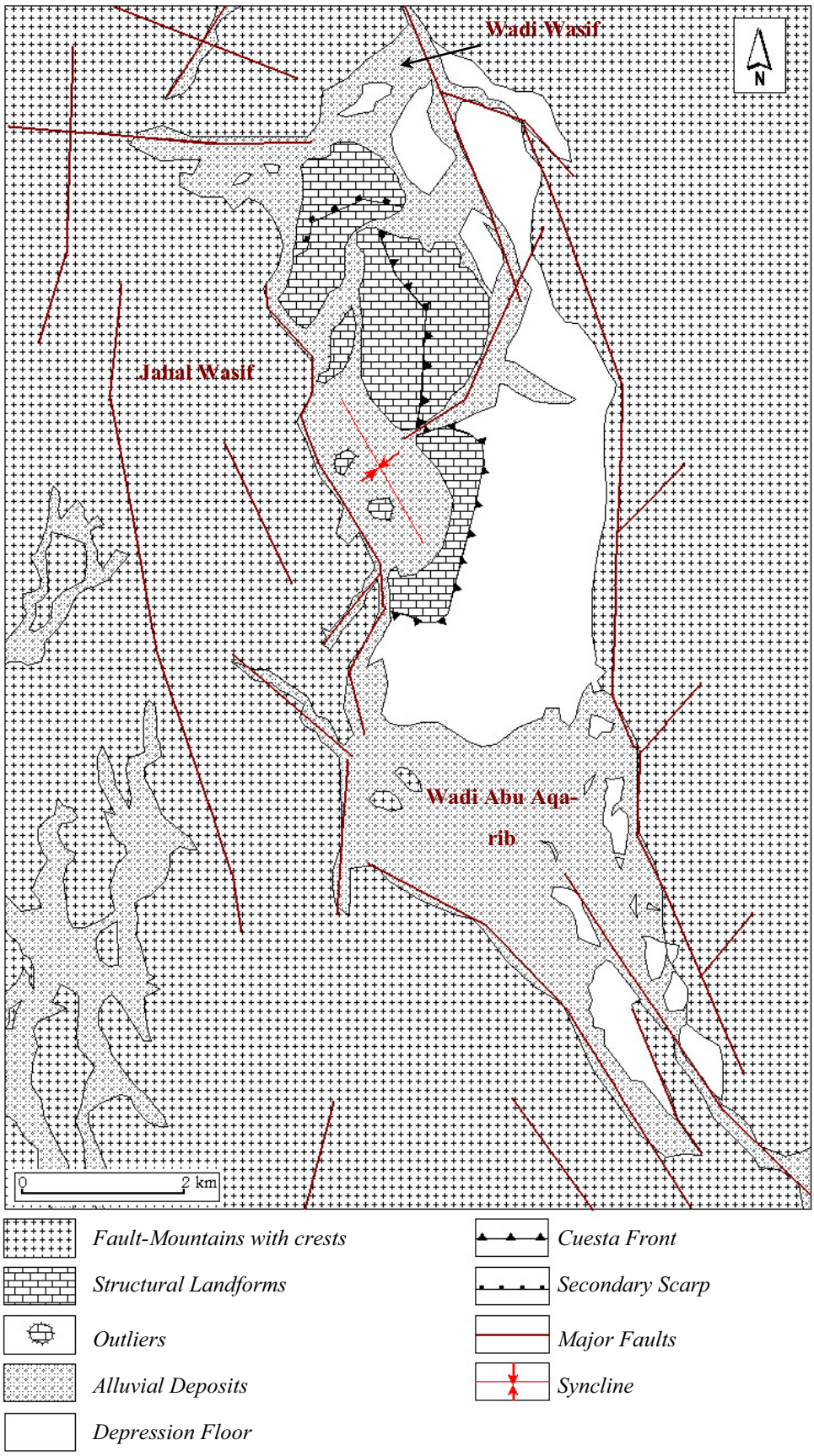

Fig. 3-29: *Geomorphological map of Wasif Basin. (Source: ETM+ Image, field work, topographic maps 1:100.000, Akkad & Dardir, 1966b and Zaky, 1999)*

Fig. 3-30: *Front of the southern cuesta of Wasif.* *(Looking westward)*

The apparent synclinal structure is owing to minor faults, which dissecting the northern and southern margins of the area into displaced blocks. These faults drag the western parts of the depression due to the upthrow of the basement rocks of Jabal Wasif on the west (Zaky, 1999).

Finally, cuestas of Wasif basin (i.e. northern, central and southern cuestas) are separated from each other along NE-SW direction by wadis Wasif and Gasus, which are probably following the weakness lines. Akkad & Dardir (1966 b) demonstrated both of them as antecedent wadis, which maintaining their watercourses across the uplifted front of the tilted block. By contrast, wadi Wasif does not incise in the basement mountain of Jabal Wasif. This might be an indication that the wadi is relatively recent and it was not synchronous with the orogenic process of the sedimentary hills. Accordingly, separation between the northern and central cuestas is probably occurred by two opposite streams, they are: *consequent* or dip stream ran towards the west and *obsequent* or anti-dip stream ran towards the east. Both of them might have been established on the eastern and western sides of the hills and pursued a major NE-SW fault line. The obsequent 'anti-dip' stream had become relative longer owing to headward erosion performing the retraction of the watershed line westward and lowering the surface. Increasing of the headward erosion resulted in connecting both streams through a gorge.

4.2.4.3. Umm al-Hawaytat Basin.

Umm al-Hawaytat basin exposes longitudinal graben spreads about 18 km from north to south. It is bounded from the west by Jabal Gasus (466 m asl) and Jabal Abu Gawa (620 m asl) and from the south by the continuations of Jabal Abu Zarabit (712 m asl). The graben is mostly enclosed since it is connected with Wasif basin through a very

narrow reach of wadi Gasus and joined the coastal depression through the lower main channel of wadi Gasus.

Geological formations and structure of Umm al-Hawaytat have been described by Ball (1913), Said (1962) and Zaky (1999), which could be summarized from top to bottom as follows:

- *Alluvium deposits.*
- *Younger limestone, clays, sandstone and conglomerates.*
- *Eocene limestone.*
- *Shales, marls and gypseous clays.*
- *Upper Cretaceous limestone and marls.*
- *The Phosphate series, grey laminated clays with phosphate and chert.*
- *Nubian Sandstone.*
- *Crystalline rocks (granites, greenstones and igneous conglomerates).*

As can be shown in figure 3-31, the basin is faulted down against the basement rocks by a series of normal faults. The western side is subjected to severe compressing executed fault drag syncline (Akkad & Dardir, 1966b; Zaky, 1999). On the other hand, the eastern side attains an elevation about 305 m asl and constituting a horst-like that separates Umm al-Hawaytat basin from the coastal depression.

The basin is occupied by low sedimentary hills that can be called hills of Umm al-Hawaytat and filled by alluvial sediments, which are deposited by wadis Abu Gawa and Gasus in the north and wadi Abu Shiqayli in the south. Wadi Gasus is seemingly antecedent or struggler one.

Umm al-Hawaytat hills are experienced severe tectonic events resulting in dissecting the hills into three blocks along normal and strike-slip faults. They are:

- The northern block is irregular in shape and extending about 2.7 km along NE-SW trend generally. It covers an area about 4.9 km^2 and varies in elevation from 129-300 m asl. It is the most important hill for mining phosphate. This block is faulted against the basement rocks on the western side along NW-SE direction, while its eastern side reveals low retreating fault scarp underwent severe erosion. Normally, the rocks dipping into the west and southwest directions with angles varying from 14º to 20º.

▪ The central block covers a small area about 1 km^2 and extends from east to west about 1.4 km. It comprises a sub-horizontal mesa, which has been separated from the northern block along E-W fault line that is occupied by an affluent of wadi Gasus. Intensive tectonic and erosion processes led to separate the western margin of this block into a number of outliers or inselbergs along a NNE-SSW fault-drag syncline on the foot slope of Jabal Gasus.

▪ The southern block is the largest one covers an area about 20.6 km^2. It extends about 7.5 km from NW to SE and varies in elevation from 221-325 m asl. The block is separated from the central block along a concealed NE-SW strike-slip fault that is followed by wadi Gasus. Normally, the rocks dipping into the west and southwest directions with angles varying from 14º-20º and manifesting symmetrical cuesta (Fig. 3-32). Center of the cuesta suffered double offsets along NE-SW and NW-SE trends resulting in vertical and strike-slip displacements. The eastern side of the cuesta depicts a denuded and retreated anti-dip scarp that is impressed by incised streams, which down-cut along the weakness lines. The streams linked together with right angles as a result of tectonic forces and run along a rock boundary separating the Nubian sandstone from the basement rocks before the streams debouching into wadi Gasus. On the south-eastern side, an obsequent or strike stream interrupts the main cuesta to comprise overlapping cuestas.

On the other hand, the western flank of the cuesta is impressed by incised short gullies, which caused a low ridge. The block is detached from the basement rocks by a NW-SE fault-drag syncline. Subsequently, five outliers are separated on the foot slopes of Jabal Abu Gawa. At the same time, the outliers are dissected from each other by NE-SW minor faults and dipping eastward between 23 º -25 º.

Finally, it could be concluded that the depression might have been subjected to lateral compression from its both eastern and western sides. This compression was in corresponding to upthrow of the basement rocks in the central part of the Eastern Desert specifically along the latitude of Wasif and Umm al-Hawaytat (Fig. 3-33).

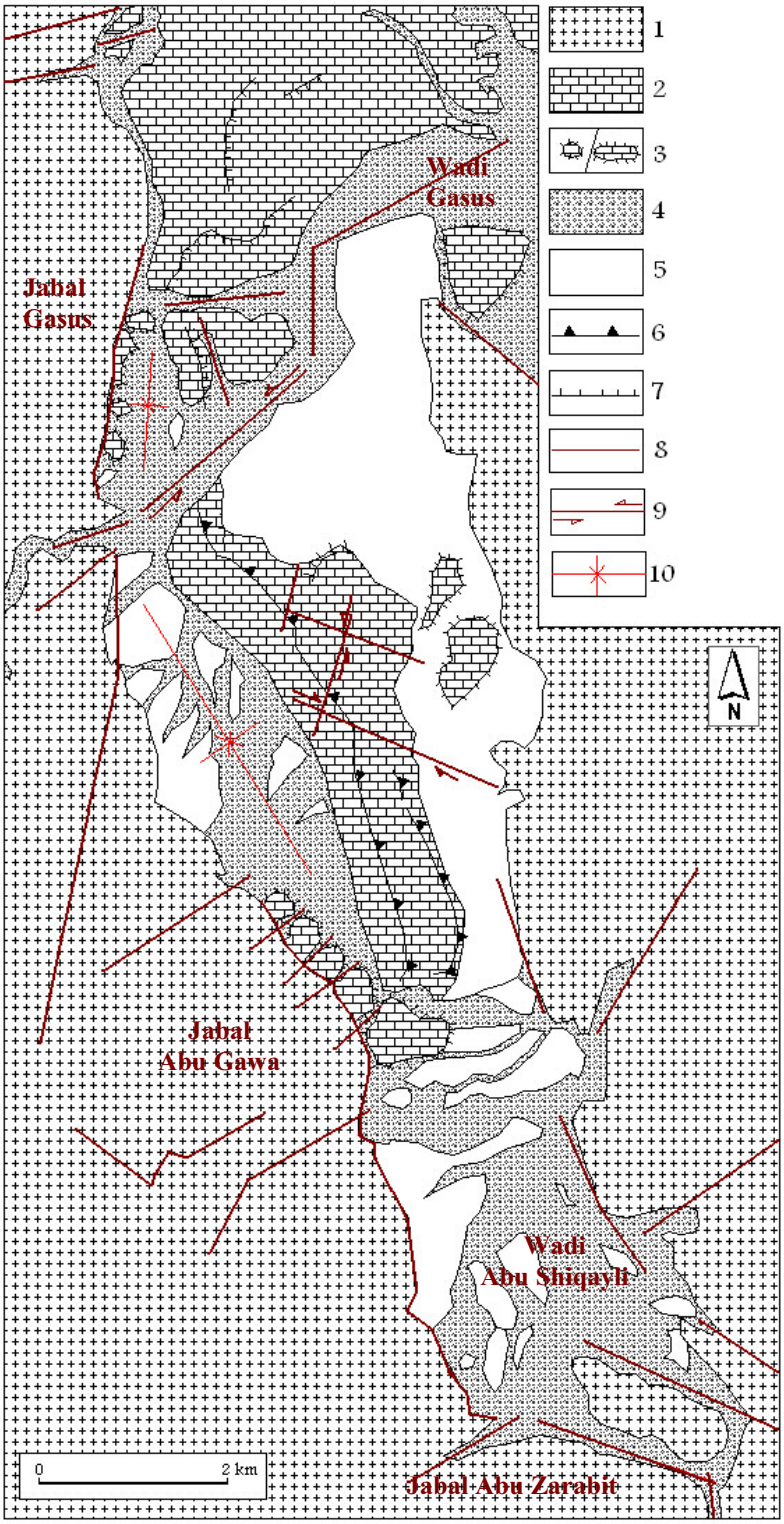

1. Fault-Mountains with crests
2. Structural Landforms
3. Outliers/Mesas
4. Alluvial Deposits
5. Depression Floor
6. Cuesta Front
7. Secondary Scarp
8. Major Faults
9. Strike-Slip Faults
10. Syncline

Fig. 3-31: *Geomorphological map of Umm al-Hawaytat Basin. (Source: ETM+ Image, lineament map, field work, topographic maps 1:100.000, and Zaky, 1999)*

Fig. 3-32: *Cuesta of Umm al-Hawaytat.* *(Looking southward)*

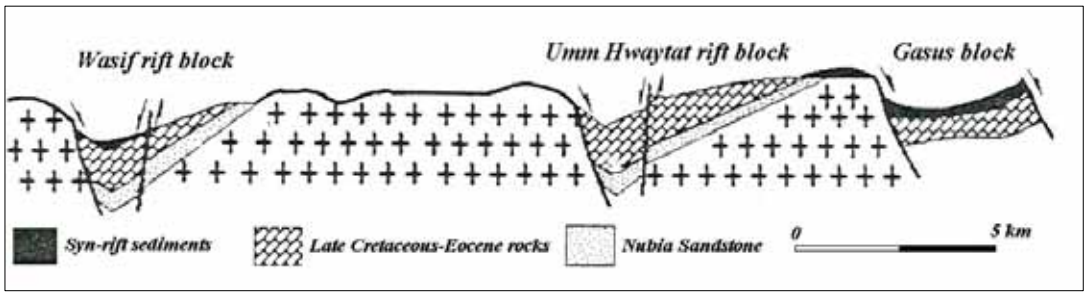

Fig. 3-33: *Simplified cross section showing the major structure along Wasif and Umm al-Hawaytat latitude.* *(After: Zaky, 1999)*

4.2.4.4. an-Nakheil Basin.

An-Nakheil basin is the largest and most conspicuous inland syncline in the central Eastern Desert of Egypt that extends WNW and NW generally about 54 km. It varies in width from 7 to 13 km and covers a total area of 348.8 km^2 approximately. The basin is bounded completely by the basement rocks and its eastern side is down-thrown along NW-SE fault trend against the basement rocks that form Jabal Umm Kajura (507 m asl) and Jabal al-Hamraween (678 m asl). As well as the western border proceeds after NW-SE normal fault trend. The dominating faults typically display a zigzag geometric pattern in general.

The basin is occupied by Jabal Duwi and its continuations in Jabal Atshan and Jabal an-Nakheil. It is filled by alluvial deposits, which unconformably overlay the Nubian sandstone. Formations of Jabal Duwi are well described by Said (1962, 1990), Abdel-Gawad (1969) and Khalil & McClay (2002). The columnar section attains an eleva-

tion about 500 m asl and composed of the following rock units from top to bottom (Fig. 3-34):

- *Thebes formation (limestone with flint and chert, chalky limestone).*
- *Esna shale.*
- *Tarawan formation (marl and marly limestone).*
- *Dakhla formation (shale, marl).*
- *Duwi formation (phosphate).*
- *Nubian Sandstone.*

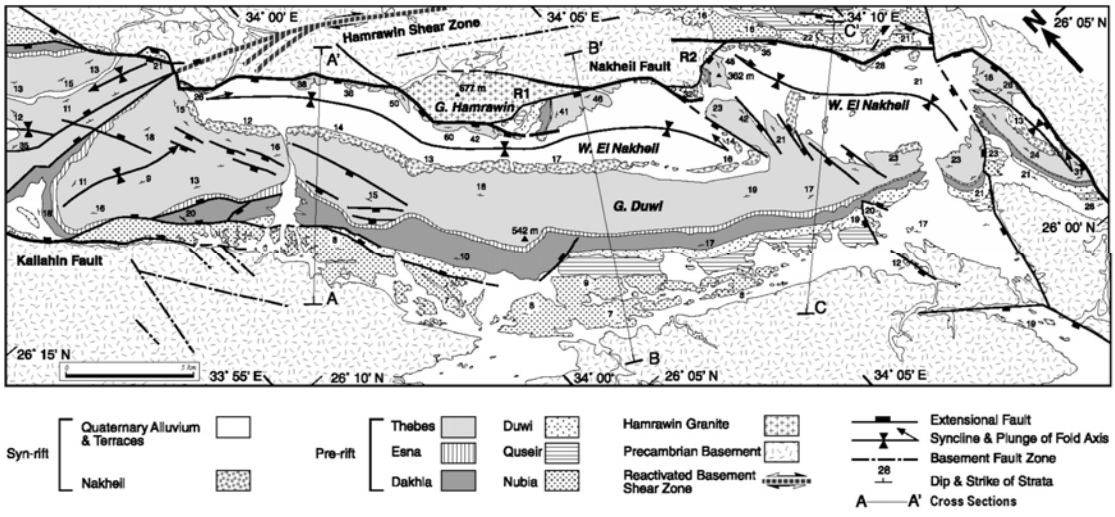

Fig. 3-34: *Geological map of Jabal Duwi. (Source: Khalil & McClay, 2002)*

Structure of Jabal Duwi is in reality a result of complicated folding and strike-faulting and the plateau reappears in many outliers as a result of complex strike faulting (Barron & Hume, 1901). In that manner, Said (1962) demonstrated that structure of Jabal Duwi is characterized by strike faults where the ancient crystalline rocks with their overlaying mantle of Cretaceous and Eocene rocks underwent intense deformation. This deformation produced a series of markedly tilted fault blocks with NNW or NW trends. Schürmann (1966) pretended that structure of Jabal Duwi might have been arisen due to rejuvenation of the Precambrian faults because of its abnormal trend that is not parallel to the present day Red Sea coast. On the other hand, Abdel-Gawad (1969) assumed that the Duwi structures constitute a distinctive shear zone that intersects the Red Sea south of EL Quseir about 30˚ and it is interrupted by NE-SW faults. He pretended that it is similar to Abu Masarib shear zone in Saudia Arabia that is now displaced approximately 150 km along the Red Sea rift. Consequently, the area has

been displaced along north-south lateral faults related to the Gulf of Aqaba-Dead Sea movement after the end of the Oligocene and continued until the Pleistocene.

Jabal Duwi is detached by wadi Sodmein into two main blocks, which would be described geomorphologically as follows (Fig. 3-35):

▪ The northern block extends about 16.4 km along NW-SE trend generally, covers an area about 94.8 km^2 and attains about 514 m height asl. It is bounded from the north by wadi el-Saqia and its tributaries and by the basement rocks from the east and the west. This block is mostly ensued as a result of intensive tectonic forces, which constrained the rock strata to incline into different directions (i.e. W, SW, S). Therefore, the block is seemingly an overturned fault block because it is reversed to the main axe of Jabal Duwi (review Fig. 3-22 E). Dip of the rocks varies generally from 11˚ to 15˚.

The block is detached from the north by wadi el-Saqia that flows NW-SE, wadi el-Kalaheen from the west and by wadi Sodmein from the south. Wadi Sodmein incises deeply through Jabal Duwi showing a 200 m deep gorge and separating the northern block from the southern one.

On the other hand, wadi el- Saqia incised the northern block along NW, NE, NW inferred faults and constituting right angle junctions (Fig. 3-36). It separates the northeastern margins of the northern block into two sub-blocks between which wadi el-Saqia comprises a sub-basin that exposes wadi el-Saqia as struggler or antecedent wadi.

On the western side of the block, wadi el-Kalaheen represents a dendritic stream pattern. It cuts down reaching the Nubian sandstone and flows westward before debouching into another NW-SE tributary of wadi el-Saqia. The later tributary pursues the contact line between the neighbouring basement mountains and the sedimentary rocks and it bounds eventually Jabal Duwi from the west before debouching into wadi el-Saqia in the north.

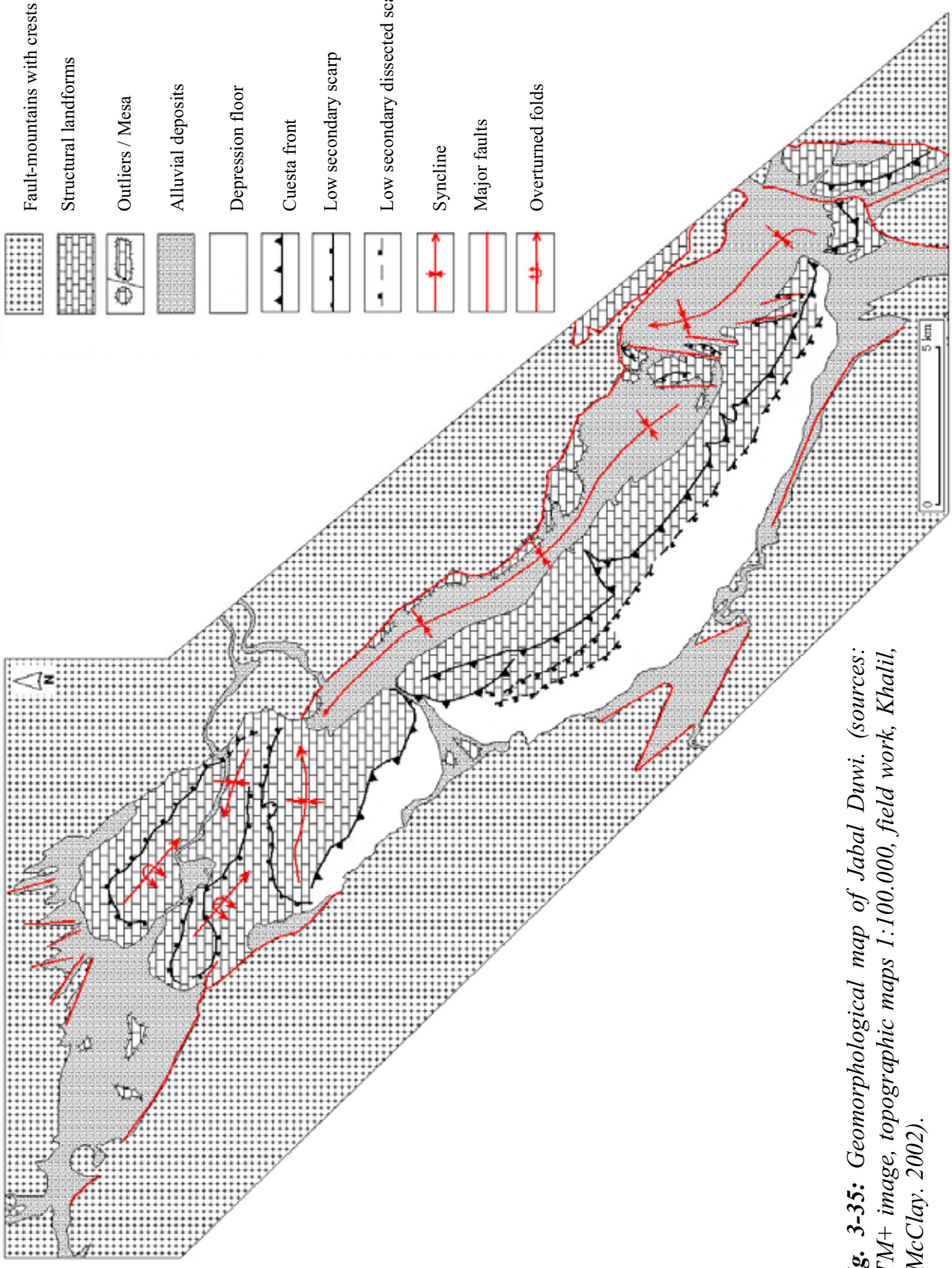

Fig. 3-35: *Geomorphological map of Jabal Duwi. (sources: ETM+ image, topographic maps 1:100.000, field work, Khalil, &McClay. 2002).*

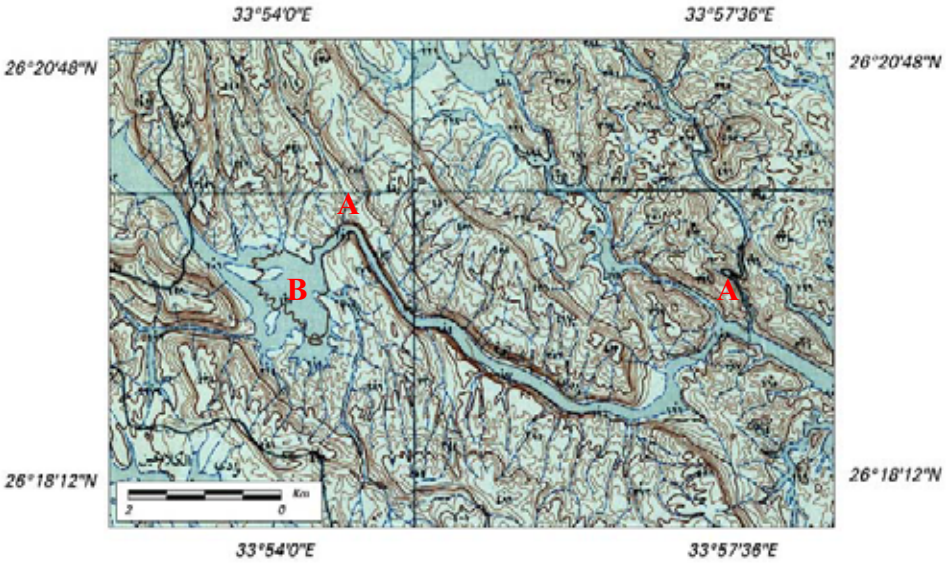

Fig. 3-36: *Extract of a topographic map 1:50.000 showing right angle junctions of wadi el-Saqia at locations (A) and a sub- basin at location (B).*

However, another tributary of wadi Sodmein incises down into the northern block less or more parallel to wadi el-Saqia. This tributary is of pinnate pattern causing numerous small tributaries to constitute a featherlike branching pattern. It is suspected to be structurally controlled where the rock strata of both sides are tilted down towards the wadi channel that is inferred to follow a fault-drag syncline (Fig. 3-37). Equally, Khalil & McClay (2002) demonstrated that the northern block of Jabal Duwi plunging gently to the north and performing the strata to dip in various directions owing to Kalahin syncline fold.

▪ The southern block of Jabal Duwi extends about 24.5 km along NW-SE trend. It covers an area about 120.8 km^2 and attains 627 m height asl. The rock dips eastwards at various angles (18˚-23˚) exposing the block as a cuesta that is experienced NNE and NE fault systems (Figs. 3-38, 3-39a).

Generally, this block forms a bold white cliff (Barron and Hume, 1901) that runs considerably along the strike faults. Its western slopes are broken by two secondary low scarps. The lower one is extensively dissected and composed mainly of Dakhla or El Quseir shale, while the other scarp is relatively higher and composed of Duwi phosphate, marl and limestone (Fig. 3-39b). The general outline of the western cliffs exhibits badland-like form.

This block is impressed by consequent and resequent effluents of wadi an-Nakheil and wadi Sodmein. The later wadi comprises a more than 200 m deep narrow gorge.

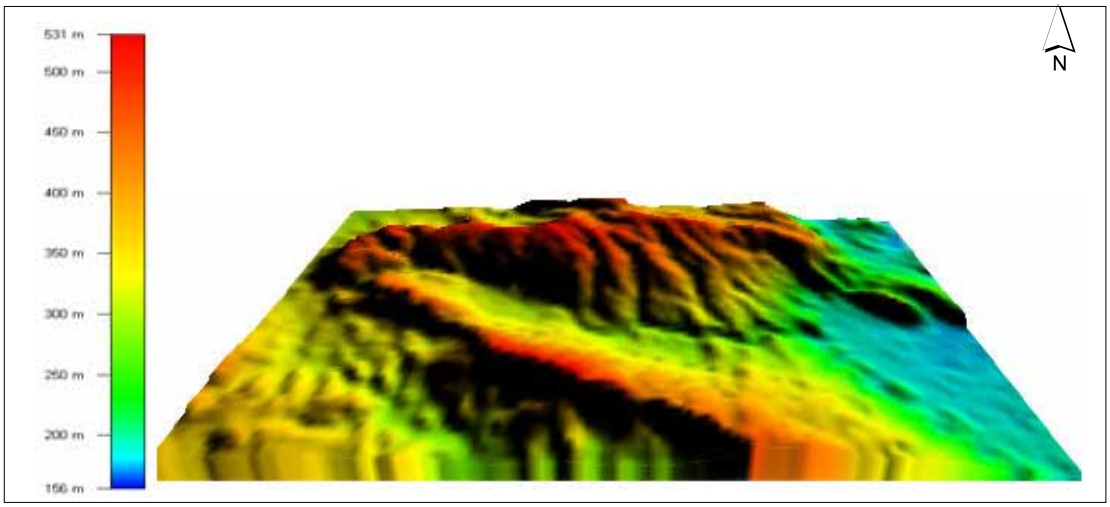

Fig. 3-37: *Colour level slice 3d view showing a tributary of wadi Sodmein that follows an inferred fault-drag syncline.* *(Extract from the DEM)*

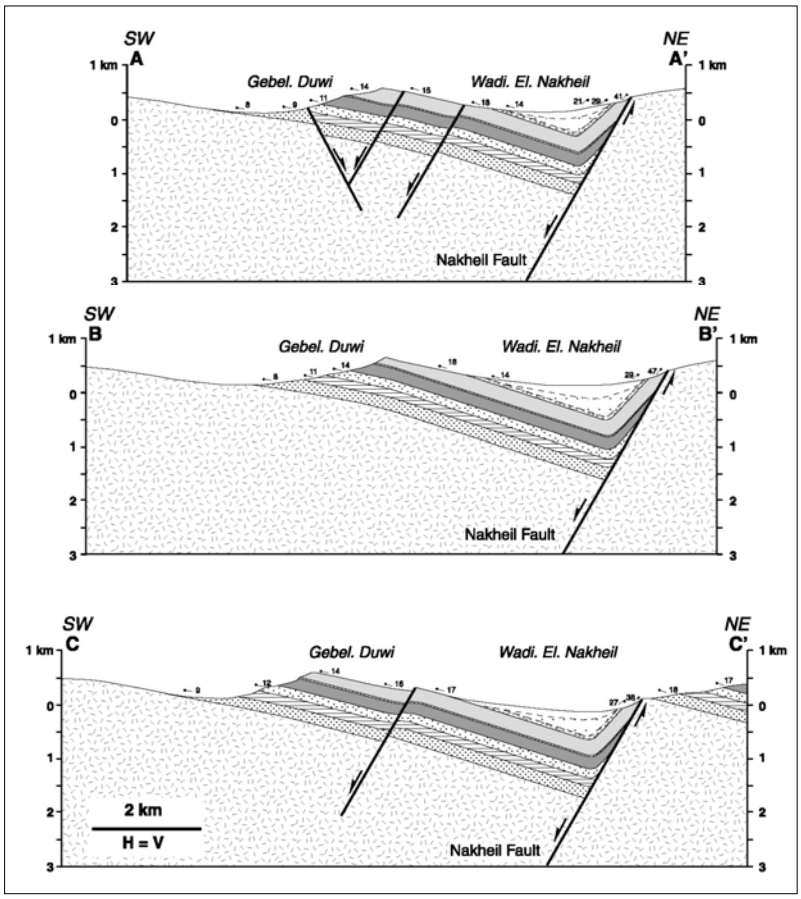

Fig. 3-38: *Structural cross sections along Jabal Duwi.* *(Source: Khalil & McClay, 2002)*
(For locations and legend review fig. 3-34)

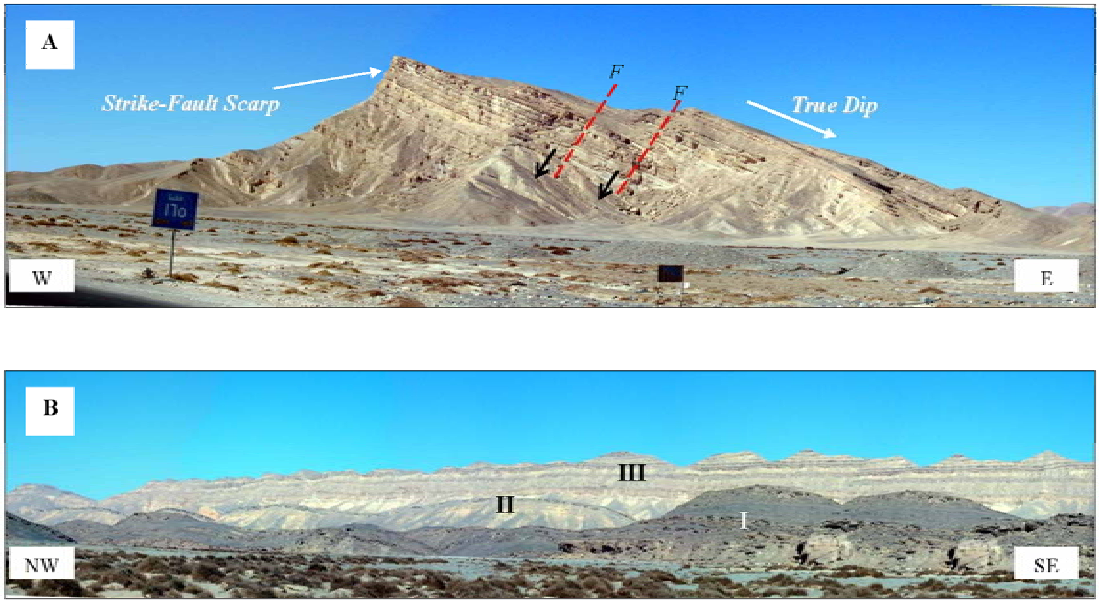

F Fault
I Dissected scarp (shale)
II Secondary low scarp (Phosphate, marl and shale)
III Major Strike-fault Scarp (Limestone)

Fig. 3-39: *(A) east-west panoramic view of southern Jabal Duwi showing microtectonic faults and (B) panoramic view of the western scarps of Jabal Duwi.*

The western cliffs of Jabal Duwi and the vertical walls of Sodmein gorge as well are subjected to tension, perpendicular and strike joint systems. Therefore, the cap rocks are vulnerable to fall and move downslope (Fig. 3-40).

Fig. 3-40: *Fallen rocks in Sodmein gorge.*

Jabal Duwi exposes distinctive solutional landforms of which Sodmein Cave, locates at 26˚14̀ 27" N, 33˚58̀ 12" E, is well developed in the lower part of a 100 m high cliff and looks over the 200 m wide wadi Sodmein at the downstream end of a 3 km long gap (Moeyersons et al. 2002). Floor of the cave is about 41 m wide and 10-20 m deep. The origin of the cave is believed to be due to the chemical action of infiltration water that penetrated the sub-vertical joints crossing Thebes limestone (Vermeersch et al. 1994).

The cave is located within a system of microfaults in the shoulder of a micrograben, traversing obliquely the gap (Fig. 3-41). Its southern and northern sides chamber coincide partly with faults and shear zones with vertical throw in the Thebes limestone of the order of 0.2–0.5 m. According to Moeyersons et al. (2002), the cavity starts deep in the Jabal with two sub-horizontal shafts or tunnels, both of them is <1 m high. At about 35 m from their inferred outlet in the cliff, both tunnels end in the ceiling of a huge chamber with a steeply dipping backwall and an open view to the wadi. The southern shaft may be an old solution feature, having affected a 50 cm thick bedding layer in Thebes limestone, about 0.5 m below the roof of the chamber.

Fig. 3-41: *Entrance of Sodmein Cave and the surrounded microtectonics.*

The backwall (Fig. 3-42) of the cave consists of a subsided slab that leans upon deposits in an underground cavity. The upper side of the slab shows a spongework of honeycomb weathering, interpreted as solutional features, a subcutaneous lapies due to important subsurface water infiltration in the bottom of the southern shaft before its collapse.

Corestones in the cave deposits are rounded and bundles of flakes are being parts of their former spheroidal weathering mantle often adhering to their surface. The roof of the modern cave is flat and rather massive, apparently resulting from the mechanical detachment of a slab of rock (Moeyersons et al. 2002). The roof as well exhibits dissolution pits of different sizes and experienced three incised joint sets; they are: sheet joints in accordance with the plain of the limestone strata, perpendicular joints and oblique joints. Where these sets intersecting together, sinkholes of the roof are well developed and become wider as a result of passing water along these joints (Fig. 3-43).

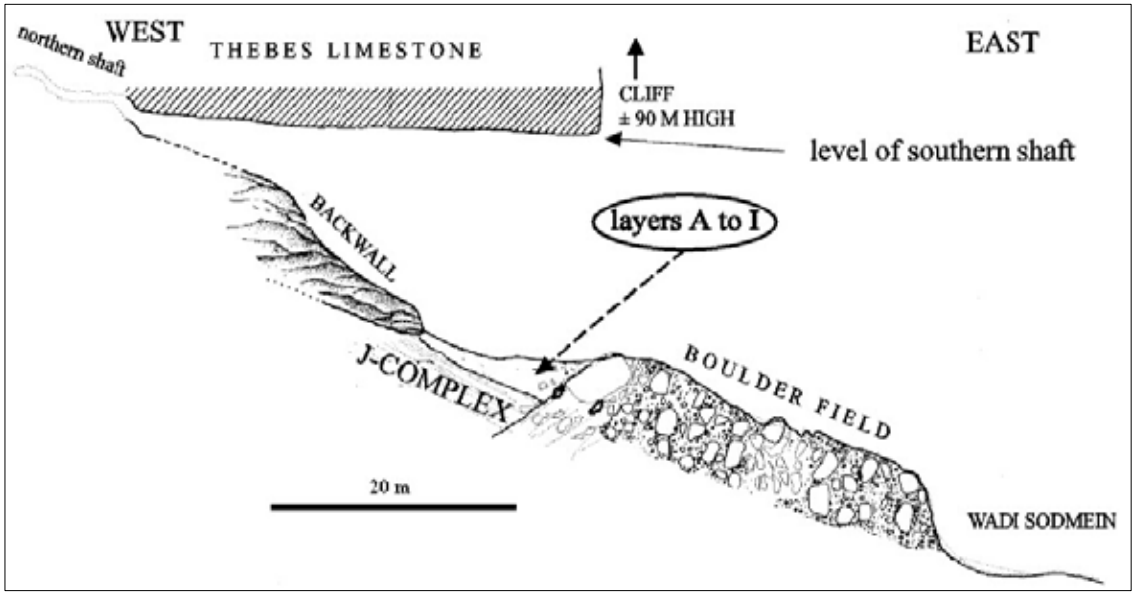

Fig. 3-42: *Section through Sodmein Cave.* *(After: Moeyersons et al. 2002)*

Fig. 3-43: *A relatively wide sinkhole in the roof of Sodmein Cave.*

On the other hand, the floor of the cave in the front of the backwall lies between 15-20 m above the wadi floor. It is relatively flat and composed primarily of fine materials and sands.

Moeyersons et al. (2002) clarified that there were different wet periods in Sodmein cave at 6.320–7.470 and ±25.000 yr BP and at ±115.000 yr BP. A fireplace has been recognized and its position was discussed by Mercier et al. (1999). He denoted the charcoal of the upper Palaeolithic level as 25.200± 500 BP. He distinguished 4 levels of the middle Palaeolithic, the second and third levels of which contain charcoal ranging in age between >30.000- >45.000 BP respectively. Organic matters are abundant and artecrafts as well. Moeyersons et al. (2002) revealed that most of the organic contents state as in animal excrements and are thought to have passed through the digestive system of the animals. These organic contents were dated between middle Palaeolithic and Neolithic (≥30.000 - ±6.320 BP). However, a blade core of limestone flake has been found buried 60 cm below the cave floor (Fig. 3-44). One edge of the core is trimmed into a rough shape and its head is relatively sharp. This blade core is likely back to middle Palaeolithic time. On the other hand, preservation of sheep and goats droppings (1 meter below the floor of the cave) suggests the idea that during the middle and upper Palaeolithic there was a wealthy wild-life in the Eastern Desert of Egypt where the climate was probably semi-arid.

Fig. 3-44: *Middle Paleolithic core of limestone flake (Sodmein Cave).*

4.3. Old Erosion Surfaces.

The concept of peneplanation is used within this study to describe the subdued old erosion surfaces of the older granite and the contact-line between the basement complex and the overlaying sedimentary rocks. An old erosion surface could be defined as "a land surface shaped and subdued by the action of erosion especially running water". The term is generally applied to level or nearly level surface. It is believed that they are of tens of millions to over a hundred million years old, generally. Such surfaces were distinguished in Egypt since 1933 by Clayton in his expedition to the western side of the Gilf Kebir, Awad (1951) in central Sinai, Philobbos & Hassan (1975) in the Eastern Desert, and Mostafa (1987) in wadi Firan. However, partially exhumed erosion surfaces are found in the Arabian shield, which inclines eastward into the Rub al-Khali basin. They are overlain by gray and tan alluvial sediments and aeolian sands (Short, 2006).

Two types of old erosion surfaces are recognized in the study area as follows:

4.3.1. Exhumed Erosion Surface.

The area lies approximately west of long. 33˚ 45̀ E forms an extent exhumed uplifted peneplain. The surface range in elevation between 500-1000 m asl, generally. Interpretation of the ETM+ images of the Eastern Desert of Egypt gives an impression that this surface has regional extensions. The surface is more or less flat with low relief or remnants (Monadnocks), which are likely preserved mainly upon the more resistant rocks and standing conspicuously above the general level (Thornbury, 1984). The most crucial reason for considering this surface as old erosion one is that the truncation of different rocks (e.g. biotite, gabbro, intermediate metavolcanics, biotite granite) of varying resistance to weathering and erosion (Fig. 3-45). It is characterized as well by general accordant levels of its interstreams and summit areas. The surface is significantly subdued, weathered and locally interposed by younger granite intrusions and the morphotectonic depressions.

On the other hand, individual horsts in the vicinity of the coastal plain exhibit limited exposure erosion surface of which horst of Umm Kujurah is well distinct. This horst is composed primarily of Hammamat group (conglomerate, gritstone, sandstone and siltstone). It attains about 250 m asl in accordance with the surrounding andesite and felsite of Dokhan Volcanics (Fig. 3-46).

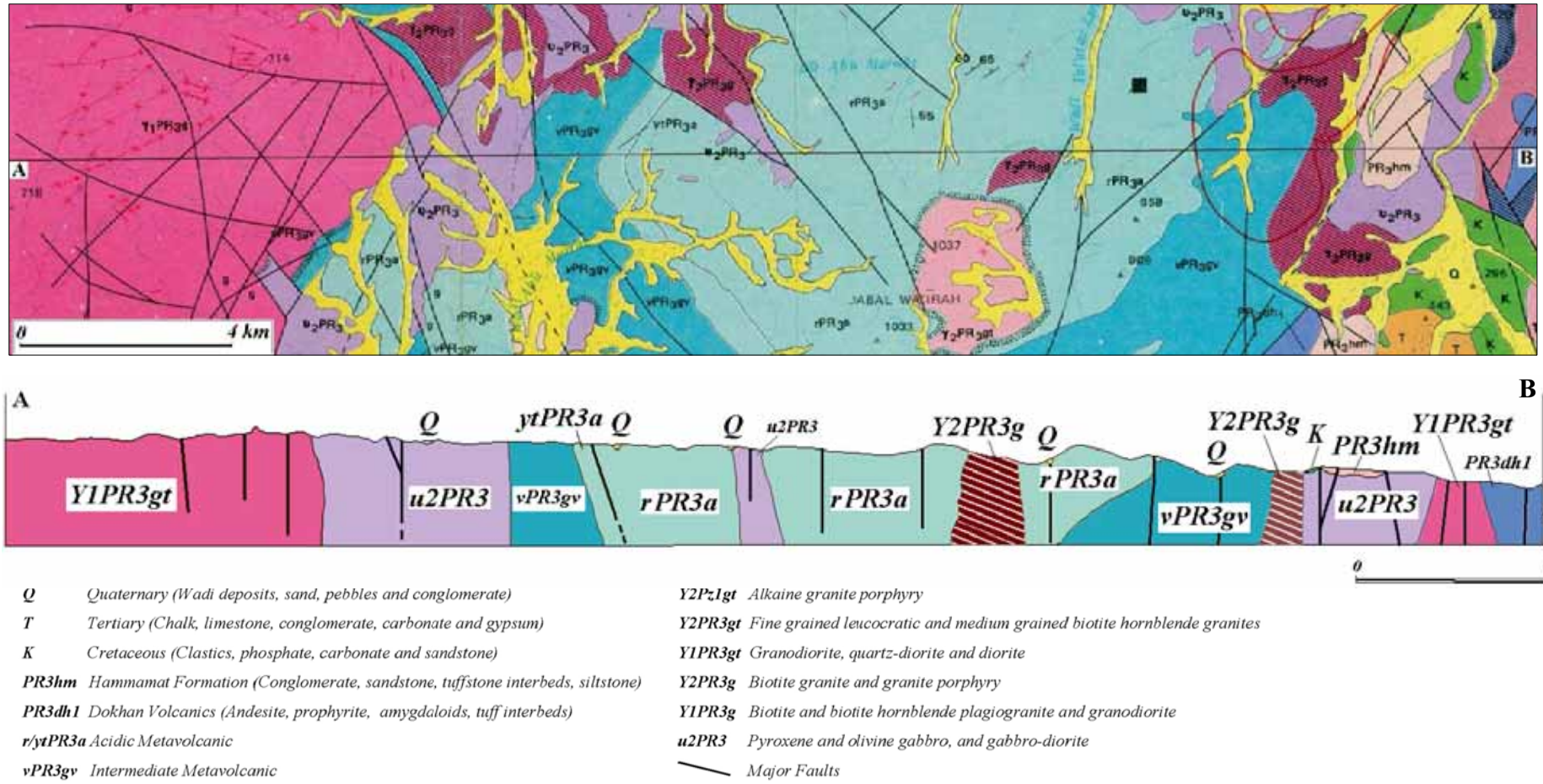

Q *Quaternary (Wadi deposits, sand, pebbles and conglomerate)*

T *Tertiary (Chalk, limestone, conglomerate, carbonate and gypsum)*

K *Cretaceous (Clastics, phosphate, carbonate and sandstone)*

PR3hm *Hammamat Formation (Conglomerate, sandstone, tuffstone interbeds, siltstone)*

PR3dh1 *Dokhan Volcanics (Andesite, prophyrite, amygdaloids, tuff interbeds)*

r/ytPR3a *Acidic Metavolcanic*

vPR3gv *Intermediate Metavolcanic*

Y2Pz1gt *Alkaine granite porphyry*

Y2PR3gt *Fine grained leucocratic and medium grained biotite hornblende granites*

Y1PR3gt *Granodiorite, quartz-diorite and diorite*

Y2PR3g *Biotite granite and granite porphyry*

Y1PR3g *Biotite and biotite hornblende plagiogranite and granodiorite*

u2PR3 *Pyroxene and olivine gabbro, and gabbro-diorite*

Major Faults

Fig. 3-45: *Geological map and profile showing the exhumed erosion surface.* *(Source: Basement rocks of Safajah quadrangle scale 1:100.000).*

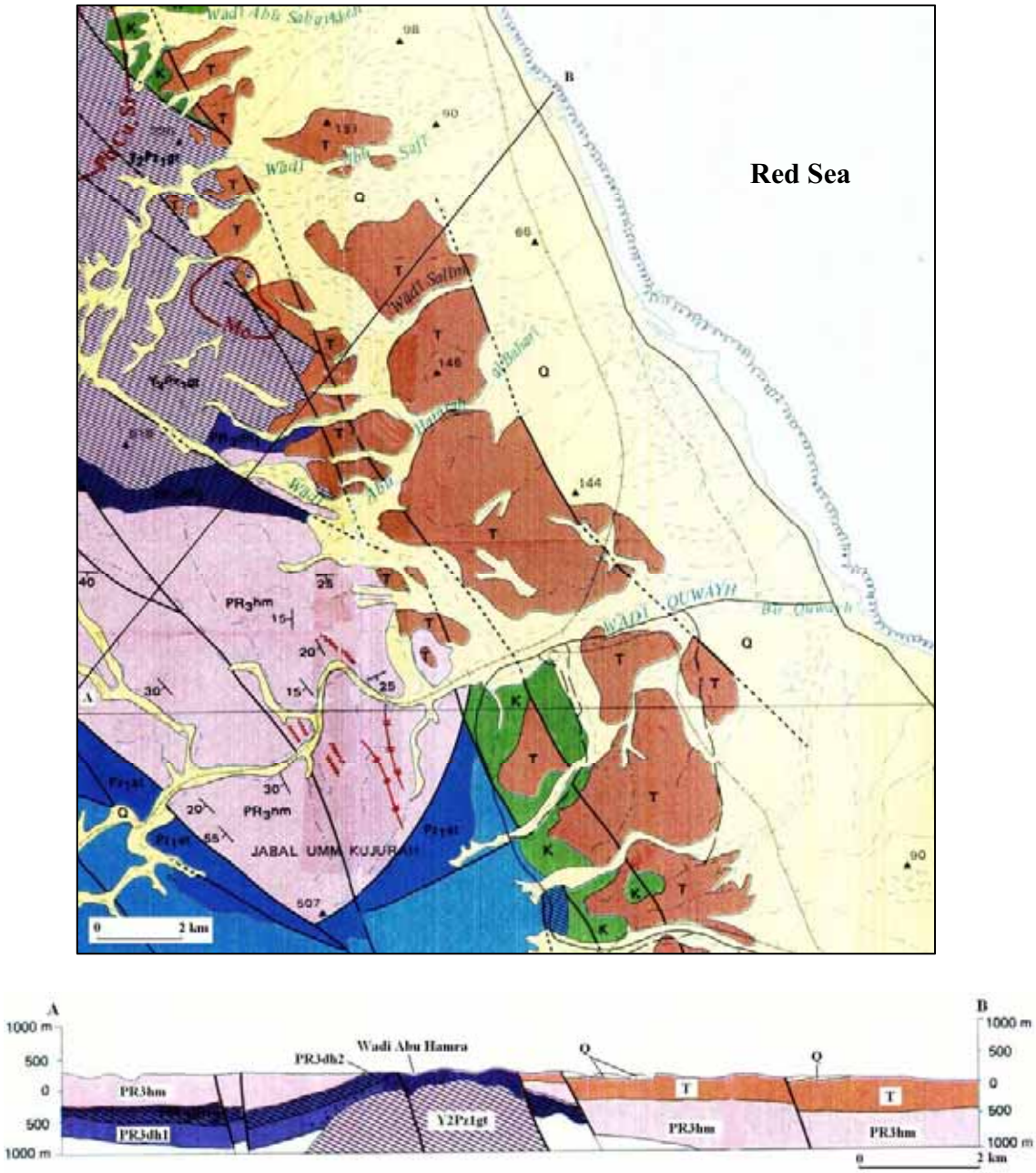

Q	*Quaternary deposits*	***PR3dh1***	*Andesite*
T	*Tertiary rocks*	***PR3dh2***	*Felsite*
PR3hm	*Hammamat group*	***Y2Pz1gt***	*Coarse grained granite*

Fig. 3-46: *Geological map of Jabal Umm Kujurah (upper) and geological profile (lower) showing exhumed and buried erosion surfaces.* *(Source: Basement rocks of Al Qusayr quadrangle, scale 1:100.000).*

4.3.2. Buried Erosion Surfaces.

Buried erosion surfaces constitute the unconformities of stratigraphic geology (Thornbury, 1984). They are well seen in limited exposures with strata above them along the eastern cliff of Jabal Naqarah, where the felsite rocks are unconformably overlain by Tertiary chalk, limestone and carbonate sediments. The Tertiary cap-rocks ranging in elevation between 250-300 m asl and the contact-line is mostly flat or uneven eastwards elsewhere (Fig. 3-47). The basement rocks of Jabal Naqarah underwent severe peneplanation processes that might be equivalent to the stage of Hammamat group (680 - 640 Ma). The peneplanation processes of Jabal Naqarah were mostly followed by submergence beneath the Tertiary Sea since the Tertiary rock mantle was deposited. Thereafter, Jabal Naqarah has been uplifted gradually and faulted along NW-SE trend that is probably occurred during Oligocene time.

The relation between the basement and tertiary rocks was examined in an-Nakheil basin. Along its eastern edge, the Tertiary rocks incline about 35˚ westward. It is not really clear whether the initial contact-line forms an old erosion surface or not, where it is considerably deformed by tectonics (Fig. 3-48).

Fig. 3-47: *An exposure section of the old erosion surface of Jabal Naqarah. The surface separating felsite rocks from the Tertiary rocks.* *(Looking westward)*

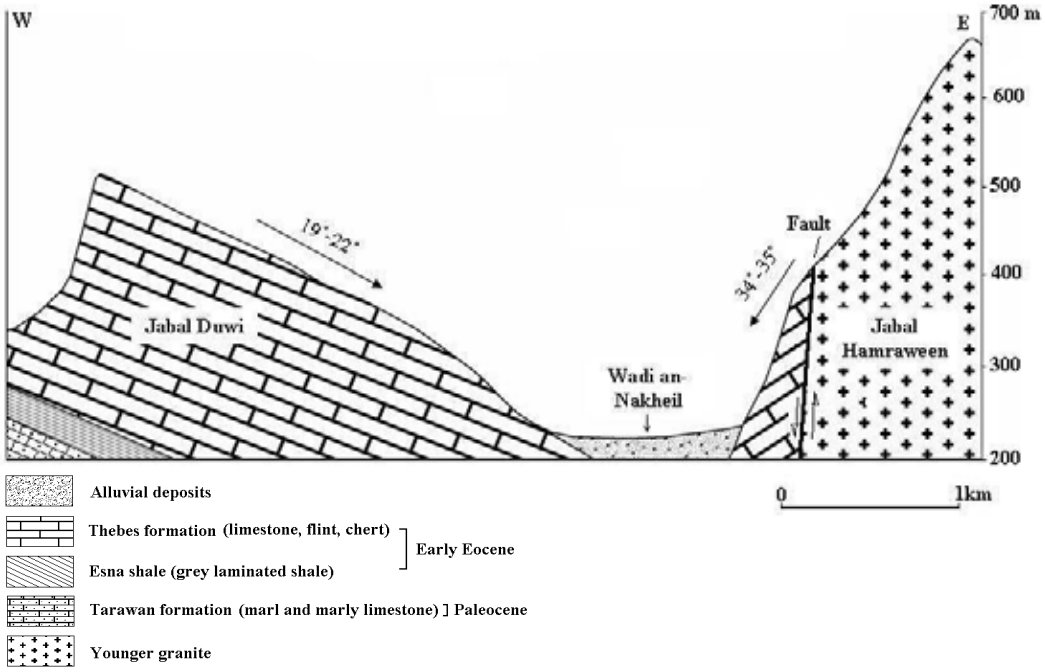

Fig. 3-48: *Cross section of wadi an-Nakheil. (Sources: field work, topographic & geologic maps)*

4.3.3. Peneplanation Phases.

Although it is difficult to determine an absolute age to these peneplains, evidence from Hammamat group indicates that significant volumes of igneous rocks in 680-640 Ma age range were vigorously eroded during the early stage of Hammamat sedimentation, which deposited in a major river system of a continental-scale (Wild & Youssef, 2002). Another proof can be deduced from figure 3-46 where a buried erosion surface separates between Tertiary rocks and Hammamat group near the coastline. They are affected together by the coastal rift faults, which indicates that there was a peneplanation phase prior to the coastal rift system that was occurred during upper Oligocene-Early Miocene time. On the other hand, the study area evidently has been uplifted several times before attaining its present-day levels and the successive sedimentary rock cover was fully or partly removed from the higher terrain, while it is still-standing in the morphotectonic basins. Therefore, at least two cycles of erosion could be determined; the first one was synchronous with the early stage of Hammamat sedimentation during upper Proterozoic and the second one was mostly occurred during upper Tertiary, where the Tertiary rocks are partially and/or fully eroded elsewhere.

4.4. Diapiric Plutons.

The Egyptian Eastern Desert has been described as one of the most intensively dyke-intruded and granitoids pluton-pierced segments of the continental crust (Fowler, 2001 after: Vail, 1968; Bentor, 1985). Diapiric plutons of the study area constitute ring structures that intruding the older rock units. Commonly, they associated with volcanic episodes and consisting of granite masses that were originated from the deeper earth crust and rose gradually to the surface because the originally hot rocks were less dense than the cooler surrounding country rocks (Summerfield, 1991).

Figure 3-49 showing the most obvious diapiric plutons in the study area; they are Jabal Ras Barud (lat. 26˚ 47̀20 "– long. 33˚ 39̀ 00"), Kab Amiri (lat. 26˚ 20̀ 58" –long. 33˚ 34̀ 55"), Jabal Umm Had (lat. 26˚ 04̀ 20" – long. 33˚ 30̀ 51") and Jabal Umm Oradah (lat. 26˚ 05̀ 44"– long. 33˚ 49̀ 59").

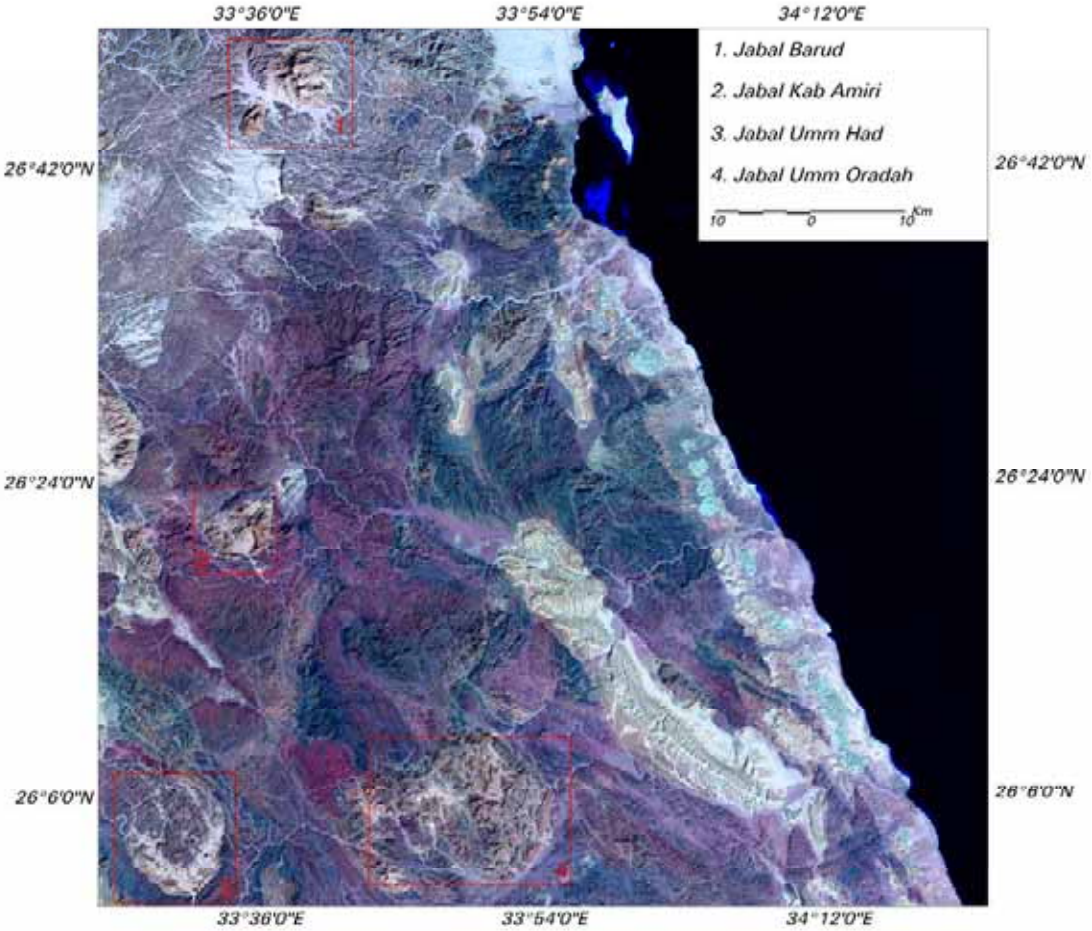

Fig. 3-49: *Spatial distribution of the plutons.*

4.4.1. Pluton of Jabal El Barud.

Jabal El Barud is detached into two granite masses by wadi El Barud El Abyad that adheres to a major fault. The northern mass is relatively huge and circular in shape (Fig. 3-50). It has a diameter of 7.4 km with maximum relief of 1.338 m asl. The southern mass is relatively smaller with a diameter of 3 km and of 1.025 m height asl. It is elliptical shaped with general trend NE-SW.

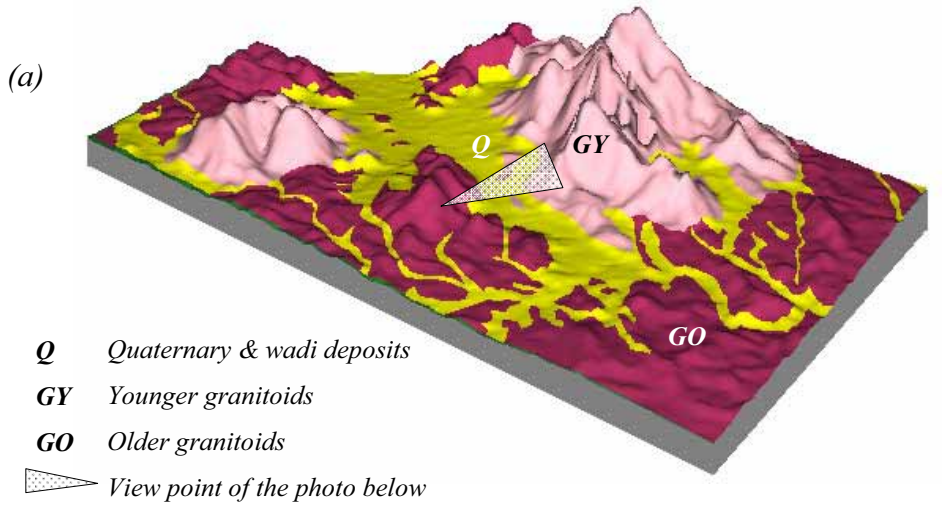

Fig. 3-50: *(a) DEM of Jabal Barud superimposed by the geological map. (b) General view to Jabal El Barud.* *(Looking northward)*

Jabal El Barud composed of coarse-grained biotite granite (Younger Granite[1]) belongs to lower Paleozoic era[2]. It is intruded by dyke swarms especially on its north-

[1] *Younger Granites as a term was firstly used by Akkad & El Ramly (1960 b) to replace that of Gattarian by Hume (1934) or Red and Pink Granites.*

eastern margins. The younger granite comprises high mountains with very rugged topography pronouncing angular joints. The Jabal intrudes the older granite rocks and contributing normal vertical and lateral offset in the contact zone. Therefore, boundaries of the pluton are significantly defined whether by faults or incised joints.

4.4.2. Jabal Kab Amiri.

This Jabal is composed of the younger granite and rises up to 900 m asl. It is subjected to intensive faulting of different trends. A major NW-SE fault divides the pluton into nearly two halves extending about15 km northwesterly. Equally, another NE-SW fault detaching the northern part of the pluton and extending about 11 km southwesterly. The western border of the pluton pursues a NNE-SSW fault extending about 5 km and the eastern border and showing zigzag-like shape. Center of the pluton has been deeply denuded to constitute a sand filled depression with steep slopes (Fig. 3-51).

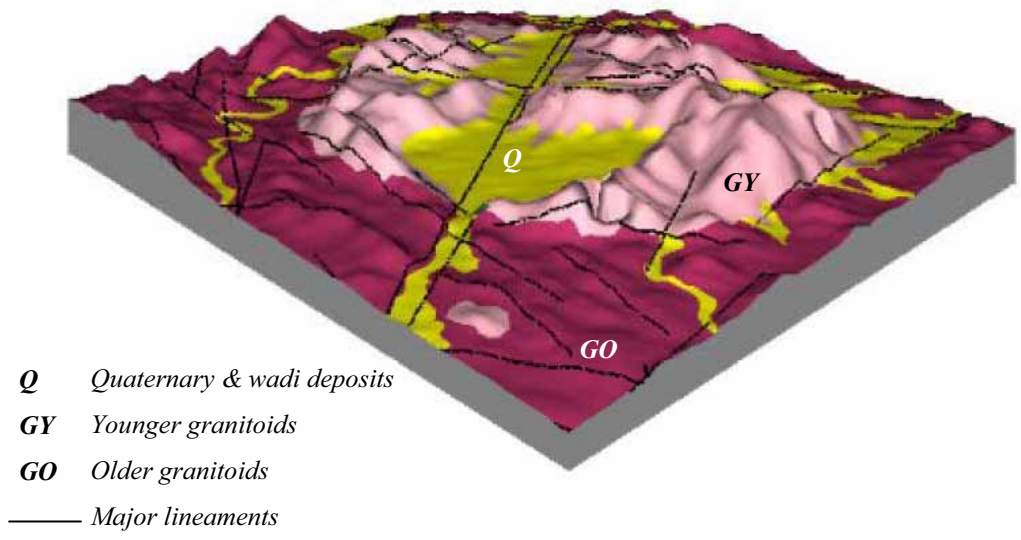

Fig. 3-51: *DEM of Jabal Kab Amiri superimposed by the geological information.*

4.4.3. Jabal Umm Had.

Jabal Umm Had adopts an approximately circular outline of 10.7 km in diameter. It attains about 595 m height asl and occupies about 103 km^2. According to Fowler (2001) the pluton is considerably defined at its western, southern and eastern margins (Fig. 3-52). It is mainly composed of the younger granite bounded by Dokhan Vol-

[2] *Basement Rocks of Safajah Quadrangle (1987) scale 1:100.000, by E.G.S.M.A. Egypt.*

canic on the east and southeast directions, Hammamat group (conglomerates, siltstones) from the south and west and by gneisses and older granite from the north and north-west directions. The area is vigorously eroded along the major faults of which NW-SE and NE-SW trends are more conspicuous. The pluton is dated at 590 ±11 Ma from Rb-Sr[1] data (Fowler, 2001 after: Ries et al. 1983). A subsurface extension of Umm Had pluton northwards is suggested in literatures on the metamorphic history of this area.

4.4.4. Jabal Umm Oradah.

Jabal Umm Oradah is partially circular intrusive granite massif of 13.3 km in diameter and 177 km^2 (Fig. 3-53). Boundaries of the pluton are intruded by various dykes, dipping outside of the pluton and are relatively lower than the center of the pluton that rises up to 800 m asl (Fig. 3-54 a). The west and east sides of the pluton are composed of paragneisses and migmatites rocks, which are relatively lower than the younger granites and vary in elevation from 300 to 400 m asl (Fig. 3-54 b). The area is primarily influenced by NW and WNW faults extending about 16 and 17 km successively. Both fault directions are crossed by another NE-SW fault extending about 18 km. Moreover, the pluton exhibiting other microtectonic features such as minor faults and folds, which resulting in markedly rugged relief and steep cliffs.

Generally, plutons of the study area are primarily controlled by endogenic processes and confined to regional structural (El-Sayed et al. 2002). As a result, they constitute vigorous dissected block mountains characterized by pinnacle summits. According to Hassan & Hashad (1990) plutons of the Eastern Desert of Egypt ranging in Rb-Sr age from 620 to 570 Ma.

---

[1] *The Rb-Sr (Rubidium- Strontium isotopes) method has widely been superceded as a tool for dating igneous rocks and metamorphic events. The utility based on the fact that different minerals in a given geologic setting can have distinctly different* $^{87}Sr/^{86}Sr$ *as a consequence of different ages, original Rb/Sr values and the initial* $^{87}Sr/^{86}Sr$.

(a)

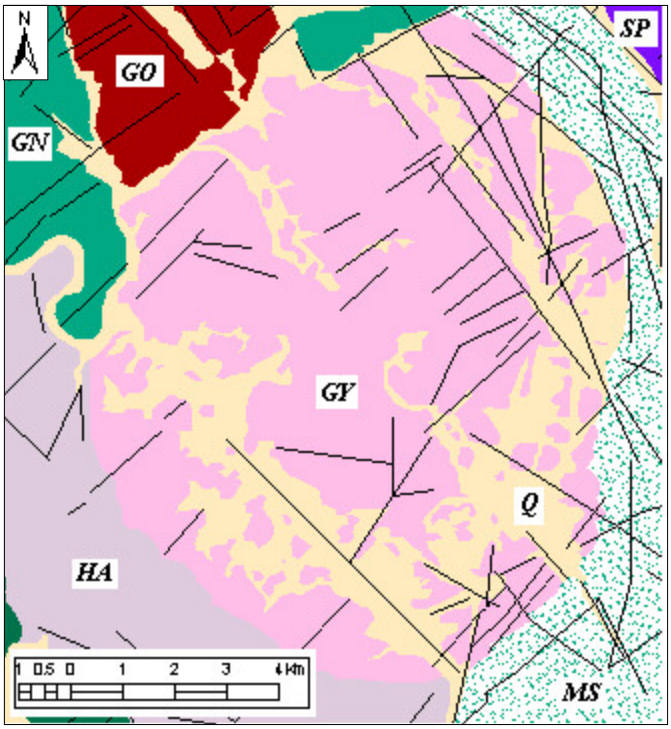

Q	*Quaternary & wadi deposits*	**SP**	*Serpentinite*
GY	*Younger granitoids*	**MS**	*Geosynclinal metasediments*
HA	*Hammamat Group*	**GN**	*Paragneisses and migmatites*
GO	*Older granitoids*	——	*Major Faults*

(b)

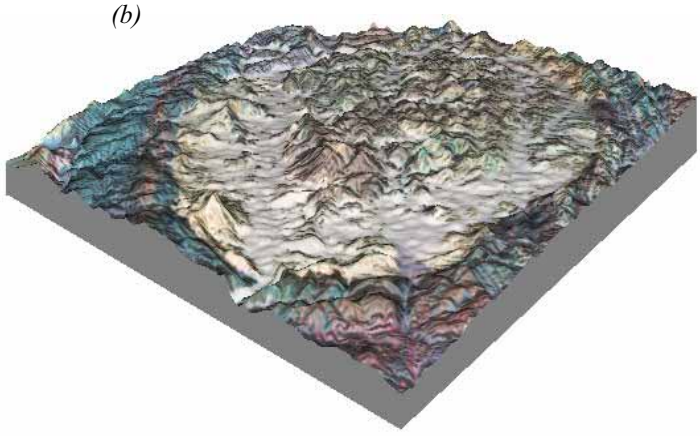

Fig. 3-52: *(a) Geological map of Jabal Umm Had. (b) DEM of Jabal Umm Had superimposed by ETM+ image band combination 7, 4, 2.*

However, exogenic processes evidently pruning the topography of the plutons of which weathering processes gain a large extent. It is widely known that granite rocks contain various minerals (i.e. Na plagioclase feldspar (white), K feldspar (pink or

white), quartz (grey), small amounts of biotite and/or amphibole (black) and sometimes muscovite). Altogether, except quartz, are sensitive to weathering processes and weather in place. Accordingly, feldspars undergo hydrolysis to form kaolinite (clay) and Na and K ions. Sodium and potassium ions remove through leaching. Biotite and/or amphibole undergo hydrolysis to form clay and oxidation to form iron oxides. Finally, quartz remains as residual minerals because it is very resistant to weathering. As a result of that, cavities of different shapes and sizes are abundant. They are mostly controlled by joint systems, so that they vary in diameter from a decimeter to several centimeters and confined only to few centimeters deep (Fig. 3-55). As well the older granite is subdued and breaks into flat sheets and fragments due to rock expansion as a result of thermal weathering and pressure release. It is breaking along joints, which are orthogonal or parallel to the ground surface producing exfoliated or rounded joint-blocks of different sizes (Fig. 3-56).

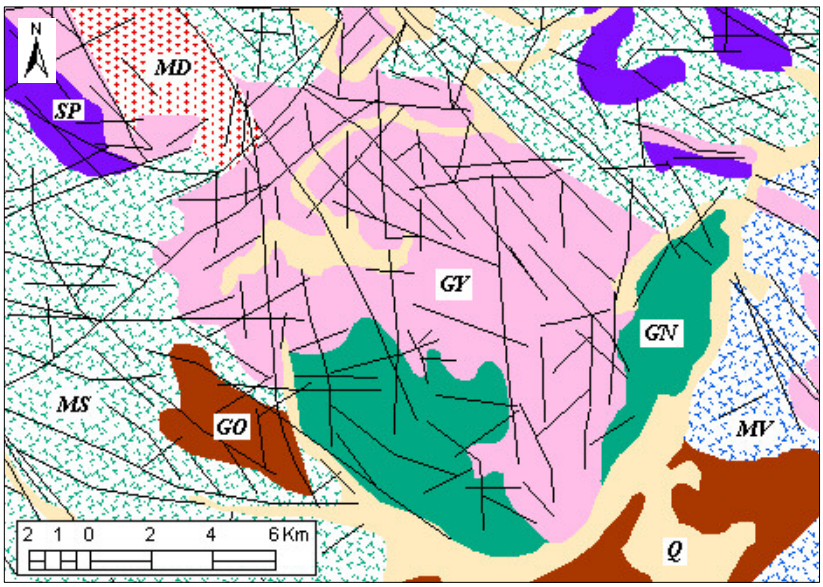

Q	*Quaternary & wadi deposits*	***SP***	*Serpentinite*
GY	*Younger granitoids*	***MV***	*Metavolcanic*
HA	*Hammamat Group*	***MS***	*Geosynclinal metasediments*
GO	*Older granitoids*	***GN***	*Paragneisses and migmatites*
MD	*Metagabbro-diorite complex*	____	*Major faults*

Fig. 3-53: *Geological map of Jabal Umm Oradah.*

Fig. 3-54: *(a) The outer rim of Jabal Umm Oradah looking northwest. (b) Parag-neisses and migmatites of Jabal Umm Oradah looking westward.*

Fig. 3-55: *Shallow cavities developed in the granite rocks.*

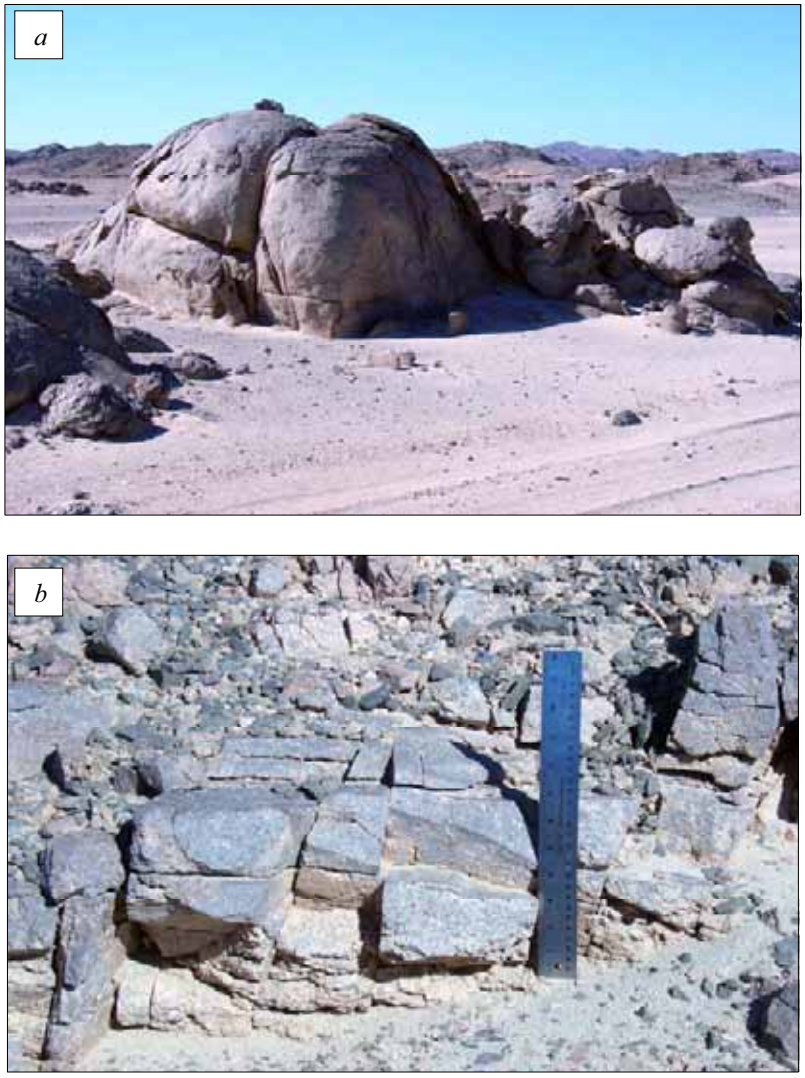

Fig. 3-56: *(a) Relatively large joint-blocks of older granite gradually rounded into smooth forms by disintegration south of wadi El Barud. (b) Cubic fragments splinting owing to thermal weathering.*

4.5. Dyke Swarms[1].

Dykes are plutonic bodies of intrusive igneous rocks formed when a vertical rock fracture is forced open by magma. These fractures conduct magma to the land surface (Strahler & Strahler, 2000). They are abundant in the Eastern Desert and firstly documented by Schürmann (1966). They comprise narrow steeply dipping bodies of few meters thick and several kilometres long (Meneisy, 1990). They crossing the basement rocks and representing several phases of intrusive activity during the formation and evolution of the basement rocks. Dykes are locally intense particularly in the diapiric plutons such as in Jabal Umm Had where numerous granitoid dykes are subparallel to the dip of the granite contacts (Fowler, 2001).

Beniamin et al. (2005) argued that during the last phase of the orogeny, the late-post tectonic granites are widely dissected by numerous dykes, veins, joints, fractures and fissures with general trend of NE-SW. Quartz veining is widespread in particular and sometimes is being hydrothermally affected and locally associated with relative enrichment of iron oxides.

Dykes within the study area filled most of the major structure weakness crossing the basement rocks, which are fractured and faulted intensively due to tectonic processes. Accordingly, they are considerably controlled by the geometric characteristics of fractures and/or the fault systems and tend to be either parallel narrow straight or sinuous lines on the ETM+ image (Fig. 3-57). Sinuous dykes characterized by their shape and irregular widths due to the movement of the magma into a fissure or cavity (Whitten & Brooks, 1972). They could be also distinguished by their dark brown colours especially where they cut through relatively light colour rocks (Fig. 3-58). On the other hand, some dykes depict green, green-yellow and green-blue colours.

As can be deduced from figure 3-58, three dyke sets are distinguished and dated relatively to each other. The first set constitutes straight dykes at location (A), which seems to be the older set because it is influenced by tectonic movements and displaced horizontally about 1 km along NW-SE trend.

[1] *Dyke swarm is a group of dykes, which may be in radial, parallel, or en-echelon arrangement. Their relationship with the parent plutonic body may not be directly observable.*

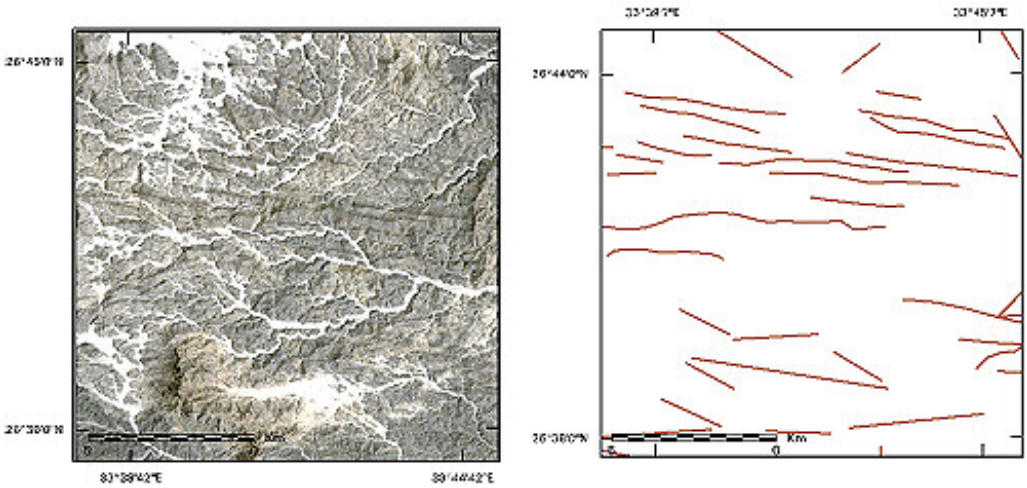

Fig. 3-57: *Parallel narrow and nearly straight dykes.*

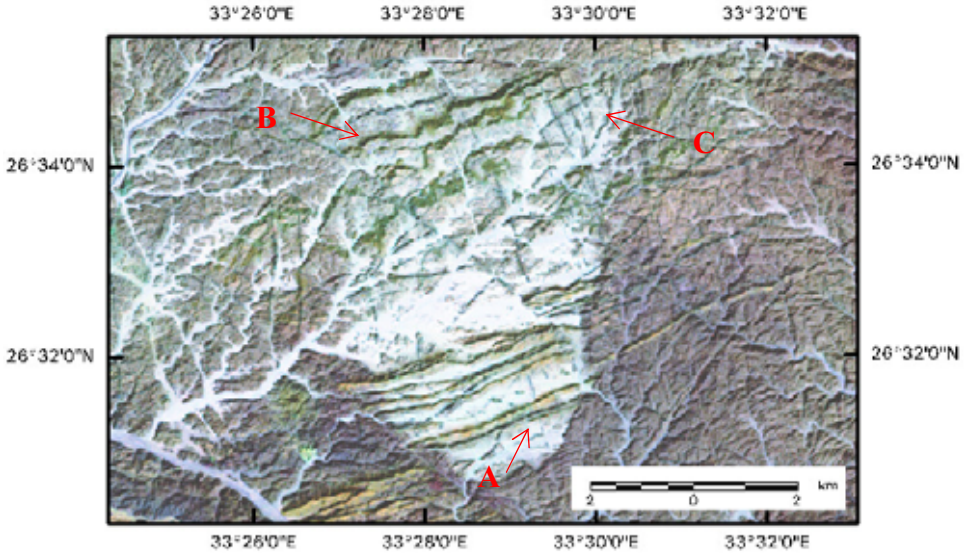

Fig. 3-58: *Dyke recognitions: (A) parallel narrow and nearly straight dykes subjected to tectonic movements and characterized by green-yellow colours. (B) Sinuous dykes and trajectories reveal green colour and irregular widths. (C) Thinly dykes showing green-blue colours.*

The second set represents sinuous dykes at location (B). It seems to be relatively recent because it does not attain any offset and slightly parallel to the previous set. The third dyke set forms thinly dykes showing green-blue colours with general trends NNW-SSE, NW-SE, NNE-SSW at location (C). This set seems to be the most recent one filled the major faults, which affected the older dyke set. As well this set crosses the second dyke set forming cross-cutting relationship commonly, but it does not depict any movements.

According to El Rakaiby (1997) dyke orientations are significantly perpendicular to the Red Sea structural trend "northwest" and less significantly parallel to this trend.

Geologically, the older dykes in the study area consist of diabase, gabbro-diabase, and porphyrite dykes, which assigned to early Gattarian complex or younger granite stage that occurred during the upper Proterozoic times. The younger dykes composed of different intrusive igneous rocks such as dolerite, dioritic porphyrite dykes, trachyte, microsyenite and bostonite, granite porphyry and felsite porphyry. They assigned to Cretaceous-Paleogene times[1].

Generalized sequence of dykes starting with the oldest is given by Francis (1972) and compiled with the geologic maps as follows:

- *Acidic dykes* form the oldest group of post-granite dykes. They include plagiogranite porphyry, fine-grained biotite granite, pegmatite, pegmatoid, diabase, gabbro-diabase, felsites, quartz-prophyries, and dacites dykes. They are usually of light yellow, pink and greyish colours.
- *Intermediate dykes* include andesites, and microdiorites. These varieties are dark colour varying from green to black. They form together with the acidic dykes the most abundant dykes in the study area.
- *Lamprophyre dykes* are represented only by plagioclase and amphibole-bearing types. The amphibole is either deep brown barkevikite or greenish-brown hornblend.
- *Basic dykes* are the least common one. They are represented by dolerites and basalt. They are dark grey to black in colour and in weathering they yield onion-like boulders.
- *Alkaline dykes* or young dykes are grouped of trachyte, microsyenite, bostonites, dolerite, and dioritic porphyrite dykes. The bostonites are fine-grained exhibiting red to reddish-brown colour.

Francis (1972) argued that none of the post granite dykes was found to cut through the upper-Cretaceous Nubian sandstone or the younger sediments overlaying the basement rocks at wadi Qena and the coastal plain.

[1] *Basement rocks of Safajah quadrangle 1:100.000, 1987and basement rocks of Al Qusayr quadrangle 1:100.000, 1988.*

On the other hand, Said (1962) and Jarrar (2001) pointed out that the Red Sea dyke system started just before the beginning of the significant subsidence and plate separation along the Red Sea and Suez Rift. Usually, dyke swarms are known from the Eastern Desert of Egypt as "post-granite dykes". They postdated at 650-550 Ma batholithic "Gattarian" or younger granites, which commonly host these dykes in the crustal block of northeastern Egypt (Abdel-Rahman, 1995). According to Meneisy (1990) dykes, which locate north of Qena-Safaga highway, are estimated to range in age between 530 and 480 Ma.

Field investigations revealed that dykes vary greatly from few centimeters to few meters in width. A sample of 30 dykes are measured from the ETM+ image clarified that they differ in length from place to place between 2-9 km in length. Because they vary greatly in composition from acidic to basic and alkaline (Embabi, 2004) they form usually positive or negative relief (i.e. dyke ridges and trenches) according to their resistance relative to the host basement rocks (Fig. 3-59). On the one hand, it has been observed that felsic dykes, which composed of feldspar and silicate, form very sharp elongated ridges and extend over considerable distances. Mafic dykes, which are composed of ferromagnesian minerals, normally form less sharp wide ridges. In addition, dykes that cutting through more resistance rocks, such as granite, are eroding more rapidly. In this case, they form elongated trenches, which are well developed because of weathering and slope wash processes that may take place during wet periods.

Quartz veins are common as well and notably intrude Jabal Umm Oradah. They are well exploited from the sides of wadi Sodmein. The veins are white in colour crossing the paragneisses and migmatites rocks showing vertical and/or semi-vertical veins of few centimetres width.

Fig. 3-59: *Positive (ridge) and negative (trench) relief formed due to relative resistance of dykes.*

4.6. Joints.

Joints are smooth planar cracks interrupting the cohesion of the rock and along which there has been almost imperceptible movement. They form in tension in response to tectonic and thermal stresses that force the rock to extend ever-so-slightly perpendicular to the plane of fracture (Davis & Reynolds, 1996). They could be classified in the study area into the following categories:

▪ *Tectonic joints* comprising breaks formed due to tensile stresses convoying uplift or lateral stretching and regional tectonic compression. Such joints are more conspicuous in the satellite image since they are relatively long, continuous, wide-spaced, and enlarged by erosion. Jabal Ras Barud exhibits well example for the regional tectonic joints interrupting the younger granitoids. Joint system[1] of Jabal Barud, as can be deduced from figure 3-60, is defined by three joint sets with notably trends NE-SW, NW-SE, and E-W. They confined to conjugate system manifesting mutually cross cutting figures (e.g. "+" or "x" intersections) where their dihedral angles[2] range between 30˚ and 60˚. Joint sets of Jabal Barud may be simultaneously or are superimposed contributing complexity. Joint spacing seems to be arbitrary and inconsistent since there is no rules can be given to control its spacing (Balk, 1948). Usually, joints are filled with granite porphyry and felsite-prophyry dykes as can be seen in the north-eastern margins of Jabal Barud.

Equally, Dokhan volcanics of Jabal Umm al-Hawaytat exhibit three notably joint sets trending NE, NW, and N (Fig. 3-61). They intersect together depicting non-orthogonal pattern with persistent sets (x intersections).

▪ *Sheeting joints* comprise a set of joints that are specifically developed more or less parallel to the ground surface and influencing the older granite.

▪ *Orthogonal joints* are a set of joints that are perpendicular to the ground surface.

Field investigations revealed that both sheeting and orthogonal joints influencing the granite masses and separating the masses into small blocks of different sizes (Fig. 3-62). In some cases, they intersected by other oblique joint set inclines approximately 45˚ relative to the ground surface.

---

[1] *The joint system involves two or more joint sets, where a joint set refers to a group of joints that have preferential direction.*

[2] *The dihedral angle refers to the angle between two joint sets in a joint system.*

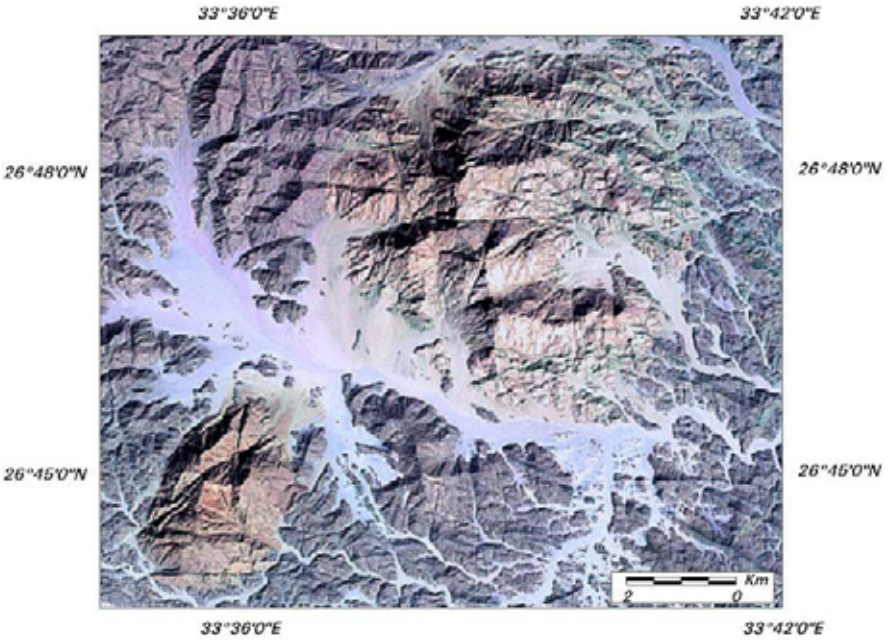

Fig. 3-60: *Conjugate joint system influencing the younger granite of Jabal Barud.*

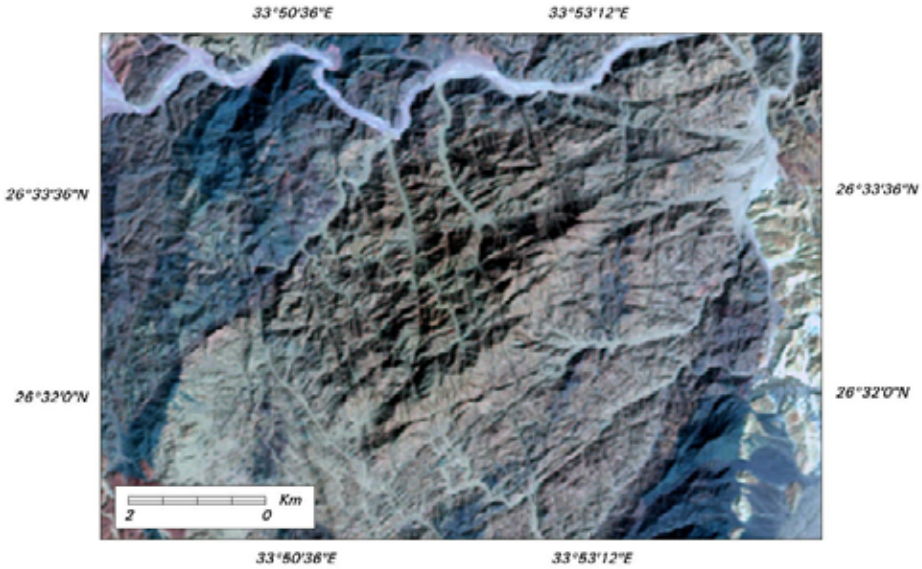

Fig. 3-61: *Non-orthogonal joint pattern crossing Jabal Umm al-Hawaytat.*

Fig. 3-62: *Orthogonal, sheeting and oblique joint sets influencing the granite masses in wadi Safaga.*

▪ *Exfoliation joints:* Normally, granite starts out in the subsurface is already fractured by joints. The pattern of fracturing splits granite into cubic-like blocks. Once the joint fractures come into contact with ground water, the water seeps into the cracks. Therefore, chemical decay takes place several meters underneath the surface and weathers the granite minerals. Normally, corners of the cube have three intersected joint sets, so they are less resistance and mostly decayed more quickly than the core-stone giving the granite block spheroidal shape (review Fig. 3-56a).

Finally, joint systems characterize the basement rocks in the study area are usually arranged in three joint sets, which have been originated and developed by shrinkage during cooling. They divided the rock into prismatic blocks and; therefore, pinnacle peaks are common as a result of intersecting different Joint systems. Conversely, joint systems that characterize the sedimentary rocks are of planer or like-strike joint set. They are parallel to bedding planes and influenced by another orthogonal joint set. They produce together joint-blocks about ±1 m width and; therefore, the cap rocks are become vulnerable to move downslope.

References:

Abdeen, M. M & Greiling, R. O. (2005) A quantitative structural study of late Pan-African compressional deformation in the Central Eastern Desert (Egypt) during Gondwana assembly. *Gondwana Research, V. 8, No. 4, pp. 457-471.*

Abdel-Gawad, M. (1969) New evidence of transcurrent movements in Red Sea area and Petroleum implications. *The American Association of Petroleum Geol. Bull. V. 53, No. 7, pp. 1466-1479.*

Abdel-Rahman, A-F. M. (1995) Tectonic -magmatic stages of shield evolution: the Pan-African belt in northeastern Egypt. *Tectonophysics, Vol. 242, pp. 223-240.*

Ait Brahim, L., Chotin, P., Tabyaoui, H., & Abdelouafi, A. (2000) The use of microtectonic and satellite data (SPOT, ERS1) to create a deformation model for the Rifain foreland (Bèni Snassen Mounts, Morocco) during the Mio-Pliocene. *Photo Interprètation images aèriennes et spatiales, Editions ESKA, Paris, vol. 38, pp. 27-29.*

Akhir, J. M. & Abdullah, I. (1997) Geological applications of Landsat thematic mapper imagery: mapping and analysis of lineations in NW Peninsula Malaysia. *http://www.gis-development.-net/aars/acrs/1997/ts10/ts10001.shtml (Accessed on 13 April 2005).*

Akkad, M. K. & Abu El Ela, A. M. (2002) Geology of the basement rocks in the eastern half of the belt between latitudes 25º 30` and 26º 30` N. Central Eastern Desert, Egypt. *Geological Survey of Egypt, Cairo. Paper No. 78, 118 p.*

Balk, R. (1948) Structural behaviour of igneous rocks. *J.W. Edwards Broths. Michigan,177 p.*

Ball, J. (1913) Topography and geology of the phosphate districts of Safaga (Eastern Desert of Egypt). *Egypt. Surv., Dept., Cairo, 19 p.*

Barron, T. & Hume, W. F. (1901) Notes on the geology of the Eastern Desert of Egypt. *Egyptian Geol. Magazine, Vol. VIII, No. 4. Cairo*.

Beadnell, H. J. L. (1924) Report on the geology of the Red Sea coast between Qoseir and Wadi Ranga. *Petroleum Research Bull. No. 13, Government Press, Cairo. 37 p.*

Beniamin, N. Y., Youssef, M. M., Azzam, H. M., Mahmoud, M. H., Salama, A. M. & Abd El Migid, A. (2005) On the main tectonic features of the central and northern Eastern Desert, Egypt. *Ministry of Petroleum, Egyptian Mineral Resources Authority, Regional Geology Department, 77 p.*

Berlin, G. L., Chavez, P. S., Grow, T. E. & Soderblom, L. A. (1976) Preliminary geologic analysis of southwest Jordan from computer enhanced Landsat 1 image data. In: proceedings, American Society of Photogrammetry. *Bethesda, MD: American Society of Photogrmmetry, pp. 543-563.*

Bishta, A. Z. & El-Tarras, M. M. (2002) Integration Landsat-7 ETM+, aero-radiometric and aeromagnatic data to delineate the tectonic framework of Dihmit district, South Eastern Desert, Egypt. *Egypt. J. Remote Sensing & Space Sci., v. 5, pp. 41-62.*

Briere, P. R. & Scanlon, K. M. (2001) Lineaments and lithology derived from a side-looking airborne radar image of Puerto Rico. *USGS Science for a changing world, http://pubs.usgs.gov /of /of00-006/htm/lineament.htm (Accessed on 23 May 2005).*

Campbell, J. B. (1996) Introduction to remote sensing. *2ed. Ed., the Guilford Press, New York, 622p.*

Clark, C. D. & Wilson, C. (1994) Spatial analysis of lineaments. *Comput. Geosci. 20, pp. 1237-1258.*

Clayton, P. A. (1933) The western side of the Gilf Kebir. *Geog. Jour. Vol.81, No.3, pp. 254.259.*

Davis, G. H. & Reynolds, S. J. (1996) Structural geology of rocks and regions. *2ed. edition, John Wiley & Sons, Inc. New York, 776 p.*

Department of the Army, US Army Crops of Engineers (2003) Engineering and design remote sensing. *Manual No. 1110-2-2907. Washington, DC 20314-1000.*

Drury, S. A. (1993) Image interpretation in geology. *Chapman & Hall, London, 2ed edition, 283 p.*

El Rakaiby, M. L. (1984) Geological and structural studies of South Central Sinai, Egypt. *Science Research Series, Vol. IV, Middle East Research Center, Ain Shams Univ., Cairo, pp. 91-111.*

El Rakaiby, M. L. (1997) Remote sensing studies for dyke swarms in the central Eastern Desert of Egypt. *Journal of African Earth Sciences, Vol. 24, No. 4, pp. 653-656.*

El-Akkad, S. & Dardir. A. A. (1966b) Geology and phosphate deposits of Wasif-Safag area. *Geological Survey, Egypt, Paper no. 36*.

El-Etr, H. A. & Abdel Rahman, M. A. (1974) Airphoto lineations of the Southern Part of the Gulf Suez region, Egypt. *Proceedings of the first international conference on the new basement tectonics, Utah Geological Association, Pub. 5. Chapter 7. Africa and Middle East, Utah, pp. 309-326.*

El-Sayed, M. M., Mohamed, F. H., Furnes, H. & Kanisawa, S. (2002) Geochemistry and petrogenesis of the Neoproterozoic granitoids in the Central Eastern Desert, Egypt. *Chemie der Erde Geochemistry, 62. Urban & Fischer Verlag, pp. 317-346.*

Embabi, N. S. (2004) The geomorphology of Egypt: landforms and evolution. *Vol. 1, The Egyptian Geographical Society, Cairo, 447p.*

ENVI Tutorials (2003) RSI. *(Research System Inc), 658 p.*

Fisher, B. (2004) Surface curvature. *http://homepages.inf.ed.ac.uk/rbf/BOOKS/FSTO/node28.html#Fig6.10.ps (Accessed on 12 October 2005).*

Fowler, T. J. (2001) Pan-African granite emplacement mechanisms in the Eastern Desert, Egypt. *Journal of African Earth Sciences, Vol. 32, No. 1, pp. 61-86.*

Francis, M. H. (1972) Geology of the basement complex in the north Eastern Desert between latitudes 27˚30̀ and 28˚ 00̀ N. *Annals of the Geological Survey of Egypt, Vol. II, pp. 161-180.*

Gomaa, M. A. (1992) Hydrological studies between Quseir - Safaga area, Eastern Desert, Egypt. *M.Sc. Thesis. Fac. Sci., Ain Shams University, 150 p.*

Hammad, F. A. & Eweida, E. A. (1989) Structure and drainage lineation analysis of the Quseir area. Egypt. *J. Geol. Vol. 33, 1-2, pp. 325-346.*

Hassan, M. A. & Hashad, A. H. (1990) Precambrian of Egypt. In: Said, R. (Ed.), The Geology of Egypt. *Balkema, Rotterdam, pp. 201-245.*

Hobbs, W. H. (1904) Lineaments of the Atlantic border region. *Geological Society American Bulletin, 15, pp. 483-506.*

Issawi, B., Francis, M., El Hinnawy, M., Mehanna, A. & El Deftar, T. (1971) Geology of Safaga-Quseir coastal plain and of Mohamed Rabah area. *Ann. Geol. Surv. Egypt. Vol. 1. 19 p.*

Jarrar, G. (2001) Dike swarms in Jordan and Sinai related to the Red Sea rifting. In: Rupturing of continental lithosphere in the Red Sea/Gulf of Suez. *March 17-23, Sharm el-Sheikh, Sinai, Egypt.*

Jensen, J. R. (2000) Remote sensing of the environment. *Upper Saddle River, NJ: Prentice Hall, 544 pages.*

Jordan, G. (2004) Terrain modelling with GIS for tectonic geomorphology. *ACTA Universitatis Upsaliensis, 42 p.*

Jordan, G., Meijninger, B.M.L., van Hinsbergen, D.J.J., Meulenkamp, J.E., & Van Dijk, P.M. (*in press***)** Extraction of morphotectonic features from DEMs: Development and applications for study areas in Hungary and NW Greece. *International Journal of Applied Earth Observation and Geoinformation.*

Khalil, S. M. & McClay, K. R. (2002) Extensional fault-related folding, northwestern Red Sea, Egypt. *Journal of Structural Geology, vol. 24, pp. 743-762.*

Kocal, A., Duzgun, H. S. & Karpuz, C. (2004) Discontinuity mapping with automatic lineament extraction from high resolution satellite imagery. *http://www.isprs.org-/istanbul2004/comm/papers/205.pdf#search='discontinuity%20mapping%20with%20automatic%20lineament%20extraction' (Accessed on 23 May 2005).*

Korrat, I. M., El Agami, N. L., Hussein, H. M. & El-Gabry, M. N. (2005) Seismotectonics of the passive continental margins of Egypt. *Journal of African Earth Sciences 41, Elsevier, pp. 145-150.*

Legeley-Padovani, A. & Mering, C. (1997) Apport des opèrateures de morphologie mathèmatique a l'extr-action des failles á partir d' images SPOT panchromatique – exemple de la faille de Hualca-Hualca (Sud Perou). *Photo Interprètation images aèriennes et spatiales, Editions ESKA, Paris, vol. 35, pp. 209-017.*

Leica Geosystems (2003) Erdas field guide. 7th edition, *Leica Geosystems GIS & Mapping, LLC, Georgia. 627 p.*

Lillesand, T. M. & Kiefer, R. W. (2000) Remote sensing and image interpretation. *John Wiley & Sons, Inc., New York, 724 p.*

Meneisy, M. Y. (1990) Volcanicity. In: Said, R. (Ed.) The geology of Egypt. Balkama, *Rotterdam, Netherlands, pp. 157-172.*

Mercier, N. Valladas, H. & Froget, L. (1999) Thermoluminescence dating of a Middle Palaeolithic occupation at Sodmein Cave, Red Sea Mountains (Egypt). *Journal of Archaeological Science, Vol. 26, pp. 1339-1345.*

Miyatake, Sh. (2002) Regional linea-ment analysis for intrusive-related copper exploration in the Myanmar central volcanic belt. *http://www.gisdevelopment.net/aars/acrs/2002-/pos3/039.pdf#search='regional% 20 lineament %20analysis' (Accessed on 10 March 2005).*

Moeyersons, J., Vermeersch, P. M., Beeckman, H. & Van Peer, P. (1999) Holocene environmental changes in the Gebel Umm Hammad, Eastern Desert, Egypt. *Geomorphology, vol. 26. pp. 297-312.*

Moeyersons. J. Vermeersch. P.M. & Van Peer, P. (2002) Dry cave deposits and their palaeoenvironmental significance during the last 115 ka, Sodmein Cave, Red Sea Mountains, Egypt. *Quaternary Science Reviews, Vol. 21, pp.837–851.*

Moore, G. K. & Waltz, F. A. (1983) Objective procedures for lineament enhancement and extraction. *Photogrammetric Engineering and Remote Sensing. Vol. 49, pp. 641-647.*

Morgan, P. (1990) Egypt in the framework of global tectonics**.** In: Said, R. (Ed.) The geology of Egypt. Balkama, *Rotterdam, Netherlands, pp. 91-111.*

Mostafa, M. R. (1987) Wadi Firan: geomorphological study. *Unpublished M. A. Thesis (in Arabic). Dept. of Geog., Fac. of Arts, Ain Shams Univ., Cairo, 279 p.*

Moustafa, A. R. (2001) Structural setting and tectonic evolution of the Suez rift. In: Rupturing of continental lithosphere in the Red Sea/Gulf of Suez, *March 17-23, Sharm el-Sheikh, Sinai, Egypt.*

O'Leary, D. W., Friedman, J. D. & Pohn, H. A. (1976) Lineament, linear lineation some proposed new standards for old terms. *Geological Society American Bulletin, 87, pp. 1463-1469.*

Peters, D. C. & Shea, V. R. (1988) Miner`s-eye view of lineaments - what's really down there. *AAPG Bull. ; Vol/Issue: 72:2; Annual meeting of the American Association of Petroleum Geologists; 20-23 Mar 1988; Houston.*

Philobbos, E. R. & Hassan, K. D. K. (1975) The contribution of palaeosoil to Egyptian lithostratigraphy. *Nature 253, 33.*

Ramsay, J. G. & Huber, M. I. (1987) The techniques of modern structural geology. *vol. 2, Academic Press, London, 700 p.*

Said, R. (1962) The geology of Egypt. *Elsevier Publishing Co. Amsterdam, 377p.*

Said, R. (1990) Red Sea coastal plain. In: Said, R. (ed.) The geology of Egypt. Balkama, *Rotterdam, Netherlands, pp. 345-359.*

Schürmann, H. M. E. (1949) The basement rocks of the northern part of the Eastern Desert of Egypt. *Bull. Soc. Geograph. Egypt, 23: pp. 35-61.*

Shabana, A. R. A. (1998) Geology of water resources in some catchment areas draining in the Gulf of Aqaba, Sinai-Egypt. *Unpub. M. Sc. Thesis, Geol. Dept. Faculty of Science, Ain Shams University, 261 p.*

Short, N. M. (2006) Remote sensing tutorial: lineaments and fractures. *http://rsd.gsfc-.nasa.gov/rsd/RemoteSensing.html (Accessed on 10 March 2006).*

Stevens, K. A. (1981) The visual interpretation of surface contours, in Brady (Ed.), Computer Vision*. pp 47-73, North Holland Publishing Company, Amsterdam.*

Strahler, A. & Strahler, A. (2000) Introducing physical geography. *2ed. edition, John Wiley & Sons, Inc, 536 p.*

Summerfield, M. (1991) Global geomorphology: an introduction to the study of landforms. *John Wiley & Sons Inc. New York, 537 p.*

Tectonic and Structural Geomorphology, *http://www.wou.edu/las/physci/taylor/g322/tectonic.pdf. (Accessed on 22 May 2005).*

Thornbury, W. D. (1984) Principles of geomorphology. *Wiley Eastern Limited, New Delhi, 2ed edition, 594p.*

Ünal Akman, A. & Tüfekçi, K. (2004) Determination and characterisation of fault systems and geomorphological features by RS and GIS techniques in the WSW part of Turkey. *(Accessed on 23 May 2005).*

Vaughn, R. W. (1983) A topographic approach for lineament recognition in satellite images. *Unpublished M.S. thesis. Blacksburg, VA: Virginia Polytechnic Institute, Department of Computer Science, 70 p.*

Vaumas, E. (1953) Review work: La Montagne du Sinai Central: Etude morphologique by Hassan Awad. *Geog. Revi., Vol. 43, No. 2, pp. 286-287.*

Vermeersch, P. M., Van Peer, P., Moeyersons, J. & Van Neer, W. (1994) Sodmein cave site, Red Sea Mountains (Egypt). *Sahara, Vol. 6, pp. 31-40.*

Whitten, D.G.A., & Brooks, J.A.V., (1972) The penguin dictionary of Geology. *Penguin Books, Great Britain, 514 p.*

Wilde, S.A. &Youssef, Kh. (2002) A re-evaluation of the origin and setting of the Late Precambrian Hammamat Group based on SHRIMP U-Pb dating of detrital zircons from Gebel Umm Tawat, North Eastern Desert, Egypt. *Journal of the Geological Society, 159, 595-604.*

Wood, J. (1996) The geomorphological characterisation of digital elevation models. *Ph.D Thesis, University of Leicester, 185 p.*

Wunderlich, J. (1983) Möglchkeiten und Greuzen einer geologisch-geomorphologischen und hydrogrphischen Satelliten-bildauswertung am Beispiel von Teilgebieten der Eastern Desert und des westlichen Sinai (Ägypten). *Magister-arbeit, Fachbereich Geographie, Philipps-Universität, Marburg, 137 S.*

Younes, A. I & McClay, K (1998) Role of basement fabric on Miocene rifting in the Gulf of Suez -RED SEA area, EGYPT. *http://pangea.stanford.edu/research/geomech/RFP/vol-/RFP1998/cdvolume/1998/papers/youne2/youne2.htm (Accessed on 29.August 2006).*

Zaky, Kh. S. (1999) Structural studies on rift geometry of south Safaga- Quseir tilted blocks. Northwestern part of the Red Sea, Egypt. *The first International Conference on the Geology of Africa. Vol. 1, pp. 313-330.*

4

MODELLING AND ANALYZING DRAINAGE SYSTEMS

1. Introduction

The concept of hydrological modelling is broadly applied nowadays to represent a digital simulation of drainage systems based primarily on terrain analysis and performing automation extraction of the drainage networks. The model executes, as well, stream orders, watershed and/or basin delineation, and quantifying the most important morphometric parameters of river catchment based on essential parameters such as area, length, width, and slope.

2. Terminology

▪ *A drainage system* is the pattern formed by streams, rivers, and lakes in a particular watershed. It is governed by gradients of the surface and topography whether the region is dominated by hard or soft rocks.

▪ *A drainage basin* is an area upon which water falls, gathers, and travels through the network to an outlet (Fig. 4-1). Other common terms for a drainage basin are: watershed, basin, catchment or contributing area. This area is normally defined as the total area flowing to a given outlet or pour point (ESRI, 1992). The basin is represented as a polygon in "shapefile" or vector "coverage".

▪ *A stream channel* is a conduit or watercourse carrying water and flows under gravity.

▪ *A reach* is a length of channel considered as a single hydrologic entity. It could be also defined as a length of river between two tributaries and it is represented as a polyline in "shapefile" or vector "coverage" used in the model (Tarboton, 2000).

▪ *A stream Network* is a set of connected flow lines or tributaries that are represented as polyline in "shapefile" or vector coverage.

▪ *A link or junction* is an intersected point between two or more streams. It is represented as a point feature in the data model.

▪ *A pour point* is the outlet or the point at which water flows out of an area. It is usually the lowest point along the boundary of the basin. The boundary between two basins is referred to as a drainage divide or watershed boundary (ESRI, 1992).

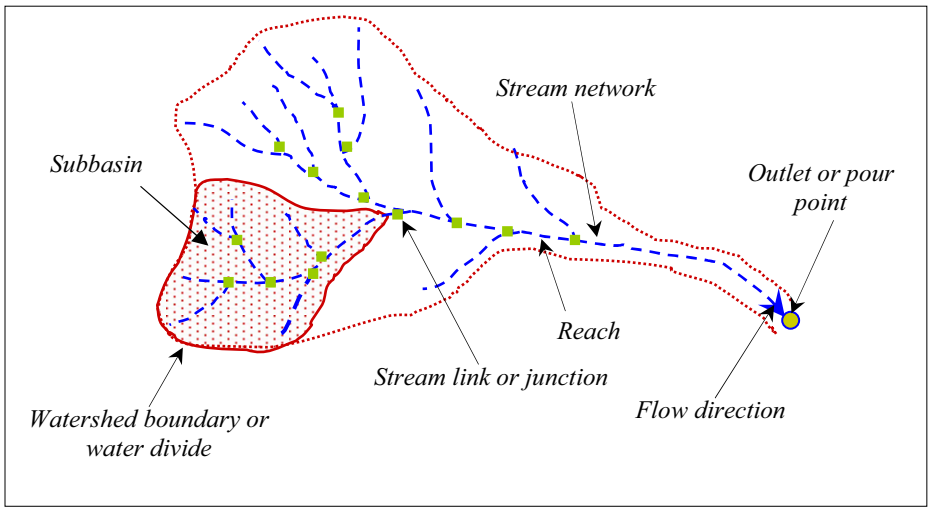

Fig. 4-1: *Drainage system components.*

3. Methodology

Hydrological model is applied in the present study according to the following steps (Fig. 4-2).

3.1. Processing Digital Elevation Model.

Using of the digital elevation model (DEM) relying on the fact that the physical characteristics of a surface determine characteristics of the water flows across it. Direction of flow is determined by the aspect, which is known as direction of the maximum rate of change in elevation and/or slope direction. Where the slope determines the energy of flow, hence the steeper slopes the higher energy of water flow and greater potential for water erosion as well.

The present study is based primarily on the processing and analyzing a pair of SRTM DTED[1] images (*N26E033* and *N26E034*) version two of 90 meters ground resolution. Using the SRTM images owing to the following reasons[2] :

[1] *Digital Terrain Elevation Data.*
[2] *SRTM editing rules: ftp://e0srp01u.ecs.nasa.gov/srtm/version2/Documentation/SRTM_edit_rules.pdf (accessed on 17 July 2006).*

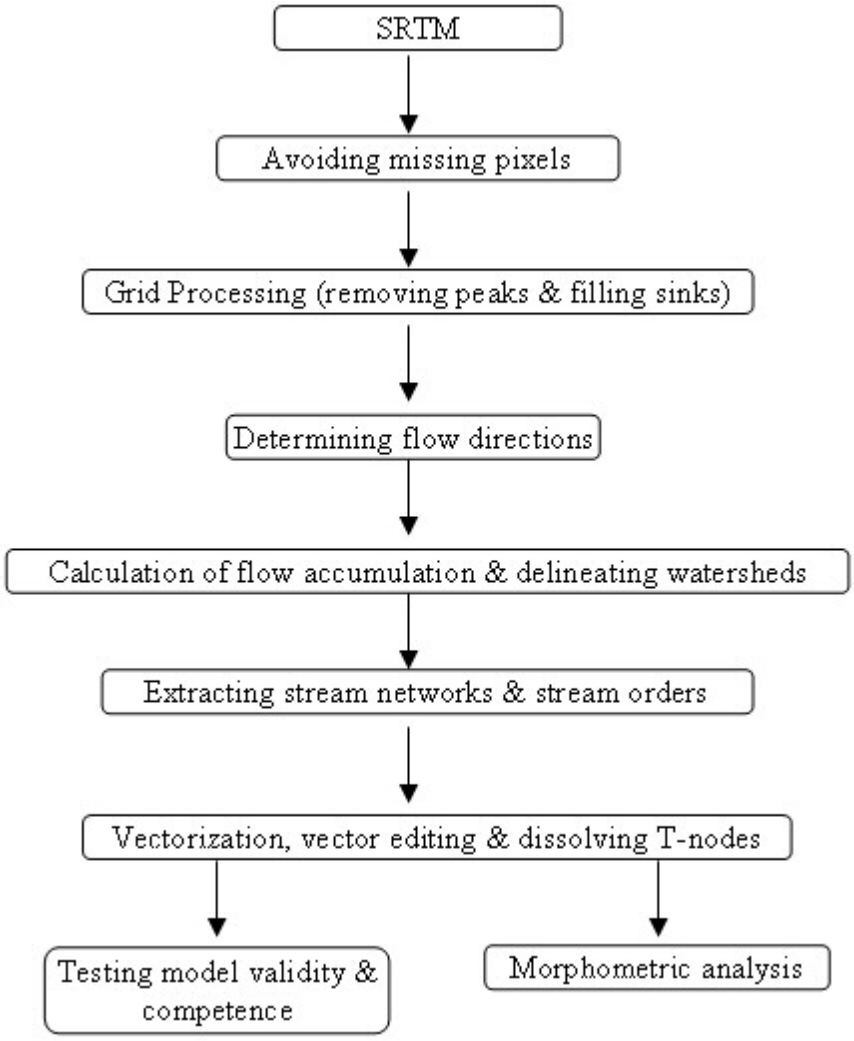

Fig. 4-2: *Scheme of the hydrological model.*

▪ Accessibility of editing feature classes and extracting the hydrological features accurately at level of detail greater than the minimum requirement.

▪ Distinguishing and extraction of flattened water bodies, such as lakes that are ≥ 600 m length and their maximum width ≥ 183 m. Therefore, lake dimensions could be simply calculated and its shoreline could be demonstrated as well.

▪ Possibility for depicting double-line drain where the river width exceeds 183 m for a length of 600 m. The depiction will end when the width of the river narrows to less than 90 m.

▪ Segregation of the coastal shoreline and coastal islands that should be at least 1 meter higher than the adjacent water.

The SRTM images are provided in HGT format as 16-bit signed integer in a simple binary raster[1]. Post-processing analysis of the DEM involved replacement and avoiding missing values, which are indicated as -32768. Missing pixels are replaced by new values interpolated from the valid neighboring pixels by using ENVI software (Fig. 4-3).

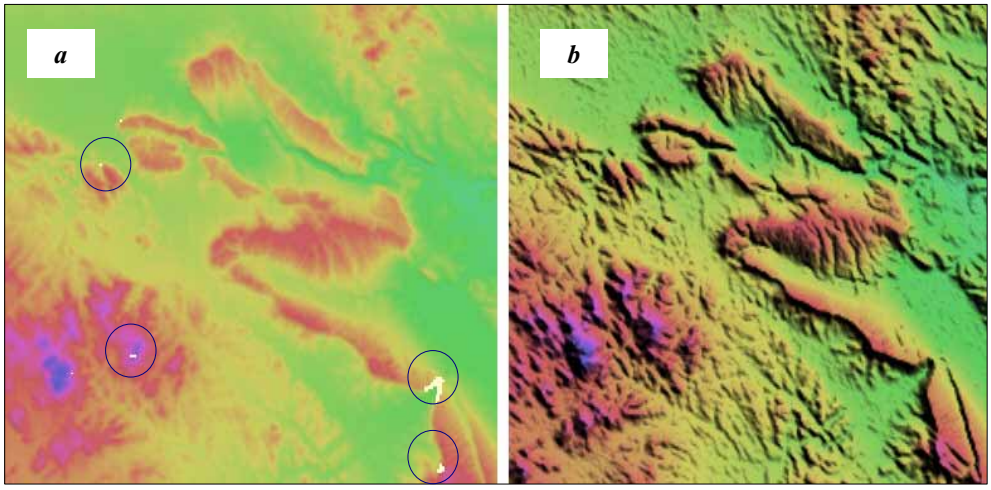

Fig. 4-3: *(a) DEM contains missing values in the circles and (b) the same DEM after avoiding missing values.*

In the view of the fact that the hydrological model, which is built-in the most analytical softwares, depends primarily on grid analysis (square or rectangular), the digital elevation model is converted into a grid of 90 x 90 meters cell size and having numeric values representing the elevation of the surface. The grid embraced little errors due to anomalies values that usually constitute either sinks or peaks (occasionally known as spikes or dams and wells or pits). A sink is a cell with undefined drainage direction; no cells surrounding it are lower, whereas a peak is a cell where no adjacent cells are higher (ARCGIS Desktop 9.1 help). They are often errors coming out as a result of insufficient or missing data, data resolution, and rounding of elevations to the nearest integer value. Although they are negligible because of the high local relief, they often exceed local true elevation differences in flatter areas of the watersheds (Mackay & Band, 1998). As well, sinks lead to discontinue the drainage

[1] *Normally known as radiometric resolution, which determines how finely a system can represent or distinguish differences of intensity, and it is usually expressed as a number of levels or a number of bits, for example 8 bits or 256 levels is typical of computer image files. The higher the radiometric resolution, the better subtle differences of intensity or reflectivity can be represented.*

network (ARCGIS Desktop 9.1 help), isolate a portion of the watershed (Tarboton, 2000), and finally giving unreliable results when calculating flow directions. Therefore, sinks should be filled to ensure proper delineation of basins and streams (Fig. 4-4).

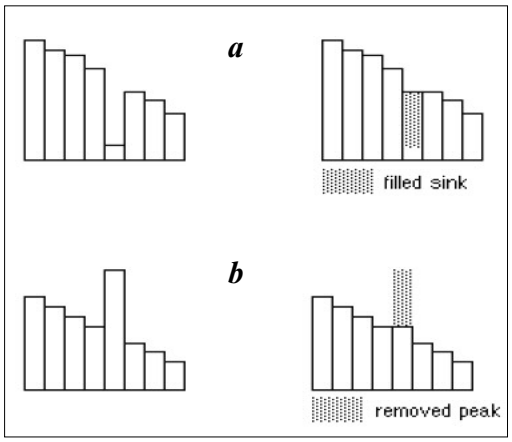

Fig. 4-4: *Grid errors: (a) profile view of a sink before and after filling and (b) profile view of a peak before and after removing.* *(Source: ARCGIS Desktop9.1 help)*

The grid consists of 1336 x 2393 cells (3.19 million cells) and 82 sinks are determined representing about 0.0026 % of the total cells. Examining each image of the mosaic separately (after replacing the missing values as formerly mentioned) revealed that sinks are insignificant (Table 4-1) in comparison with non-SDTS USGS 30-meter resolution DEMs (Tarboton et al. 1991).

Table 4-1: *Percentage of sinks in the involved SRTM images.*

Image ID	*No. Cells*	*No. Sinks*	*Sinks %*
N26E033	1201 x 1201	112	0.0077
N26E034	1201 x 1201	2	0.0001
Mosaic*	1336 x 2393	82	0.0026

* *The mosaic consisting of extractions of the upper two SRTM images.*

3.2. Determining Flow Direction.

The flow direction procedure determines the direction of flow for each cell to its steepest downslope neighbor as:

$$\textit{Change in elevation / distance} \times 100$$

The distance is determined between centers of the cells and; therefore, distance between two orthogonal cells is 90 m and between two diagonal cells is about 127 m (Fig. 4-5). It means that each extracted drainage stream will be ≥ 90 m in the case of using 1 cell as threshold for stream delineation.

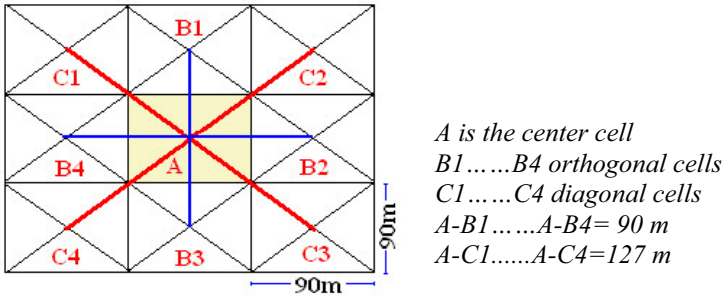

Fig. 4-5: *Determining distances between orthogonal and diagonal cell centers.*

The flow direction function is executed for every 3x3 cell neighborhood, the grid processor stops at the center of each cell and determines which neighboring cell is lowest. Depending on the direction of flow, the output grid is of an integer raster whose values range from 1 to 255. The grid is divided into eight directions, usually known as D8 flow model (Jensen & Domingue, 1988) relating to the eight adjacent cells into which flow could travel (Fig. 4-6). If the descent to all adjacent cells is the same, the neighborhood is enlarged until the steepest descent is determined. Once the direction of flow of each cell is known, it is possible to demonstrate how many cells would flow into any given cell.

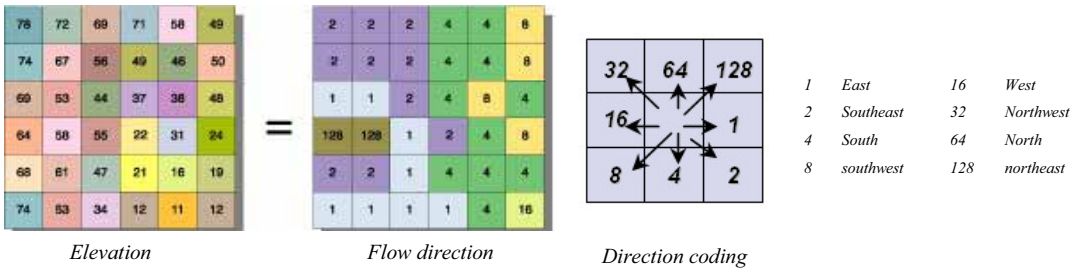

Fig. 4-6: *Determining flow direction.* *(Source: ARCGIS Desktop9.1 help)*

3.3. Calculating Flow Accumulation and Delineating Watersheds.

The flow accumulation function calculates the flow as the accumulated weight of all cells flowing into each downslope cell. Cells of high flow accumulation are areas of concentrated flow and are used to identify the main channels. According to Martinez-Casasnovas & Stuiver (1998), different threshold area values are examined for de-lineating drainage networks, of which a threshold value ≥10 cells giving the most reliable flow accumulation in the study area. Consequently, the flow accumulation layer is executed with a threshold value ≥10 cells as the minimum number of cells

required to constitute a stream and the layer is classified as well using natural breaks[1]. By this mean, the model delineates streams that are ≥900 m length and the relation is defined by multiplying the distance between two orthogonal cell centers by the threshold value.

Watershed delineation from DEM data has become standardized on the eight-direction pour point model in which each cell is connected to one of its eight neighbor cells (four on the principal axes and another four on the diagonals) according to the direction of steepest descent. Drainage basins are identified as a set of all cells draining through a given cell.

3.4. Extracting Stream Networks, Orders and Automatic Vectorization.

Stream networks are extracted by assigning the flow accumulation layer to integer values ≥ 1 for representing stream networks and *No-data* for representing the background. Thereafter, streams are ordered according to Strahler (1957) where the smallest fingertip tributaries are designated order 1. Where two first-order channels join, a channel segment of order 2 is formed; where two of order 2 join, a segment of order 3 is formed; and so forth. The trunk stream through which all discharge of water and sediment passes is the stream segment of highest order. Then, the stream order layer is assigned to an integer numbers referring to the stream orders (ARCGIS Desktop 9.1 help). Eventually, the layer is converted into contiguous vector features *(shapefile format)* with the same stream orders.

It has been observed that the model orders each *reach* as a separate stream segment and, therefore, stream numbers differ greatly from the actual stream numbers. As a result of that, law of stream numbers versus stream orders that assumed by Horton (1945) and proved by many workers (e.g. Schumm, 1957; Strahler, 1957-1964) could not be fulfilled. The problem is arisen due to stream *links* (nodes), which separating a stream of the same order into many *reaches* as a result of stream intersections. Overcoming this problem required extraction of each stream order separately and consid-

[1] *The natural breaks classes are based on natural groupings inherent in the data. The model identifies break points by picking the class breaks that best group similar values and maximize the differences between classes. The features are divided into classes whose boundaries are set where there are relatively big jumps in the data values (ARCGIS 9.1 help).*

ering such nodes as *pseudo nodes*. Once the *pseudo nodes* were determined they removed and stream lines are dissolved (Fig. 4-7).

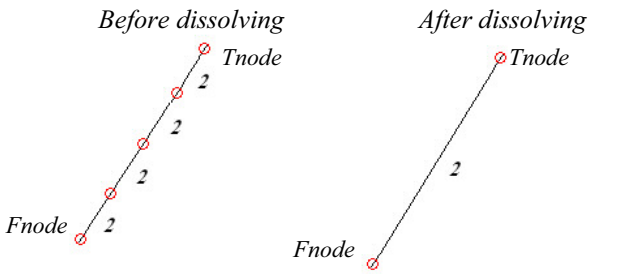

Variables	*Before dissolving*	*After dissolving*
No. nodes	5	2
No. 2nd order	4	1

Fig. 4-7: *Comparison between original and dissolved features.*

In the case of intersecting two streams of the same order, the dissolving process considers both of them as one line. In this case, such lines are separately selected and a new node is re-allocated to separate between both of them. Although the process is of time consuming, it is worthy mentioning where the results are much accurate as can be shown in figure 4-8.

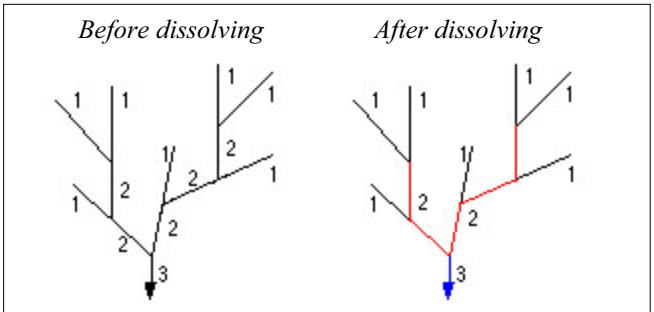

Stream orders	*No. streams*	
	Before dissolving	*After dissolving*
1st	7	7
2nd	5	2
3rd	1	1

Fig. 4-8: *Number of streams before and after dissolving.*

4. Model Validity and Competence

Assessment of using SRTM images for modelling small-scale hydrographs could be sustained in comparison with topographic maps of scales 1:100.000 and 1:50.000. The maps are scanned and geometrically co-registered exactly to the same coordinate system and projection of the SRTM image. Stream networks of eight drainage basins (i.e. Barud, Naqarah, Umm Iffinah, Safaga, Gasus, Abu Shiqayli, Queih and Ambagi) varying in drainage areas and stream numbers are manually digitized and ordered in accordance with Strahler method. The study assumed that drainage area is a constant variable that would not change from data source to another. Stream numbers as well as stream lengths are expressed as independent variables obtained from the involved data sources for each stream order separately. On the other hand, average stream length, drainage density, stream frequency and bifurcation ratio are considered as dependent variables, which would vary corresponding to the independent variables. The study concerns primarily in variance analysis of independent and dependent variables for demonstrating differences and/or similarities among the available data sources and proving the competence of simulating hydrological model using the SRTM image for such small-scale drainage systems.

4.1. Variable Analysis.

Table 4-2 is showing changes of the independent variables (stream numbers and lengths) obtained from the SRTM image and the topographic maps. Noticeable dissimilarity could be stated as follows:

- Stream orders revealing significant differences between the SRTM image and the topographic map 1:100.000 obviously in wadis Barud, Naqarah, Umm Iffinah, Safaga, Queih and Ambagi. As a result of that, orders of the trunk stream vary from data source to another. However, noticeable, though small, similarities in stream orders between the SRTM and the topographic map 1:50.000 are deduced with the exception of wadi Umm Iffinah.
- Stream numbers clarifying greatly variations specifically in low orders (e.g. first and second orders) and the total stream numbers considerably vary from data source to one another.

Table 4-2: *Independent variables analysis.*

Wadi	Source	Nu							∑N	∑Lu							∑L
		1st	2ed	3rd	4th	5th	6th	7th		1st	2ed	3rd	4th	5th	6th	7th	
Barud	SRTM	1473	244	54	13	3	1		1788	780.69	292.8	137.7	73.06	43.325	28.1		1355.7
	1:100.000	325	83	18	5	1			432	529.75	136.95	61.02	33.9	36.37			797.99
	1:50000	1910	449	108	24	5	1		2497	872.6	361.5	176	72.13	43.4	35.7		1561.3
Naqarah	SRTM	170	39	8	2	1			220	67.83	38.789	16.762	2.198	12.655			138.23
	1:100.000	31	5	2	1				39	14.88	9.8	5.5	9.3				39.48
	1:50000	170	46	12	3	1			232	98	36	17	3.5	13			167.5
Umm Iffinah	SRTM	86	13	2	1				102	35.26	14.69	10.5	7.18				67.63
	1:100.000	12	3	1					16	17.04	5.49	8.7					31.23
	1:50000	78	20	5	2	1			106	43.68	12.4	9.1	6.3	5.9			77.38
Safaga	SRTM	2137	1000	486	22	6	2	1	3654	921.8	1285.7	1403.8	153.79	50.039	28.814	22.557	3866.5
	1:100.000	375	91	25	5	2	1		499	720.75	209.3	98.55	18.2	38.572	20.122		1105.5
	1:50000	2656	637	156	41	12	3	1	3506	1336	510	280.6	169.8	67	22	45.8	2431.2
Gasus	SRTM	469	94	25	5	1			594	195.57	112	48.713	22.666	19.338			398.29
	1:100.000	120	34	9	3	1			167	141.36	42.704	22.5	10.95	18.399			235.91
	1:50000	506	115	30	6	1			658	277.4	85.3	36.8	28	18.4			445.9
Abu Shiqayli	SRTM	493	104	21	8	1			627	212.88	109.2	58.38	28.849	20.25			429.56
	1:100.000	149	38	11	4	1			203	153.47	34.2	27.94	6.28	15.57			237.46
	1:50000	460	109	24	7	1			601	231.84	83.93	33.6	14.7	20.17			384.24
Queih	SRTM	5425	902	214	45	11	4	1	6602	2170	1082.4	535	265.5	92.4	88.4	56.6	4290.3
	1:100.000	1800	401	99	24	5	1		2330	2214	637.59	275.32	121.68	85.87	49.243		3383.7
	1:50000	7327	1766	400	94	22	4	1	9614	3613	1375.1	640.4	289.5	155.47	90.5	52.3	6216.3
Ambagi	SRTM	10857	1696	378	105	24	4	1	13065	3018.3	1201.9	630	320.5	112.1	133.5	20.5	5436.8
	1:100.000	1109	285	64	14	3	1		1476	155.26	478.8	198.4	100.8	84.66	15.09		1033
	1:50000	3214	711	209	43	8	2	1	4188	893.49	186.99	317.26	123.04	37.36	66.74	20.49	1645.4

Nu Stream numbers
∑N Sum of stream numbers
∑Lu Stream lengths
∑L Sum of stream lengths

▪ Likewise, length of streams of each order differs greatly and equally the total stream length.

▪ The dependent variables involved in the analysis (average stream length, drainage density, stream frequency, and bifurcation ratio) revealing significant differences since they considerably depending on to the former variables (Table 4-3).

4.2. Variance Analysis.

Competence of the model is sustained by computing the coefficient of variation C_v to demonstrate variances and/or convergences of the hydrological data obtained from the SRTM image versus the data obtained from the topographic maps. The coefficient of variation is expressed as a dimensionless number allows comparison of the variation of populations that have significantly different mean values. It is often used when discussing the normal distribution for positive mean values with a standard deviation significantly less than the mean. The coefficient is defined according to the following equation:

$$C_v = \sigma/\mu$$

Where: σ = standard deviation and μ= arithmetic mean.

When the mean value is near zero, the coefficient of variation is sensitive to change in the standard deviation, limiting its usefulness. Distributions with $C_v < 1$ are of low-variance, while those with $C_v > 1$ are of high-variance.

The coefficient of variation is computed for the total stream numbers ΣN and the total stream lengths ΣL for the SRTM data versus the topographic maps 1:100.000 and 1:50.000 respectively (Table 4-4). The coefficient of the SRTM data versus the topographic map 1:100.000 varies between 0.67 for wadi Queih and 1.12 for wadi Ambagi. Three wadis indicating high variance since their C_v is higher than 1; they are: wadis Umm Iffinah, Safaga and Ambagi. On the other hand, the coefficient of the SRTM versus the topographic map 1:50.000 varies from 0.027 for wadi Umm Iffinah and 0.728 for wadi Ambagi indicating low variance since it is less than 1.

Comparison of the C_v values (columns 4 and 7 in table 4-4) reveals that the SRTM image is not only of low variance from the topographic map 1:50.000 (Fig. 4-9), but also it is providing more details in stream numbers specifically in the lower stream orders.

Concerning the total stream length (Table 4-5) the C_v of the SRTM data versus the topographic map 1:100.000 varies between 0.16 for wadi Queih and 0.96 for wadi Ambagi. The C_v of the SRTM data versus the topographic map 1:50.000 vary from 0.07 for wadi Abu Shiqaily and 0.75 for wadi Ambagi. Generally, both of them reveal low variance since the C_v values are less than 1, but the coefficient is relatively smaller for the topographic map 1:50.000 indicating relatively convergence to the SRTM data than the topographic map 1:100.000 (Fig. 4-10).

Table 4-3: *Dependent variables analysis.*

Wadi	***Source***	***Ĺu km***							***D_d***	***F_s***	***R_b***
		1st	*2ed*	*3rd*	*4th*	*5th*	*6th*	*7th*			
Barud	SRTM	0.53	1.20	2.55	5.62	14.44	28.10		2.67	3.52	5.74
	1:100.000	1.63	1.65	3.39	6.78	36.37			1.57	0.85	4.03
	1:50000	0.46	0.81	1.63	3.01	8.68	35.70		3.07	4.91	4.25
Naqarah	SRTM	0.40	0.99	2.10	1.10	12.66			2.53	4.02	4.40
	1:100.000	0.48	1.96	2.75	9.30				0.72	0.71	5.36
	1:50000	0.58	0.78	1.42	1.17	13.00			3.06	4.24	3.73
Umm Iffinah	SRTM	0.41	1.13	5.25	7.18				2.63	3.97	6.48
	1:100.000	1.42	1.83	8.70					1.22	0.62	3.78
	1:50000	0.56	0.62	1.82	3.15	5.90			3.01	4.12	3.80
Safaga	SRTM	0.43	1.29	2.89	6.99	8.34	14.41	22.56	5.15	4.87	4.08
	1:100.000	1.92	2.30	3.94	3.64	19.29	20.12		1.47	0.66	4.04
	1:50000	0.50	0.80	1.80	4.14	5.58	7.33	45.80	3.24	4.67	4.12
Gasus	SRTM	0.42	1.19	1.95	4.53	19.34			2.54	3.79	4.79
	1:100.000	1.18	1.26	2.50	3.65	18.40			1.50	1.06	3.55
	1:50000	0.55	0.74	1.23	4.67	18.40			2.84	4.20	4.32
Abu Shiqayli	SRTM	0.43	1.05	2.78	3.61	20.25			2.54	3.71	4.73
	1:100.000	1.03	0.90	2.54	1.57	15.57			1.40	1.20	3.76
	1:50000	0.50	0.77	1.40	2.10	20.17			2.27	3.55	4.27
Queih	SRTM	0.40	1.20	2.50	5.90	8.40	22.10	56.60	2.27	3.49	5.69
	1:100.000	1.23	1.59	2.78	5.07	17.17	49.24		1.79	1.23	4.40
	1:50000	0.49	0.78	1.60	3.08	7.07	22.63	52.30	5.08	5.08	4.20
Ambagi	SRTM	0.28	0.71	1.67	3.05	4.67	33.38	20.50	3.60	8.64	6.03
	1:100.000	0.14	1.68	3.10	7.20	28.22	15.09		0.68	0.98	4.02
	1:50000	0.49	0.78	1.60	3.08	7.07	22.63	52.30	1.09	2.77	4.34

Ĺu *average stream length, km.* ***D_d*** *drainage density.*
F_s *stream frequency.* ***R_b*** *bifurcation ratio.*

Eventually, the results permit the conclusion that the SRTM image is suitable for modelling such small-scale drainage basins and it is virtually similar to the topographic map of scale 1:50.000 generally.

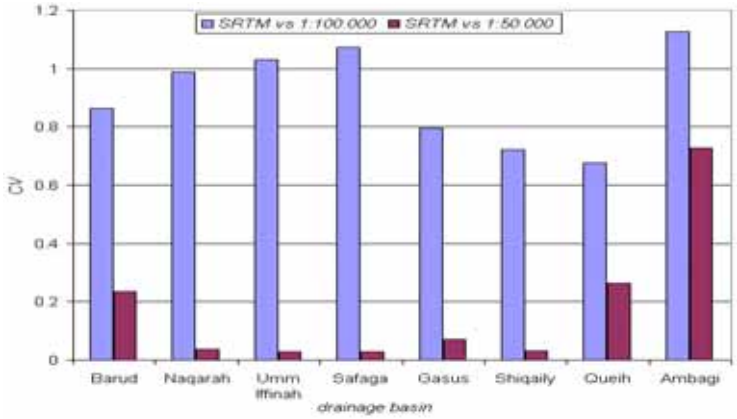

Fig. 4-9: *Coefficient of variation of the total stream numbers.*

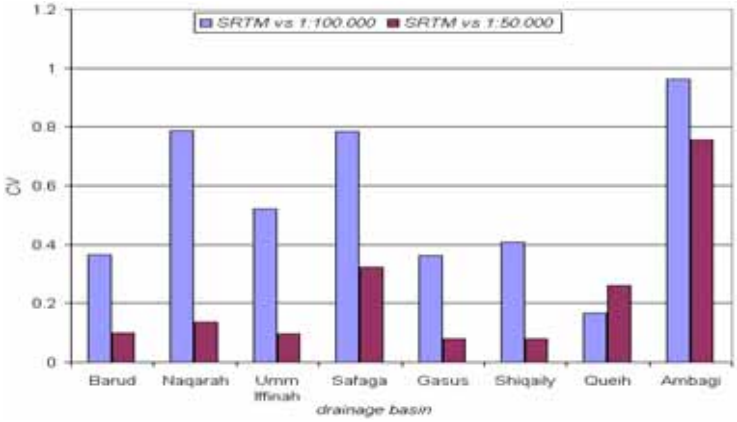

Fig. 4-10: *Coefficient of variation of the total stream lengths.*

Table 4-4: *Coefficient of variation of the total stream numbers.*

Wadis	***SRTM vs 100.000***			***SRTM vs 50.000***		
	μ	σ	Cv	μ	σ	Cv
Barud	1110	958.837	0.864	2142.5	501.339	0.234
Naqarah	129.5	127.986	0.988	226	8.485	0.038
Umm Iffinah	59	60.811	1.031	104	2.828	0.027
Safaga	2076.5	2230.922	1.074	3580	104.652	0.029
Gasus	380.5	301.935	0.794	626	45.255	0.072
Shiqaily	415	299.813	0.722	614	18.385	0.030
Queih	4466	3020.760	0.676	8108	2129.806	0.263
Ambagi	7270.5	8194.660	1.127	8626.5	6276.987	0.728

Table 4-5: *Coefficient of variation of the total stream lengths.*

Wadi	*SRTM vs 100.000*			*SRTM vs 50.000*		
	μ	σ	C_V	μ	σ	C_V
Barud	1076.83	394.34	0.366	1458.50	145.41	0.100
Naqarah	88.85	69.82	0.786	152.86	20.69	0.135
Umm Iffinah	49.43	25.73	0.521	72.50	6.89	0.095
Safaga	2485.97	1952.30	0.785	3148.83	1014.88	0.322
Gasus	317.10	114.82	0.362	422.09	33.66	0.080
Shiqaily	333.51	135.82	0.407	406.90	32.04	0.079
Queih	3837.00	641.06	0.167	5253.28	1361.86	0.259
Ambagi	3234.88	3113.91	0.963	3541.06	2680.90	0.757

5. Drainage Basins

Drainage basins and networks, which have been extracted using the model, are from north to south as follows:

5.1. El Barud.

Wadi El Barud extends about 508 km² (9.5 % of the total drainage area) and 51.24 km in length along its principle stream channel that attains the 6th order. The wadi drains the younger granite of Jabal El Barud (1338 m) and the relatively low surrounding mountains such as Jabal Umm Taghir at-Tahtani (599 m) and Jabal Ras Abda (608 m). Wadi El Barud flows from west to east generally adhering to the dominant structural weakness that trending WNW-ESE and NE-SW respectively. The main channel is bifurcated into two sub-channels; they are: wadi El Barud in the north and wadi Umm Taghir in the south. The later one is occupied by Safaga – Qena highway. Both tributaries get together before the trunk stream cuts through the northern margins of Jabal Naqarah for debouching into the Red Sea at Safaga City.

The dominant drainage pattern of wadi El Barud is dendritic and sub-dendritic (Fig. 4-11), where its tributaries are irregularly branching in many directions and at almost any angle considerably less than right angle (Zernitz, 1932; Thornbury, 1984). It is a result of the uniform resistance of the granite rocks. Parallel and sub-parallel patterns noticeably characterise the upstream area where the lower stream orders surprisingly descending from the mountains. The pattern is less commonly trellis and rectangular as well (Yehia et al. 1999).

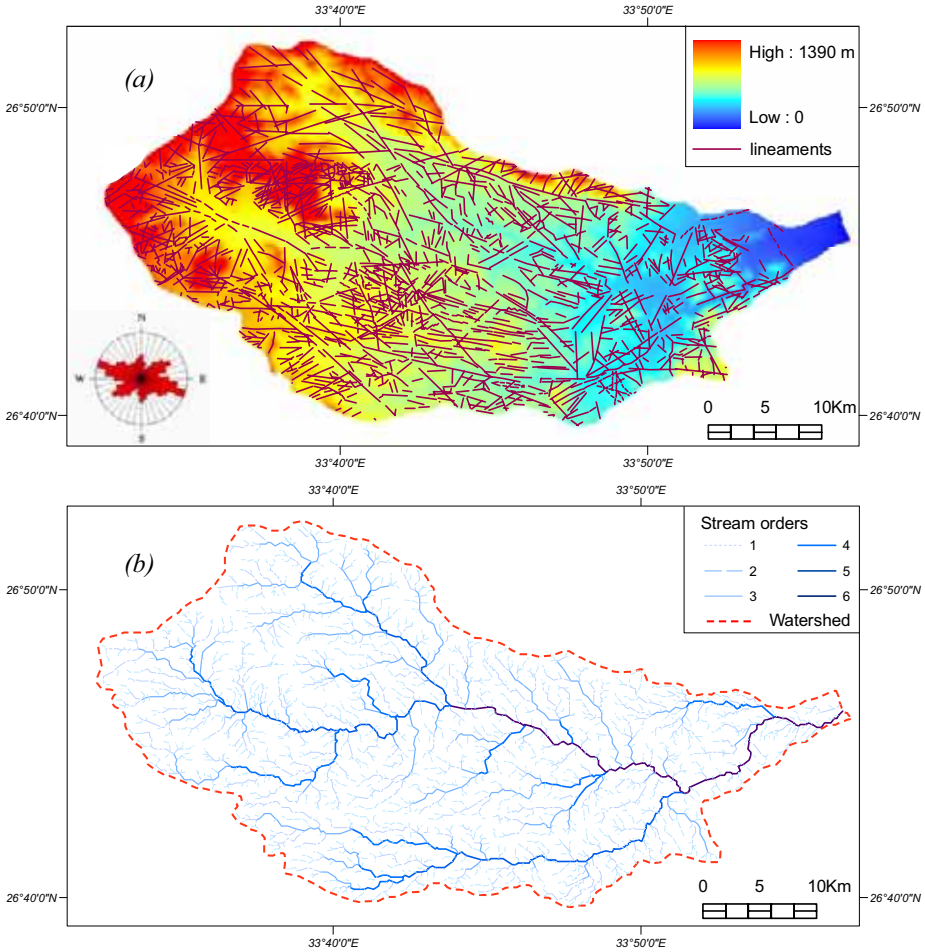

Fig. 4-11: *Wadi El Barud: (a) DEM and linear features and (b) watershed and drainage network.*

5.2. Abu Asala.

Wadi Abu Asala is the smallest drainage basin in the study area occupying about 16.72 km² (0.3 % of the total drainage area). The trunk stream is of the 4th order and attains about 8.24 km in length. The wadi drains Jabal Naqarah (833 m) and it is inferred that the trunk stream adheres to lateral or strike-slip fault extends E-W. Dendritic drainage pattern dominates specifically at the upstream area (Fig. 4-12).

5.3. Naqarah.

Wadi Naqarah occupies about 54.73 km² (1.03 % of the total drainage area) and the trunk stream attains about 18.28 km in length and it is of the 5th order. The wadi drains the southern half of Jabal Naqarah adhering to the contact line between the felsite rocks dominating Jabal Naqarah and the younger granite. Accordingly, the wadi is seemingly annular or ring-like in pattern (Zernitz, 1932) for the reason that

the trunk stream detours around Jabal Naqarah owing to structure influences (Fig. 4-13).

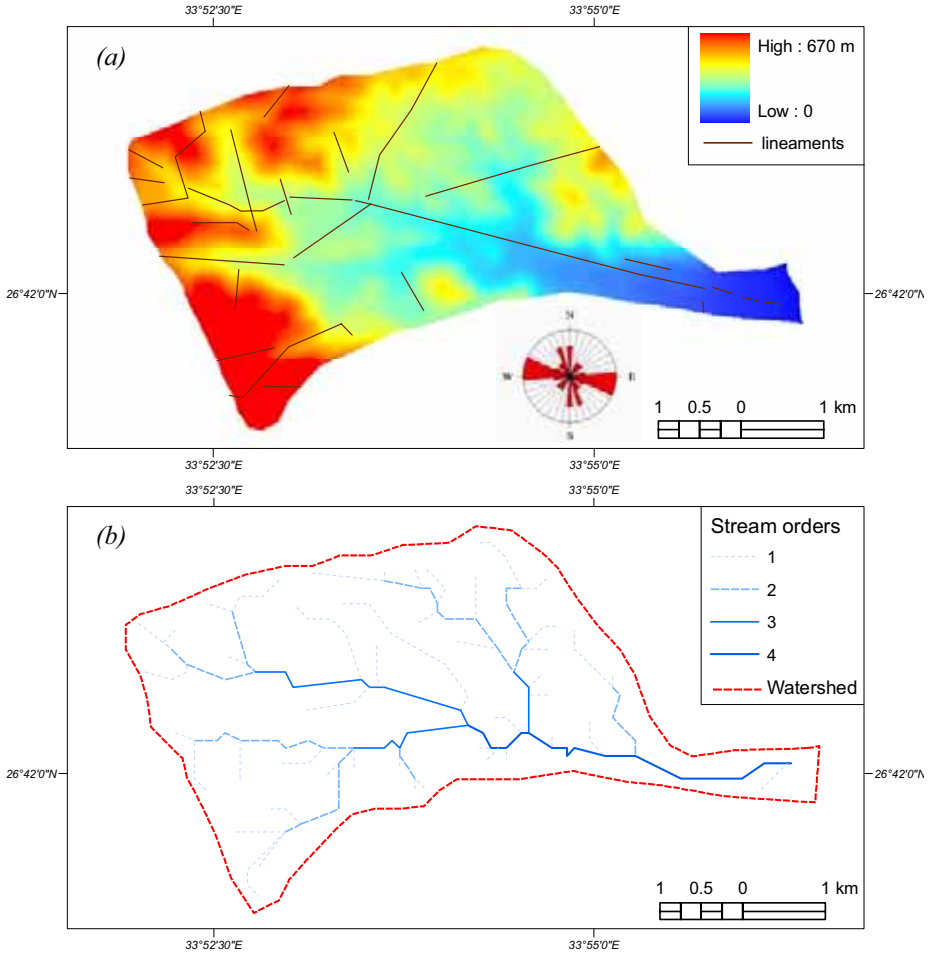

Fig. 4-12: *Wadi Abu Asala: (a) DEM and linear features and (b) watershed and drainage network.*

5.4. Umm Iffinah.

Wadi Umm Iffinah covers an area about 25.7 km² (0.48 % of the total drainage area) and the trunk stream is about 16 km in length and belonging to the 4th order. The wadi drains the Red Sea terrain and cuts along the rock boundaries among the older granite, intermediate metavolcanics, and gabbro. Drainage network is mostly parallel to sub-parallel pronouncing regional structure and slope controls (Fig. 4-14).

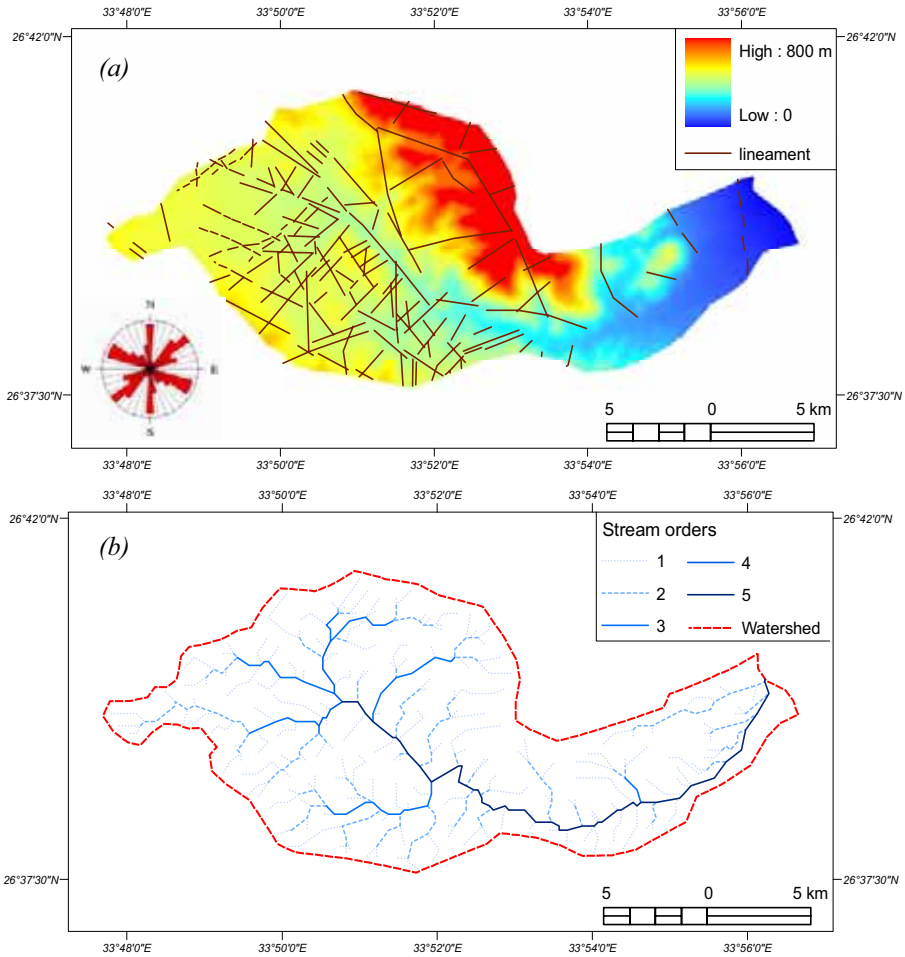

Fig. 4-13: *Wadi Naqarah: (a) DEM and linear features and (b) watershed and drainage network.*

5.5. Safaga.

Wadi Safaga is one of the largest drainage basins of the study area that covers about 750.4 km² (14.1 % of the total drainage area). The trunk stream extends generally from west to east about 68.42 km in accordance with the main structures and rock contacts and attains the 7th order (Fig. 4-15). The wadi drains primarily the Red Sea terrain and, to a lesser degree, the uplifted tablelands of Mohamed Rabah, Wasif, and the coastal tablelands. The basin includes several mountainous peaks such as Umm Taghir el-Fuqani (900 m), Abu Firad (1029 m), Jabal Umm al-Hawaytat (485 m), hills of Mohamed Rabah (435 m), and hills of Wasif (443 m).

Obviously, wadi Safaga is structurally controlled and cuts through a great variety of basement and sedimentary rocks, which led the trunk stream to bend several times at various directions before debouching into the sea. Some of its linkages are at right

angles such as wadi Talat el-Zarqa, indicating structure constraints. The wadi is bifurcated into three major tributaries; that are:

1.Wadi Mohamed Rabah in the north that drains Jabal Abu Firad and Mohamed Rabah hills. It flows commonly NW-SE and N-S in accordance with the major faults. It has been inferred that the wadi is an antecedent one since it maintains its water course through the uplifted hills of Mohamed Rabah.

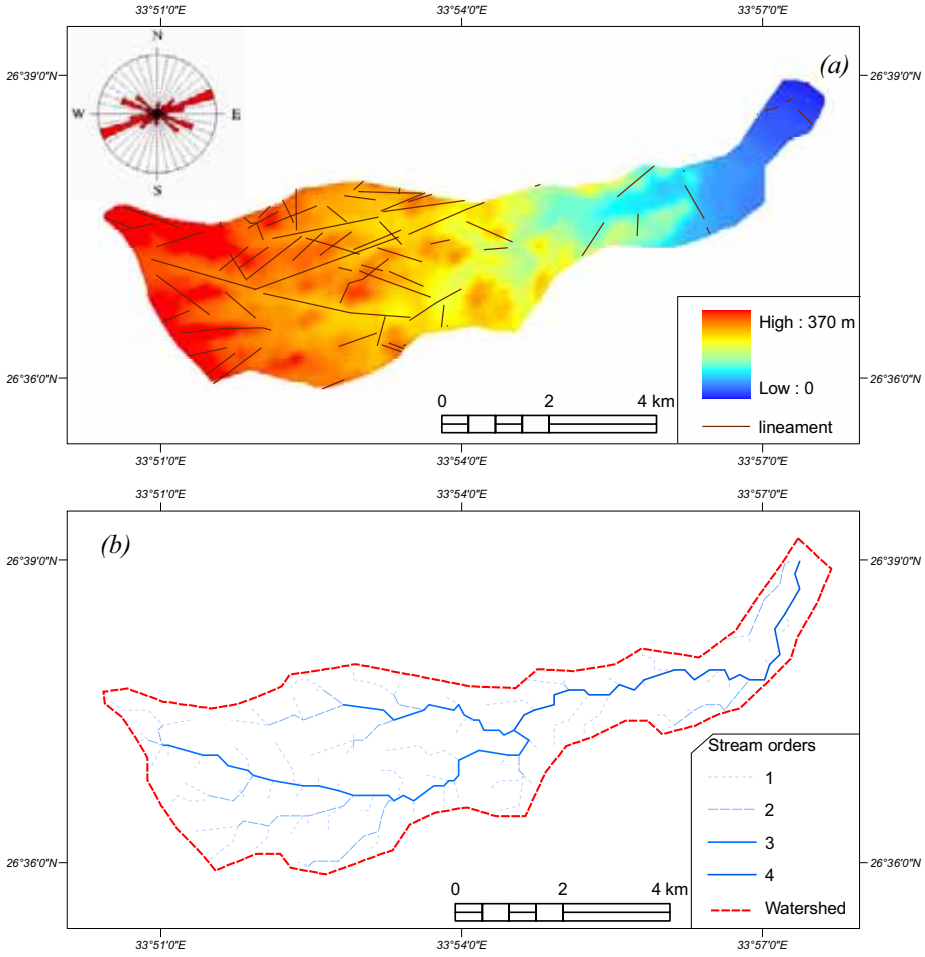

Fig. 4-14: *Wadi Umm Iffinah: (a) DEM and linear features and (b) watershed and drainage network.*

2.Wadi Abu Firad in the middle that drains Jabal Abu Firad and extends NW-SE generally corresponding to the dominant fault system. The lower watercourse adheres to the contact line between gabbro and intermediate metavolcanics. Consequently, the trunk stream is constrained to bend at several locations before debouching into the trunk stream of wadi Safaga.

3.Wadi el-Pulah in the south drains Jabal Umm Taghir el-Fuqani and extends NW-SE. The upper streams draining the older granite and; therefore, they comprise an ideal parallel drainage type due to structural controls. The down streams adhering to rock contacts and structural weakness; accordingly, the main channel of wadi el-Pulah bends at almost right angles before debouching into the trunk stream of wadi Safaga.

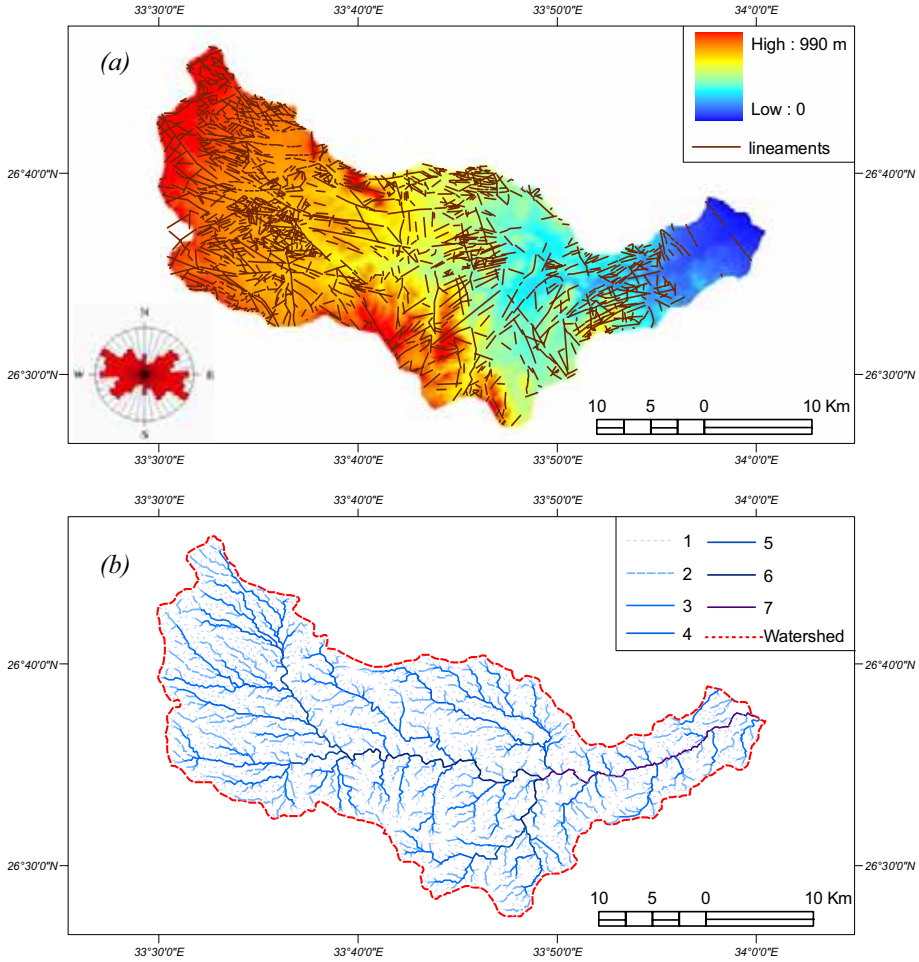

Fig. 4-15: *Wadi Safaga: (a) DEM and linear features and (b) watershed and drainage network.*

5.6. Gasus.

Wadi Gasus occupies an area about 156.82 km² (2.95 % of the total drainage area) and 31.61 km in length along its main channel that attains the 5th order. The wadi drains Jabals Gasus (466 m), el-Diba (592 m), and Abu Gawa (648 m). Dendritic drainage pattern characterises the drainage basin owing to the homogeneity of the Dokhan Volkanics and the limestone rocks dominating in the middle course of the

basin (Fig. 4-16). The drainage pattern dominates the upstream area is mostly parallel and/or sub parallel due to slope and structure controls.

Generally, wadi Gasus is subjected to two fault systems trending NE-SW and NW-SE. As a result, the trunk stream bends at various directions and the network is bifurcated into three major tributaries; they are: wadi Gasus that comprises the trunk stream and extends from west to east, wadi Abu Gawa in the middle drains Jabal Abu Gawa and flows SW-NE, and finally another unnamed tributary flows S-N along the western border of Umm al-Hawaytat basin.

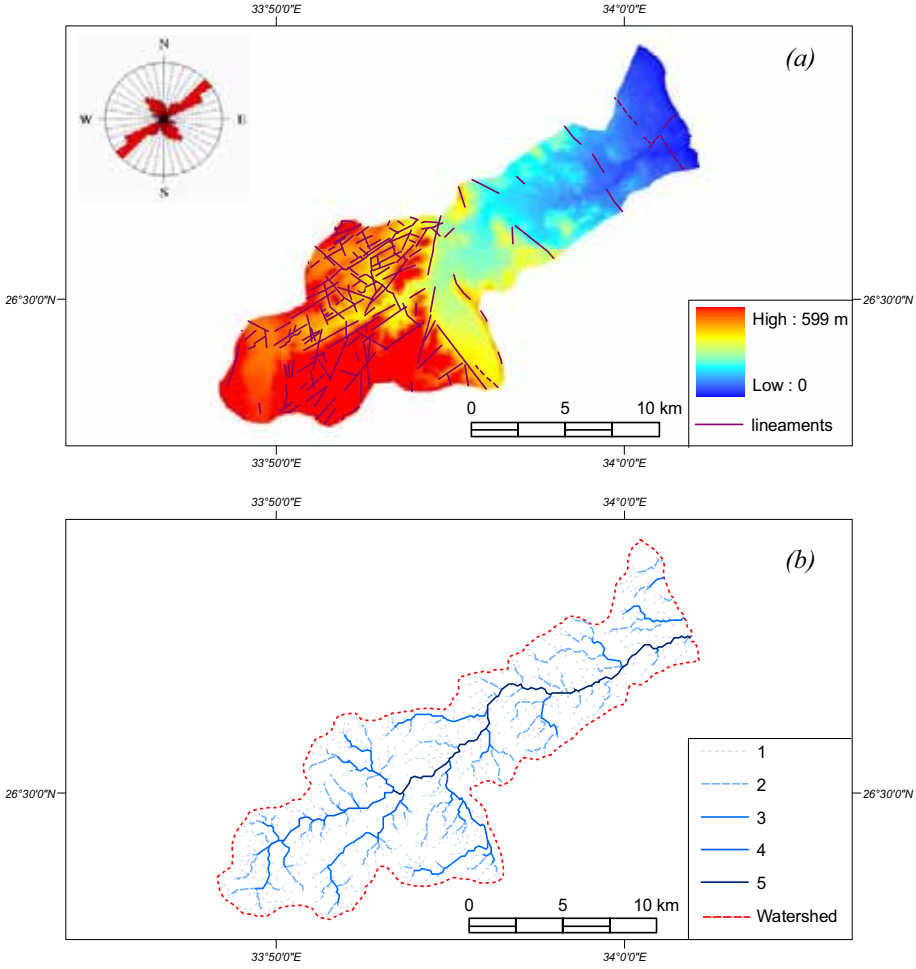

Fig. 4-16: *Wadi Gasus: (a) DEM and linear features and (b) watershed and drainage network.*

5.7. Abu Shiqayli.

Wadi Abu Shiqayli is about 169.21 km² (3.1 % of the total drainage area) and the trunk channel is about 27.7 km in length that is of the 5th order. The wadi drains primarily the northern slopes of Jabal Abu Zarabit and the coastal tablelands.

Wadi Abu Shiqayli flows generally SW-NE through Umm al-Hawaytat basin. Dendritic and sub-dendritic patterns dominantly characterize the drainage network of Abu Shiqayli. In spite of that, the lower stream orders involving the higher orders at almost right angles as a result of the prevailing fault trends in the basin (i.e. NW-SE and NE-SW) (Fig. 4-17).

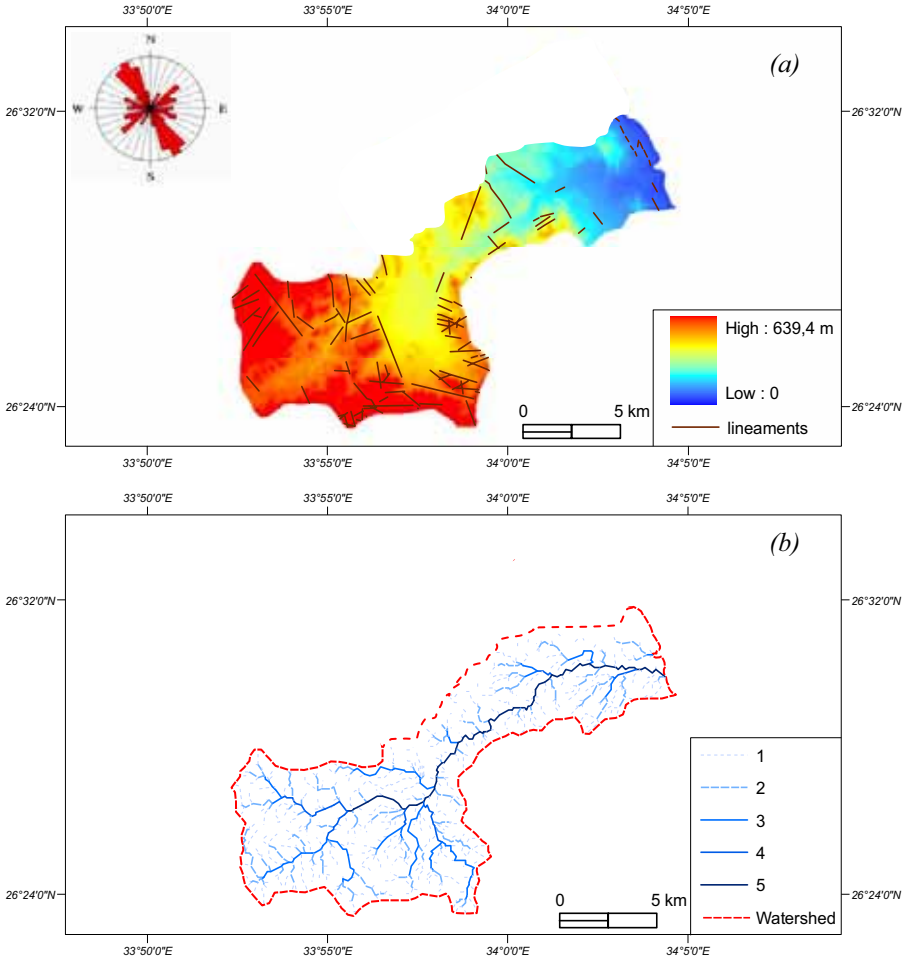

Fig. 4-17: *Wadi Abu Shiqayli: (a) DEM and linear features and (b) watershed and drainage network.*

5.8. Abu Sebekha.

This wadi is one of the smallest drainage basins in the study area although it attains the 5th order. It covers about 48.52 km² (0.9 % of the total drainage area) and 15 km in length. It drains the coastal tablelands and flows from west to east generally since it is slightly influenced by a notably NW-SE fault system. Drainage network is of parallel and sub parallel drainage pattern where the wadi is considerably a consequent one depicting slope controls (Fig. 4-18).

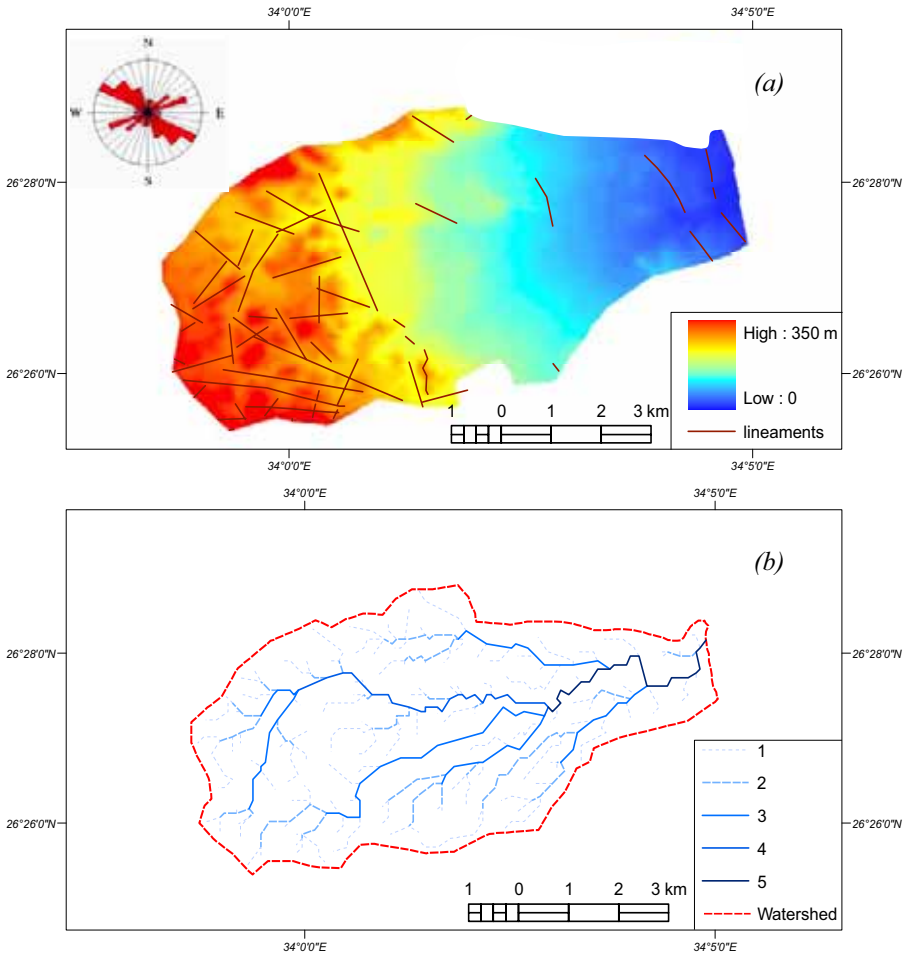

Fig. 4-18: *Wadi Abu Sebekha: (a) DEM and linear features and (b) watershed and drainage network.*

5.9. Queih.

Wadi Queih is the largest drainage basin in the study area constituting 35.64 % of the total drainage area (1892.65 km² approx.). The trunk stream attains about 86.23 km in length and it is of the 7th order. The wadi drains and cuts through a very complex terrain that distinguishes the central Eastern Desert and involves several peaks i.e. Abu

Zarabit (706 m), Umm Kujurah (507 m), Duwi (619 m), el-Hamir (798 m), Umm Halham (886 m), Abu Aqarib (773 m), el-Murr (780 m), Maitiq (944 m), Waira (1037 m), el-Rubshi (996 m), and Semna (1062 m).

The trunk stream flows generally west-east and it is significantly structurally controlled where it adheres to Queih shear zone. As a result, tributaries of wadi Queih have distinctive directions that are NW-SE, NE-SW, and W-E. The lower course of wadi Queih as well runs mostly along an E-W fault that is probably extends below the mean sea level.

The trunk stream as well meanders in the vicinity of el-Saqia area and curves directly southward. The wadi is bifurcated into three main tributaries corresponding to the major faults; they are: wadi el-Saqia runs NW-SE, wadi Semna flows NW-SE, and wadi Sodmein trends NE-SW. These tributaries draining the Red Sea Mountains and cutting through Jabal Duwi producing gorge-like incisions of which Sodmein gorge is the most conspicuous and well known for preserving Sodmein Cave. Drainage pattern is commonly dendritic to sub-dendritic and changes locally into parallel and less trellis specifically in the upstream area (Fig. 4-19).

5.10. Abu Hamra.

Wadi Abu Hamra is one of the smallest drainage basins in the study area, covers about 93.85 km² (1.7 % of the total drainage area). The trunk stream is of the 5^{th} order and extends about 21.31 km from west to east generally. Wadi Abu Hamra drains the coastal tablelands and its trunk stream is considerably influenced by geologic structure specifically along NW-SE and NE-SW trends respectively. As a result, the trunk stream considerably bends at SW-NE and NW-SE successively and looks like an annular drainage pattern (Fig. 4-20). On the other hand, the network is commonly distinguished by parallel to sub-parallel patterns, which imply either pronounced slope controls and/or geologic structure.

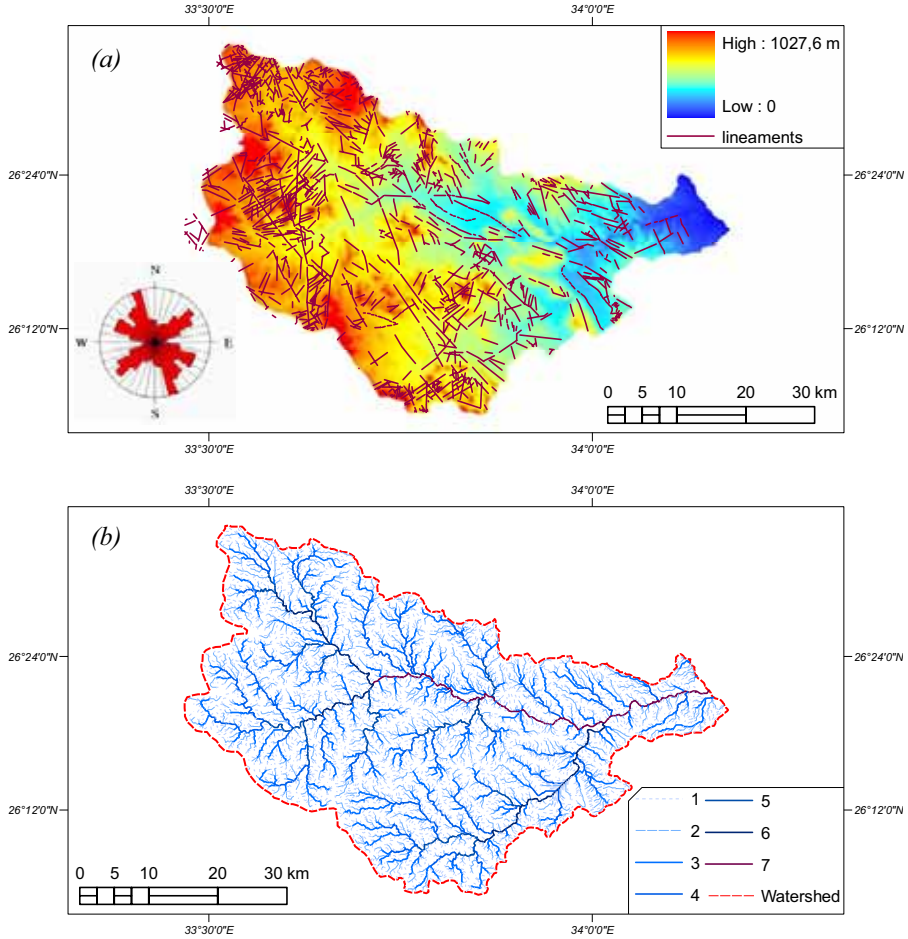

Fig. 4-19: *Wadi Queih: (a) DEM and linear features and (b) watershed and drainage network.*

5.11. Hamraween.

Wadi Hamraween covers an area about 81.61 km² (1.5 % of the total drainage area) and its trunk stream is about 21.97 km in length and it is of the 5th order. It drains the Red Sea terrain and the coastal tablelands as well, and extends WSW-ENE generally. Dendritic drainage pattern dominantly distinguishes the drainage network because it is slightly influenced by geologic structure (Fig. 4-21).

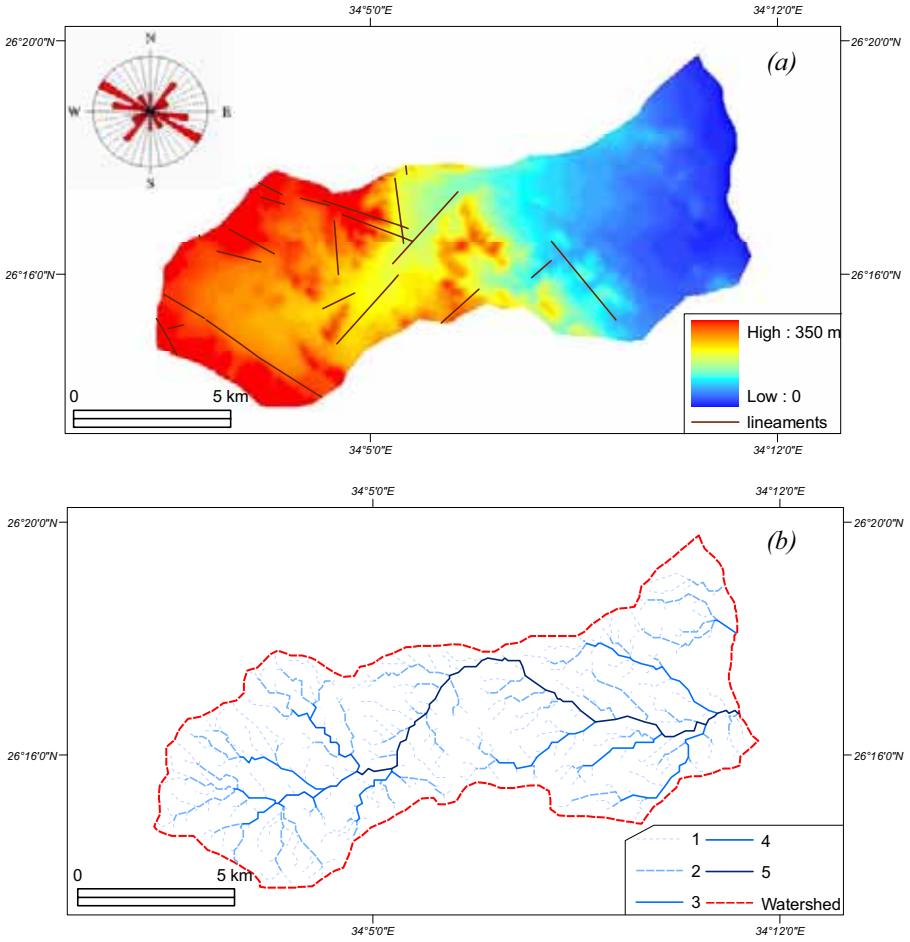

Fig. 4-20: *Wadi Abu Hamra: (a) DEM and linear features and (b) watershed and drainage network.*

5.12. al-Ambagi.

Wadi al-Ambagi is the second largest drainage basin in the study area after wadi Queih, covers about 1511.46 km² (28.4 % of the total drainage area) and 77.89 km in length along the main channel that attains the 7th order. The wadi drains the Red Sea Terrain and the inland tablelands and; therefore, a variety of peaks are distinguished; they are:

Jabal Hamraween (677 m), Jabal an-Nakheil (362 m), Jabal Duwi (619 m), Jabal At-shan (323 m), Umm Oradah (973), Umm Khors (912 m), Umm Dokal (874 m), Nasb el-Kash (899 m), Abu Haban (611 m), Hamadat (432 m), el-Nasb el-Azrak (1062 m), Umm Homies (790m), Umm Shaghir (652 m), and Jabal el-Muelah (829 m).

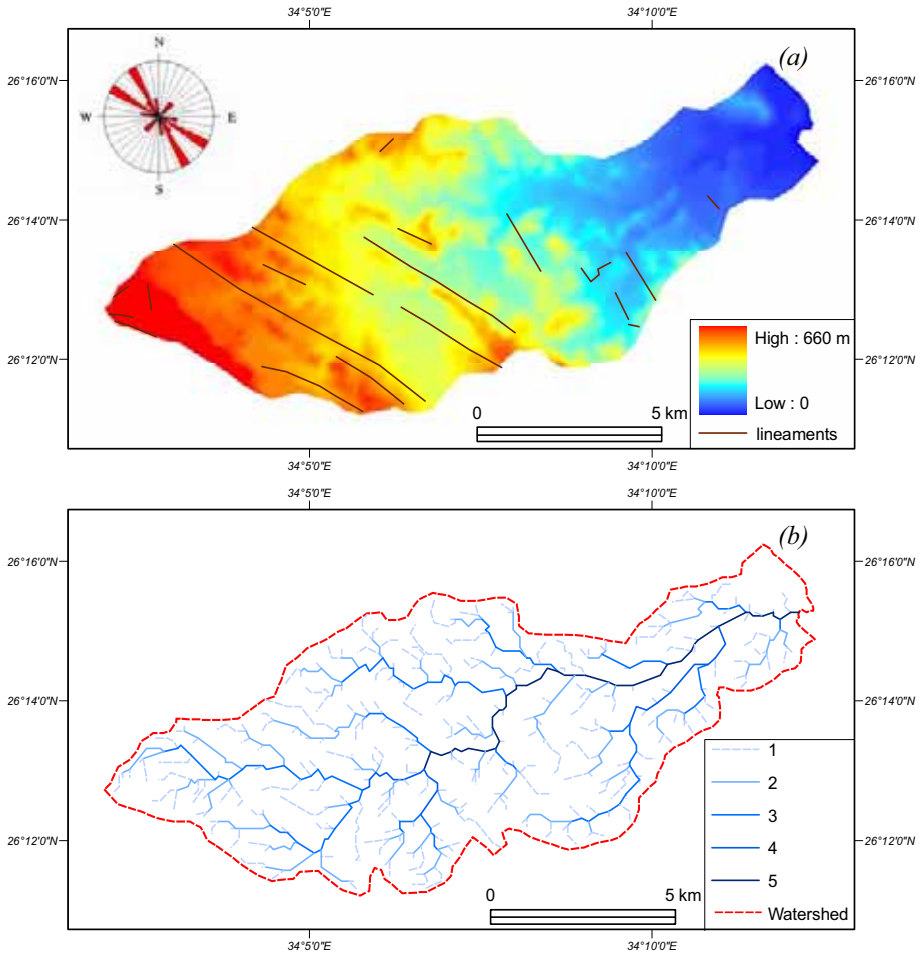

Fig. 4-21: *Wadi Hamraween: (a) DEM and linear features and (b) watershed and drainage network.*

Wadi al-Ambagi is fashioned by coalescence a number of sub-basins that are sometimes larger than the coastal drainage basins (e.g. Abu Asala and Hamraween). These sub-basins are determined as follow:

1.Wadi an-Nakheil flowing out from NW-SE generally because it is restricted to an-Nakheil morphotectonic basin. The wadi drains Jabal Duwi, Jabal Hamraween, and Jabal an-Nakheil and; therefore, most of its tributaries manifesting parallel to sub-parallel patterns owing to the main inclination of Jabal Duwi and Jabal an-Nakheil.

2.Wadi al-Atshan drains the Red Sea Terrain and elongates generally from south to north in accordance with the major structure. As a result, its main channel considerably bends from west to east in the vicinity of al-Atshan mines and debouching into the trunk stream of wadi al-Ambagi at almost right angle.

3.Wadi Karem drains the Red Sea Mountains; that are: el-Nasb el-Azrak, Umm Khors, Nasb el-Kash, and Jabal Hamdata. The wadi is widely experienced to structural influences. Accordingly, it extends from south to north between Jabal Nasb el-Kash and its junction with wadi Umm Khors. Thereafter, the wadi extends SW-NE as far as Jabal Hamdat; henceforth, the main direction is being south to north. Drainage network of wadi Karem reveals parallel to sub-parallel patterns and it is less trellis and rectangular specifically in the upstream area where the secondary streams essentially parallel to the master-stream or other stream into which the primary tributaries debouching. They are usually elongated and approximately at right angles to the streams into which they flow (Zernitz, 1932).
4.Wadi Umm Shaghir drains Jabal Umm Shaghir, Jabal Umm Homies, and the northern slopes of Jabal Muelah. Its trunk stream is structurally controlled and it is annular-like extending SW-NE generally.

The trunk stream of wadi al-Ambagi is considerably influenced by NW-SE and NE-SW fault systems. As a result, direction of the trunk channel differs from place to place i.e. in the vicinity of Jabal Umm Homies the channel extends SW-NE until its linkage with wadi el-Haramia. Thereafter, it turns NW-SE up to el-Beida well and its linkage with wadi Karem. Eventually, it flows out from west to east for debouching into the Red Sea at el Quseir city. The wadi is recognized as coarse dendritic, parallel, trellis, and to a lesser degree rectangular drainage patterns since the geologic structure considerably determines shapes and directions of its streams (Fig. 4-22).

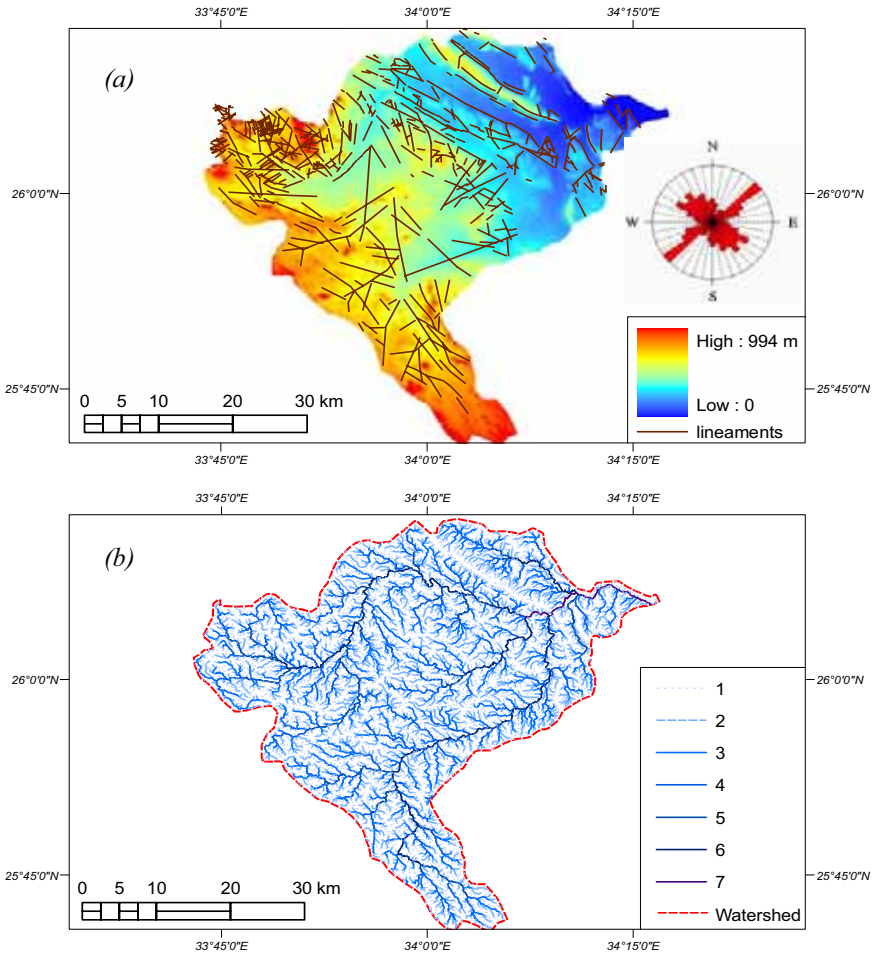

Fig. 4-22: *Wadi al Ambagi: (a) DEM and linear features and (b) watershed and drainage network.*

6. Morphometric Analysis

Table 4-6 summarizes the principle morphometric analysis of the drainage basins, which would be discussed as the following:

6.1. Linear Aspects.

6.1.1. Basin Length, Width, and Perimeter.

Length of a basin *(L_m)* is expressed as the longest dimension of the basin parallel to the principal drainage line (Schumm, 1956). Total length of the trunk streams *(ΣL_m)* is about 443.54 km with an average 36.69 km/basin. The length differs greatly from 8.2 km for wadi Abu Asala to 86.23 km for wadi Queih. Two groups of basin lengths could be distinguished; they are:

- The first group ranges in length between 8.24-31.16 km and represents 36.2% (159.76 km) of the total basin lengths. It includes wadis Abu Asala, Abu Sebekha, Umm Iffinah, Naqarah, Abu Hamra, Hamraween, Abu Shiqayli, and Gasus respectively.
- The second group ranges between 51.24-86.23 km length and represents 63.98% (283.78 km) of the total basin lengths. It includes wadis Barud, Safaga, Ambagi, and Queih.

Average width *(W_b)* of the drainage basins varies greatly from 2 km for Abu Asala and Umm Iffinah to 23.4 km for wadi Ambagi. Most of the basins are less than 10 km width; they are: wadis Abu Asala, Umm Iffinah, Naqarah, Abu Sebekha, Abu Hamra, Hamraween, Gasus, and Abu Shiqayli representing 30.40% of the total basin widths. On the other hand, 33.4 % of the basin counts (i.e. wadis Barud, Safaga, Ambagi, and Queih) ranging from 10 to 24 km width and representing 69.6% of the total basin widths.

Basin perimeters *(P)* vary greatly from one basin to another between 20.7 km for wadi Abu Asala to 245.5 km for wadi Queih. Obviously, basin perimeter is strongly correlated to basin length ($r = 0.9$) and drainage area ($r = 0.96$).

***Table 4-6**: Morphometric parameters of drainage basins and networks.*

Wadi	$\sum L$	P	W_b	U	$\sum N$	R_b	L_m	A	R_c	R_e	D_d	F_s	C	H	S_u	R_h	T_r	H_i
Barud	1355.68	112.55	10	6	1788	5.74	51.24	508.52	0.50	0.50	2.66	3.51	0.44	1390	36.86	0.03	15.89	0.35
Abu Asala	37.89	20.76	2	4	57	4.99	8.24	16.72	0.49	0.56	2.27	3.41	0.44	670	12.29	0.08	2.75	0.37
Naqarah	138.23	36.80	3	5	220	4.41	18.28	54.73	0.51	0.46	2.52	4.02	0.43	800	22.85	0.04	5.98	0.36
Umm Iffinah	67.63	31.36	2	4	102	6.48	16.08	25.70	0.33	0.36	2.63	3.97	0.44	370	43.47	0.02	3.25	0.66
Safaga	3866.46	163.14	11	7	3566	4.08	68.42	750.41	0.35	0.45	5.15	4.86	0.19	990	69.11	0.01	15.73	0.66
Gasus	398.29	76.39	5	5	594	4.79	31.16	156.82	0.34	0.45	2.53	3.79	0.43	600	51.93	0.02	7.78	0.4
Abu Shiqayli	429.56	77.56	6	5	627	4.73	27.70	169.21	0.35	0.53	2.53	3.71	0.43	640	43.28	0.02	8.08	0.34
Abu Sebekha	103.94	31.67	3	5	150	4.44	15.02	48.52	0.61	0.52	2.14	3.09	0.47	350	42.90	0.02	4.74	0.67
Queih	4290.30	245.56	22	7	6602	5.69	86.23	1892.65	0.39	0.57	2.26	3.49	0.44	1030	83.71	0.01	23.86	0.45
Abu Hamra	225.55	50.03	4	5	357	4.57	21.31	93.85	0.47	0.51	2.40	3.80	0.42	350	60.89	0.02	7.14	0.64
Hamraween	189.28	48.56	4	5	318	4.64	21.97	81.61	0.43	0.46	2.32	3.90	0.43	660	33.29	0.03	6.55	0.25
Ambagi	5436.75	217.31	23.4	7	13065	6,03	77.89	1511.46	0.40	0.56	3.59	8.64	0.27	999	80.63	0.01	14.22	0.39

** Drainage basins are from north to south.*

Notations:

$\sum L$	Total length of streams, km	R_e	Elongation ratio
P	Basin perimeter in km	D_d	Drainage density, km/km^2
W_b	Average basin width in km	F_s	Stream frequency
U	Main stream order	C	Constant of channel maintenance
$\sum N$	Sum of stream numbers	H	Basin relief
R_b	weighted mean bifurcation ratio	S_u	Slope average of the trunk stream
L_m	Basin length along the principle stream channel in km	R_h	Dimensionless relief ratio
A	Basin area in km2	T_r	Texture ratio
R_c	Circularity ratio	H_i	Hypsometric integral

6.1.2. Stream Numbers and Orders.

The total stream numbers $(\sum \mathcal{N})$ is about 27446 streams of which the 1st order streams possess 76.17 %. According to the law of stream numbers assumed by Horton (1945), stream numbers decrease in reverse to their orders and yielding generally a linear relationship (Fig. 4-22). Bifurcation ratio $(\mathcal{R}_b)$ of the average number of branching is calculated for each successive pair of orders in each stream basin. Then, the weighted mean bifurcation ratio is obtained according to Strahler (1953) by multiplying the bifurcation ratio of each successive pair of orders by the total number of streams involved in the ratio and taking the mean of the sum of these values (Schumm, 1956). As a result, drainage basins under study vary in their bifurcation ratio between 4.41 for wadi Naqarah and 5.74 for wadi Barud. These results are of dimensionless values expressing the form of the drainage systems and normally ranging from 2 for flat or rolling drainage basins up to 3 or 4 for mountainous or highly dissected drainage basins (Horton, 1945). On the other hand, Strahler (1964) revealed that abnormal high bifurcation ratio might be expected in regions of steeply dipping rock strata where narrow strike valleys are confined between hogback ridges. Generally, bifurcation ratios are relatively high in the study area as a result of structure distortions where they exceed the normal ranges proposed by Horton (1945).

As previously mentioned, stream networks are ordered according to Strahler method (1957). Thereby, drainage basins ranging between 4th and 7th orders and they fall into the following divisions:

- Basins of the 4th order include wadis Abu Asala and Umm Iffinah constituting 16.6 % of the basin counts and 0.57 % of the total stream numbers.
- Basins of the 5th order include wadis Naqarah, Gasus, Abu Shiqayli, Abu Sebekha, Abu Hamra, and Hamraween constituting 50 % of the basin counts and 8.2 % of the total stream numbers.
- Only wadi Barud is of the 6th order that constitutes 6.5 % of total stream numbers.
- Basins of the 7th order include wadis Safaga, Queih, and Ambagi. Although they represent only 25% of the basin counts, they possess alone 84.64% of the total stream numbers.

6.1.3. Total Stream Length.

The total stream length *(∑L)* is about 16,539.56 km with a general average 2,544.55 km/basin. Stream lengths vary greatly from basin to one another. Abu Asala is the shortest one form 0.22 % (about 37.8 km) of the total stream length, whereas wadi al-Ambagi is the largest one 32.8 % (about 5,436.75 km) of the total stream length. Two main divisions of stream lengths are distinguished as:

- Drainage basins less than 1000 km length include wadis Abu Asala, Umm Iffinah, Abu Sebekha, Naqarah, Hamraween, Abu Hamra, Gasus, and Abu Shiqayli. They attain 9.6 % (about 1,590.37 km) of the total stream lengths.
- Drainage basins greater than 1000 km length include wadis Barud, Safaga, Queih, and Ambagi. They possess 90.38 % (about 14,949.19 km) of the total stream lengths.

6.1.4. Average Stream Length.

The average length of streams per order ranges between 5.4 and 99.62 km for the 1st and 7th orders successively (table 4-7). According to the law of stream length introduced by Horton (1945), average length of streams tends closely to approximate a direct geometric series where it is increasing in accordance with stream order and yielding a linear relationship with very little scatter (Fig. 4-23).

Table 4-7: *Average stream lengths versus stream orders.*

Stream Order	*Ave. Length km*	*Stream Order*	*Ave. Length km*
1st	5,45	5th	119,72
2nd	13,72	6th	92,49
3rd	33,16	7th	99,62
4th	49,88		

6.2. Spatial Analysis.

6.2.1. Drainage Area.

Total drainage area *(∑A)* of the whole drainage basins is about 5310.20 km^2. Drainage basins fall into three distinctive areal categories; they are:

- Drainage basins less than 200 km^2: they are wadis Abu Asala, Umm Iffinah, Abu Sebekha, Naqarah, Hamraween, Abu Hamra, Gasus, and Abu Shiqayli. They constitute 66.6% of the basin counts and only 12.18 % (about 647.16 km^2) of the total drainage area.

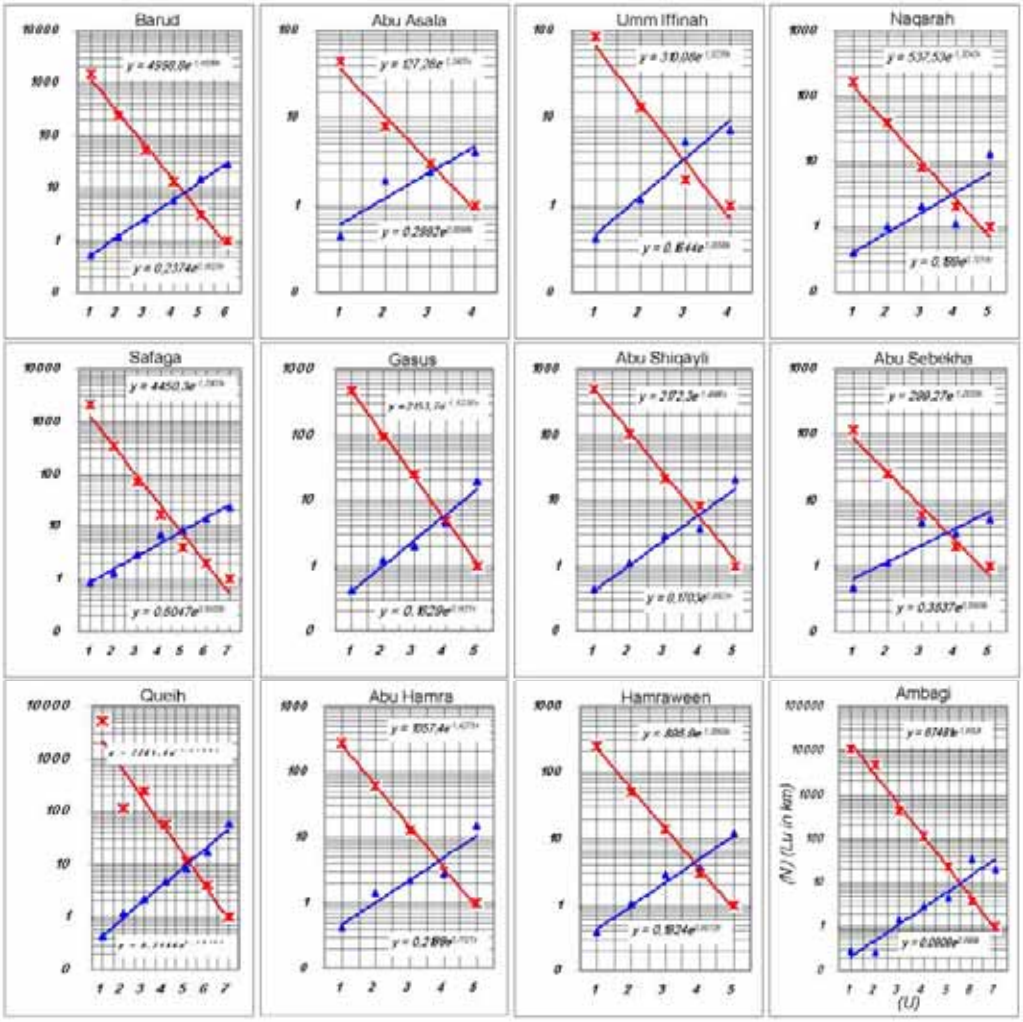

Fig. 4-23: *Bifurcation ratio to number of streams and relation of stream lengths to stream orders.*

▪ Drainage basins ranging in area between 400-800 km^2 including wadis Barud, and Safaga. They constitute 23.7 % (1258.93 km^2) of the total drainage area.

▪ Basins larger than 1000 km^2: this category includes wadis Ambagi and Queih, which possess alone 64.1% (3404.11 km^2) of the total drainage area.

6.2.2. Basin Shape.

Basin shape analysis hypothetically reflects the way that the runoff will discharge at the outlet. It is based on the concept that a circular watershed would result a runoff from various parts of the watershed reaching the outlet at the same time producing high flood peak. On the other hand, an elliptical watershed of the same area as another circular watershed would spread out the runoff over time producing a smaller

flood peak than the circular one. A number of watershed parameters have been developed for representing basin shape. The following are a few common and typical parameters:

6.2.2.1. Circularity Ratio.

The ratio is computed according to Miller (1953) as:

$$\mathcal{R}_c = \mathcal{A}/\mathcal{A}_c$$

Where $\mathcal{A}$ is the drainage area and $\mathcal{A}_c$ is the area of a circle has a perimeter equals to basin perimeter. The result is equal to one for circular basins and approaches zero for a straight line. Accordingly, drainage basins are distinguished as either circular or elliptical as follows:

- Circular where $\mathcal{R}_c$ ranges between 0.50 and 0.61 such as wadis Barud, Naqarah, and Abu Sebekha.
- Elliptical drainage basins where $\mathcal{R}_c$ ranges between 0.33 and 0.49 such as wadis Umm Iffinah, Gasus, Abu Shiqayli, Safaga, Ambagi, Queih, Hamraween, Abu Hamra, and Abu Asala.

6.2.2.2. Elongation Ratio.

The ratio is expressed according to Schumm (1956) as:

$$\mathcal{R}_e = \mathcal{D}_c/\mathcal{L}_m$$

Where $\mathcal{D}_c$ is the diameter of a circle with the same area as the basin area and $\mathcal{L}_m$ is the basin length parallel to the principal drainage line (Schumm, 1956). Similar to circularity ratio, the result is equal to one for circular and approaches zero for a straight line. As a result, drainage basins are distinguished as either circular or elliptical as follows:

- Circular basins: where $\mathcal{R}_e$ ranges between 0.50 and 0.57 such as wadis Barud, Abu Hamra, Abu Sebekha, Abu Shiqayli, Abu Asala, Queih, and Ambagi.
- Elliptical basins: where $\mathcal{R}_e$ ranges between 0.36 and 0.46 such as wadis Umm Iffinah, Safaga, Gasus, Naqarah, and Hamraween.

A comparison between $\mathcal{R}_c$ and $\mathcal{R}_e$ values revealed considerable differences; they are:

▪ 50 % of the drainage basins are steady at their shape category although they exhibit tiny changes in their shape factor values (e.g. Umm Iffinah, Safaga, Gasus, Hamraween, Barud, and Abu Sebekha).

▪ By applying the elongation ratio the other 50 % of the drainage basins exhibit significantly changes. As a result, wadis Abu Shiqayli, Abu Asala, Queih, Abu Hamra, and Ambagi have become circular and; therefore, count of the circular basins is increased from 3 to 7 basins. On the other hand, wadi Naqarah is seemingly elliptical and the count of elliptical basins is decreased from 9 to 5 basins.

6.2.3. Drainage Density.

Drainage density $(\mathcal{D}_d)$ is an important indicator of the linear scale of land-form elements in stream-eroded topography and it may be thought of an expression of the closeness or spacing of channels (Strahler, 1964). Since it measures the dissection of the surface by streams (Máčka, 2001) it is strongly influenced by hill slope processes (Tucker & Bars, 1998). Average drainage density of the basins under study is 2.7 km/km^2. The absolute values are greatly convergent ranging between 2.14 km/km^2 for wadi Abu Sebekha to 3.59 km/km^2 for wadi Ambagi. Therefore, the basins are poorly drained[1] (<8 km/km^2) and the surface texture is coarse (Morisawa, 1985). Poor drainage density is an ordinary result of differences of annual rainfall, relief, and rock resistance. According to Abdel-Rahman et al. (1979) the mean drainage density is being lower on the granite rocks of the central Eastern Desert rather than other basement rocks.

6.2.4. Stream Frequency.

Stream frequency $(\mathcal{F}_s)$ represents the total number of streams $(\sum \mathcal{N})$ in a drainage basin of areal unit $(\mathcal{A})$ (Horton, 1945). It expresses the texture of drainage net exactly like drainage density, but each of them treats a distinct aspect (Strahler, 1964). Although Horton (1945) denoted that values of stream frequency for small and large drainage basins are not directly comparable, stream frequencies of the drainage basins under study are greatly convergent, excluding wadi Ambagi, ranging between 3.09 streams per km^2 for wadi Abu Sebekha to 4.86 streams per km^2 for wadi Safaga. Stream frequency is corresponding analogous to climatic conditions and geologic structure.

[1] *Horton (1945) assumed that the poorly drained basin has a drainage density 2.74, where the well-drained one is 0.73 or one fourth as great.*

Wadi Ambagi is of a relatively high stream frequency 8.64 streams per km^2 indicating the relatively intensive surface denudation.

6.2.5. Constant of Channel Maintenance.

According to Schumm (1956) the constant of channel maintenance *(C)* determines the minimum limiting area required for developing a drainage channel and it is represented as the inverse of drainage density *(1/Dd)*. The relation is computed in the present study in kilometers. As a result, the average constant is about 0.40 km^2 that is required to support each linear kilometer of stream channels. The constant of channel maintenance ranges between 0.19 km^2 for wadi Safaga and 0.47 km^2 for wadi Abu Sebekha. Generally, the absolute values are seemingly identical and low as a result of coarse texture and intensive dissection of drainage areas.

6.3. Relief Analysis.

6.3.1. Basin Relief.

Basin relief *(H)* refers to difference in elevation between highest and lowest points in a drainage basin (Strahler, 1964). Where the studied drainage basins debouching into the Red Sea (zero level), the basin relief, therefore, is defined as the highest contour line that defines the watershed line. Investigation of the DEMs of the drainage basins depicts that basin relief varies greatly from 350 m asl for wadis Abu Sebekha and Abu Hamra to 1390 m asl for wadi Barud with an average 737 m asl height. Three relief categories could be determined as:

- Drainage basins ≤ 400 m height (i.e. wadis Umm Iffinah, Abu Sebekha, and Abu Hamra).
- 400-800 m height (i.e. wadis Abu Asala, Naqarah, Gasus, Abu Shiqayli, and Hamraween).
- Drainage basins ≥ 800 m height (i.e. wadis Barud, Queih, Safaga, and Ambagi).

6.3.2. Slope Average.

Slope average *(S_u)* is computed by dividing basin length *(L_m)* by basin relief *(H)* in the same unit (meters) for expressing changes of the slope between the upstream area and the pour point. As a result, slope average ranges between 12.2 for wadi abu Asala and

83.71[1] for wadi Queih. The total slope average of the whole basins is about 48.34. Slope average is relatively high due to the magnitude of basin relief.

Significance of slope average is clarified through stream incisions due to the down-head erosion. The slope plays an important role for estimating flood hazardous where steep slopes could lead to severe flash floods.

6.3.3. Relief Ratio.

Relief ratio $(\mathcal{R}_h)$ is a dimensionless ratio measures the overall steepness of a drainage basin and it is an indicator for the intensity of erosion processes operating on slopes of the basin (Strahler, 1964). Relief ratio is defined as the ratio between basin relief and the longest dimension of the basin parallel to the principle stream. It could be expressed also as the inverse of slope average formula where the resultant is equal to the tangent of the angle formed by two plans intersecting at the mouth of the basin. Therefore, various basins could be compared regardless of the topographic differences (Schumm, 1956). Thus, the relief ratio ranges between 0.01 for wadis Safaga, Queih, and Ambagi to 0.08 for wadi Abu Asala. Great similarity is deduced owing to homogeneity of climatic conditions, surface relief, rock formations, and geologic structure.

6.3.4. Texture Ratio.

Texture ratio $(\mathcal{T}_r)$ indicates topographic texture by measuring stream spacing and/or closeness. It is represented in the present study as number of contour crenulations $(\mathcal{N})$ divided by basin perimeter $(\mathcal{P})$ (Smith, 1950). Accordingly, the ratio ranges between 2.75 km for wadi Abu Asala and 23.8 km for wadi Queih and the mean texture ratio of the whole basins is about 9.66 km. It is significantly correlated to drainage area $(\mathcal{A})$ producing positive linear relationship ($r = 0.94$) and less correlated to drainage density ($r = 0.12$).

According to Smith (1950), topographic texture of the drainage basins under study fall into three divisions; they are:

---

[1] *Slope average is used in the same unit i.e. 1:12 slope average means that a basin drops one meter vertically each 12 meters horizontally.*

▪ Coarse texture ($\mathcal{T}_r$< 4 miles) such as wadis Abu Asala, Naqarah, Umm Iffinah, and Abu Sebekha, which form 33.33% of the basin counts.

▪ Medium texture (4 < $\mathcal{T}_r$ < 10 miles) such as wadis Barud, Safaga, Gasus, Abu Shiqayli, Abu Hamra, Hamraween, and Ambagi, which constitute 58.33 % of the basin counts.

▪ Wadi Queih is of a fine texture ($\mathcal{T}_r$>10).

6.3.5. Hypsometric Analysis.

The use of hypsometric analysis has been restricted in the past because of the intensive computation required. Strahler (1952) acknowledged that for the effort involved using a planimeter would be more efficient to make a visual assessment of the contours. However, with the advances in computer and GIS technology since 1952, hypsometry is worth reinvestigating as a mean of objectively quantifying catchment characteristics (Dowiling et al. 1998). Nowadays, hypsometry has become easier by using DEMs, which are obtained from satellite images such as SRTM and ASTER data. The present study spots a method for computing hypsometric analysis in quantitative terms for representing area versus altitude based essentially on the analysis of the extracted DEM from the SRTM image as follows:

▪ The DEM of the study area is clipped into 12 DEMs representing drainage basins.

▪ The clipped DEMs are converted into GRID format because of editing accessibility.

▪ Normally, the database of a GRID contains two columns; one represents cell values that refer to elevation and the other one refers to the total number of cells in each elevation.

▪ Using map query and editing tools, the GRID is simply apportioned into elevation intervals (i.e. 25 or 50 meters height).

▪ By implementing map-algebra, the total area of each elevation interval is determined as $C_C \times \mathcal{P}_a$ where C_C is cell counts per elevation interval and $\mathcal{P}_a$ is the individual pixel area in square meters.

▪ Eventually, the area is descending accumulated and the hypsometric curve is plotted for representing relative height $y = (h/H)$ versus relative area $x = (a/A)$ to give a dimensionless value between 0.0 and 1.0; where y is the ratio of height of a given elevation

h to the total basin height H and x is the ratio of horizontal area a to entire basin area A (Strahler, 1964 & McCullagh, 1978).

Using dimensionless hypsometric analysis is beneficial for comparing different drainage basins in order to study influences of different rock types, or balance between tectonic and erosion. On the other hand, significances of the hypsometric analysis for drainage basins under study could be demonstrated according to the following statements (Fig. 4-24):

- Since the hypsometric analysis verifying the relationship between area and altitude, hypsometric curves significantly differ from one basin to another. They are either convex (i.e. wadis Umm Iffinah, Safaga, Abu Sebekha, and Abu Hamra), S-shape (i.e. wadis Barud, Abu Asala, Naqarah, Queih, and Ambagi), and concave (i.e. wadis Gasus, Abu Shiqilly, and Hamraween).
- Configuration of the curve essentially reveals the geomorphologic stage. Therefore, convex curves representing young stage, curves that are in the vicinity of the fit-line representing mature stage, and concave curves representing old stage or monadnock phase (Strahler, 1964).
- S-shape curves are of convex-concave shape revealing inequilibrium between the upstream area and the downstream outlet owing to the interaction between tectonics and erosion (Weissel et al. 1994). As a result of that, relative proportions of basin area might have been significantly uplifted. It is obvious at wadis Barud, Abu Asala, Naqarah, Umm Iffinah, Queih, and Ambagi where their hypsometric curves intersecting with the fit line and protruding upward at low elevations. This may support the idea that the coastal plain has been uplifted causing tilting of the Quaternary deposits (±10°) (Issawi et al. 1971).
- According to Hurtrez et al. (1999), where the drainage area is relatively small, hill slope processes would be dominant and; accordingly, hypsometric curve would be convex with an integral close to 1, such as wadis Umm Iffinah, Safaga, Abu Sebekha, and Abu Hamra. Conversely, with increasing drainage area, the importance of river processes would increase and the hypsometric integral close to zero such as wadis Queih and Ambagi. This relation is not quite clear in the study area, where some small drainage basins are of low hypsometric integral such as wadis Abu Asala and Naqarah.

▪ As can be deduced, large portions of the drainage areas lie at low elevations because the drainage basins have been subjected to peneplanation for a long-time, specifically where the older granite dominates the drainage area. At the same time, small proportions of an area characterize the higher altitudes and normally representing the relatively recent rocks (e.g. younger granite).

▪ However, hypsometric integral *(HI)* is expressed as a percentage of the area under the hypsometric curve that refers to the percentage of the remaining area of the original basin and it is calculated according Hurtrez et al. (1999) as:

$$HI = (alt - alt_{min}) / (alt_{max} - alt_{min})$$

Where alt is the mean elevation of the basin, alt_{min} and alt_{max} are minimum and maximum elevations within the basin respectively. The hypsometric integral of the drainage basins ranges from 0.25 for wadi Hamraween to 0.67 for wadi Abu Sebekha. Strahler (1952) observed that the hypsometric integration value of 0.3 and less indicates monadnock phase and, therefore, the watershed is stabilized and no further erosion is expected such as wadi Hamraween. HI value between 0.3 and 0.6 indicates equilibrium or mature stage of watershed such as wadis Barud, Abu Asala, Naqarah, Gasus, Abu Shiqayli, Queih, and Ambagi. $HI >= 0.6$ refers to inequilibrium or young stage indicating the susceptibility of watershed to erosion (Strahler, 1952) such as wadis: Umm Iffinah, Safaga, Abu Sebekha, and Abu Hamra.

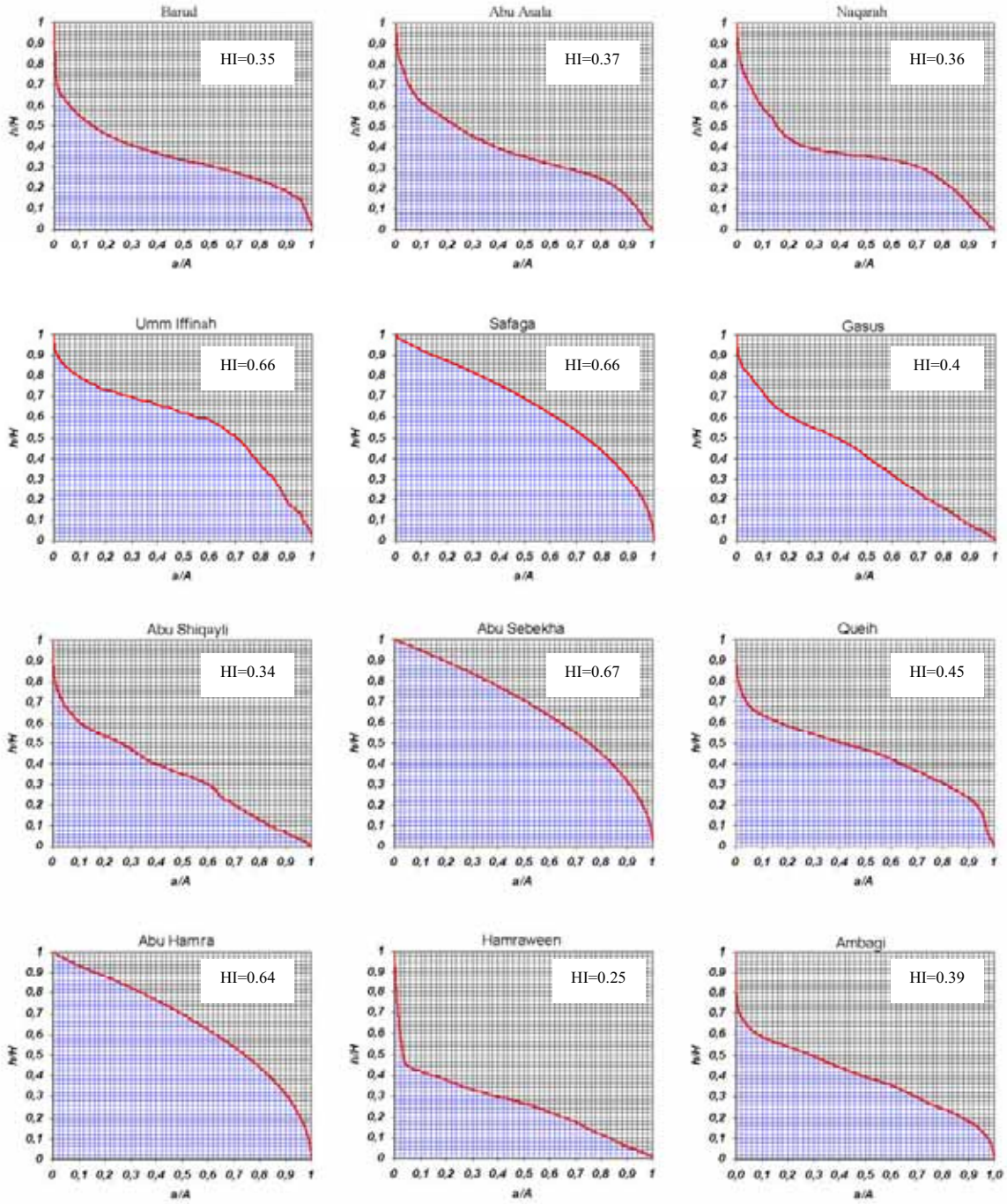

Fig. 4-24: *Hypsometric curves and integral of the drainage basins.*

7. Fluvial Landforms

Although the present-day climate of the study area is significantly hyper-arid as previously stated in chapter one, remarkable ancestral fluvial landforms characterize the study area. Before pointing out the main fluvial landforms it is worthy discussing briefly initiation of the drainage system in the study area.

7.1. Drainage Initiation.

The present-day drainage system could not be initiated under the contemporary climatic conditions. Therefore, it should have been excavated during the preceding wetter periods. Dating the coastal Red Sea drainage system is controversial issue because of structure complexity and climate changes.

Ball (1939) pointed out that during the end of the Miocene period the River Nile was joined to tributaries from the Red Sea Mountains, which eroded the deep channels that now form the principle wadis of the Eastern Desert. According to him, it was the result of a general movement combined with a good deal of folding and faulting in the eastern parts of Egypt. Regarding the antecedent channels in the study area (e.g. wadis Sodmein, Mohamed Rabah) they maintain their watercourses through a wide variety of fault blocks ranging in age from upper Cretaceous to middle Miocene. This implies that such drainage systems were probably synchronize (if not prior) to the orogenic process that is postdated to late Oligocene-early Miocene times (Montenant et al. 1988; Purser et al. 1990; Jarrige et al. 1990; Purser & Bosence 1998; Zaky, 1999; Khalil & McClay, 2001; Beniamin et al. 2005). This means that such ancestral drainages were synchronize to the Gilf System assumed by Issawi & McCauley (1993) as the major Oligocene drainage system in Egypt that was developed due to the uplift of the southern corner of Egypt and the Red Sea Range (Fig. 4-25). During the early Miocene, volcanism and an accelerated uplift were taken place along the western flanks of the Red Sea Range. These associated with tropical wet climatic conditions and emergence of the ancestral wadi Qena (Early Qena River) and other consequent tributaries (Embabi, 2004). A comparable system to Early Qena River existed during Tertiary in the Arabian Peninsula, starting from the Higaz and Asir Highlands in the west and ending in the Arabian Gulf (Embabi, 2004; after Anton, 1984).

During the late Miocene (hot and arid period) the Mediterranean Sea level was lowered by several thousand meters (maximum 4.030 m). The Eonile that was the first river eroding the present-day Nile Valley was receiving enough water from the numerous wadis, which debouching today into the Nile Valley (Embabi, 2004). Most of these wadis drain the Eastern Desert of Egypt (Fig. 4-26). The Eonile continuously eroded the surface to attain its base-level and formed a huge canyon larger and deeper than the Grand Canyon of the Colorado River, northern USA (Said, 1993).

Undoubtedly, during this epoch fluvial erosion was extremely active eliminating the fractured sedimentary rocks, which were covered the present-day Red Sea Terrain. As a result, the drainages are being superimposed-like on the basement rocks adhering to the major structure. It may be also inferred that the principle drainage basins in the study area might affiliate with late Oligocene-early Miocene epochs such as wadis Barud, Safaga, Gasus, Queih, and Ambagi. Quoting figure 2-3 in chapter two, the early Miocene rocks are approximately absent along the Red Sea coast and; therefore, the middle Miocene successions unconformably overlay the basement rocks. This implies that during the early Miocene there was a great peneplanation phase owing to fluvial erosion primarily where most of the land was relatively higher than the early Miocene Sea level. At the same time, ancestral drainages could not belong to the middle Miocene since the prevailed climatic conditions were probably very hot and the Red Sea, as well as Mediterranean Sea, had become a vast evaporation basin in which gypsum and salt patches were deposited (Braithwaite, 1984).

Eventually, the relatively smaller drainage basins are probably not older than late Pliocene (if not Pleistocene) since they drain principally the coastal tablelands, which are composed of middle Miocene and Pliocene rocks. It is approved that during the early Pliocene the land was sinking gradually relative to the Tethys sea-level and the Red Sea was invaded by the Mediterranean water and had become for the first time connected with the Indian Ocean as well. During the latter part of Pliocene the subsidence of the land ceased and followed by a great vertical movement, which in the eastern parts of Egypt was combined with intense folding and faulting (Ball, 1939).

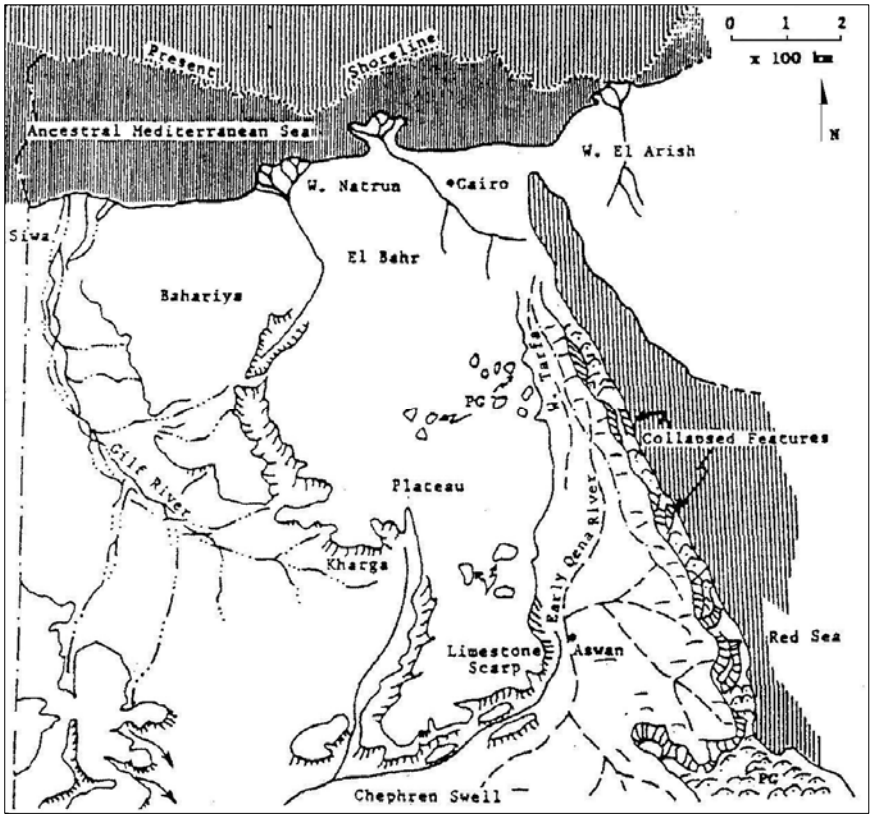

Fig. 4-25: *Middle Miocene drainage systems in Egypt.* *(Issawi & McCauley, 1993)*

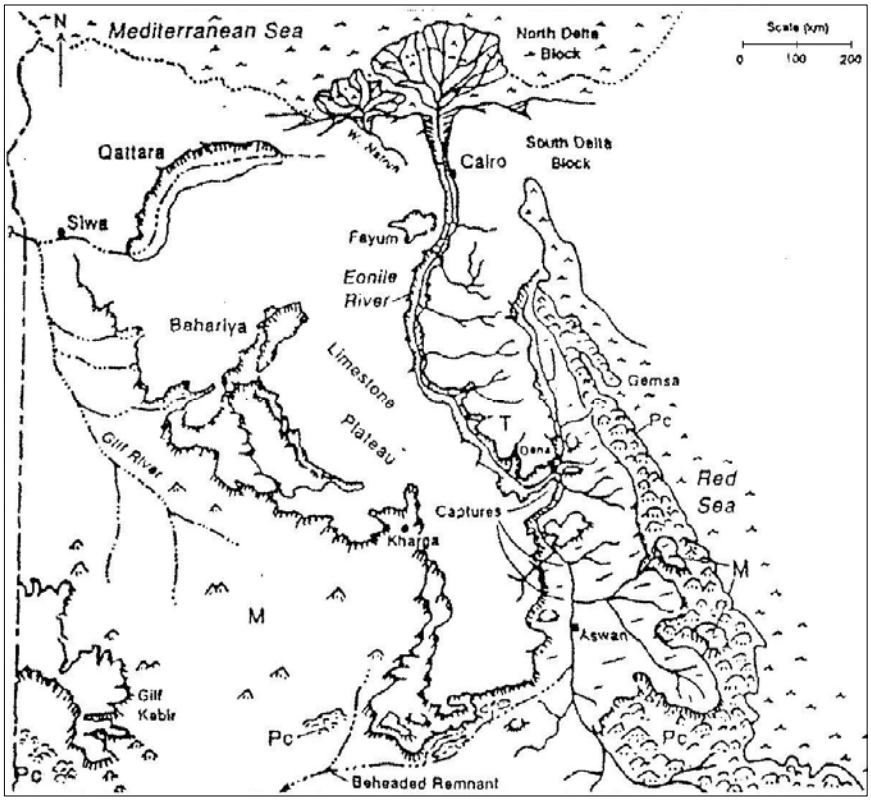

Fig. 4-26: *Late Miocene drainage systems in Egypt.* *(Issawi & McCauley, 1993)*

7.2. Deltas and Alluvial Fans.

It is believed that the coastal plain of the Eastern Desert is primarily a result of coalescing deltas alternating with reefal plain. Morphology of the deltas differs from one to another and, theoretically, it is proportional and highly correlated to drainage basin characteristics. A digital model is designed for studying the deltas in the study area based on the DEM analysis and topographic maps. Deltaic boundaries are visually identified and manually digitized from the topographic maps of scale 1:50.000 and the ETM+ image. The boundary layer is overlaid on the DEM and new contour map is extracted by contour interval of 5 meters (Fig. 4-27). By this means, morphometric parameters are identified i.e. area, length, maximum width, apex width, slope, and shape. The results are stated as follows (Table 4-8):

▪ Total deltaic area of the whole basins is about 137.56 km^2. The individual areas vary greatly between 2.8 km^2 for wadi Abu Asala and 30.25 km^2 for wadi Safaga because they are proportional to drainage areas and manifesting a linear relationship (Fig. 4-28). Investigation of the bathymetric contours along the coastal plain depicts that deltaic cones of the larger wadis (e.g. Safaga, Queih, and Ambagi) are probably extending about ±500 m below the present-day sea level (Fig. 4-29).

Table 4-8: *Morphometric characteristics of the deltas.*

Wadi	A_d	L_d	W_d	*Apex* W_d	S_d	R_{ed}
Barud	13.8	8.3	2.6	1.3	1.1	0.53
Abu Asala	2.8	3.2	1.6	0.55	1.8	0.28
Naqarah	3.7	4.7	1.6	0.49	1.3	0.25
Umm Iffinah	4.7	3.8	2.5	0.31	1.5	0.39
Safaga	30.25	9.86	6.07	1.14	5.7	0.98
Gasus	8.19	5.34	2.36	0.89	0.4	0.49
Abu Shiqayli	10.43	6.34	3.65	0.7	0.9	0.52
Abu Sebekha	6.36	7.5	1.6	0.34	1.4	0.27
Queih	18.78	7.63	4.7	1.3	0.4	0.78
Abu Hamra	11.57	8.7	2.8	0.7	0.8	0.42
Hamraween	4.78	8.04	0.74	0.36	0.7	0.19
Ambagi	22.2	7.83	5.5	0.5	3.1	0.90

A_d	*deltaic area in km^2.*	*Apex* W_d	*width at the apex, km.*
L_d	*length along the principle stream, km.*	S_d	*Slope degree.*
W_d	*maximum width, km.*	R_{ed}	*shape factor.*

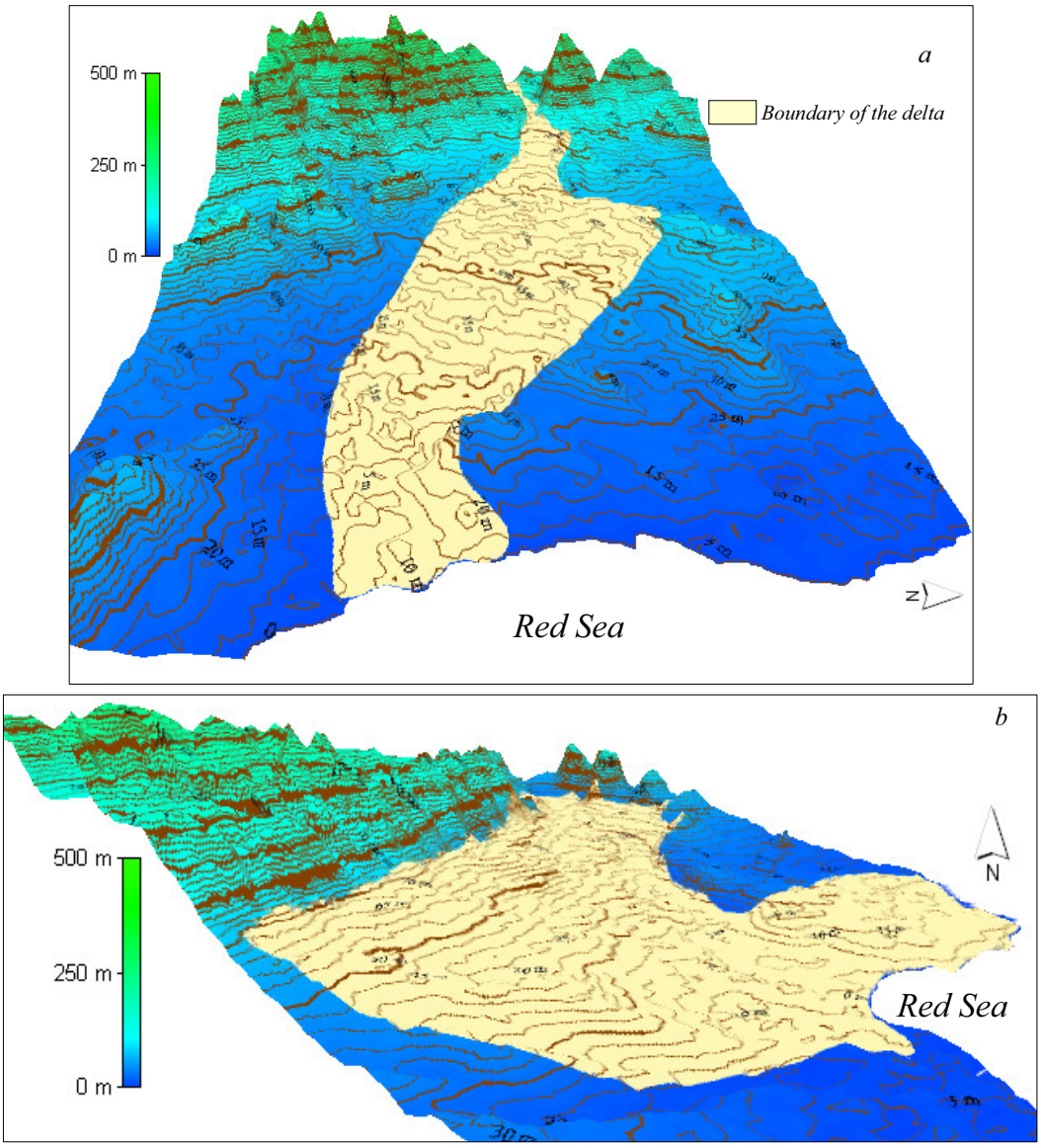

Fig. 4-27: *Examples of the data model output: a. delta wadi Abu Hamra and b. delta wadi Ambagi.*

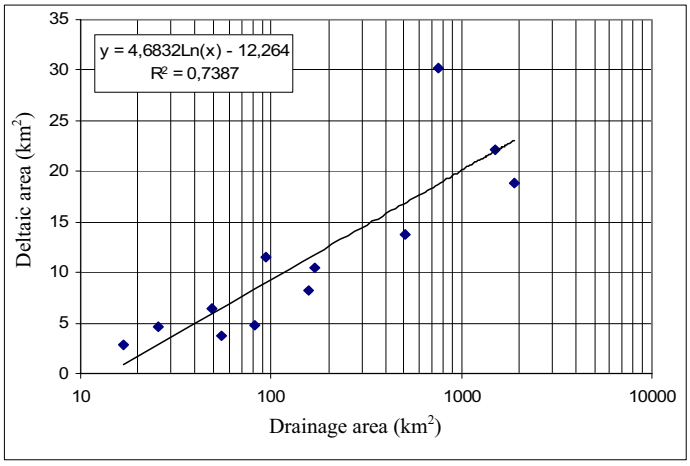

Fig. 4-28: *Relation between drainage and deltaic areas.*

Fig. 4-29: *Extract of a topographic map 1:200.000 showing extension of the deltaic cones below the present-day Red Sea level.*

▪ Length of the deltas measured along the principle channels and it varies from 3.2 km for wadi Abu Asala to 9.86 km for wadi Safaga.

▪ The deltas attain their maximum width near the coastline where the alluvial deposits spread in fan-like shape. The maximum width varies from 0.74 km for wadi Hamraween to 6 km for wadi Safaga.

▪ Width of the deltaic apex differs from 0.31 km for wadi Umm Iffinah to 1.3 km for wadis Barud and Queih.

▪ Slope of each delta is defined as height differences between deltaic apex and toe divided by deltaic length L_d and the results are represented in degrees. Accordingly,

the slope ranges between 0.4˚ and 5.7˚ (Fig. 4-30). Regarding the slopes, the deltas are divided into three categories according to Saito & Oguchi (2005):

* Steep deltas with slope more than 1.5˚ include deltas of wadis Abu Asala, Umm Iffinah, Safaga, and Ambagi. They possess 43.6 % (59.95 km^2) of the total deltaic area.

* Medium slope deltas (0.5˚ to 1.5˚) include deltas of wadis Barud, Naqarah, Abu Shiqayli, Abu Sebekha, Abu Hamra, and Hamraween. They represent 36.8 % (50.64 km^2) of the total deltaic area.

* Gentle slope deltas (slope less than 0.5˚) include deltas of wadis Gasus and Queih. They represent 19.6 % (26.97 km^2) of the total deltaic area.

▪ The deltas are considerably irregular shaped and characterized by relatively wide and straight fronts or toes in the vicinity of the sea (Fig. 4-31). Deltaic shapes are defined by using the elongation ratio after Schumm (1956) with minor modification as follows:

$$\mathcal{R}_{ed} = \mathcal{D}_c / \mathcal{L}_d$$

Where $\mathcal{D}_c$ is the diameter of a circle with the same area as the deltaic area and $\mathcal{L}_d$ is the deltaic length along the principal channel. As a result, deltas of wadis Barud, Safaga, Abu Shiqayli, Queih, and Ambagi are of rotund shapes where their shape factors ranging from 0.52 and 0.98. In contrast, the other deltas manifest straight or elliptical shapes varying between 0.19 for wadi Hamraween and 0.49 for wadi Gasus. No distinct relationship is obvious between deltaic shapes and basin shapes (r = -0.1).

However, the intermountain basins are primarily filled with alluvial deposits of which some ideal alluvial fans are distinguished such as in wadi el-Saqia (Fig. 4-32). Occasionally, slope processes perform talus cones of fan-like shape that compose chiefly of angular pebbles manifesting the action of the mechanical weathering (Fig. 4-33).

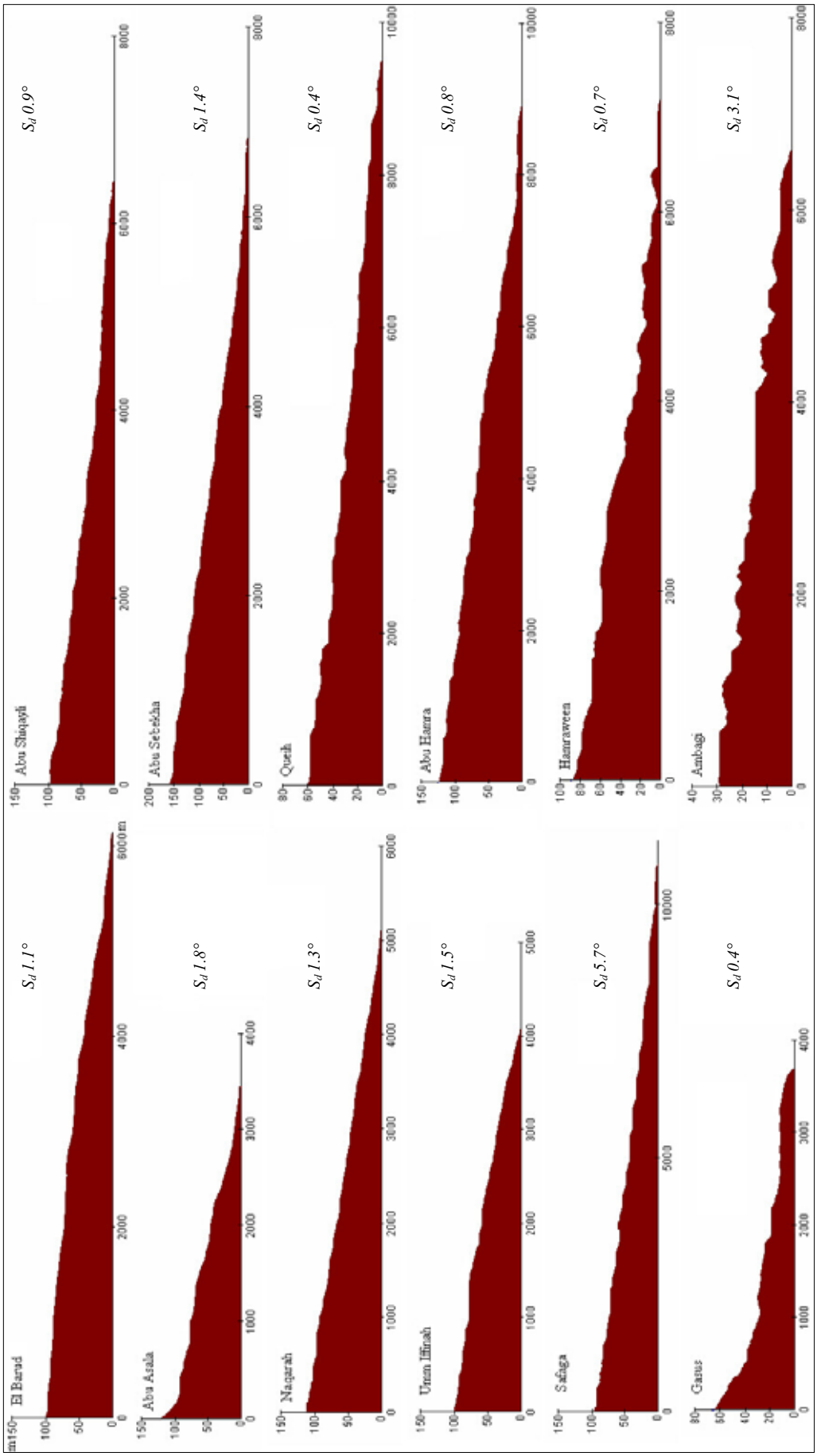

Fig. 4-30: *Slope profiles of the deltas along the principal channels. (Extracted from the DEM)*

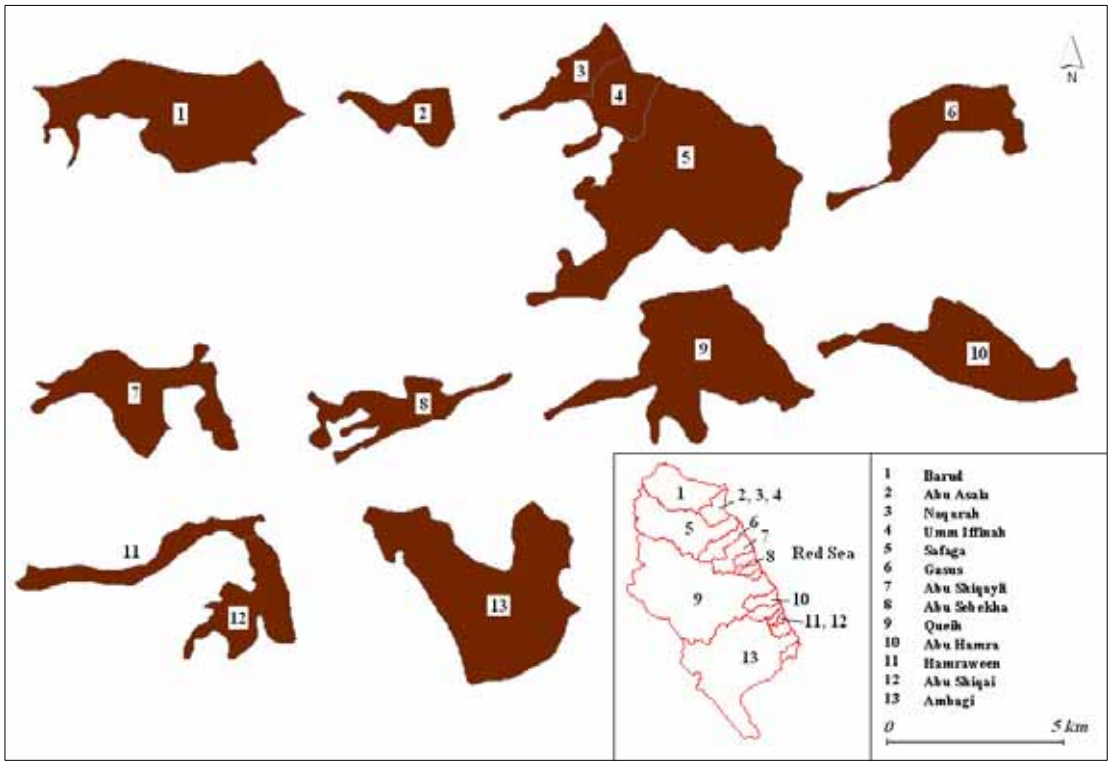

Fig. 4-31: *Morphology of the deltas under study. (Source: topographic maps 1:50.000 & ETM Image)*

Concerning the alluvial deposits, they are normally of coarse sands at the upstream area owing to quartz disintegration from the basement rocks. Sometimes, the sands are quite white such as in wadi el-Barud al-Abyiad* that gains its name because of the sand colour (Fig. 4-34). Boulders, pebbles and cobbles dominate at apexes of the deltas and alluvial fans. The size gradually decreases towards the sea and sands of various sizes are dominating alternating occasionally with pebbles and cobbles.

* *al-Abyiad means white.*

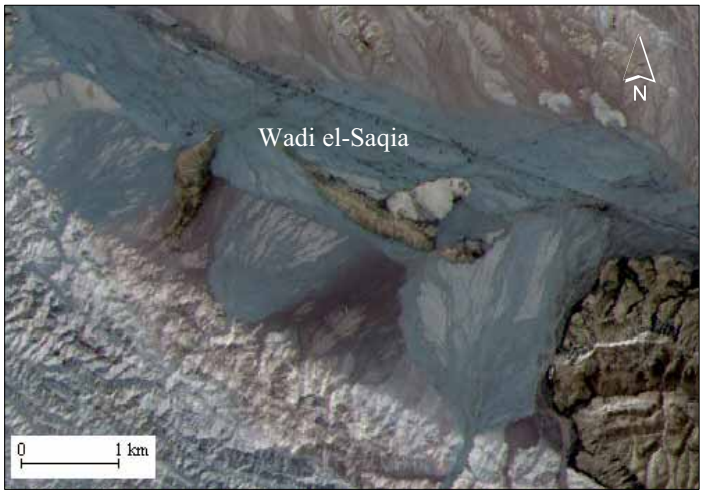

Fig. 4-32: *Inverted colour ASTER image showing examples of the inland alluvial fans in wadi el-Saqia, NW Jabal Duwi.*

Fig. 4-33: *Talus cone of fan-like shape, wadi Umm Taghir.*

Fig. 4-34: *White sands filling wadi el-Barud (Looking northeast).*

7.3. Wadi Terraces.

Fluvial terraces are the most distinctive landforms along the lower courses of the Red Sea drainage system. They have been long-term reported by Beadnell (1924), Sandford & Arkell (1939), EL-Akkad & Dardir (1966b), Butzer & Hansen (1968), El-Bassyony (1982), and Minbary (1990). Number of terraces differs along the Red Sea coast from wadi to one another. For example: Sandford & Arkell (1939) reported five terraces in wadi Ambagi at heights of 27-30, 21, 15, 9-6 and 4-3 m above the wadi floor. They referred as well to two terraces at wadi Safaga (7.5-3 m) and Hamraween (15-13 m) and only one terrace at wadi Queih (15 m). According to Budel[1] (1952), height of the terraces differs from what is mentioned by Sandford and Arkell. He pointed out five terraces in wadi Ambagi at elevations of 60, 40-30, 12-10, 6 and 4-1.5 meters above the wadi floor. However, alluvial terraces were investigated in the field within several locations. Table 4-9 and figure 4-35 revealing the most conspicuous levels founded within the study area.

Table 4-9: *Heights of the wadi terraces.*

Wadi	*I*	*II*	*III*	*IV*	*V*	*VI*
Safaga		2.5-3	6			
Gasus			5-6	12-13		
Queih				10-12	15-16	
Abu Hamra			6-8		15	
Hamraween			5-6		15	
Abu Safi			5-6			
Abu Swateir			5-6			
El Quseir El Qadim			5-6			
an-Nakheil	1-1.5					
Ambagi	1-1.5		4.5-5	10-12		20-21

**Heights above the wadi floor in meters. (Source: field work)*

Terraces ≤ 1.5 m are the result of the present-day climate and they are too tiny to be presented in figure 4-35. Terraces of 2.5-3 and 5-6 m are well distributed along the coastal plain where they unconformably overlay the old coral reefs with exception of that one of wadi Ambagi. Terraces of 10-12, and 13 m are preserved in wadis Gasus and Queih. In wadi Ambagi terrace of 10-12 and 20-21 are broadly quarried nowadays.

[1] *After Butzer & Hansen (1968).*

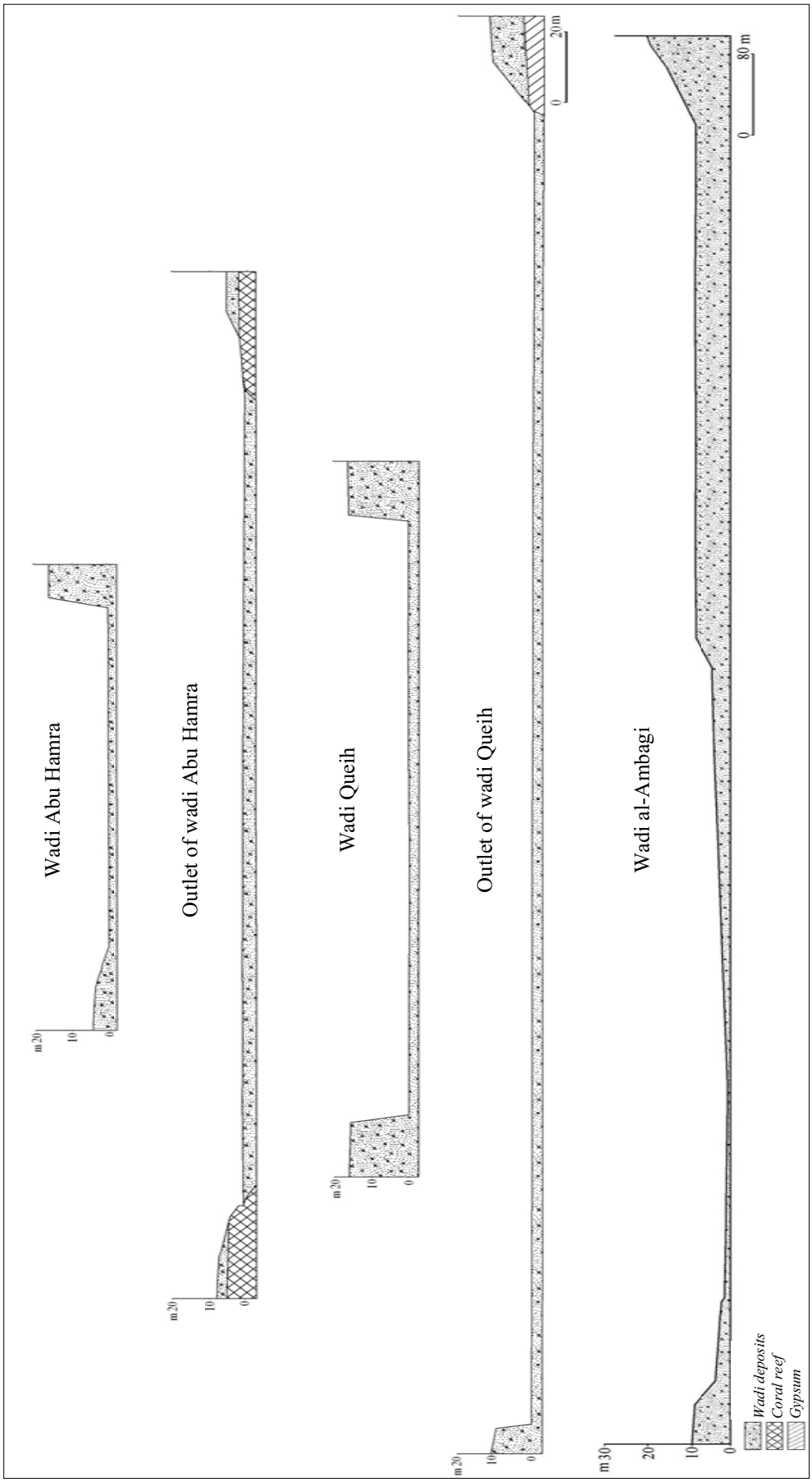

Fig. 4-35: *Cross profiles showing the alluvial terraces in wadis Abu Hamra, Queih, and al-Ambagi.*

The present study has distinguished four terraces in the lower reach of wadi al-Ambagi extending from Ain el-Ghazal gorge-like (about 8.5 km northwest El Quseir city) to the wadi mouth; they are:

▪ The lower terrace is the recent one ranging in elevation between 1-1.5 m above the wadi floor. It is formed mainly of clay (less than 2 μm), silt, and medium to fine sands. Undoubtedly, this terrace is formed under the present-day climate because it reveals great homogeneity with the modern wadi deposits, which cover the present day wadi channel.

▪ Terrace 4.5-5 m above the wadi floor: The surface of the terrace is mostly flat (≤ 1°) and armoured-like by angular varnished gravels owing to insolation and chemical weathering.

▪ Terrace 10-12 m: Surface of this terrace inclines slightly towards the north and it is composed primarily of unconsolidated gravels and cobbles. Width of the terraces is about 300 m. An exposed 3 m thick profile was investigated revealed that the terrace is composed of different materials ranging from coarse sands to angular boulders of various sizes (Fig. 4-36). The terrace is of paired type where it is recognized on both sides of the wadi (Fig. 4-37). The section could be apparently divided according to its lithological characteristics into three sub-divisions; they are:

1. The lower division is about 1.6 m thick and composed essentially of coarse round to sub-angular gravels, cobbles, and boulders, which have been primarily derived from the basement and the Tertiary rocks. This division is distinguished due to the relative homogeneity of its deposits. It could be inferred that it is probably deposited under a homogenous relatively humid climate. However, the size of the deposits diminishes gradually from base to top indicating that the climate was going less humid.
2. The middle division is about 1.5 m thick but it differs completely from the previous one where it is formed of heterogeneous laminas of various sizes ranging from medium sands to coarse gravels. The laminas were probably deposited during irregular runoff, signifying the greatly changes in the runoff regime. Therefore, it could be concluded that this division is a result of a torrential regime that was probably similar to the contemporary climate.

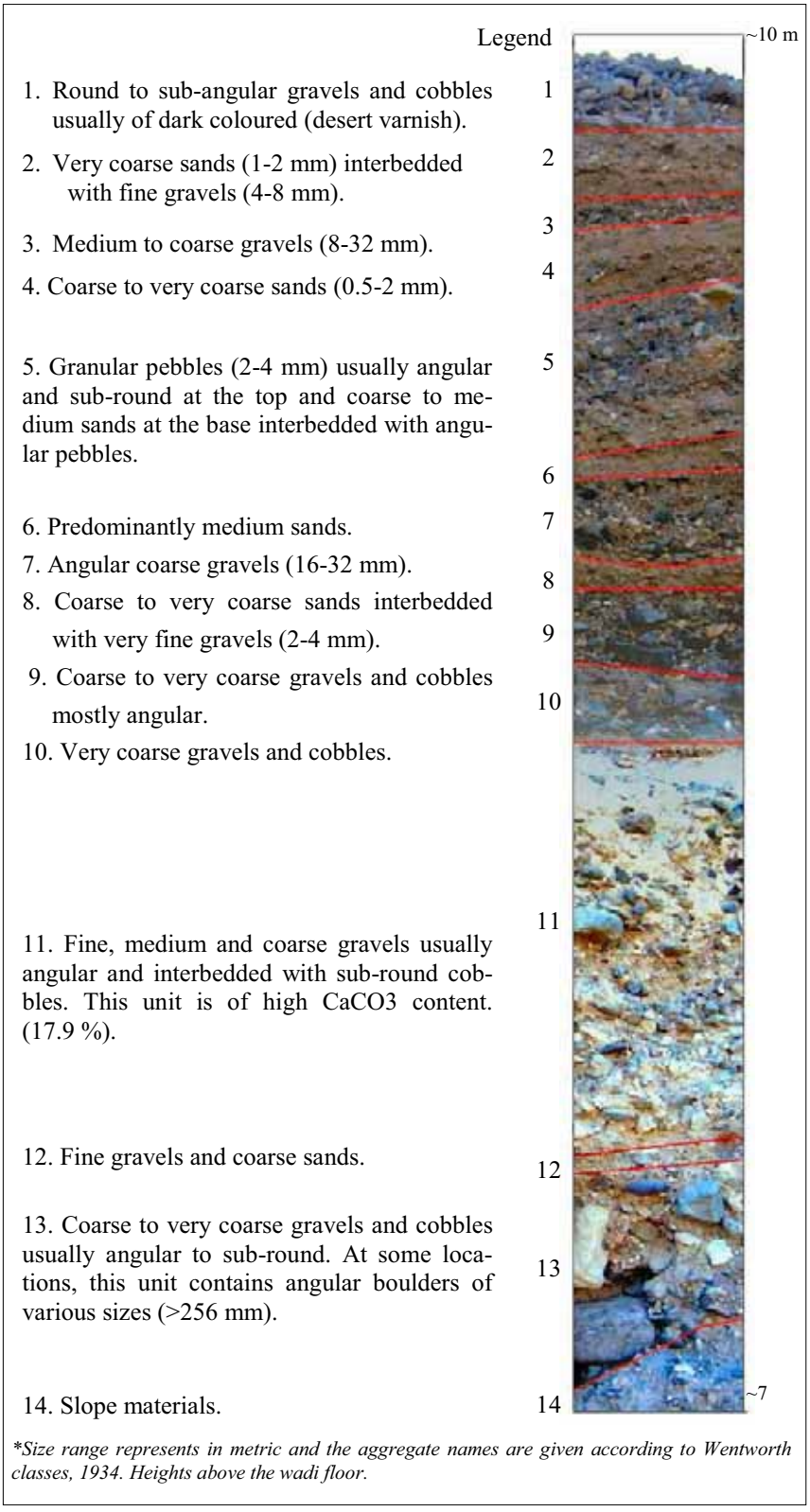

Fig. 4-36: *Sedimentological section of the 10-12m terrace of wadi al-Ambagi.*

Fig. 4-37: *Paired wadi terraces at wadi al-Ambagi.* *(Looking northward)*

1. Angular gravels and cobbles of dark coloured (desert varnish).

2. Medium sands.

3. Medium to fine sands occasionally interbedded with thinly gypsum laminations.

4. Medium to fine sands of relatively high *Calcium Carbonate* contents (11.82 %).

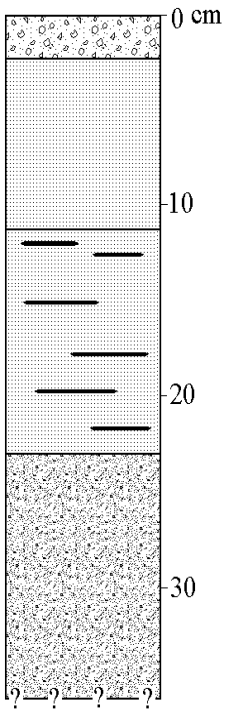

Fig. 4-38: *A soil profile of the 20-21m terrace of wadi al-Ambagi.*

3. The upper division is very thin (about 20 cm thick) representing the surface of the terrace. It is composed of unconsolidated round to sub-angular cobbles and gravels of dark colours as a result of chemical weathering.

▪ Terrace 20-21 m: The terrace is about 1 km width and characterized by considerably flat surface. It is composed primarily of gravels and cobbles of different sizes. The terrace is separated from the third terrace by a wide tributary that is filled by coarse materials experienced desert varnish. A 35 cm profile is dug showing materials of different sizes ranging between gravels and fine sands. However, the horizon 11-23 cm contains gypsum laminations and the lower horizon is of high *Calcium Carbonate (CaCO3)* content as well. Regarding the pedogenesis process, the profile is anyhow not well developed (Fig. 4-38).

Generally, terraces of wadi Ambagi are dissected by short rills and gullies debouching into the main channel of wadi Ambagi. Occasionally, they overlay the Mio-Pliocene? reefal limestone, which manifests some caverns at its base owing to the chemical weathering.

At Ain el-Ghazal, the scenery differs completely where a modern channel occupies a little part of the wadi floor and manifesting a collapsed terrace of 2 meters height and knick point (±1 m waterfall-like). The terrace underwent considerable undercutting due to the running water from Ain el-Ghazal and the neighbouring mines and, therefore, it is split into blocks of different sizes. The terrace is composed primarily of consolidated fine materials of high carbonate content and patches of gypsum are locally found at its base. Sometimes, the terrace is covered by a hard crust of crystalline salts owing to extremely evaporation. The higher reach of this channel manifest white colour owing to salt accumulations and at the top of the knick point travertine has been distinguished, which is often white to brown due to impurities; it overlooks a cavernous (Fig. 4-39).

This terrace is seemingly recent since it is a result of flowing water from Ain el-Ghazal and neighboring mines. Therefore, it is probably not correlated to the former terraces group of wadi Ambagi.

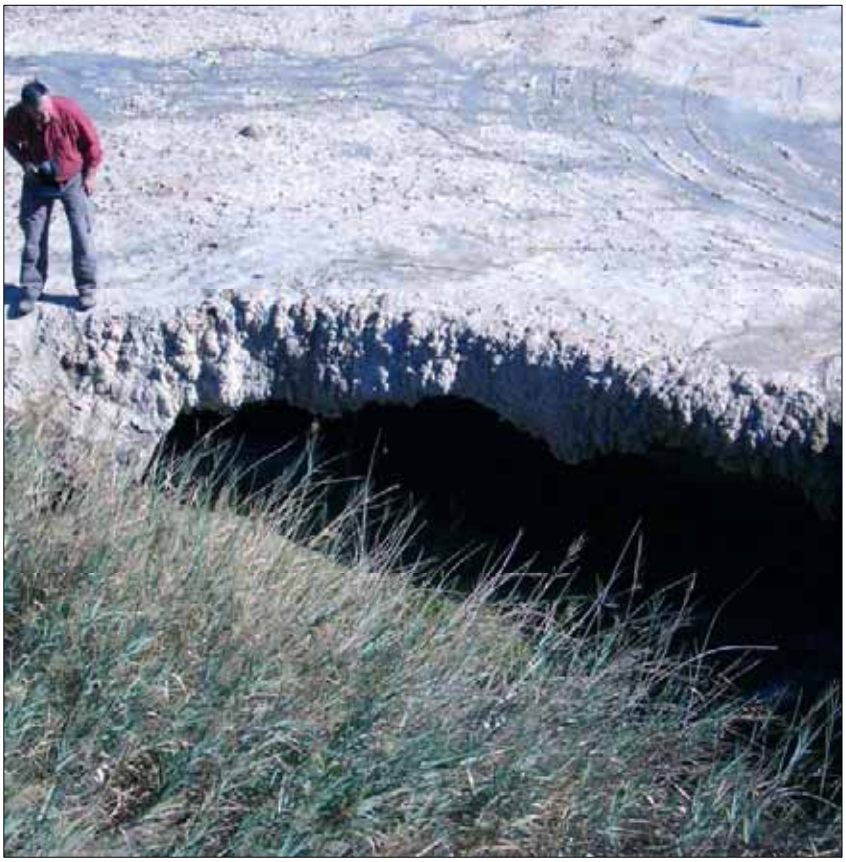

Fig. 4-39: *Travertine deposits overlooking a cavernous.*

In wadi Queih, the terraces are located within the lower two kilometers of the main channel. Terrace of 10-12 m is connected in a very short distance with the higher one 15-16 m, and it is being of paired type. The sedimentological section is greatly similar consisting primarily of alluvial deposits of different sizes and boulders are abundant in addition. The most important phenomenon distinguishes this terrace is that the effects of neotectonics, which reveal a slight vertical displacement.

In wadi Gasus, terrace 12-13 m (26˚ 32̀ 45″ N; 33˚ 56̀ 12″ E) is a unique case (Fig. 4-40), where the sedimentological section differs completely than the other ones in the study area. The terrace starts at the bottom with a layer of boulders that is overlain by a ±5 m thick of re-worked aeolianite-like layer. The later one is seemingly of heterogeneous materials (Fig. 4-41), which are locally interbedded with pebbles, cobbles, which interrupted by tiny laminations of duricrusts and evaporites. The terrace as a whole tilts westward. The re-worked aeolianite-like layer is overlain by about ±9 m

thick of alluvial deposits. The terrace is experienced 10-15 cm vertical displacements, which are mostly owing to the effects of the neotectonic.

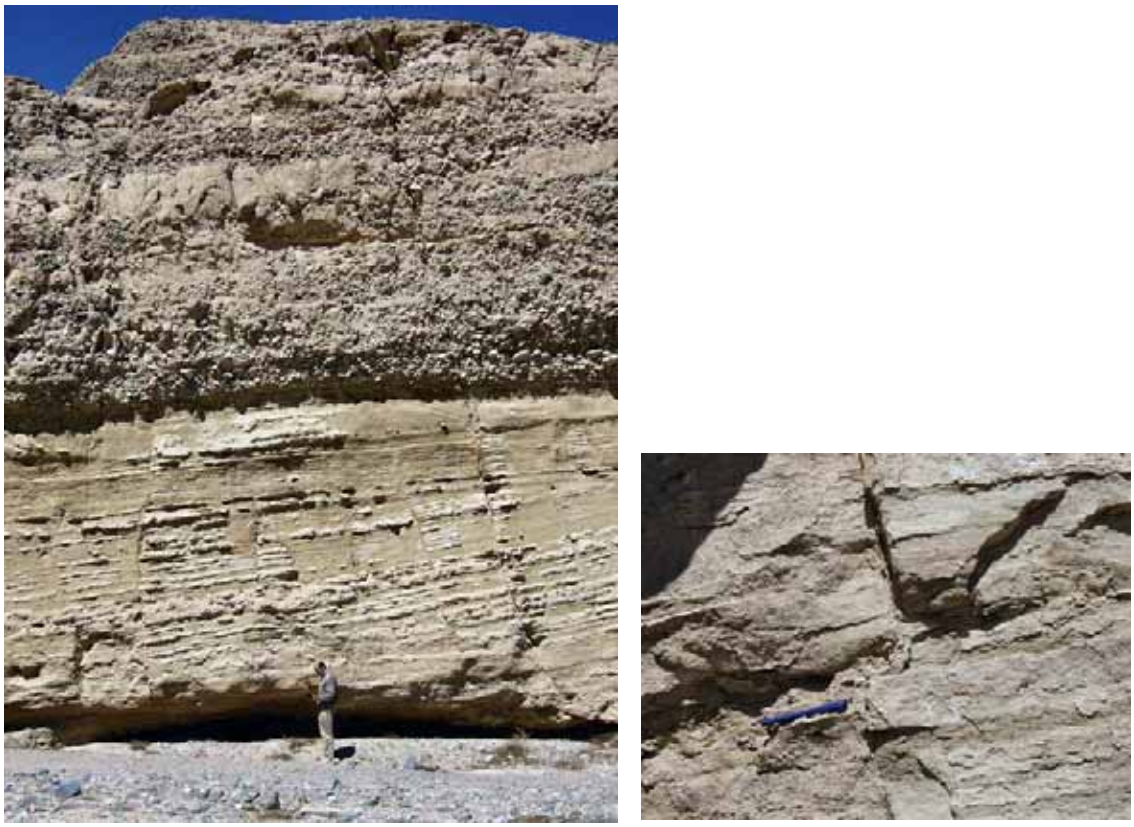

Fig. 4-40: *Terrace 12-13 m in wadi Gasus (left) and influences of neotectonics and evaporites laminas (right).*

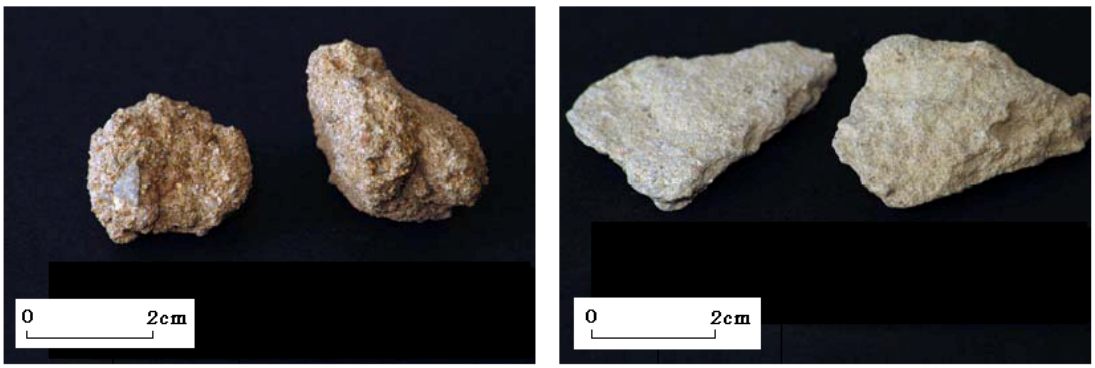

Fig. 4-41: *Microscopic views showing the heterogeneous materials (left) and the re-worked aeolianite-like (left).*

On the other hand, the wadi terraces are conspicuous along the coastline where they overlay the raised coral reefs (±6 m height) and/or salina deposits, which are all located within a complex Neogene rift frame (Plaziat et al. 1995). The most obvious sections usually found exposed in several locations on the sides of the main estuaries or at the wadi mouths. These terraces were investigated at the end of wadis Abu Safi (26° 26̀ 43″ N; 34° 05̀ 23″ E) and Umm Ayish (26° 28̀ 58″ N; 34° 04̀ 45″ E). The section of wadi Abu Safi overlays a 7 m height raised coral reef and attains about 1.2 m thick. At its base, the section is characterized by a sequence of fine to medium consolidated gravels, which are mostly of fluvio-marine origin owing to their roundness and flattened shapes. Thereafter, it is dominated by a sequences of sands occasionally interbedded with gravels and, at least, two thinly duricrusts are distinguished. The hard crusts confined to few centimeters thick (1-3 cm) indicating short periods of evaporation (Fig. 4-42).

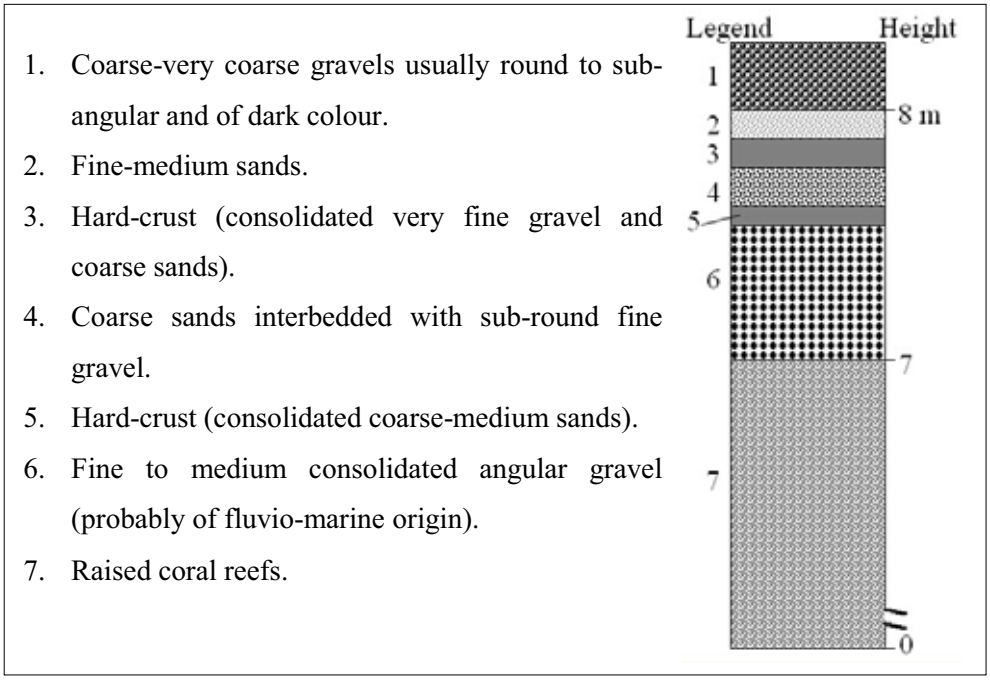

Fig. 4-42: *Showing the alluvial deposits overlaying the coastal raised coral reefs at the mouth of wadi Abu Safi.*

It may be concluded that such successions of different sizes and materials were deposited under an oscillatory climate distinguished by irregular precipitation. The climate was probably, to some extent, similar to the present day climate but it was a little bit wetter than today.

Eventually, it is believed that the wadi terraces along the Egyptian Red Sea coast belonging to the Pleistocene time. This resets essentially on the implements of the Palaeolithic age, which were found buried in the alluvial gravels and well described in the classical works of Seligman (1921), Sandford & Arkell (1929), Murray (1951), and Hayes (1964). These works concluded some facts, which could be stated as follows:

- Seligman (1921) pointed out series of implements discovered by Murray from the gravels of the alluvial fans at Hammama, Wasif, and wadi Dib in the Eastern Desert, which are belonging to the older Palaeolithic age. He is of the opinion that the main earth-sculpture had taken place before middle Pleistocene.
- Sandford & Arkell (1929) found Mousterian[1] implements in situ in gravel terraces in wadi near, and draining into, the Red Sea near El Quseir. They documented that the wadi gravels pass into raised beaches and raised coral reefs.
- Terraces of wadi Qena have been defined by Sandford (Ball, 1939) at heights of 34, 15, 9, and 3 meters above the wadi floor. From which Sandford concluded the associated flint implements to be of Chellean[2], pre-Mousterian, early Mousterian and late Mousterian age respectively.
- Sandford & Arkell (1939) assumed that the Palaeolithic implements found in wadis Hamraween and Ambagi at 4, 5-3 m terraces belonging to middle Palaeolithic.
- Murray (1951) pretended that during early Pleistocene, the rain was eroding the limestone plateaus of the Eastern Desert and lining its watercourses with gravel terraces.
- Hayes (1964) pointed out that the Acheulian implements are encountered alone in the Eastern Desert at many places of which Rabah and Wasif are distinctive and in the vicinity of the Red Sea coast. According to him, the Middle Palaeolithic work or camp-sites have been observed at Rabah and Wasif and near the coast of the Red Sea as well.

---

[1] *The Palaeolithic age is usually divided into three subdivisions:*
-Lower Palaeolithic (2,500,000 - 300.000 / 250,000 bp. approx.) known in Europe as Abbevillian, formerly Acheulean.
-Middle Palaeolithic (300,000 - 40.000 / 30,000 bp. approx.) known as Mousterian.
-Upper Palaeolithic (40,000 - 11,000 / 10.000 bp. approx.).

[2] *An early Stone Age industry characterized by crudely worked hand axes. The implements from Chelles in France that gave the industry its name are now grouped with the Acheulian industry. The term Chellean, in the sense of earliest hand-ax culture, has been replaced by Abbevillian industry.*

▪ Dittmann (1990) denoted a stone place (Steinplatz) southeast of Safaga city near the coast. Ashes and charcoals, which were found in this place, are dated by C^{14} to 3.880 ±65 BP. He thinks that during the early Palaeolithic the climate of the northern Eastern Desert was semi-arid and favoured for wild-life like the present day one in Sahel and southwest Africa. He assumed that the main wadi deposits at wadi El Deir should have been accreted after the middle Palaeolithic period (80.000- 35.000 yr BP)

▪ In wadi Hamraween, a side scraper implement was found on the wadi floor. It is made of flint (Fig. 4-43). According to its shape, the implement mostly belongs to middle Palaeolithic time.

Fig. 4-43: *Side scraper implement found in wadi Hamraween.*

Where the alluvial deposits overlay and/or cover the Miocene and Pliocene formations in many parts, thereupon they belong to Quaternary. So far as I know, no absolute dating has been given to the wadi terraces along the Red Sea coast based on a definite dating method. However, there are several publications concerning dating the raised coral reefs along the Egyptian Red Sea coast. Relying on such that, wadi terraces of the study area could be dated relatively to such raised corals but first of all one should keep in mind the following postulates:

▪ The peripheral parts of the NW Red Sea rift were inactive during the last 120.000-150.000 years (Hoang & Taviani, 1991, Arvidson et al. 1994, El Moursi et al. 1994, Plaziat et al. 1995, and Orszag-Sperber et al. 2001). This implies that most of the raised corals are a result of eustatic sea level changes and some of which underwent local uplift such as in Jabal Zeit at the southern Gulf of Suez.
▪ Developing of the raised coral reefs mostly occurred during the interglacial periods of high sea stands. On the other hand, wadi terraces of the same levels as the raised corals should have been deposited as alluvial plains during the same interglacial periods and they should have been detached and incised by streams during the glacial periods accompanied by lowering sea level. This is a very important issue for distinguishing between time of initiation and time of dissection. Therefore, dissection and construction of two successive terraces at different heights were probably synchronous.

Pursuantly to that above, terraces of wadi al-Ambagi could be relatively dated as follows:

▪ Terrace **I** is corresponding to the coral terrace (0- 0.8; 1 m asl), which has developed during the Holocene high sea level and has remained at or about the present sea level for the last 5.000 yr (El-Asmer, 1997 after Carter, 1988, El Moursi et al. 1994). It is suggested that it has developed when the sea level attained its present day level about 4.000 yr BP (El-Asmer, 1997). Choukri et al. (2002) gives such corals an age ranging between 4.000 to 7.300 yr BP with an average value of 5.240 ±0.91yr BP. Along the Jordanian Gulf of Aqaba, the Holocene corals ranging between 3.070 ±49-3.171 ±27 yr BP (Scholz, 2005).

▪ Terrace 4.5-5 m is probably corresponding to the last interglacial (5e) reefs (8 m asl) north of El Quseir (Plaziat et al. 1995) and it is in accordance to Pleistocene reefs at Ras Jemsah at +13.5 m, which is dated between 124.700 (+7.6, -6.4) and 125.500 (5.8, -5.5) yr BP (Plaziat et al. 1995). Moreover, Arvidson et al. (1994) pointed out raised corals of 6-8 m asl, which back to 120.000 yr BP. It may be, as well, in accordance with the youngest system that is found at +6 to +8m at Zabargad and northern Brother Islands by Hoang & Taviani (1991) those postdate between 125.000-138.000

yr BP. The terrace is also equivalent to the coral terrace of 3-6 m asl in South Sinai, which is equated with the last interglacial where the global sea level was about 2-6 m asl (El-Asmer, 1997). Finally, it could be concluded that this terrace was formed corresponding to 5e climatic substage (emian: Riss-Würm or Sangamon interglacial) that is dated between 115.000-130.000 yr BP approximately.

▪ Terrace 10, 12-13 m seemingly correlates to the raised coral reefs of 10-12 m along the Red Sea coast, which are postdated between 200.000-320.000 yr BP high-stands (Arvidson et al. 1994). It may be compatible as well with the oldest raised corals at Zabargad and northern Brother Islands at elevations of +10 to +15 m, which have been distinguished by Hoang & Taviani (1991) and are dated to >290.000-300.000 yr BP. In addition, the terrace is equivalent to the same coral terrace in South Sinai (10-12 m asl), which is dated to late middle Pleistocene stage 7 (200.000 yr BP) (El-Asmer, 1997). However, the dates indicating an age of Holstein interglacial period (Mindel-Riss/Yarmouth) during middle Pleistocene that is mostly dated between 200.000-300.000/380.000 yr BP.

▪ Concerning terrace 20-21 m, it may be equivalent to the patches coral terrace at height of 25-35 m asl that are distinguished by El-Asmer (1997) along Sharm El Sheikh-Ras Mohamed Road in southern Sinai. El-Asmar supposed that it is older than 300.000 yr BP and related to isotope stage 11 where the sea level was about 13-20 meters above the present-day sea level as a result of melting the ice sheets of Greenland and west Antarctica (Droxler et al. 2003). However, the terrace should be older than the third one and, therefore, it can be dated older than 300.000 yr BP. In that manner, it may be corresponding to the oldest cycle of reefs distinguished by El Moursi et al. (1994) that is ranging in age between 300.000-330.000 yr BP, although the elevation of these corals is not in accordance with the elevation of the terrace.

7.4. Microforms.

Numerous fluvial microforms are also noticed whether in the field or from the satellite images and the topographic maps. From which braided streams and gorges are the most conspicuous. Braided streams are common in the wadi floors as a result of irregular runoff. They are usually of brighter colours on the satellite image than the surrounding deposits. They are a result of an extreme reduction in water velocity and

rapid deposition on the wadi floor. The deposits are normally fashioning bars and/or islands of gravels and/or sands, which are of few centimetres high above the modern channel. However, they are of a great mobility and changing significantly during flood events because of the lateral movement of the channels via differential runoff velocity (Fig. 4-44).

On the other hand, gorges are yielded where the drainage network incises through the basement rocks adhering to a straight structure segments. Therefore, some channels manifest deep narrow passage (ravine-like) with steep rocky sides (Fig. 4-45). Gorge-like form of wadi Sodmein is well known from previous works. Wadi Sodmein incises through Jabal Duwi separating it into two major fault-blocks. The sides of the gorge ranging in elevation between 150-60 m above the wadi floor and the wadi is inferred as antecedent (Fig. 4-46).

Fig. 4-44: *Braided streams in wadi Safaga.* *(Google Earth 2006, view elevation 895 m)*

Fig. 4-45: *An incised reach of wadi Umm Taghir.*

Fig. 4-46: *Gorge of wadi Sodmein.* *(Looking towards the east)*

References:

Abdel-Rahman, M. A., El-Etr, H. A. & Yousif, M. S. M. (1979) Quantitative analysis of lithological effects upon some drainage network parameters in the Central Eastern Desert, Egypt. *Egyptian Computer Science Jour. V. II, No. 1.*

Arvidson, R., Becker, R., Shanabrook, A., Luo, W., Sturchio, N., Sultan, M., Lotfy, Z., Mahmood, A., & El Alfy, Z. (1994) Climatic, eustatic and tectonic controls on Quaternary deposits and landforms, Red Sea, Egypt. *Journal of Geophysical Research, Vol. 99, No. B6, pp. 12,175-12,190.*

Ball, J. (1939) Contribution to the geography of Egypt. *Survey & Mines Department, Gov. Press, Cairo, 308 p.*

Braithwaite, C. J. R. (1984) Geology and paleography of the Red Sea region. In: Edwards, A. J. & Head, S. M. (ed.) Red Sea, *Pergamon Press, Oxford, pp. 22-44.*

Bras, R. L. (1990) Hydrology: an introduction to hydrologic science. *Addison-Wesley, 660 p.*

Butzer, K. W. & Hansen, C. L. (1968) Desert and river in Nubia, geomorphology and prehistoric environments at the Aswan Reservoir. *The University of Wisconsin Press, London, 560 p.*

Chorley, R. J. (1969) Introduction to fluvial processes. *Methuen and Co. Ltd. London, 218 p.*

Choukri, A., Reyss, J-L., Hakam, O-K., & Plaziat, J-C (2002) A statistical study of ^{238}U and $^{234}U/^{238}U$ distributions in coral samples from the Egyptian shoreline of the northwestern Red Sea and fossil mollusc shells from the Atlantic coast of High Atlas in Morocco: Implications for $^{230}Th/^{234}U$ dating. *Radiochim, Acta, Vol. 90, pp. 329-336.*

Dittmann, A. (1990) Zur Paläogeographie der ägyptischen Eastern Desert. *Marburger Geographische Schriften, Heft 116, Marburg/Lahn, 174 s.*

Dowling, T. I., Richardson, D. P., O'Sullivan, A., Summerell, G. K. and Walker, J. (1998) Application of the hypsometric integral and other terrain based metrics as indications of catchment health: a preliminary analysis. *CSIRO Land and Water, Canberra, Australia, 49 p.*

Droxler, A. W., Poore, R. Z., & Burckle, L. H. (ed.) (2003) Earth's climate and orbital eccentricity: the tarine isotope stage 11 question. *Geophysical Monograph Series, Vol. 137, 240 p.*

El Moursi, M., Hoang, C. T., El Fayoumy, I. F., Hegab, O., & Faure, H. (1994) Pleistocene evolution of the Red Sea coastal plain, Egypt: evidence from uranium-series dating of emerged reef terraces. *Quaternary Science Reviews, Vol. 13, pp. 345-359.*

El-Asmer, H. M. (1997) Quaternary isotope stratigraphy and paleoclimate of coral reef terraces, Gulf of Aqaba, South Sinai, Egypt. *Quaternary Science Reviews, Vol. 16, pp. 911-924.*

Embabi, N. S. (2004) The geomorphology of Egypt: landforms and evolution, *Vol. 1, The Egyptian Geographical Society, Cairo, 447p.*

ESRI (1992) Cell-based modeling with GRID 6.1: supplement hydrologic and distance modeling tools. *ESRI. Inc. pp. 1-17.*

Hayes, W. C. (1964) Most Ancient Egypt: chapter II. Paleolithic Man in Egypt. *Journal of Near Eastern Studies, Vol. 23, No. 3, pp. 145-192.*

Hoang, C. T. & Taviani, M. (1991) Stratigraphic and tectonic implications of uranium series-dated coral reefs from uplifted Red Sea islands. *Quaternary Research, Vol. 35, Issue 2, pp. 264-273.*

Horton, R.E. (1945) Erosional development of stream and their drainage basins: hydrophysical approach to quantitative morphology. *Geological Society of America Bulletin, v. 56, pp. 275-370.*

Hurtrez, J. E., Sol, C. & Lucazeau, F. (1999) Effect of drainage area on hypsometry form an analysis of small-scale drainage basins in the Siwalik hills (Central Neapal). *Earth Surf. Process. Landforms. Vol. 24, pp. 799-808.*

Issawi, B., Francis, M., El Hinnawy, M., Mehanna, A. & El Deftar, T. (1971) Geology of Safaga-Quseir coastal plain and of Mohamed Rabah area. *Ann. Geol. Surv. Egypt. Vol. 1. 19 p.*

Issawi, B. & McCauley, J. (1993) The Cenozoic landscape of Egypt and its river system. *Annals Geol. Survey Egypt, v.19, pp. 357-384.*

Máčka, Z. (2001) Determination of texture of topography from large scale contour maps. *Geografski vestnik 73-2, pp. 53-62.*

Mackay, D. S. & Band, L. E. (1998) Extraction and representation of nested catchment areas from digital elevation models in lake-dominated topography. *Water resources research, vol. 34, No. 4, pp. 897-901.*

Maidment, D. (ed.) (2002) Arc hydro: GIS for water resources. *ESRI. 222 p.*

Maidment, D.R. (1993) Handbook of hydrology. *McGraw-Hill, Inc. New York, 1424 p.*

Martinez-Casasnovas, J. A. & Stuiver, H. J. (1998) Automatic delineation of drainage networks and elementary catchments from digital elevation models. *International Journal of aerospace Survey and Earth Sciences (ITC Journal), 1998-3/4, pp. 198-208.*

McCullagh, P. (1978) Modern concepts in geomorphology. *Oxford University Press, London, 128 p.*

Minabary, N. Y. (1991) Some geomorphological features along the Red Sea Coast, south of Suez Gulf- Egypt. *Unpub. Ph.D Thesis (in Arabic), Dept .of Geography, Faculty of Arts, Ain Shams University, Cairo, 454 p.*

Morisawa, M. E. (1962) Quantitative geomorphology of some watersheds in the Appalachian plateau. *Geol. Soc. America Bull. Vol. 73, pp. 1042-1045.*

Morisawa, M. E. (1985) Rivers. *Longman Inc. New York, 222p.*

Murray, G. W. (1951) The Egyptian climate: an historical outline. *The Geographical Journal. Vol. 117. No. 4, pp. 422-434.*

Nilsson, E. (1941) Die Eiszeit in Indien nach H. De Terra und T. T. Paterson: nebst einem Versuch zu einer zeitlichen Parallelisierung der quartären Klimaschwankungen in Indien, Ostafrika und Europa. *Geografiska Annaler, Vol. 23, pp. 1-23.*

Orszag-Sperber, F., Plaziat, J.-C., Baltzer, F., & Purser, B. H. (2001) Gypsum salina-coral reef relationships during the Last Interglacial (Marine Isotope Stage 5e) on the Egyptian Red Sea coast: a Quaternary analogue for Neogene marginal evaporates? *Sedimentary Geology, Vol. 140, pp. 61-85.*

Phillipson, D. W. (2005) African archaeology. *3rd ed. Cambridge University Press, 389 p.*

Plaziat, J-C., Baltzer, F., Choukri, A., Conchon, O., Freytet, P., Orszag-Sperber, F., Purser, B., Raguideau, A. & Reyss, J-L. (1995) Quaternary changes in the Egyptian shoreline of the northwestern Red Sea and Gulf of Suez. *Quaternary International, Vol. 29/30, pp. 11-22.*

Purser, B. H. & Bosence, D. W. J. (ed.) (1998) Sedimentation and tectonics in rift basins Red Sea-Gulf of Aden. *Chapmen & Hall, 663 p.*

Said, R. (1993) The River Nile: geology, hydrology and utilization. *(In Arabic), 2ed edition, Dar El Hilal, Cairo, 342 p.*

Saito, K. & Oguchi, T. (2005) Slope of alluvial fans in humid regions of Japan, Taiwan and the Philippines. *Geomorphology, Vol. 70, pp. 147-162.*

Sandford, K. S. & Arkell, W. J. (1929) On the relation of Paleolithic man to the history and geology of the Nile Valley in Egypt. *Man, Vol. 29, pp. 65-69.*

Sandford, K. S. & Arkell, W. J. (1939) Paleolithic man and the Nile Valley in Lower Egypt, with some notes upon a part of the Red Sea littoral. *The University of Chicago Press, Chicago, Orient. Inst. Publ. 46..*

Sarangi, A., Bhattacharya, A. K., Singh, A. & Singh A. K (2001) Use of geographic information system (GIS) for determination of erosion status of watersheds. *Indian Journal of Soil Conservation,* 29(3), pp.190-195.

Sarangi, A., Madramootoo, C. A. & Enright, P. (2003) Development of user interface in ArcGIS for estimation of watershed geomorphology. *CSAE/SCGR, Meeting Montréal, Québec, July 6 - 9, 34 p.*

Scholz, D. (2005) U-series dating of diagenetically altered fossil reef corals and the application for sea level reconstructions. *Ph.D. thesis, Combined Faculties for the Natural Sci-*

ences and for Mathematics of the Ruperto - Carola University of Heidelberg, Germany, 172 p.

Schumm, S. A. (1956) Evolution of drainage systems and slopes in badlands at Perth Amboy, New Jersey. *Geol. Soc. Amer. Bull. vol.67, pp. 597-646.*

Seligman, C. G. (1921) The older Paleolithic age in Egypt. *The Journal of the Royal Anthropological Institute of Great Britain and Ireland, Vol. 51, pp. 115-153.*

Smith, K. G. (1950) Standards for grading texture of erosional topography. *Amer. J. Sci., 248, pp. 655-668.*

Smith, P. E. L. (1966) The Late Paleolithic of Northeast Africa in the light of recent research. *American Anthropologist*, *New Series, Vol. 68, No. 2, Part 2.*

Strahler, A. N. (1952) Hypsometric (area-altitude) analysis of erosional topography. *Geological Society of America Bulletin, 63, pp. 1117-1141.*

Strahler, A. N. (1957) Quantitative analysis of watershed geomorphology. *Am. Geophys. Union. Trans. 38 (6), pp. 913-920.*

Strahler, A. N. (1958) Dimensional analysis applied to fluvially eroded landforms. *Bull. Geol. Soc. Am., vol. 69, pp. 279-300.*

Strahler, A. N. (1964) Quantitative geomorphology of drainage basins and channel networks. *In Chow, V. T. (ed.): Handbook of applied hydrology, McGraw-Hill, New York, pp. 439: 476.*

Tarboton D. G., Bras, R. L. & Rodriguez-Iturbe, I. (1991) On the extraction of channel networks from digital elevation data. *Hydrological Processes, Vol. 5, pp. 81-100.*

Tarboton, D. (2000) Distributed modeling in hydrology using digital data and geographic information systems. *Course presented at the University of Padua May 15 to 26, 2000.*

Tucker, G. E. & Bars, R. L. (1998) Hillslope processes, drainage density and landscape morphology. *Water Resources Research, Vol. 34, No. 10, pp. 2751-2764.*

Wang, X. & Yin, ZY. (1997) An evaluation of using ArcInfo to extract basin physiographic parameters from DEMs. *http://gis.esri.com/library/userconf/proc97/proc97/to250/pap-215/p215.htm. (Accessed on 26. Sept. 2006).*

Weissel, J. K., Pratson, L. F. & Malinverno, A. (1994) The length-scaling properties of topography. *Journal of Geophysical Research, Vol. 99, pp. 13997-14012.*

Yehia, M. A., Ashmawy, M.H., El-Etr, H.A., Abdel Monsef, H., El Shamy, I.Z., Hermas, E.A., Higazy, M.N. & Hassan, S.M. (1999) Flash flooding threat to the Red Sea coast towns of Safaga, Quseir and Marsa El Alam, *Egypt. J. Remote Sensing & Space Sci., V. 2, pp. 69-86.*

5

FLASH FLOODS: ASSESSMENT AND VULNERABILITY ANALYSIS

The main purposes of this chapter are to analyze the community that induces exceptional runoff accompanied by flash floods and determining probability of annual occurrence and return period in a historical framework. Thereafter, verifying flood potentiality and clarifying the role of human agent in order to identify flood magnitude and vulnerable sites.

1. Data and Methods

Rainfall data are available for the period 1925-1997 for the coastal stations (Hurghada and El Quseir) and acquired from the Egyptian Meteorological Authority, Cairo. Rainy days are selected and reviewed by using the daily weather reports for the same period and other historical reports for picking out events that accompanied by flash floods. Primarily analysis of these data revealed that runoff will ordinary occur in the study area owing to exceptional torrential rainfall. However, due to deficiency of rain gauges over the Red Sea Mountains, maximum rainfall (P_{max}) is estimated by extrapolation of 37 rainfall records representing the maximum rainfall per day and rain gauges of the available meteorological stations in the central Eastern Desert and Nile Valley. Rain gauge records are processed after Gheith & Sultan (2002) for the year 1994. Using both data type (i.e. maximum rainfall per day and rain gauge data) is owing to the fact that rainfall over the Red Sea Mountains is generally higher than the rainfall in the coastal stations. In that manner, Gheith & Sultan (2002) revealed that on 2nd November 1994, 13 mm of rain were reported from Asyut airport rain gauge station that is located at 226 m asl compared to 8.6 mm reported from the nearby Asyut rain gauge station that is 52 m asl. They observed a general increasing about 25% in precipitation with elevation.

Data involved in the extrapolation process are irregularly spaced points, which have x, y coordinates describing their location and z-values describing the rainfall records.

Rainfall extrapolation is manipulated by using inverse distance weighted method (IDW) that is the most adequate for interpolation of scatter points. The IDW based on the assumption that the interpolation surface (i.e. maximum rainfall) should be mostly influenced by the nearby points and less by the more distant points. The output cell values would be determined using a linear-weighted combination set of sample points and the weight would assign to each scatter point diminishes as the distance from the interpolation point to the scatter point increases. As can be deduced from figure 5-1, the maximum rainfall varies greatly from 4.5 mm to 34 mm generally and equally varies from one basin to another between 24.2 mm at wadi Abu Sebekha and 34 mm at wadi Ambagi (Table 5-1).

***Table 5-1**: Analysis of rainfall and runoff.*

Wadi	P_{max} *(mm)*	*I (mm/hr)*	*A (km^2)*	*L (m)*	*S*	*Q (m3/sec)*	T_c *(hr)*
Barud	32.60	16.30	508.52	51238	0.027	182.75	5.51
Abu Asala	29.10	14.55	16.72	8237	0.081	5.36	0.88
Naqarah	27.00	13.50	54.73	18283	0.043	16.29	2.07
Umm Iffinah	26.50	13.25	25.70	16083	0.023	7.51	2.41
Safaga	26.99	13.50	750.41	68420	0.014	223.27	8.77
Gasus	25.60	12.80	156.82	31157	0.019	44.25	4.29
Abu Shiqily	25.10	12.55	169.21	27697	0.023	46.82	3.65
Abu Sebekha	24.20	12.10	48.52	15016	0.023	12.95	2.27
Quieh	25.80	12.90	1892.65	86225	0.011	538.29	11.29
Abu Hamza	27.30	13.65	93.85	21310	0.016	28.24	3.40
Hamraween	28.20	14.10	81.61	21973	0.030	25.37	2.76
Ambagi	34	17	818.95	7789	0.137	311.86	0.69

P *max. rainfall* ***A*** *drainage area* ***S*** *watershed gradient* ***Q*** *peak discharge*
I *rain intensity* ***L*** *basin length* T_c *time of concentration*

Rainfall intensity *(I)* is calculated by dividing the maximum rainfall (P_{max}) by rain duration *(t)*. Because of the rainfall data represent the maximum amount per 24 hour, which is not consistent to the actual status in view of the fact that such storms disperse within few hours, average rain duration is assumed to be two hours that are within the range of storms observed in the general region (e.g. Gheith & Sultan, 2002; Foody et al. 2004). Accordingly, rain intensity varies from 12.10 mm/hr for wadi Abu Sebekha to 17 mm/hr for wadi Ambagi with general average 13.85 mm/hr. Rainfall

intensity is observed for the nearby Quseir station of the Egyptian Meteorological Authority on 14th November 1996 as 30 mm/hr (Foody et al. 2004).

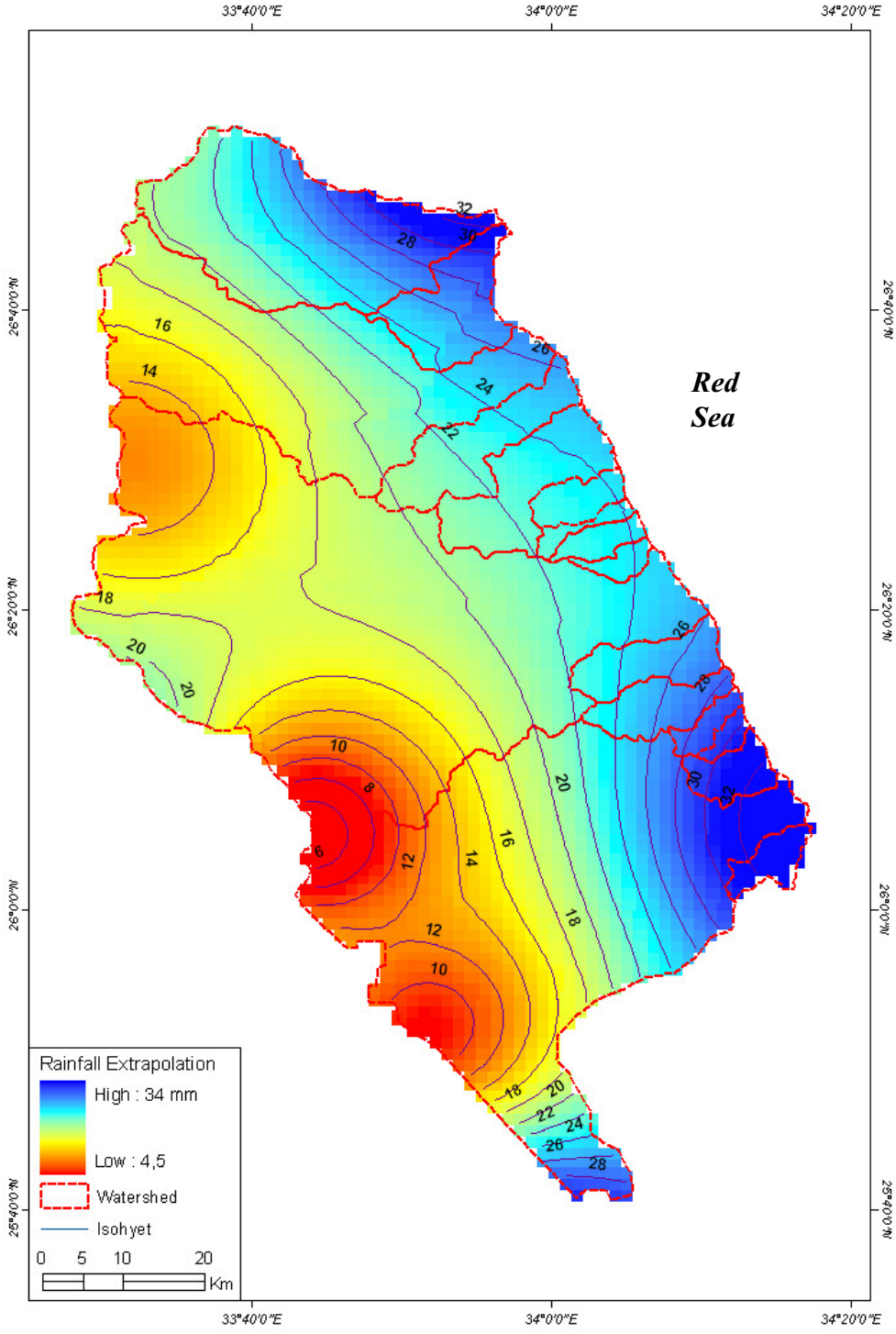

Fig. 5-1: *Extrapolated isohyetal map.*

2. Runoff Prediction and Analysis

Various empirical methods are examined for predictiing and analyzing drainage run-off of which peak discharge and time of concentration are the most convenient for the study area.

2.1. Peak Discharge.

Rational method is widely used for estimation of peak discharge because it is simple and easy to apply. The method determines peak discharge by using rainfall intensity, watershed area and a coefficient of runoff regardless of infiltration, surface detention, and time of concentration. Peak discharge is estimated using the following equation (Trommer et al. 1996):

$$Q = 0.0028\ CIA$$

Where:

Q = the peak discharge m^3/sec.

0.0028 = conversion coefficient from cubic-feet to cubic-meter.

C = coefficient of runoff that is related to surface and soil characteristics.

I = average rainfall intensity in inches per hour.

A = drainage area in acres.

Coefficient of runoff (C) used in the initial estimates based on the prepared tables as 0.80 *(Appendix I)* in the study area representing poorly drained watersheds and shallow soil, which covers impervious rocks. As a result, peak discharge varies between 5.36 m^3/sec for wadi Abu Asala and 538.29 m^3/sec for wadi Ambagi (Table. 5-1). Three categories could be distinguished as (Fig. 5-2a):

- Low peak discharge (Q< 10 m^3/sec) including wadis Abu Asala and Umm Iffinah.
- Intermediate peak discharge (10< Q <50 m^3/sec) including wadis Naqarah, Gasus, Abu Shiqily, Abu Sebekha, Abu Hamza and Hamraween.
- High peak discharge (+100 m^3/sec) including wadis Barud, Safaga, Queih, and Ambagi.

2.2. Time of Concentration.

Time of concentration is the time required for water to flow from the most points of the drainage area to the outlet once the soil has become saturated and minor depressions filled. It is assumed that when the duration of the storm equals to time of concentration all parts of the watershed would contribute water simultaneously to the discharge at the outlet. Time of concentration is computed using Kirpich's equation (1940) as follows:

$$\mathcal{T}_c = 0.0195\ \mathcal{L}^{0.77}\ \mathcal{S}^{-0.385}$$

Where:

$\mathcal{T}_c$= time of concentration in minutes.

$\mathcal{L}$ = maximum length of flow in meters.

$\mathcal{S}$ = watershed gradient or difference in elevation between the outlet and the most remote point divided by the length $\mathcal{L}$.

In view of that, average time of concentration is about 4 hrs and varying greatly from 0.69 hr (41.5 minutes) to 11.29 hrs (677.24 minutes) for wadis Ambagi and Queih respectively (Fig. 5-2b).

Time of concentration is divided into low ($\mathcal{T}_c \leq 6$ hrs), intermediate (6-10 hrs), and high (+10 hrs). Accordingly, 83.3% of the drainage basins are of low time of concentration; they are: Barud, Abu Asala, Naqarah, Umm Iffinah, Gasus, Abu Shiqily, Abu Sebekha, Abu Hamza, Hamraween, and Ambagi. Wadi Safaga is of intermediate time of concentration and wadi Queih is of high time of concentration.

3. Historical Background

Flash floods that influenced the study area are revised in a historical context based on climatological normals and historical documents. Table 5-2 summarizes the major events, which have been occurred since 1925 such as rain amounts, the general situation, and casualties. A synoptic view to the events revealed the following statements:

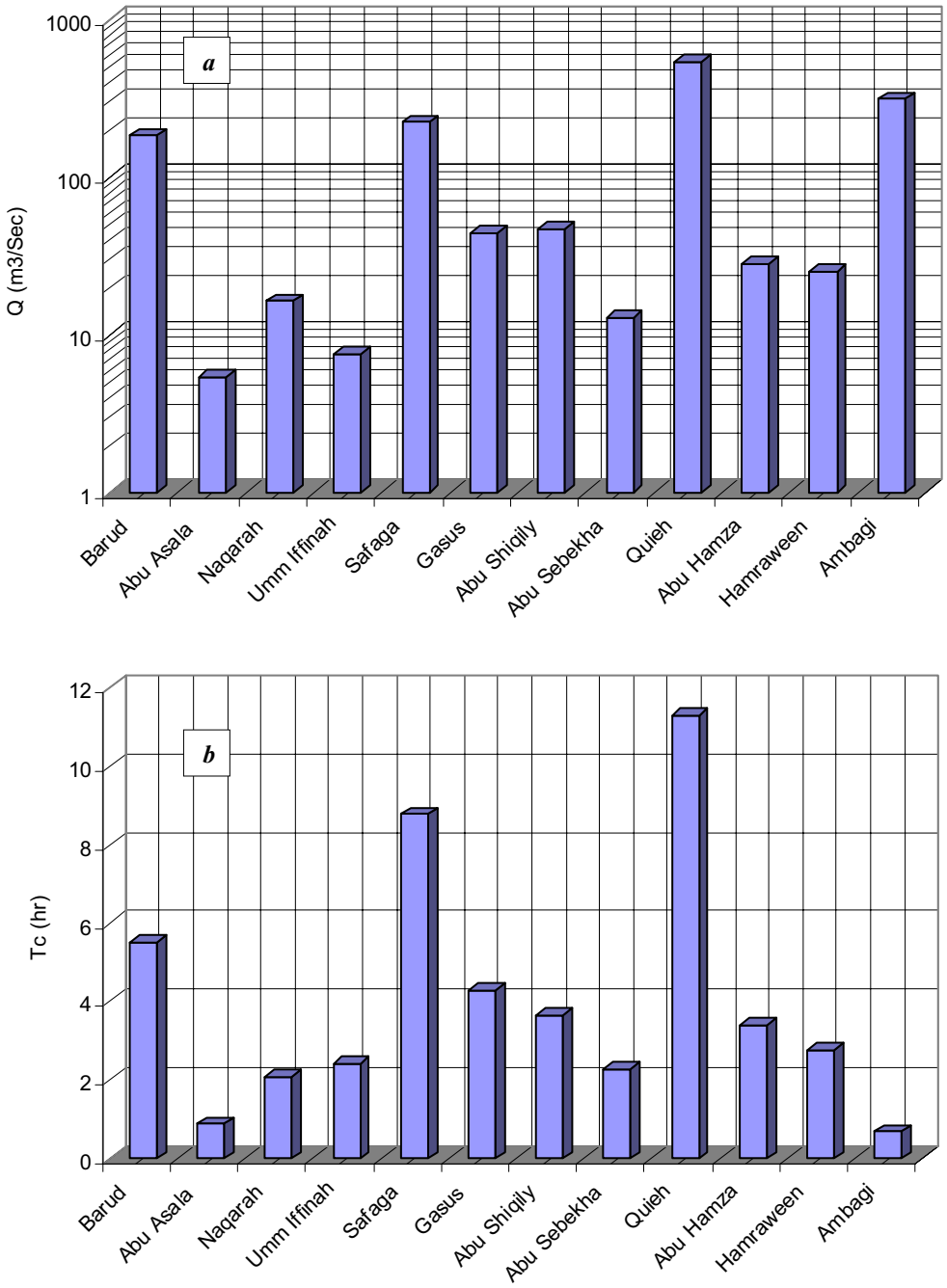

Fig 5-2: *Peak discharge (a) and time of concentration (b).*

Table 5-2: *Extreme rainfall events (1925-1997).*

Date	*Hurghada*	*Safaga*	*Quseir*	*Red Sea*	*General Situation & Casualties*
18 November1925		Heavy rain?			A torrential flash flood swept away houses and livestock at port Safaga and the rain was so heavy affected several places such as Abbassiya, Jabal El Ahmar, Banha and Damietta accompanied with thunder and lightning. The reported rainfall was about 11 mm at Suez.
December 1930			15		
06 November1934	2		34		
08 November1939	42		2		
December 1941	9,2				
November 1944			20		
28 Oktober 1945			11		
31 Mars 1953			9		
December 1954				17	
December 1955				12	Light thundery rain affected Hurghada and El Quseir.
January 1956				16	
June 1965			60		
07/10 October 1969	2,7		8,3		Heavy rain led to flash floods on Lower Egypt, Giza, Beni Suwayf and Aswan.
19/20 February 1975	11		0,3		Heavy rain led to flash floods on Upper Egypt (Beni Suwayf, Minya, Asyut, Sohag) and the Eastern Desert.
3 May 1979	6		20,6		Flash floods partially damaged the railway and settlements in Upper Egypt particulary in Aswan and Kom Ombo.
20 October 1979			10		Flash floods partially damaged Qena-Safaga intermountain road and the settlements in El Quseir, Mersa Alam and Aswan. 19 persons died and about 500 livestock perished as well. The rainfall attained 48 mm in Ras Benas.
16 October 1987	4,3		10,1		
20 October 1990	10				Flash floods damaged the coastal highway and locked Safaga harbour. The rainfall got 60 mm at Ras Benas.
12 October 1991					Heavy rain contributing flash flood and affected Mersa Alam for 7 hours and discharged about 37.000 m^3 of water and about 20.000 m^3 deposits towards the town.
02 November 1994			4,5		Heavy rain contributing flash floods on Asyut governorate and the Eastern Desert. Floods led to fissure about 5191 houses at Hammraween and Umm Al Hawaytat villages, stoppage mining activities and damaged the asphaltic road of wadi Gasus. The rainfall attained 35.3 mm in Ras Benas on the Red Sea Coast and about 58.4 mm over the mountains near El Quseir and 12.1 mm in Hurghada.
9-14 November 1996			27		Heavy rain contributing flash floods on Mersa Alam partially damaged Idfu-Mersa Alam road, Qena-Safaga road and the coastal highway of the Red Sea. On the other hand, the floods damaged the settlement of Mersa Alam and broken-down the electricity circuit and water desalination station in Hurghada.
18 October 1997			20		

Rainfall in millimeters.
Source: assembled from various sources.

▪ Dating flash floods in the study area is prior to the commencement date of Hurghada and El Quseir meteorological stations that have been established since 1927.

▪ Data committed in the table represents extreme rainfall events at the coastal plain where Hurghada and El Quseir stations elevate +3 and +7 m asl successively. The rainfall amounts over the Red Sea Mountains could be estimated by incrementing about 25% according to Gheith & Sultan (2002).

▪ Reviewing the daily climatological reports depicts that such extreme rainfall accompanied by thunder storms affected different parts of Upper and Middle Egypt and the Red Sea coast as well.

▪ Verification of the historical documents revealed that flash floods have taken place during such storms and caused property and victim casualties during the years 1925, 1955, 1969, 1975, 1979, 1990, 1991, 1994, and 1996.

▪ Other extreme events are committed in the table but without mentioning whether they accompanied by flash floods or not. Such events are reported during the years 1930, 1934, 1939, 1941, 1944, 1945, 1954, 1956, and 1965. A comparison of the maximum rainfall of these years with the former ones manifest that flash floods might have been taken place since the rainfall varies from 9.2 mm at Hurghada during 1941 and 60 mm at El Quseir during 1965.

▪ During the committed years, flash floods partially influenced the study area where the rainfall was not equivalent at both stations. For instance, on 06th November 1934 El Quseir station received 34 mm, whereas Hurghada received only 2 mm on the same date.

▪ During the period 1954 - 1956 the records satisfied mentioning the rainfall over the Red Sea regardless of mentioning the observed stations.

▪ Number of extreme events is relatively higher in El Quseir (13 events) started since 1930 to 1996 and attain a frequency of one event every 5 years. In Hurghada the events are confined to 7 events started since 1925 to 1997 and attain a frequency of one event every 10.2 years with the exclusion of the years 1954, 1956 and 1991.

▪ The committed events have been occurred throughout the year with the exception of months July and August and frequently occurred during October (7 times), November (6 times), and December (4 times).

▪ The maximum rainfall reported is about 60 mm in El Quseir during June 1965 and 42 mm in Hurghada during November 1939.

3.1. Probability of Annual Occurrence and Return Period.

Rather than the simple frequency mentioned before, probability of annual occurrence and return period are calculated based on the following equations (FAO, 1991):

$$\mathcal{P}(\%) = (m-0.375) / (\mathcal{N}+0.25) x100$$

$$\mathcal{T} = 100/\mathcal{P}$$

Where:

$\mathcal{P}$ = probability in percentage of the observation of the rank m.

m = rank of the observations where $m = 1$ for the largest and $m = 21$ for the lowest.

$\mathcal{N}$ = total number of observations (21).

$\mathcal{T}$ = return period in years.

Number of events $(\mathcal{N})$ involved in the analysis is 21 events, which are reported in Hurghada, Safaga and El Quseir as shown in table 5-2. Rainfall over the Red Sea Mountains is estimated by increasing the maximum rainfall 25 % according to Gheith & Sultan (2002) (Fig. 5-3). Therefore, values less than 10 mm are excluded and missed value of the year 1925 is assigned to 10 mm as the minimum rainfall required for generating weak flash floods in the Eastern Desert (Ali, 2001). Subsequently, mountainous rainfall is ranked from 1 for the largest to 21 for the lowest and the probability is computed according to the former equation. The results reveal that probability of occurrence is high (92.3 %) where the rainfall over the Red Sea Mountains equals to 10 mm and it is very low (2.9 %) where the rainfall attains about 75 mm (Table 5-3). Plotting the ranked observations against the corresponding probabilities revealed linear relationship gives the possibility to obtain the probability of occurrence of a rainfall of a specific magnitude (FAO, 1991). Inversely, it is also possible to obtain the magnitude of the rain corresponding to a given probability (Fig. 5-4).

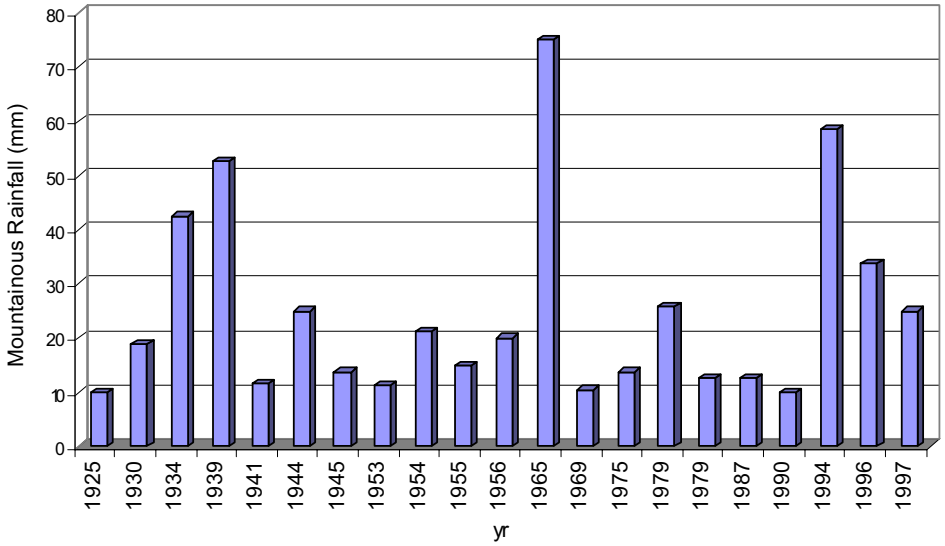

Fig. 5-3: *Approximate rainfall over the Red Sea Mountains (1925-1997).*

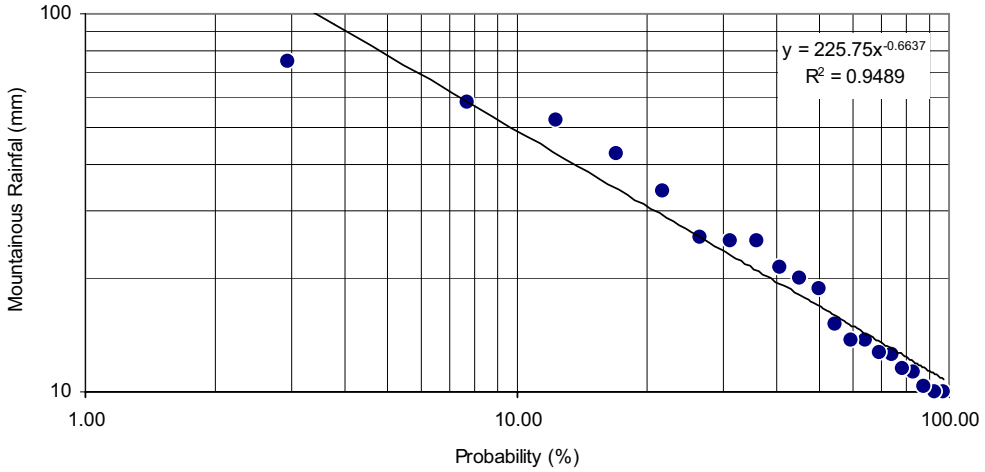

Fig. 5-4: *Probability of annual occurrence of the mountainous rainfall.*

On the other hand, the return period *(T)* or recurrence interval represents an estimation of the likelihood of a flash flood. Where it is proportional to rainfall, events of low rainfall (e.g. 10 mm) are estimated to occur every 1.3 yr because it is of the high occurrence probability (92 %). Inversely, events of high rainfall (e.g. 75 mm) are estimated to occur every 34 yr since it is of a very low probability (2.9 %). Likewise, Rainfall interval between each two successive events is computed in column one showing a great variation from 0.8 to 9 yr with general interval average of 3.4 yr.

Eventually, it could be concluded that the study area is frequently subjected to flash floods that are irregular in time and space since the rainfall is not equivalent from north to south.

Table 5-3: *Probability of annual occurrence and return period analysis.*

Interval (yr)	*Years*	*Max. Rainfall*	*Mountainous Rainfall*	*Rank*	*P (%)*	*T(yr)*
?	1925	-	*10	20	92.35	1.08
5	1930	15	18.75	11	50.00	2.00
4	1934	34	42.5	4	17.06	5.86
5	1939	42	52.5	3	12.35	8.10
2	1941	9.2	11.5	17	78.24	1.28
3	1944	20	25	7	31.18	3.21
1	1945	11	13.75	13	59.41	1.68
8	1953	9	11.25	18	82.94	1.21
1	1954	17	21.25	9	40.59	2.46
1	1955	12	15	12	54.71	1.83
1	1956	16	20	10	45.29	2.21
9	1965	60	75	1	2.94	34.00
4	1969	8.3	10.37	19	87.65	1.14
6	1975	11	13.75	14	64.12	1.56
2	1979	20.6	25.75	6	26.47	3.78
0.8	1979	10	12.5	16	73.53	1.36
8	1987	10.1	12.62	15	68.82	1.45
3	1990	-	*10	21	97.06	1.03
4	1994	4.5	**58.4	2	7.65	13.08
2	1996	27	33.75	5	21.76	4.59
1	1997	20	25	8	35.88	2.79

**Assumption value.*

*** Rain gauge at El Quseir after Gheith & Sultan (2002).*

4. The Synoptic Weather Pattern Leads to Torrential Rain

Based on the historical background, flash floods frequently affect the study area although its climatic regime spans from hyper-arid regions as previously mentioned in chapter one. In the view of the fact that a flash flood depends on a community of drainage basins, surface characteristics, and rainfall; it is worthy mentioning briefly the synoptic weather pattern leading to such exceptional torrential rainfall in the study area. Under very specific conditions the Red Sea coast is vulnerable to thunderstorms especially during October and November owing to movements of the Sudan monsoon depression (Red Sea trough) towards the north (El-Fandy, 1948). Although frequency

of these storms is small, sometimes they are very violent and accompanied by heavy rain and hail (Soliman, 1972). The Red Sea trough extends into the southern and eastern Egypt from equatorial eastern Africa, northward along the Red Sea. It is accompanied by a pronounced quasi-stationary upper-level disturbance trough that develops over Egypt and favouring the development of severe convection storms (Dayan & Morin, 2006).

Figure 5-5 reveals that such state was dominated over northern Red Sea during flash flood events for the period 1990-1997 and accompanied by general instability throughout the troposphere and Mesoscale Convection System (MCS) with warm air masses. Simultaneously, the subtropical jet stream (STJ) serves as a conveyor belt of moisture in mid-and upper tropospheric layers, often originating from tropical Africa (Kahana et al. 2002; Dayan & Morin, 2006).

Flash floods occurred on 2nd November 1994 for instance, were associated with the northward penetration of a zone with unusually strong convergence. Before the rainy day, the Inter Tropical Convergence Zone ITCZ was located to the north of its usual position over the tropical part of eastern Africa in northern of equator. Krichak et al. (2000) assumed that it could be the reason for excessive pumping air moisture of the tropical area into the mid-latitudes. However, El Desoki (1995) pretended that on 2nd November 1994 the Polar Jet Stream propagated and influenced the Upper Egypt.

Generally, it could be concluded that flash floods are an ordinary result of the instability condition, which dominates over northern Red Sea, accompanied by jet stream that pushes the moisture towards the upper and Middle Egypt. Usually, the rainfall is of torrential sporadic type, extremely irregular in time and space and varies greatly in intensity since it may be of 2 mm or more per minute (Soliman, 1972). It leads to flash floods, which have severe influences on the vital infrastructure along the coastal area such as roads, housing, electricity, harbours, tourist centers…etc.

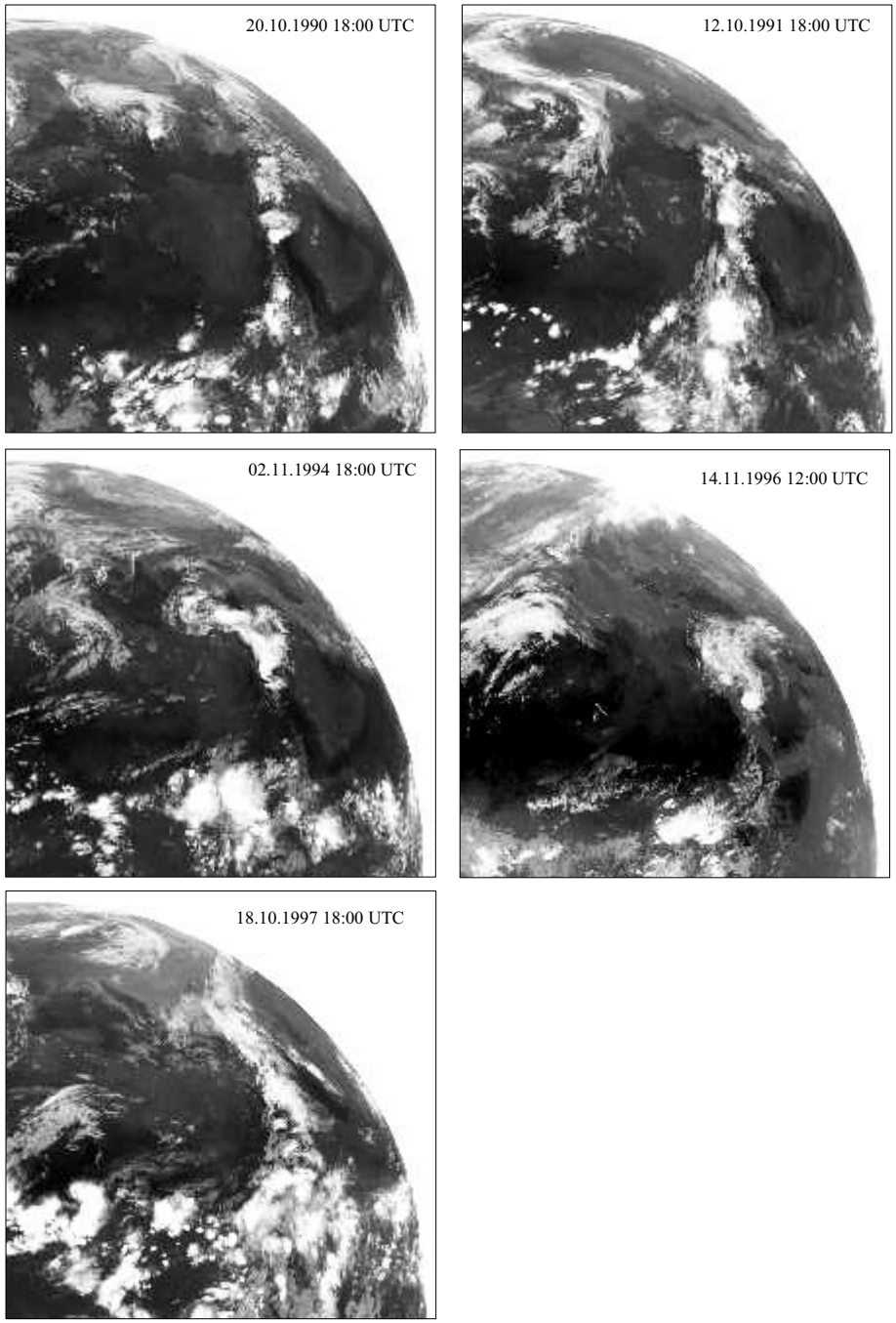

Fig. 5-5: *METEOSAT infrared images covering northern Red Sea showing convection clouds during the major flash flood events for the period 1990-1997.*

It is noticeable that disasters of the Red Sea storms not only confine to flash floods, but also occasionally dangerous for ferries crossing the Red Sea as well. For instance, on the 2nd February 2006 an Egyptian ferry carrying more than 1.300 people sank in the northern Red Sea as strong storms swept across the region. While the exact cause of the disaster was not certain, the most likely reason was bad weather and high seas. At the time of the incident, a potent storm was advancing eastward over Egypt and the eastern Mediterranean Sea. Out ahead of this advancing storm, strong southerly winds drew warm moist air up from the south. These conditions favour the development of severe storms (http://earthobservatory.nasa.gov).

The Tropical Rainfall Measuring Mission (TRMM) satellite observed the storm at 04:20 UTC on February 3, 2006 (6:20 a.m. in Egypt) (Fig. 5-6), just few hours after radar contact with the ferry was lost. The image shows the horizontal distribution of rain rates (top-down view) observed by the TRMM satellite. The image reveals that an intense thunderstorm complex had just come ashore on the Saudi Arabian coastline, after having crossed the northern Red Sea.

The storm complex contained a sizeable area of heavy rain, with rates of 50 mm/hr (dark red areas). Although a direct measurement of storm intensity was impossible, heavy rain, shape, and orientation of the storm indicating that the storm was severe. In this image, rain rates in the center swath are from the TRMM Precipitation Radar, while rain rates in the outer swath are from the TRMM Microwave Imager. The rain rates are overlaid on infrared data from the TRMM Visible Infrared Scanner (http://earthobservatory.nasa.gov).

5. Flash Flood Potentiality and Risk Assessment

Rate of discharge is specified by several morphometric variables, which characterize the drainage basins such as bifurcation ratio, stream frequency, drainage density, and basin shape. Flood potentiality assessment is based essentially on the significance of such variables and could be concluded as the following (Fig. 5-7):

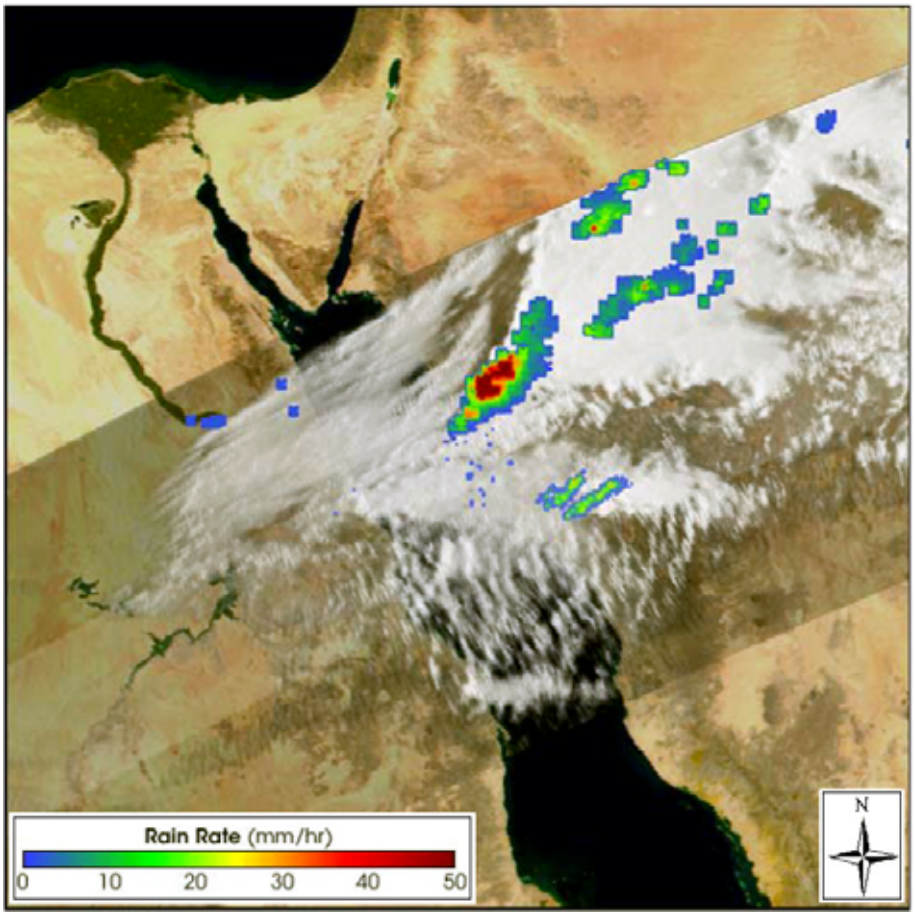

Fig. 5-6: *TRMM image reveals the Red Sea condition on 3rd February 2006.*
(Source: http://earthobservatory.nasa.gov)

▪ As the bifurcation ratio $(\mathcal{R}_b)$ is relatively high varies from 4.41 to 42.96, rate of discharge after exceptionally heavy rains and flood potentiality as well are likely low.

▪ Drainage basins maintaining rotund shape by implementing circular and elongation ratios (e.g. Barud and Abu Sebekha) are considered as high flood potentiality where their tributaries tend to concentrate discharge from most of the basin into the main stream during a relatively short period of time producing a relatively high flood peak (McCullagh, 1978).

▪ Drainage basins maintaining elliptical shapes by implementing circular and elongation ratios (e.g. Umm Iffinah, Safaga, Gasus and Hamraween) are of low flood potentiality where their drainage networks are arranged that discharge from tributaries is distributed relatively over the course of the trunk streams and peak discharge is reduced by being extended over a much longer time period (McCullagh, 1978).

▪ Drainage basins changed in shape due to application of circularity and elongation ratios are estimated to be of intermediate flood potentiality such as: Abu Asala, Naqarah, Abu Shiqayli, Queih, Abu Hamra, and Ambagi.

▪ In spite of the fact that impermeable rocks with low infiltration capacity are being usually accompanied by high drainage density (D_d), drainage density of the study area varies between 2.14 and 2.4 mile/mile^2 indicating low and poor density where the ground texture is coarse (Morisawa, 1985). Also, low and poor drainage densities are a result of precipitation and the present day hyper-arid conditions.

▪ Stream frequency is relatively high (2.04-4.02 stream/km^2) indicating high drainage frequency that gives more possibilities for collecting the surface runoff (Hammad et al. 1989).

It is worthy mentioning that Hammad et al. (1989) assumed that drainage basins of El Quseir area are of high flood potentiality owing to small bifurcation ratio, high stream frequency and drainage density**!** Yehia et al. (1999) demonstrated that wadis Barud and Ambagi are of moderate to high flooding potentiality.

On the other hand, flash flood potentiality is also assessed according to El Shami (1995) by representing some hydro-morphometric variables that are stream frequency (F_s) and drainage density (D_d) against bifurcation ratio (R_b) on a logarithmic plot (Fig. 5-8). The plot is divided into three belts representing risk intensity where belt A represents low risk basins, belt B is of intermediate risk, and belt C is of high risk. The relation between R_b and F_s revealed that only wadis Safag and Ambagi are of intermediate risk (belt B), whereas the other drainage basins are of low risk potentiality (belt A). However, the relation between R_b and D_d depicts that wadi Safaga is of high risk potentiality (belt C), whereas the other drainage basins are of low risk potentiality.

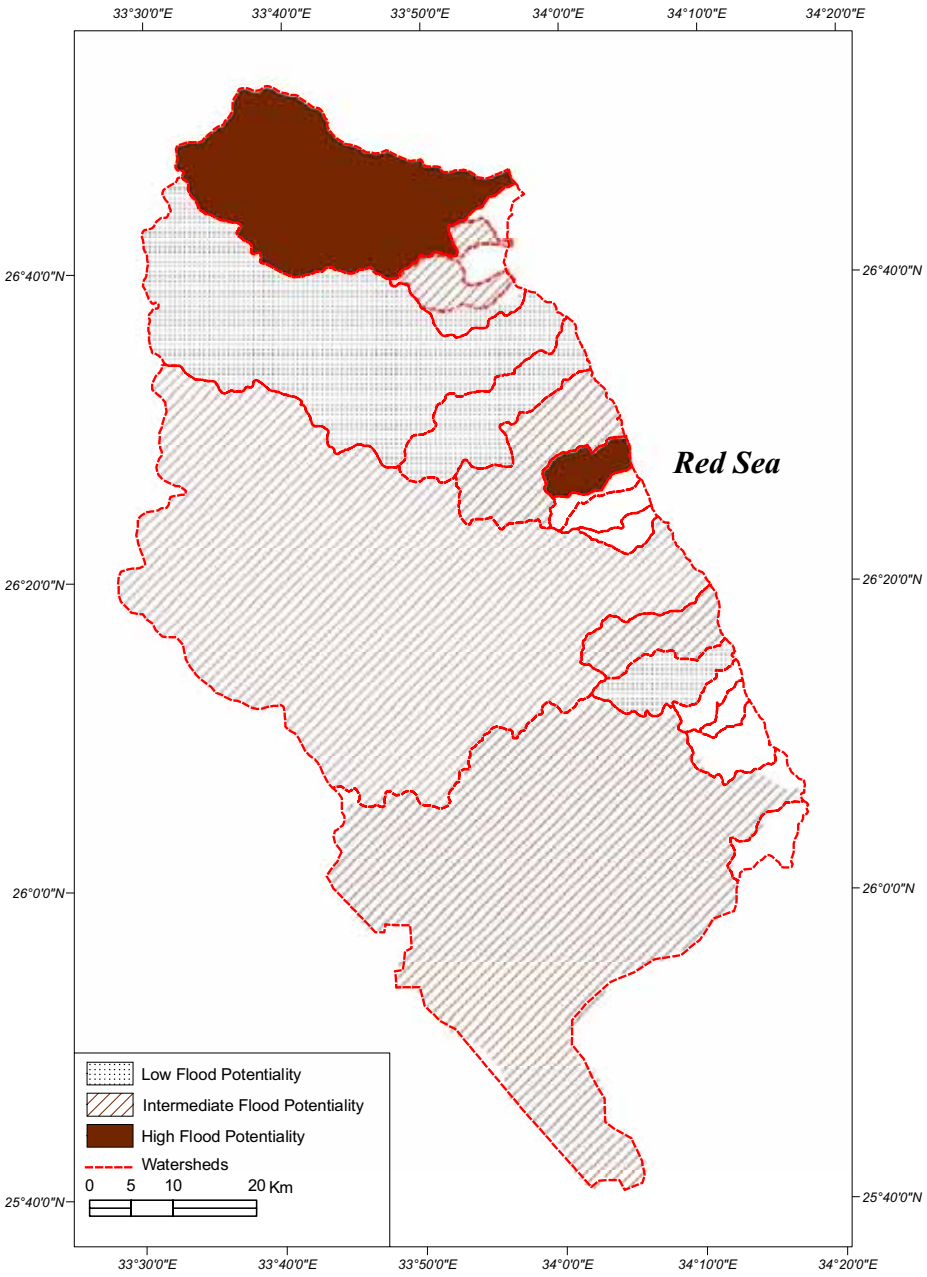

Fig. 5-7: *Flash flood potentiality assessment.*

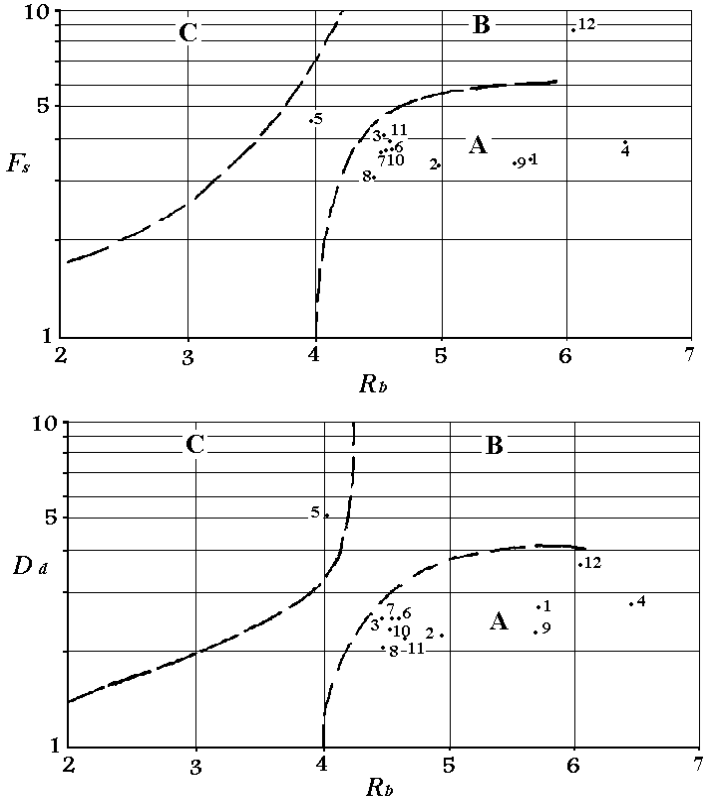

Drainage basin
1. Barud
2. Abu Asala
3. Naqarah
4. Umm Iffinah
5. Safaga
6. Gasus
7. Abu Shiqayli
8. Abu Sebekha
9. Queih
10. Abu Hamra
11. Hamraween
12. Ambagi

Risk assessment
A. Low risk
B. Intermediate risk
C. High risk

Fig. 5-8: *Flash flood potentiality assessment using bifurcation ratio (R_b), stream frequency (F_s), and drainage density (D_d). (After El Shami, 1995)*

6. Human Interference

Actually, flash floods along the Red Sea coast are not of high magnitude since the rainfall is restricted to few millimeters, in comparison with rainfall in temperate regions for instance. In spite of that, people have a dual role specifying flood magnitude through their arbitrary interferences, reactions, and lack of experience to deal with the hazard and diminish its efficiency. Human interferences referring to patterns of land utilization and their spatial locations attributed to drainage basins.

Clarifying the roles of the human agent, human interferences are recognized and surveyed in each drainage basin using Hybrid images (Google Earth Plus 2006), ASTER images, topographic maps of scale 1:50.000, and field work. Table 5-4 summarizes the most obvious human interferences within the main drainage basins, where on the other hand, human interferences are confined within the other relatively small basins to the coastal highway and some quarries. By this way, drainage basins are weighted

and divided according to diversity and intensity of the human interferences into three categories they are:

- Low interference: where the human interferences are confined to very limited utilization such as the coastal highway, which crosses through the trunk streams from north to south. This category includes wadis Abu Asala, Naqarah, Umm Iffinah, Abu Shiqily, Abu Sebekha, and Abu Hamra.
- Intermediate interference: where the interferences are confined to some dispersed spots that are usually related to phosphate mines, cargo stations and worker dwellings such as wadis Safaga, Gasus and Queih. It is worthy mentioning that mining process is completely stopped but the companies still preserving their machines in the fields nevertheless.
- High interference: where most of the alluvial fan is permanently inhabited and; therefore, patterns of land use vary from place to place. This category includes wadis Barud, Hamraween, and Ambagi.

7. Flood Magnitude and Vulnerability

Flood magnitude is expressed in the present study as a community of relationships between flood probability, peak discharge, time of concentration, and humane interferences for each drainage basin. Applying factor analysis method depicted that flood magnitude is more sensible to peak discharge, time of concentration and human interferences where flood probability is defused. Therefore, flood magnitude is divided into low, intermediate, and high according to the following statements (Table 5-5):

- Drainage basins of high peak discharge, short time of concentration and high human interferences are considered as high flood magnitude whether they are of high flood probability or not such as wadis Barud and Ambagi.
- Drainage basins of intermediate peak discharge, low time of concentration and high human interferences are considered as intermediate flood magnitude such as wadi Hamraween.
- Drainage basins of intermediate peak discharge, low time of concentration and low human interferences are considered as intermediate flood magnitude as well, such as wadis Naqarah, Abu Shiqily, Abu Sebekha, and Abu Hamra.

Table 5-4: *Patterns of human interferences.*

Wadi	*Human interferences*
Barud	Safaga City
	Safaga Harbour
	The coastal highway
	Safaga-Qena highway
	Oil pipeline and tanks
Abu Asala	Boats anchorage
	The coastal highway and railway
Naqarah	Tourist centers
	The coastal highway and railway
Safaga	The coastal highway
	Umm Hwaytat dwellings
	Phosphate mines (abandoned)
	Phosphate cargo station and railway (abandoned)
Gasus	The coastal highway
	Umm Hwaytat village (abandoned)
	Boats anchorage
	Umm Hwaytat mines (abandoned)
Queih	Sinai company dwellings (abandoned)
	10th of Ramadan dwellings (abandoned)
	The coastal highway
	Cargo station and railway (abandoned)
	Hamraween gypsum mine
	Umm Hammad mines (abandoned)
Hamraween	Hamraween village
	Sinai-El Hamraween company dwellings
	Phosphate factory
	Hamraween harbour
Ambagi	El Quseir City
	The coastal highway
	El Quseir-Qeft highway
	Electric power lines
	El Beida mine
	El Atshan mine

Table 5-5: *flood community and magnitudes.*

Wadi	*Flood Potentiality*			*Peak Discharge*			*Time of Concentration*			*Human Interference*			*Flood Magnitude*		
	L	*I*	*H*	*L*	*I*	*H*	*L*	*I*	*H*	*L*	*I*	*H*	*L*	*I*	*H*
Barud			●			●	●					●			●
Abu Asala		●		●			●			●			●		
Naqarah		●			●		●			●				●	
Umm Iffinah	●			●			●			●			●		
Safaga	●					●		●			●			●	
Gasus	●				●		●				●		●		
Abu Shiqily		●			●		●			●				●	
Abu Sebekha			●		●		●			●				●	
Queih		●				●			●		●		●		
Abu Hamra		●			●		●			●				●	
Hamraween	●				●		●					●		●	
Ambagi		●				●	●					●			●

L=Low I=Intermediate H=High

▪ Drainage basins of high peak discharge, intermediate or high time of concentration, and intermediate human interferences are considered as intermediate flood magnitude such as wadi Safaga.
▪ Drainage basins of low peak discharge and low human interferences are considered of low flood magnitude even if they have low time of concentration such as wadis Abu Asala and Umm Iffinah.
▪ Wadis Gasus and Queih are exceptional cases because all of their dwellings and mines are abandoned; accordingly, they are assumed to be of low flood magnitude.

Vulnerable sites or sites under threatening are defined as the following:

▪ In Safaga city, figure 5-9 reveals the diversity of land utilizations in the city such as: inhabitancy, tourist, harbours…etc. It is remarkable that tourist centers, harbours and superior dwellings appropriated to the Red Sea coast and they are well planned. On the western and south sides of the city, the built up area is slummy expanding from the older core of Safaga city. They confront to the fringes of wadi El Barud and the southern built up area is established over the recent ephemeral channels draining Jabal Naqarah. Unfortunately, the situation may become worst in Safaga since the fuel tanks have been arbitrary located over the recent ephemeral channels to the west of the city and exposed to flood attacks. In the case they are subjected to floods they would be exploded inducing heavy smoke and flame that could be moved by floods towards the eastern side of the city. This scenario is exactly similar to that one occurred in Drunka village in Asyut governorate owing to the flash flood on 2nd November 1994 that provoked many victims due to fire and dyspnea.

▪ The condition in EL Quseir city is not better than in Safaga but the risk might be of a lesser degree. Likewise Safaga city, tourist and superior dwellings are well planned and appropriated to the coast. Where on the other hand, slummy and deteriorated dwellings depart from the coast towards the high lands, overlaying the ephemeral channels. As a result of that, the city is non-perceptual expanded towards the south plugs up the outlet of wadi El Ambagi (Fig. 5-10).

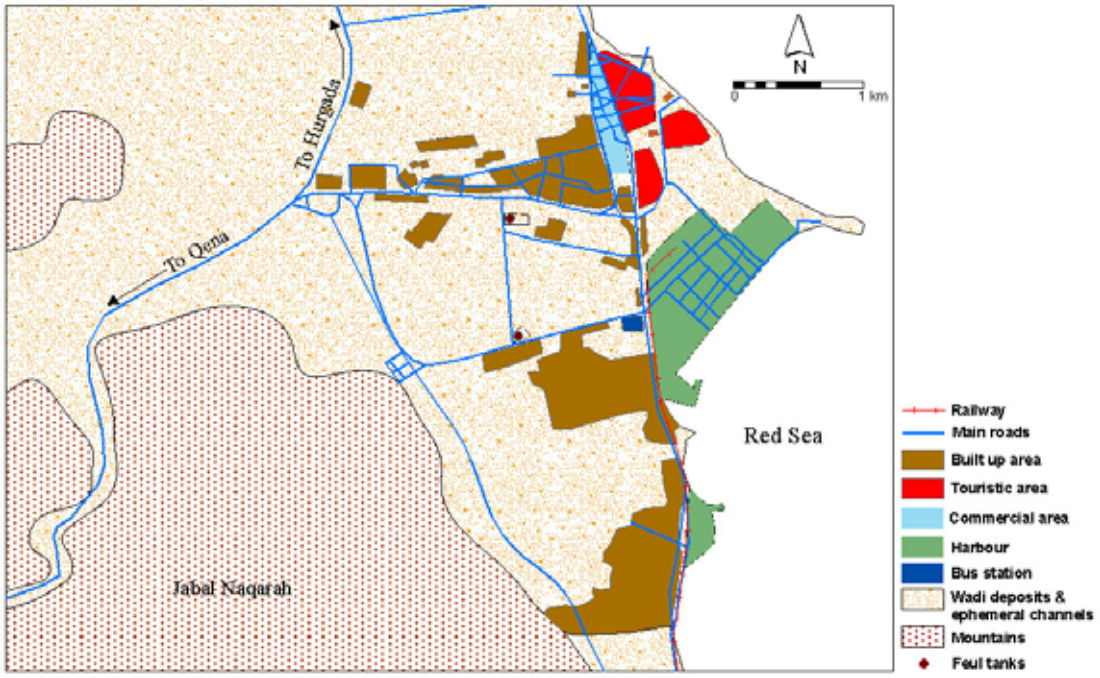

Fig. 5-9: *Pattern of land utilization in Safaga city.*

(Sources: Hybrid & ASTER images, topographic maps 1:50.000, and field study)

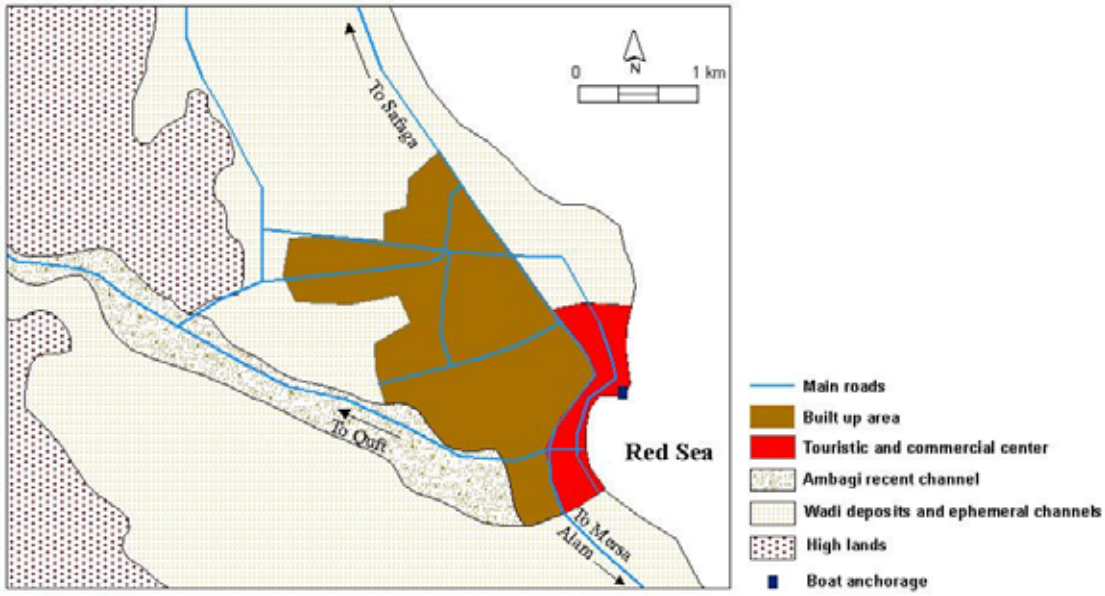

Fig. 5-10: *Pattern of land utilization in El Quseir city.*

(Sources: Hybrid & ASTER images, topographic maps 1:50.000, and field study)

▪ Umm El Hwaytat village in wadi Safaga are pounded and crossed by ephemeral channels that would be exposed to flood attacks (Fig. 5-11).

Fig. 5-11: *Recent ephemeral channels crossing and bounding Umm al-Hwaytat village in wadi Safaga.* *(Source: Google Earth 2006)*

▪ The coastal highway and the phosphate railway are vulnerable to tear down in several locations. Although they are supplied with many culverts and bridges where they intersect the trunk streams, some culverts are blocked by blown sands and garbage and require regular maintenance. Sometimes, culverts and bridges are too narrow to assimilate the overflow waters (Fig. 5-12).

▪ The intermountain roads are prone to floods and are partially or completely destroyed, specifically where they cross through incised valleys since the road is confined to the main stream channels such as the road between Umm al-Hwaytat and Wasif Basin (Fig. 5-13).

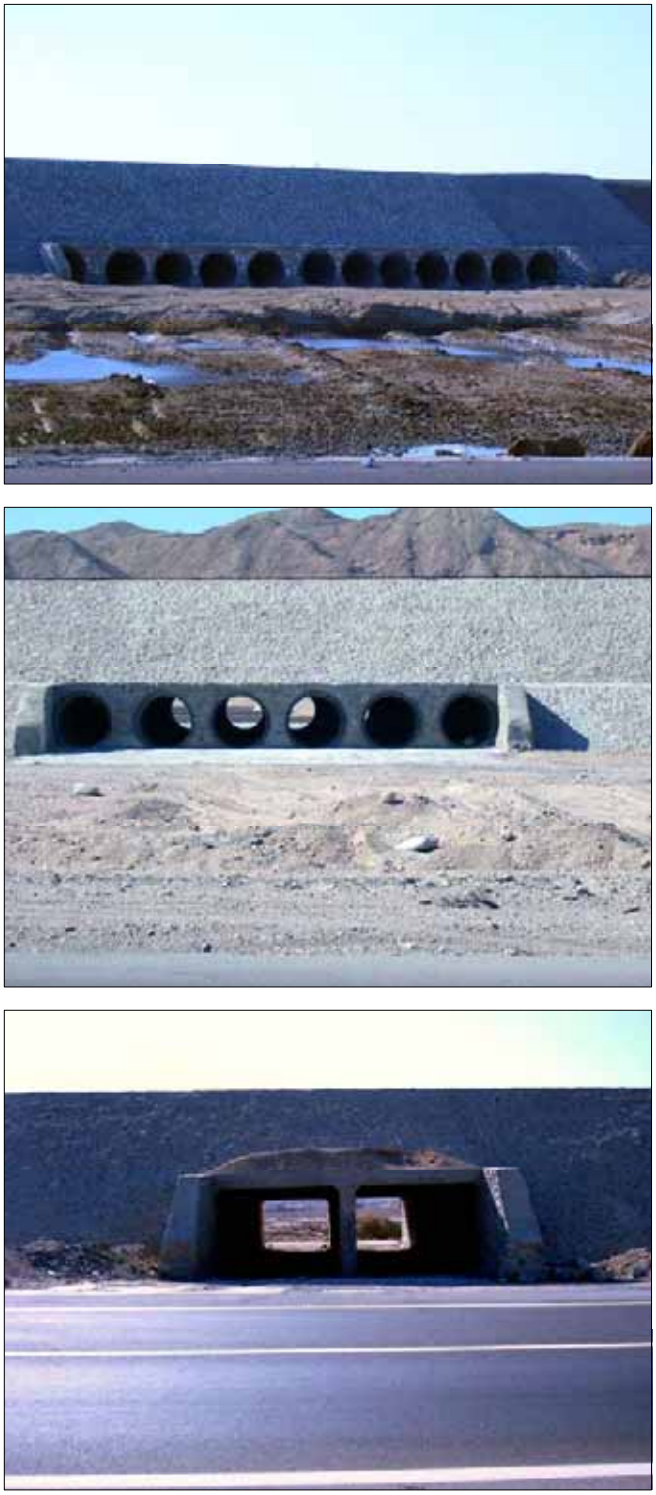

Fig. 5-12: *Culverts and bridges used to preserve the coastal highway and railway.*

Fig. 5-13: *Effects of floods on Umm al-Hwaytat – Wasif road.*

Appendix I: Runoff coefficients for rational equation.

	Hydrologic Soil Group			
Land Use, Crop, and Management	A	B	C	D
CULTIVATED, with crop rotations				
Row Crops, poor management	.55	.65	.70	.75
Row Crops, conservation mgmt	.50	.55	.65	.70
Small Grains, poor management	.35	.40	.45	.50
Small Grains, conservation mgmt	.20	.22	.25	.30
Meadow	.30	.35	.40	.45
PASTURE, permanent w/moderate grazing	.10	.20	.25	.30
WOODS, permanent, mature, no grazing	.06	.13	.16	.20
Urban residential				
30 percent of area impervious	.30	.40	.45	.50
30 percent of area impervious	.50	.60	.70	.80

Hydrologic Soil Group Descriptions:

A -- Well-drained sand and gravel; high permeability.

B -- Moderate to well-drained; moderately fine to moderately coarse texture; moderate permeability.

C -- Poor to moderately well-drained; moderately fine to fine texture; slow permeability.

D -- Poorly drained, clay soils with high swelling potential, permanent high water table, claypan, or shallow soils over nearly impervious layer(s).

Source: http://pasture.ecn.purdue.edu/~engelb/agen526/Runoff/C_table.html (Accessed on 14th Nov. 2006).

Appendix II: Conversion factors.

Multiply by to obtain	
inch (in.)	*25.40 millimetres*
foot (ft)	*0.3048 meter*
mile (mi)	*1.609 Kilometer*
inch per hour (in/hr)	*25.40 millimetre per hour*
feet per mile (ft/mi)	*0.1894 meter per kilometre*
square mile (mi2)	*2.590 square kilometres*
acre	*0.4047 hectare*
acre-foot (acre-ft)	*1.233 cubic meter*
cubic feet (ft^3)	*0.02832 cubic meter*
cubic feet per second (ft^3/s)	*0.02832 cubic meter per second*

References:

Abdel Moneim, A. A. (2005) Overview of the geomorphological and hydrological characteristics of the Eastern Desert of Egypt. *Hydrogeology Journal, Vol. 13, pp. 416-425.*

Ali, M. A. (2001) Analysis of rainfall and flash floods on the Red Sea and Sinai (In Arabic). *Meteorology, No. 21, pp. 27-35.*

Ashour, M.M. (2002) Flash floods in Egypt. *Bul. Soc. Geog. Egypte. Tome LXXV, pp. 101-114.*

Dartmouth Flood Observatory: Global flood archive available at: *http://www.dartmouth.edu/%7Efloods/index.html. (Accessed on 12 November 2006).*

Dyan, U. & Morin, E. (2006) Flash flood producing rainstorms over the Dead Sea: A review. *Geological Society of America, Special Paper 401, 10 p.*

El Desoki, T. M. (1995) Climatological characteristics accompanied by flash floods November 1994 (In Arabic). *Symposium Water of the Arab nations, Egyptian Geographical Society, vol.1, pp. 35-59.*

El Shami, I. Z. (1995) Flash floods under control (In Arabic). *Symposium Water of the Arab nations, Egyptian Geographical Society, vol.1, pp. 61-75.*

El-Fandy, M.G. (1948) The effects of the Sudan Monsoon low on the development of thundery condition in Egypt, Palestine and Syria. *Quart. J.R. SOC. Vol. 74, pp. 31-38.*

Foody, G. M., Ghoneim, E. M. & Arnell, N. W. (2004) Predicting locations sensitive to flash flooding in an arid environment. *Journal of Hydrology 292, pp. 48–58.*

FAO Corporate Document Repository (1991) Water harvesting, available at: *http://www.fao.org/docrep/u3160e/u3160e00.HTM* (*Accessed on 27 November 2006).*

Gheith, H. & Sultan, M. (2002) Construction of a hydrologic model for estimating wadi runoff and groundwater recharge in the Eastern Desert, Egypt. *Journal of Hydrology 263, pp. 36-55.*

Hammad, F.A., Eweida, E. A. and El Fakharany, M. A. (1989) Structure and drainage lineation analysis of the Quseir area. *Egypt. J. Geol. 33, 1-2, pp. 325-346.*

Kahana, R., Ziv, B., Enzel Y. & Uridyan (2002) Synoptic climatology of major floods in the Negev Desert, Israel. *International Journal of Climatology, vol. 22, pp. 867–882.*

Krichak, S. O. & Alpert, P. (1998) Role of large-scale moist dynamics in November 1-5, 1994, hazardous Mediterranean weather. *Journal of Geophysical Research, v. 103, pp. 19,453-19,468.*

Krichak, S. O., Tsidulko, M. & Alpert, P. (2000) November 2, 1994, severe storms in the southeastern Mediterranean. *Atmospheric Research 53, pp.45–62.*

Maidment, D. R. (ed.) (1993) Handbook of hydrology. *McGraw-Hill, Inc. New York.1424 p*

McCullagh, P. (1978) Modern concepts in geomorphology. *Oxford University Press, London, 128 p.*

Ministry of Public Works, Physical Department (1931) Meteorological report for the year 1925. *Government Press, Cairo, 176 p.*

Ministry of Public Works, Physical Department (1933) Meteorological report for the years 1927-1930. *Govt. Press, Cairo. 285 p.*

Ministry of Public Works, Physical Department (1940) Meteorological report for the years 1934. *Govt. Press, Cairo. 235 p.*

Ministry of Public Works, Physical Department (1947) Meteorological report for the years 1939. *Govt. Press, Cairo. 233 p.*

Ministry of Public Works, Meteorological Department (1948) Meteorological report for the years 1941-1944. *El-Eetemad Printing Press, Cairo. 225 p.*

Ministry of Public Works, Meteorological Department (1950) Meteorological report for the years 1945-1947. *Minerbo Press, Cairo. 185 p.*

Ministry of War and Marine, Meteorological Department-Weather Section: Unpublished daily weather report 1953.

Ministry of War and Marine, Meteorological Department-Weather Section: Unpublished daily weather report 1954.

Ministry of War and Marine, Meteorological Department: Unpublished monthly weather report for the years 1955-1956.

Ministry of Scientific Research- Meteorological Department: Unpublished monthly report for the year 1965.

Ministry of Scientific Research- Meteorological Department: Unpublished monthly report for the year 1969.

Earth Observatory, Natural hazards: Severe storm over the Red Sea, *http://earthobservatory.nasa.gov (Accessed on 01 Mars. 2006).*

Rizq, Y. L. (2001) A diwan of contemporary life 395. *Al-Ahram Weekly Online, 21-27 June 2001, Issue No. 539. www.ahram.org.eg/weekly (Accessed on 12 Nov.2006).*

Soliman, K. H. (1972) The climate of the United Arab Republic. In: Griffiths, J. F. (ed.), World survey of climatology, climate of Africa*, Vol. 10. Elsevier Publ. Co. Amsterdam, pp. 79-92.*

The Egyptian Meteorological Authority: Unpublished monthly weather report for the years 1974, 1975, 1979.

The New York Times Archive: Death Toll in Egypt Likely to Pass 500 *http://select.nytimes.com/gst/abstract.html?res=F50F16F73E5A0C768CDDA80994DC494D81 (Accessed on 07 November 2006).*

Trommer, J. T., Loper, J. E. & Hammett, K. M. (1996) Evaluation and modification of five techniques for estimating stormwater runoff for watersheds in West-Central Florida. *U.S. Geological Survey, water-resources investigation report 96-4158, Tallahassee, Florida, 41p.*

U.S. Soil Conservation Service (SCS) (1986) Urban hydrology for small watersheds. *(USDA) U. S. Department of Agriculture, Technical Release 55, 164 p.*

Yehia, M. A., Ashmawy, M.H., El-Etr, H. A., Abdel Monsef, H., El Shamy, I. Z., Hermas, E.A., Higazy, M. N. & Hassan, S.M. (1999) Flash flooding threat to the Red Sea coast towns of Safaga, Quseir, and Marsa El Alam, *Egypt. J. Remote Sensing & Space Sci., V. 2, pp. 69-86.*

6

COASTAL LANDFORMS

The study area has a great variety of coastal landforms. Erosional, submerged, and emerged features are the most common. Depositional landforms are patchy distributed and are being formed as a result of erosion and transportation of unconsolidated material.

1. Erosional Forms

1.1. Coastal Cliffs and Wave-Cut Platform.

Coastal cliffs are the most widespread erosional landforms along the coastline. They are significantly vertical, or near vertical owing to wave-induced erosion near sea level and the subsequent collapse of rocks at higher elevation. The ideal coastal cliff in the study area is composed primarily of reef limestone (1-4 m thick) overlain by alluvial deposits (±1 m thick). Locally, the reef limestone is replaced by salina deposits such as at the mouth of wadi El Quseir El Qadim. Height of the cliffs varies generally from +1 to +7 m asl. Coastal cliffs of the study area are less continuous since they are interposed by sharms or embayments of different sizes. As the cliffs overlook the sea, sea notches are well developed at the base. However, since the wave action is limited, the wave-cut platforms are restricted to a very narrow horizontal (0.5˚-1.5˚ seaward) coastal strip that is less or more continuous. Width of the wave – cut platform varies from few meters to few hundreds of meters, generally. The wave-cut platforms usually covered by a thinly sand beach and wadi deposits or standout exposed to the wave action. In the former case, surface of the platform is impressed by various solution holes of various shapes and sizes. As wave energy and tidal amplitude are limited, rates of cliff retreat are negligible.

2. Depositional Forms

2.1. Beaches and Sand Spits.

Beaches in the study area are whether sandy or shingle. Although, sandy beaches are the most common, they are restricted to a narrow strip along the coast (few tens of meters width) owing to limited sand supply. They developed in the estuaries, few

centimeters thick, and interrupted by the coastal cliffs. Sometimes, a thinly sand cover overlies the coastal coral terrace. Generally, shallow sea bottom is the major source of sand supply in the study area, whereas the role of the wind and the wadis is very limited. Therefore, sandy beaches are actually the result of accumulating the eroded materials of the modern coral reefs, which are supplemented to the beach by littoral drift from north to south generally. Sands are poorly sorted ranging in size from fine to medium grains. However, beach face of the sandy beaches slopes gently (2˚-3˚) seaward. Occasionally, sand ripples are seen in the shallow water in the protected areas where actions of waves and currents are feeble. Where the sand supply is relatively available, small-scale sand spites have developed in the same direction of the longshore current parallel to the shoreline. Sand spites are formed at the southeast of wadi Abu Hamra where a community of Mangroves is preserved and northern of wadi Queih where a sand spite of few meters long is developed (Fig. 6-1).

On the other hand, shingle or pebble beach has been only recorded in the mouth of wadi Abu Swatier. The beach manifests a narrow pocket-like embayment about 50 m width that is formed by shell and coral fragments interposed by sand beach and granite pebbles. Symmetrical cusps are well developed showing horns of ±1.5 m long.

Fig. 6-1: *Small-scale sand spite northern of wadi Queih mouth.*

2.2. Nebka.

Nebkas are sand accumulations formed around plants along the coast where groundwater is available for vegetation. They exhibit isolated mounds around individual plants, normally known as coppice dunes. Nebkas are very rare along the

coastal plain and confined to a patch area northern of wadi Queih. They attain about 0.5 m height and ±1.5 m long in the NW-SE direction.

3. Submerged Forms

3.1. Estuaries.

Likewise the north-western coast of Egypt estuaries[1] markedly characterize the Egyptian Red Sea coast. They vary from few meters to few hundreds of meters width. According to the physical process responsible for their formation, estuaries in the study area are of drowned river valley or coastal plain estuary type that is formed as a result of rising sea level (Fig. 6-2). Generally, it has been suggested that such drowned fluvial valleys possibly formed because of the last eustatic and rapid rise in sea level of the Flandrian transgression (Perillo, 1995) where the sea level was probably risen ± 100 m to attain its present day level (12.000-5.000 yr BP).

Water circulation of the estuaries is essentially controlled by water salinity. The inshore salinity of the Red Sea may rise dramatically and have given rise to the terms hyperhaline[2] (80-180 ‰) and hypersaline (80-300 ‰) as a result of little interchange between the open sea and the coastal lagoons or pools (Por, 1972; Jones, et al. 1987). Nasr (1955) demonstrated that the salinity of the coastal pools in Hurghada is both high and variable. According to him, the extreme range of salinity in tide-pools ranges from 41.29 ‰ to 44.09 ‰. At the same time, salinity of the open sea ranges from 39-41 ‰ in the upper layer. Therefore, estuaries of the Red Sea could be classified as inverse estuaries as a result of fresh water scarcity and high evaporation. Surface salinity does not decrease from the open sea to the inner-estuary; instead, water loss from evaporation leads to increase salinity as the inner end of the estuary is approached. This results in increasing density and sinking of high salinity water at the inner end and the water moves inward (landward) at the surface and seaward at the bottom consequently (Tomczak, 1996-2000).

[1] Sharm is the local name used by the native people for referring to an estuary in the Red Sea.
[2] Hyperhaline refers to water that contains more than 40 parts per thousand of dissolved salts. Water with salinity greater than normal sea water is called hypersaline.

Fig. 6-2: *Sharm wadi Umm Ayish. (Looking southeast)*

3.2. Offshore Islands.

The offshore islands confine to Safagah Island and Brother Islands. The next paragraphs give a preliminary explanation for these islands.

3.2.1. Safaga Island.

The island departs about 1 km from Safaga eastward. It extends NW-SE for 8.5 km and varies in width from few meters to 3 km. It is composed mainly of Pliocene rocks and Quaternary deposits revealing that the island was a part of the coastal terrain and has been mostly separated as a result of a major NW-SE fault showing the enclosed area as a graben deeps ± 55 m (bsl) (Fig. 6-3). The island is bordered by fringing corals that rise up to –0.5 m. The eastern side of the island rises up to 25 m and manifesting small-scale plateau-like form. However, the western side reveals low relief varying in elevation between 1 to 5 m. The most conspicuous geomorphological features are the mangrove communities on the western coast of the island, coastal lagoons, and sand bars.

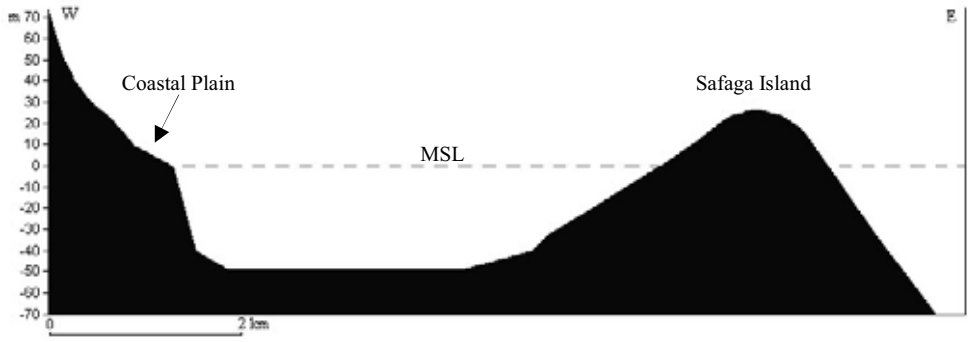

Fig. 6-3: *Bathymetric profile showing Safaga Island.*

(Source: topographic maps 1:50.000, 1:250.000).

3.2.2. Brother (Al Akhawein) Islands.

Brother or Al Akhawein islands are two small islands situated 67 km offshore east of El Quseir. The little brother island covers an area of 0.1 km², while the older brother island covers 0.3 km². The two islands are only 1 km apart. The older brother island is about 400 m long and 90 m wide and is surrounded by a supreme reef, which drops off to big depths. The northern front of the island is exclusively eroded by the wave revealing costal cliffs of ±3 m height and an intertidal wave-cut platform (Fig. 6-4).

On the other hand, the little brother island is surrounded by steep walls that lead to great depths ±40 m (Fig. 6-5). Black coral, notches and lots of hard and soft coral are obvious. No more information is available about the geological formation, but both islands are likely the exposed tips of two massive reef pillars that rise from the sea. The pillars cover the pinnacles of two undersea mountains rising from the depths of the abyss[1] about 300 m bsl. The older brother island has on the north-west side some ship wrecks. The Aida II an Italian ship that was carrying troops one night in 1957 when it hit the island. A large wreck with much intact superstructure, its shallowest point is at 15 m and ends below 45 m. There are other older wrecks scattered at depths between 9 and 40 meters. The famous Numidia is to find in the northern tip of the island. The wreck starts at a depth of 8 m, it lies on the steep drop-off at an almost vertical angle and the soft coral covers it nicely until 55 m bsl.

3.3. Modern Coral Reef.

The modern coral reefs as an expression refers to corals that have developed mainly over the past 5.000 years in response to rising sea level that is in turn the result of melting glacial ice left from the last great ice age. The rate of this rise has been approximately 1-2 metres per 1.000 years. It has been estimated that an upward (landward) growth of one metre can take anywhere between 300-3.000 yr BP. In addition to upward growth, reefs also grow in an outward or seaward direction at similar rates.

3.3.1. Physical Limiting Factors.

Growing of coral reefs is limited to various environmental aspects of which temperature, light, salinity, and wave energy are the most important.

[1] http://www.discovery-divers.com/north_brother.htm.

▪ Temperature influences the Co2 absorption capacity of the water and; therefore, it is crucial for the calcification process of hermatypic (reef-building) corals. Generally, coral reefs are restricted to water temperatures ranging between 16-34˚ C (Kleypas et al. 1999b). According to Neuman and McGill (1962) surface water temperature of the northern Red Sea is less than 25˚ C. Mohamed (1988) demonstrated that the surface water temperature averages 21.7˚ C in the northern Red Sea between latitudes 27˚ N-28˚ N during winter season. However, Radwan (2001) stated that the surface water temperature ranges from 20˚ C to 27˚ C in summer season with a general average of 24.9˚ C. Jones et al. (1987) argued that the surface water temperature of the Red Sea may reach over 45˚ C in summer.

Fig. 6-4: *The older brother island.*

Fig. 6-5: *The little brother island.*

▪ Light is essential for determining the vertical distribution of the corals and for the photosynthesis process since different species of corals have varying light requirements. As a result, corals are generally restricted to clear, shallow water (Vandersträte, 2006-2007) and to the photic zone. They, generally, occur up to a depth of 40 to 60 m (Spencer & Viles, 2002). Since photosynthesis directly influences coral calcification, it has been shown that under reduced light corals produce more fragile skeletons, which are more subjected to breakage (Yentsch et al. 2002). However, depth to which reefs can form is mainly limited by light penetration and the upper limit of coral growing is set by sea level. Accordingly, corals do not survive exposure to air and they would be dehydrated and die unless they receive water or splashes by tides and/or high waves.

▪ Salinity: Commonly corals are very sensitive to salinity and normally grow in a salinity range between 32 and 40 PSU[1] (Hoegh-Guldberg, 2000). Salinity of the Red Sea ranges from 39-41‰ in the upper layers (Jones et al. 1987). According to Neuman and McGill (1962) surface salinity of the northern Red Sea reaches up to 40.5 ‰. Salinity slightly differs from season to one another, for instance salinity in the area of Hurghada reaches 40.31, 40.06, 40.58, and 40.24 ‰ in winter, spring, summer, and autumn respectively (Radwan, 2001; after: Marine water, Red Sea studies, Report III, 1981). However, torrential rains and seasonal flooding by the wadi system can cause sudden decrease in salinity and severe damage to corals at the wadi mouths.

▪ Wave Energy: as the probable wave height in the study area differs from 0.6 to 1.5 m and wave celerity ranges between 2.21-3.1 m/sec (recall from chapter one), wave energy is relatively limited. These permit growing corals and are necessary to provide food and oxygenated water to the sedentary polyps.

3.3.2. Types of Coral Reef.

Corals of the Red Sea are generally embedded under the following coral categories:

▪ Fringing reefs: These are the most dominate coral types in the Red Sea that lie very close and parallel to the shore line. Usually, they are separated from the shore by narrow, shallow lagoons owing to lack of upward and outward growth. Fringing reefs

[1] Practical Salinity Units, 35 psu for instance are exactly equals 35 grams of salt per litre of solution.

reveal a platform-like form owing to a combination of constructive and destructive processes. The living coral forms a thin veneer over a platform composed mostly of the remains of previous coral generations. Sometimes, this platform varies generally from few tens to hundreds of metres width. The outer-seaward margin of the fringing reefs act as wave breaker in the study area, leading to decrease and limiting wave energy.

▪ Barrier reefs: Head (1987) argued that true reefs as defined by Darwin as ″steady growing reef systems in subsidence environment ″, do not occur in the Red Sea. According to him, barrier-like structures extending over several kilometres. Their distribution depends on the Red Sea tectonics where they are mainly founded on the seaward edges of large fault blocks or on the top of elongated salt diapirs (Head, 1987). Barrier reefs in the Red Sea are known as ridge reefs by Guilcher (1988) as they form elongated narrow framework running in the general direction of the Red Sea.

▪ Atolls are annular reefs that develop at or near the surface of the sea when islands that are surrounded by reefs subside. Vandersträte (2006-2007) revealed that the formation of such atoll-like structures is associated with smaller salt diapirs and, anyhow, are not well developed in the Red Sea. Atolls separate a central lagoon from the sea and are circular or sub-circular.

▪ Patch reefs: many reefs without a clear linear structure are defined as patch reefs. They vary from very small-simple coral on coral structure to large patches. They reach the low tide level and are formed by aggregation of a few enormous coral colonies.

▪ Coral Carpets: Riegl and Piller (1997) used the term “coral carpet” in Hurghada for referring to the more or less continuous veneers of coral framework following the existing seafloor morphology.

3.3.3. Spatial Distribution.

Figure 6-6 showing the main coral sites in the study area that are summarized as follows:

▪ Shab Safaga.

Shab safaga forms an atoll of triangular shape. Its maximum length is about 4.5 km and the width varies greatly between few hundreds of meters to 2.7 km. The atoll is

interposed by a lagoon in the center and its margins are characterized by accretions of sand bars.

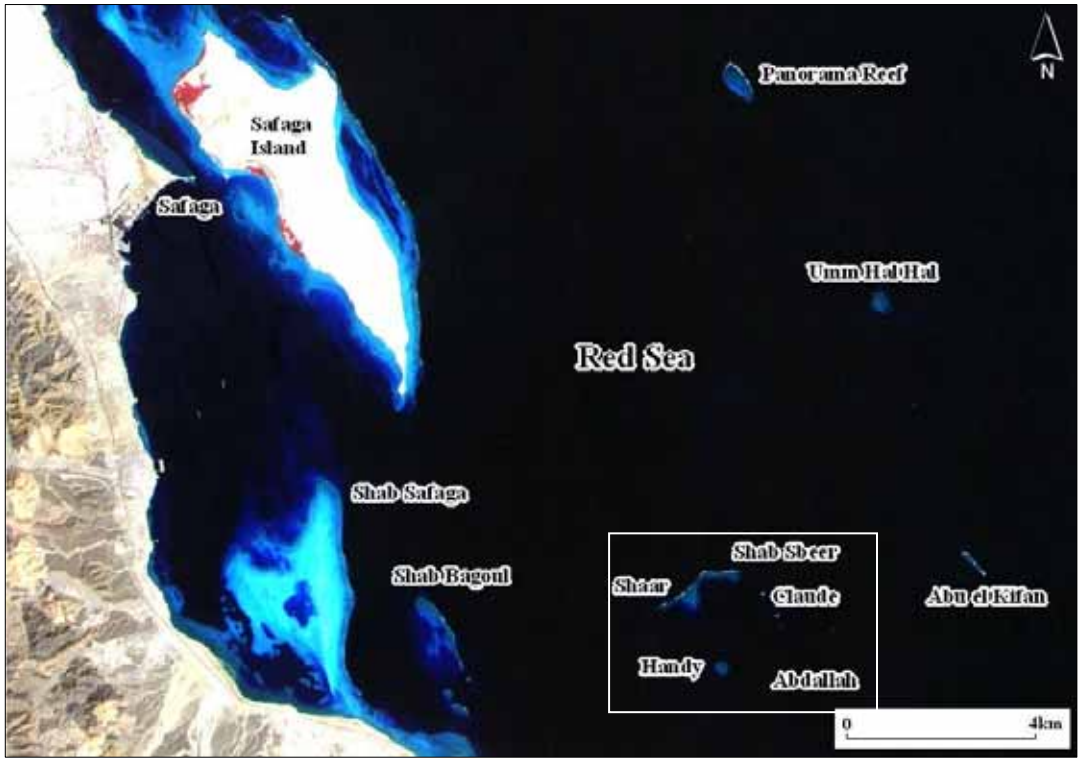

Fig. 6-6: *Spatial locations of the main reefs near Safaga.* *(Source: ASTER image)*
(The boxed area approximately shows location of figure 6-7)

- Panorama reef.

Panorama reef is one of the biggest patch reefs in Safaga. The reef has an oval shape extending NW-SE generally for about 800m. The width of the reef varies greatly from north to south between 400 to 200m. It covers an area about 3.5 km^2 and its perimeter is about 2.3 km. The reef is interposed by an elongated lagoon that extends about 300 m along the general trend of the reef. Panorama reef is the most attractive in Safaga area for diving since it includes huge coral formations and numerous sea notches and overhangs, canyons and soft corals. Walls of the reef dropping over 200m (bsl)[1].

- Umm Hal Hal.

[1] http://www.gooddive.com/egypt/safaga_dive_sites.htm (Accessed 11. May. 2007).

This is a semi-circular patch reef, its major diameter is about 0.5 km and the short diameter is about 0.3 km. The reef attains a total area of 1.5 km^2. Umm Hal Hal reef is rarely chosen for diving in the south of Safaga, for this reason it is still quite virgin. The north side is a drop off descending to -80m and its southern side manifests wonderful coral gardens with sea notches and canyons.

- Shaar, Shab Sbeer, Shaab Claude, Handy and Abdallah.

This group of reefs form actually an annular atoll. Most parts of this atoll are submerged under the present sea level, while Shaar, Shab Sbeer, Shaab Claude, Handy and Abdallah reefs are the most emergent parts of the atoll (Fig. 6-7). Shaar and Shab Sbeer form the northern emergent rim of the atoll extending west-east generally for about 2 km and their width varying greatly from place to place between 80 to 400 m. Claude and Abdallah reefs are so tiny emergent reefs on the eastern rim of the atoll. On the southern margins of Abdallah reef an Egyptian ferry called Salem Express was founded on 16th December 1991 and this is a proof that the reefs are extending away under sea level. Handy reef lies approximately in the center of the atoll manifesting semi-circular reef. It is mostly connected with Shaar and Shab Sbeer through submerged coral bridge-like or platform. The perimeter of the atoll as a whole is about 11 km covering an area of 9.5 km^2 approximately. The longest diameter is about 3.4 km from west to east and the shortest one is about 2.9 km from north to south.

- Abou El Kefin.

It is one of the most popular diving sites in Safaga. It extends NW-SE generally for about 0.6 km. The northern part of the reef exhibits plateau-like form and the southern part depths about 30 m (bsl).

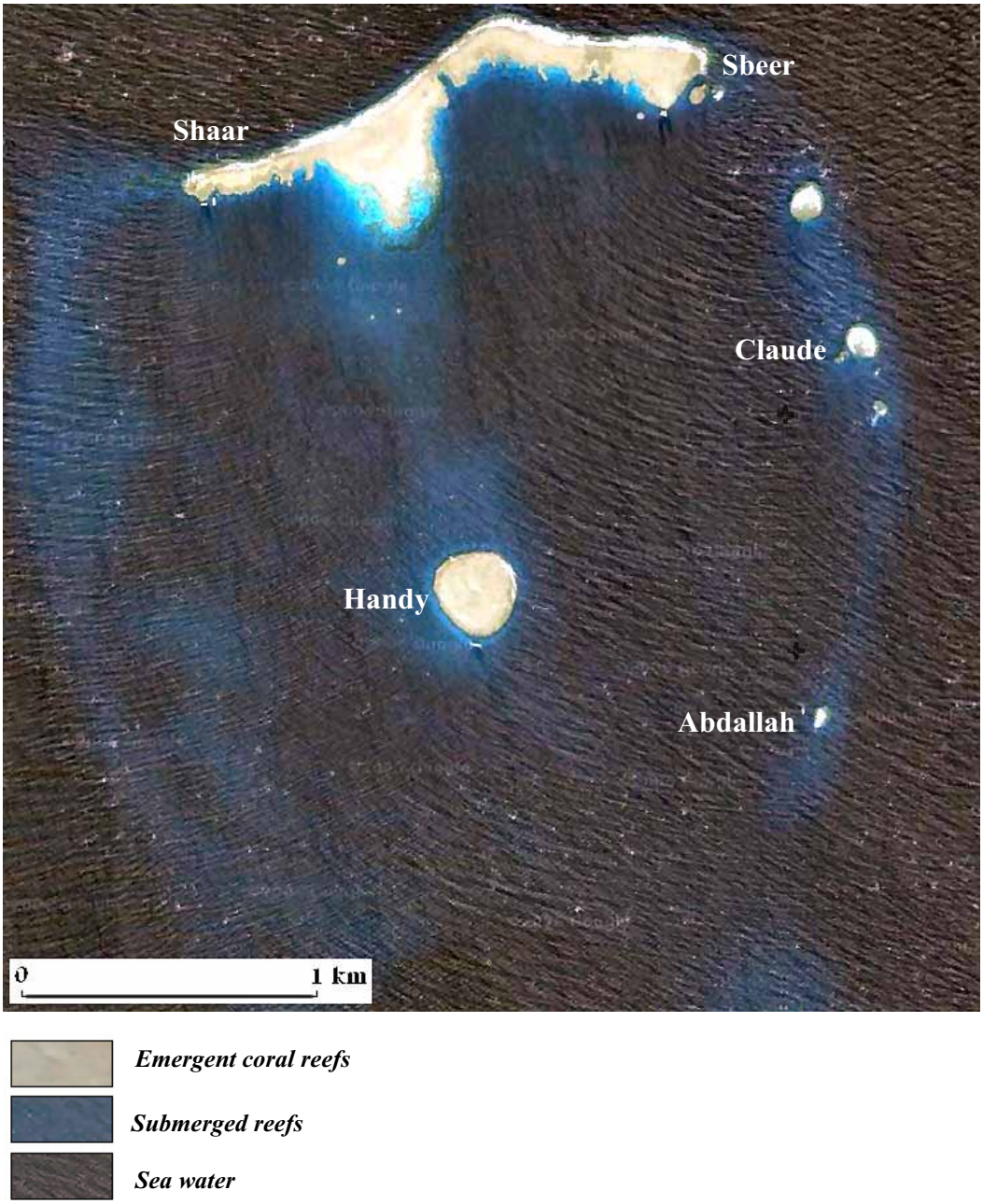

Fig. 6-7: *Reefs of Shaar, Sbeer, Claude, Handy and Abdallah, south eastern Safaga.*
(Source: Google Earth, 2007)

3.4. Lagoons.

The Red Sea coast is impressed by shallow water bodies of salt or brackish water (lagoons) separated from the sea by sand barriers or coral reefs. Lagoons of the study area are distinguished as:

- Non-reef lagoons.

The non-reef lagoons extend generally parallel to the coastline and are separated from the sea by sand barriers, which are formed by wave-action and/or longshore currents (Fig. 6-8). The lagoons have inlets cut through the barrier and permit tidal currents to transport water into and out of the lagoons. Accordingly, water conditions in the lagoons can differ significantly from the open sea water. This type is recorded at several locations; they are from north to south: mouth of wadi Naqarah, south of wadi Abu Hamra mouth, and northern of wadi Queih mouth. These lagoons are confined to few hundreds of meters long (100-700 m) and few tens of meters wide (40-90 m generally). For that reason, hardly they could be seen using the ETM image or the available topographic maps of scale 1:50.000.

- Reef barrier lagoons.

Occasionally, the fringing reefs form a barrier or platform-like against the open sea, behind which shallow protected lagoons are developed, particularly at the mouths of the wadis such as mouth of wadi Abu Shiqayli (Fig. 6-9). Usually, the barriers are about 1-2 m below sea level, which allows exchanging the water between the sea and the lagoon.

- Inter-lagoons.

The coral platform is often disturbed by inter-lagoons or pool-like. These lagoons are mostly oval or circular in shape of few meters in diameter and depth. They are recognized from the QuickBird images in the shallow water along the coastline of the study area, mostly without exceptions (Figure 6-10).

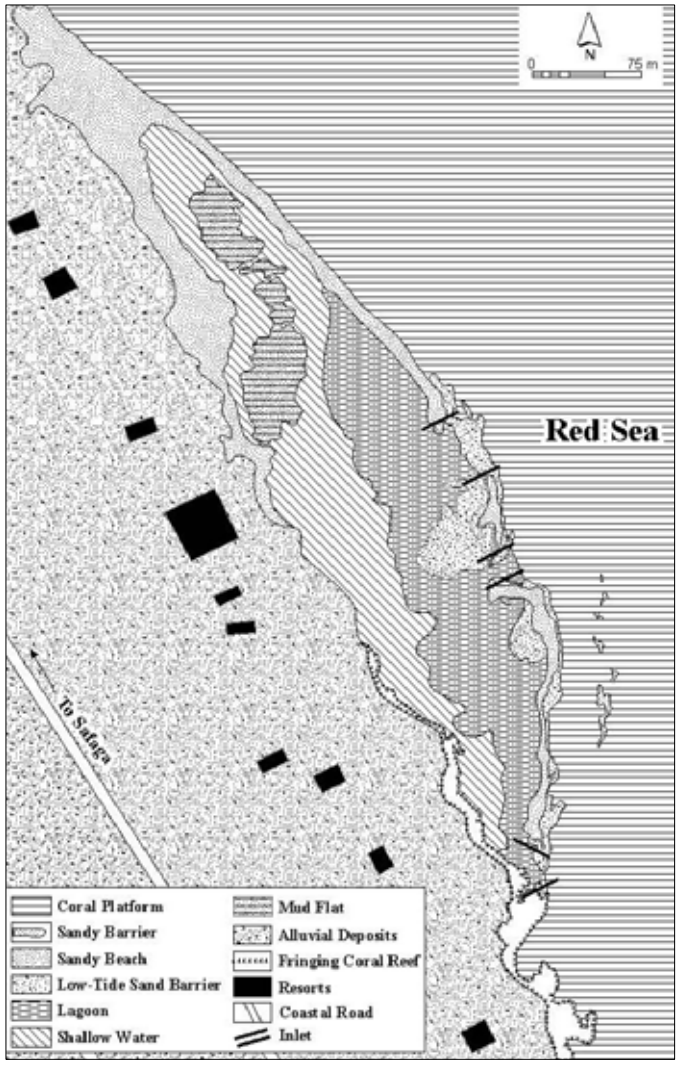

Fig. 6-8: *Geomorphology of the non-reef lagoon at sharm wadi Naqarah.* *(Source: Google Earth 2077, Topographic maps 1:50.000, field work)*

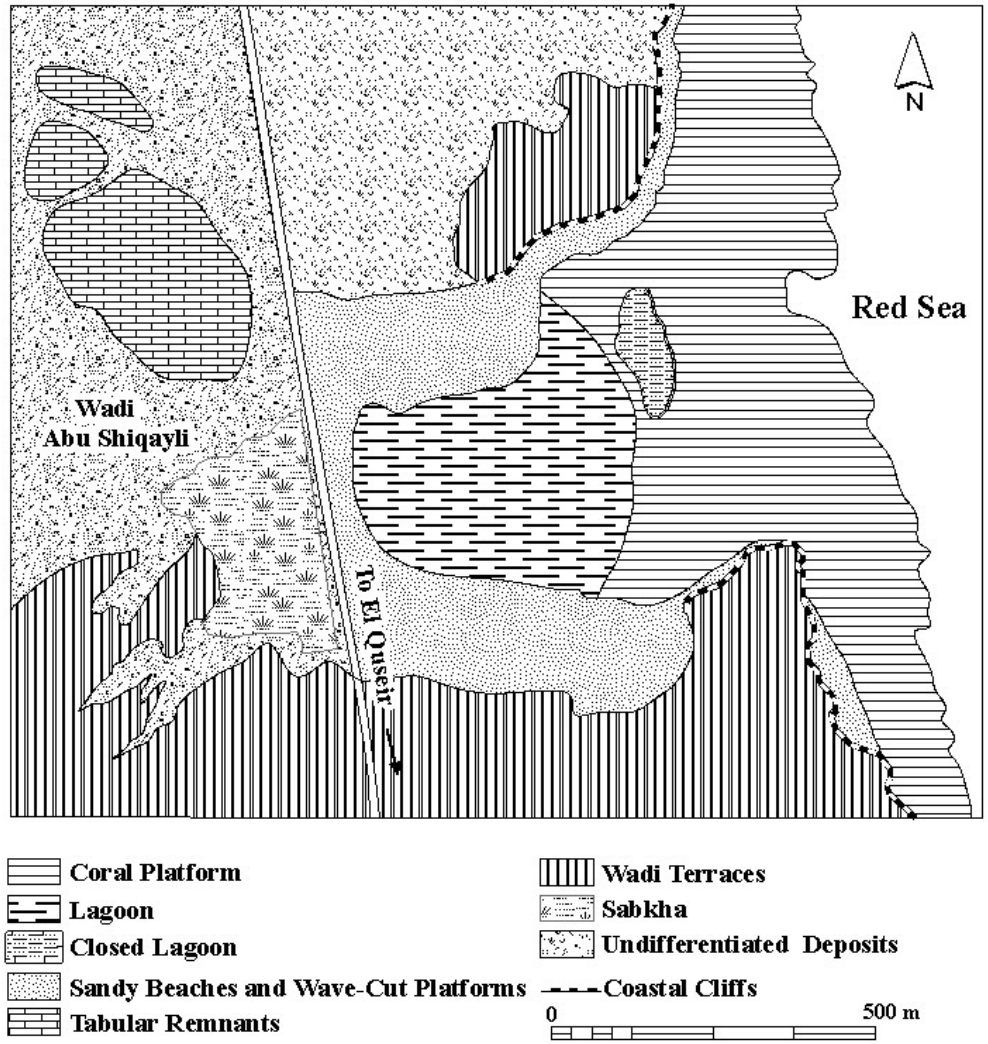

Fig. 6-9: *Geomorphology of the reef barrier lagoon at sharm wadi Abu Shiqayli.* *(Source: Google Earth 2077, Topographic maps 1:50.000, field work)*

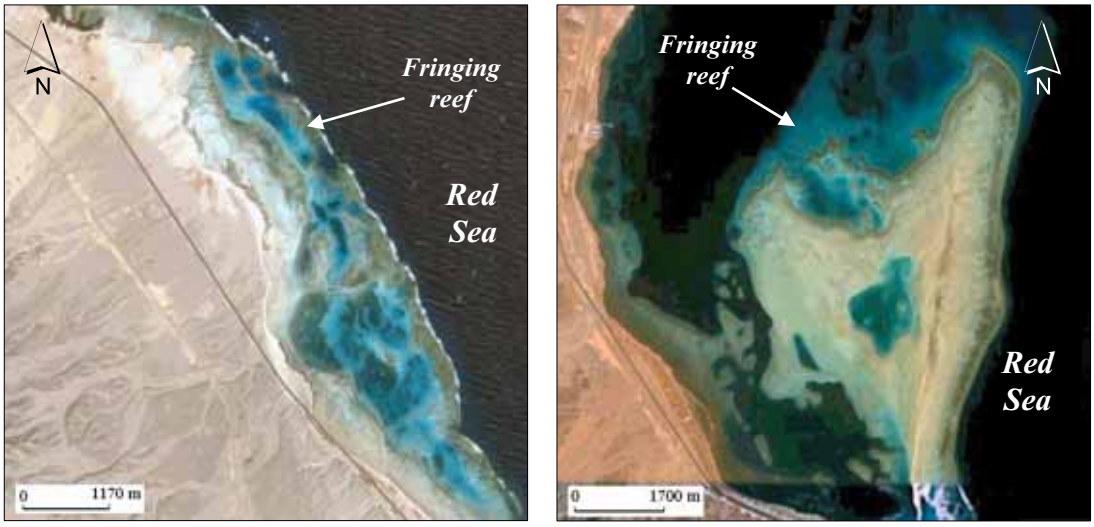

Fig. 6-10: *Inter-platform lagoons at Shaab Safaga (right) and north of sharm wadi Queih (left).* *(Source: Google Earth, 2007)*

3.5. Mangrove Communities.

Mangrove trees are a part of the coastal habitations that inhabit warm water of tropical depositional coastal environments. Specially, where fine sediments, often with high organic content, collect in areas protected from high energy wave action and periodically submerged by tidal flows. Therefore, they tend to occur in patches down the coast especially where a lagoon is developed behind the coral and/or sand barriers (Fig. 6-11). Mangroves were recognized in the study area in three locations:

- Around the offshore Safaga island where the mangroves patchy occupy the protected coastal lagoons. It is well developed along the western coast of the island rather than the eastern one.
- Along the beach profile extending from wadi Safaga to wadi Abu Boal, the mangroves trees manifest longitudinal strip parallel to the coast line and interrupted by a channel of unnamed wadi into two small patches.
- The coastal lagoon that lies about 200 m southeast of wadi Abu Hamra.

Generally, mangroves have been developed in the Red Sea in high rather than low salinity areas, and salinity levels together with high temperatures and low oxygen levels combine to limit the faunal diversity (Jones et al. 1984). They are being naturally flexible plants that are able to withstand severe damage of winds, waves, and changing tides for thousands of years.

Fig. 6-11: *Mangroves community in the lagoon south east of wadi Abu Hamra. (Looking eastward)*

Roots of mangroves either rise out of the ground like stilts, or upwards growths from the roots that poke out of the ground, both of them are adapted to ensure that the roots get enough oxygen. The most common species in Egypt are Avicennia marina that is known locally as 'Shura'. The leaves are shiny dark green on the top, oblong and pointed at the tip. The undersides of the leaves are a dull green color with short dense hairs - glands - which excrete salt. The leaves serve as a back-up system for ridding mangrove of the salt that has not been excreted by the roots.

After rainy days, the wadis usually support mangroves by annual freshwater, which makes life easier for the mangrove trees. Mangroves have been used throughout the Red Sea for thousands of years, since they are one of the few sources of timber in this arid region. Traditional fishing boats are often made partly of mangrove wood, and buildings in the ancient cities of Arabia have beams made of mangrove wood.

3.6. Submarine Topography.

Submarine terraces and canyons have been distinguished in several locations along the Red Sea coasts in Sharm El Sheikh, Gulf of Elat, Sudan, and Saudia Arabia (Emery 1964, Gvirtzman et al. 1977, Fricke 1983, and Reaches 1987). Processing the bathymetric map of scale 1:200.000 combined with the DEM reveals many of submarine terraces and canyons at different levels (Fig. 6-12).

3.6.1. Submarine Terraces.

On the one hand, the submarine terraces are mostly flat surfaces and differ in depth and width from place to place. They are discontinuous in character and establishing near the outlet of the major wadis (i.e. Barud, Safaga, Queih, and Ambagi) as short strips and/or patches over a distance of a few kilometers from the coastline. Three terraces are recognized as:

- Terrace 20 m below sea-level (bsl) represents a very narrow strip along the coast north of Safaga island, and a relatively wide platform in the front of wadi Queih, about 6 km width (Fig. 6-13, profile 6).
- Terrace 50 m (bsl) varies in width from 6 to 10 km. It is distributed northern of Safaga island and in the front of wadi Safaga (Fig. 6-13, profiles 1, 2). The terrace is considerably dissected by incised canyons at several locations.
- Terrace 100 m (bsl) differs in width from 2 to 5 km. It distributes over 2.5 km from the coast southeast of wadi Safaga mouth (Fig. 6-13, profiles 3, 4). The terrace is significantly detached by a canyon of 250 m deep that is likely of tectonic origin.

The submarine terraces of the study area are in accordance with those submarine terraces recorded in southern Sinai at elevations 20, 60, and 120 m (bsl) (Gvirtzman, 1994). Another 60-90 m (bsl) terrace was recorded in Sharm El Sheikh and Ras Burka (Fricke & Schuhmacher, 1983, Reiss & Hottinger, 1984) and at about 50-90 m (bsl) in Elat (Reches et al. 1987). Terrace of Elat has likely developed between 70.000-50.000 yr BP, when the sea level was 100 to 60 m below the present level (Reches et al. 1987).

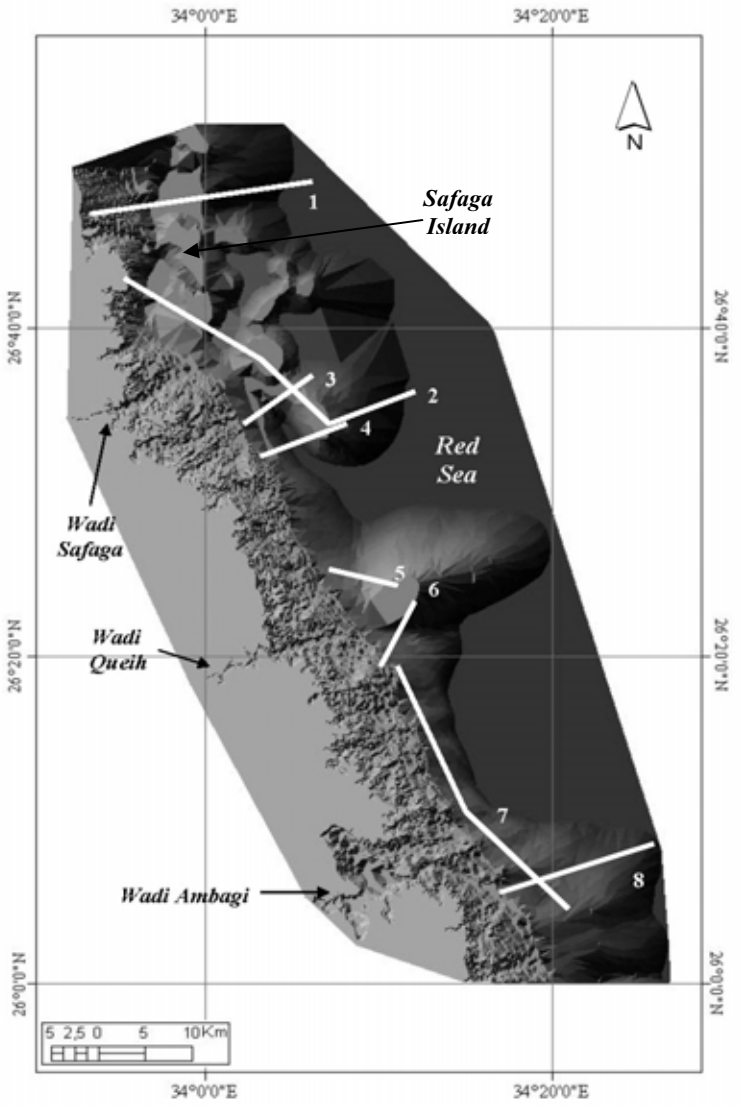

Fig. 6-12 a: *Shaded relief map showing the main submarine topography. White lines refer to profile locations of figure 6-13.*

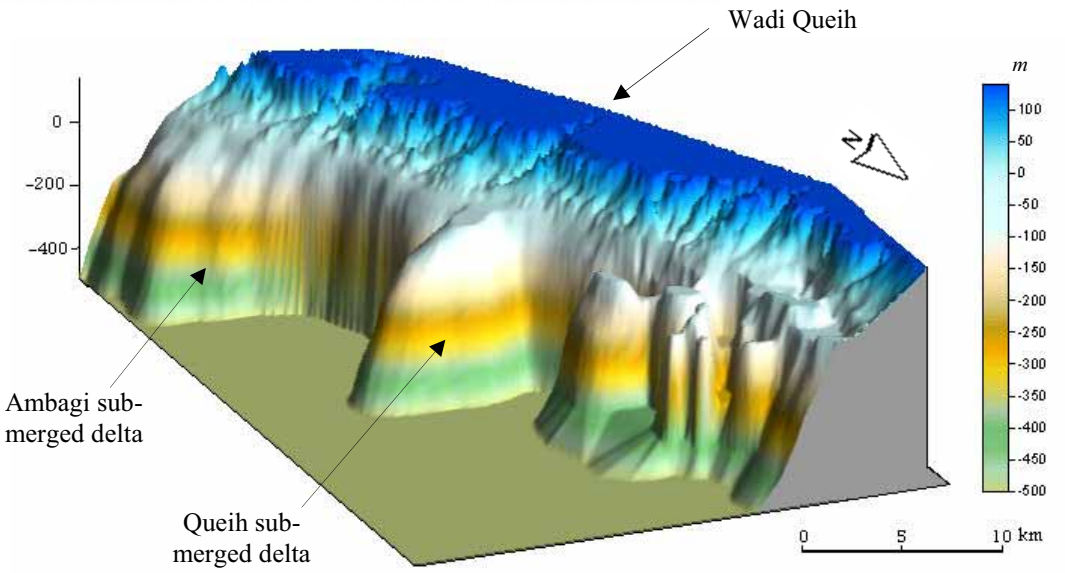

Fig. 6-12 b: *3d view showing the main submarine topography and the submerged deltas.* *(exaggeration 2.5 times)*

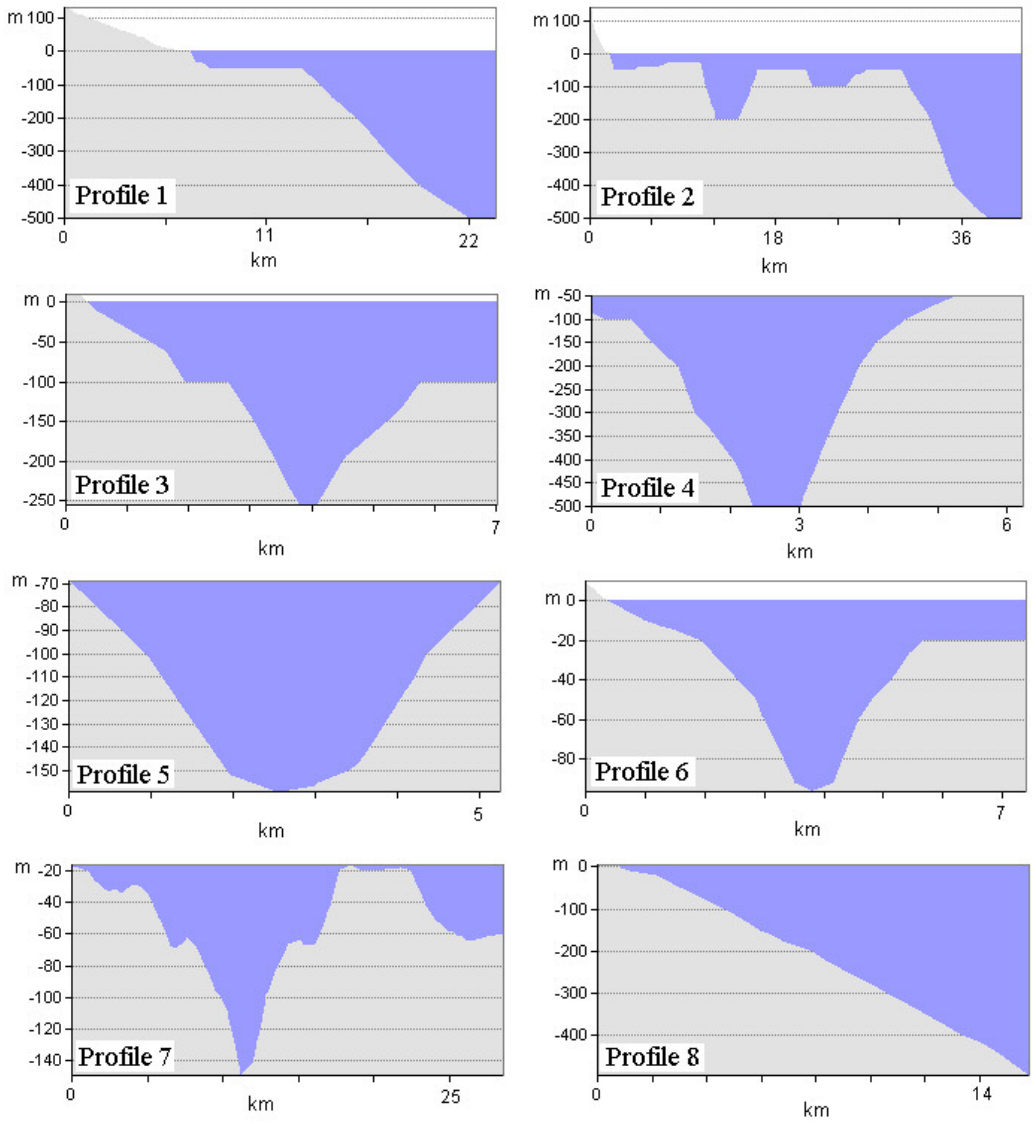

Fig. 6-13: *Topographic and bathymetric profiles of the nearshore zone.*

(For profile locations review fig. 6-12a)

Generally, shapes of the terraces represent probably the submerged deltas of the drainage systems as can be deduced from the submarine terraces of wadis Queih and Ambagi. These terraces are noticeably detached by deep canyons or trenches of different depths. The sedimentological characteristics and age of the submarine terraces will still be mysterious in anticipation of further researches. However, correlation between the submarine terraces and the global sea-level curve during the last glacial stage may be reasonable to give a relative age for the three submarine terraces (Fig. 6-14). Terrace -100 m may be in corresponding to the last glacial maximum (LGM) in the age range of melt-water pulse (MWP) 1A0 and 1A (~19.000-16.000 yr BP) when the ocean level rose rapidly 10-15 m in less than 500 yr during

the MWP-1A0 and followed by another increase about 16-24 m during the MWP-1A (Gornitz, 2007). Terrace -50 m is probably in accordance with the melt-water pulse-1B (11.500-11.000 yr BP) when the sea level may have jumped by 28 m. Terrace -20 m is mostly formed during the fourth melt-water pulse 1C (8.200-7.600 yr BP) that is supported by stratigraphic data from elsewhere including Chesapeake Bay (USA), the Mississippi River delta, the Yellow River in China, coastal Lancashire (UK), and north-western Denmark (Gornitz, 2007).

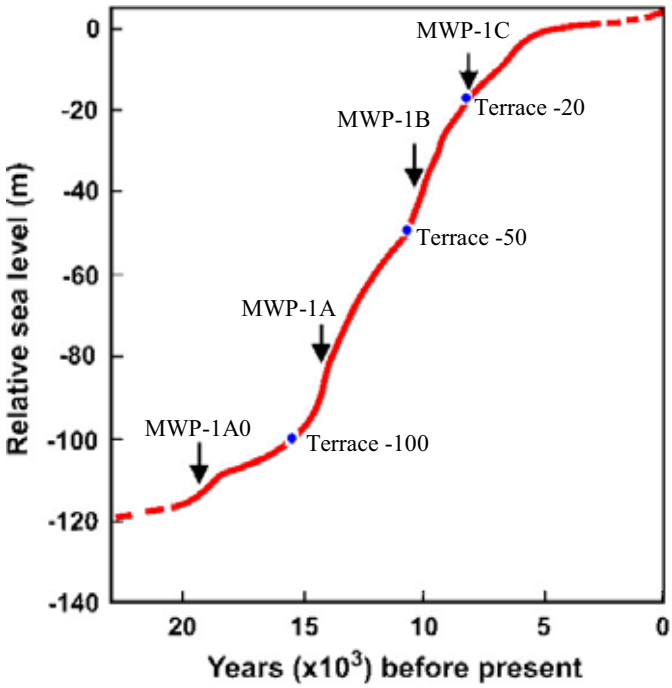

Fig. 6-14. *Correlation between the submarine terraces (100, 50, and 20 m bsl) and the generalized curve of sea level rise since the last ice age. MWP-1A0, c. 19,000 yr BP, MWP-1A, 14,600 to 13,500 yr BP, MWP-1B, 11,500-11,000 yr BP, MWP-1C, ~8,200-7,600 years ago. (Source: Gornitz, 2007).*

3.6.2. Submarine Canyons.

The recognized submarine canyons are from north to south as follows:

▪ Submarine canyon of wadi Safaga: This canyon represents a trench of wall-like sides. It departs about 12 km from the coastline and attains about 4 km width at level 50 m (bsl) (Fig. 6-13, profile 2). The general trend of the canyon is SW-NE adhering to the general trend of wadi Safaga for about 15 km beneath the sea to penetrate the submarine terrace of -50 m. The canyon manifests staircase, where two nickpoints or abrupt changes in slope separate the canyons into two main segments (Fig. 6-15). The

uppermost segment drops 200 m (bsl) and its walls elevate about 150 m above the canyon floor. It is separated from the lower segment of the canyon by a steep ridge varying in elevation from 300-200 m (bsl). The lowermost segment drops 300 m (bsl) and its walls are of 250 m above the canyon floor. This segment is separated from the deep sea by another steep ridge varying between 400-300 m (bsl).

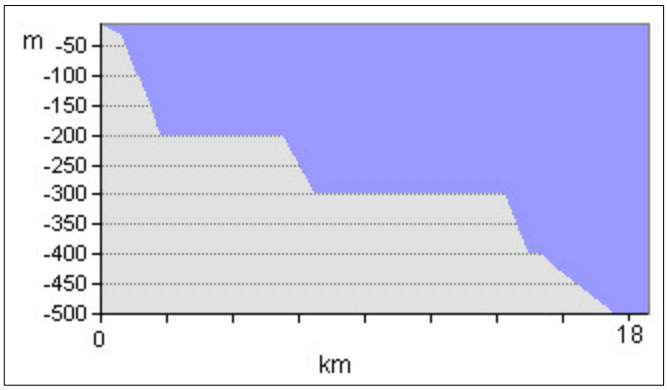

Fig. 6-15: *Submarine profile of wadi Safaga canyon.*

▪ The middle canyon extends about 15 km NW-SE generally parallel to the coastline. It pierces the submarine terrace of -100 m and exhibits **V** shape. Depth of the canyon differs between 250 (bsl) at its apex to 500 m (bsl) (Fig. 6-13, profiles 3, 4). The sides of the canyon range in elevation between 150-400 m above the canyon floor.

▪ Submarine canyons of wadi Queih: The main submarine feature at the mouth of wadi Queih penetrates probably its submerged delta. This delta is detached by two opposite canyons (Fig. 6-13, profiles 5, 6). The northern one oriented SE-NW for 12 km and attains about 160 m (bsl) depth. Sides of the canyon are of 90 m height above the canyon floor. This canyon is about 5 km width at a depth 70 m (bsl). The southern canyon extends NW-SE for 10 km and drops about 100 m (bsl). Sides of the southern canyon are about 85 m above the canyon floor and the width of the canyon is about 4.5 km at depth 25 m (bsl).

▪ The southern canyons: The submarine profile extends from wadi Hamraween to wadi Ambagi (Fig. 6-13, profile 7) reveals a number of submarine canyons; they are from north to south: 30, 70, 145 m (bsl). The last canyon (145 m bsl) belongs to wadi Ambagi that is of 8 km long from west to east. The canyon exhibits **V** shape of 75 m high walls. Width of the canyon is about 5 km at elevation 60 m (bsl). This canyon

mostly detaches the submerged delta of wadi Ambagi that manifests cone shape and convex slope profile (Figs. 6-12, 6-13, profile 8).

The submarine canyons could be classified according to their formation into:

▪ Tectonic troughs: This category includes mostly the submarine canyons of wadi Safaga, the middle canyon and canyons of wadi Queih. Although the submarine canyon of wadi safaga is an ordinary extend from the wadi, its form reveals garben-like with flat-wide floor and high walls (150 above its floor). As well, the staircase form of the canyon may be a result of stair normal faults, which separate the canyon into two levels from the open sea. However, the middle canyon is parallel to the present-day coast and relatively deeper (500-200 m bsl); these give the impression that it is structurally controlled. Tectonic canyons are common and predictable along the Red Sea coasts. Such troughs were recognized in the southern Gulf of Suez of which strait of Bughaz depths about 30 m (bsl), Sharafi channel downs to 50 m (bsl), and strait of Jubal depths about 80 m (bsl); those are characterized by mountainous fault-controlled margins (Roberts & Murray, 1984). In addition, Reches et al. (1987) recognized submarine faults in the Gulf of Elat.
▪ Sea-level fall bellow the shelf edge: The other distinguished submarine canyons in the study area are mostly a result of previous sea-level fall that accompanied by canyon incision across the entire shelf (Talling, 1998).

Although time of canyon initiation is a controversy issue, Reches et al. (1987) has the opinion that the submarine canyons in Elat (140-280 m bsl) were formed during the late Pleistocene, when the sea level was 90 to 130 m below the present sea level. Gvirtzman et al. (1977) assumed that the Red Sea canyons were eroded subaerially within the limits of the last Pleistocene sea level changes. Gvirtzman (1994) interpreted the submarine canyon (-120 m) as the lowest erosional base level during the last glacial maximum. Fricke (1983) denoted that flash floods often of catastrophic nature, which influencing the Red Sea region, carrying large amounts of sediments into the sea. Accordingly, he suggests that the occasionally gravity flows fed initially by sediments from aligned wadis are a major agent in cutting the deep submarine canyons into steep edges of the narrow Red Sea shelves. He is of the

opinion that the subaerial erosion below the level of the deepest Pleistocene terrace seems unlikely.

4. Reef Terraces

Reef terraces are the result of sea-level changes. They are formed mainly of massive coral colonies parallel to the present-day coastline. El Moursi et al. (1994) recognized eight emerged reef terraces along the Red Sea coastline between Hurghada and Mersa Alam, based on continuity, lithologic features, fossil content, stratigraphic relations, and altitude; they are:

- Terrace **I** is about 1.5-2 m. It is the most continuous one recorded along the coastline in the study area. The terrace exhibits about 0.8 m notch in which deposits of an old shoreline as well as the present-day coastal deposits are preserved. Occasionally, its surface is covered by beach sands and/or alluvial deposits.
- Terrace **II** varies in elevation between 3-4 m. The terrace is made up of massive coral colonies in growth position, while its upper surface is generally abraded and covered either with raised beaches or alluvial deposits.
- Terrace **III** attains about 6 m. It forms mostly a continuous rock platform dissected at the mouths of the major wadis. Its upper surface is covered either by raised beaches consisting of calcareous sands and gravels or by alluvial deposits.
- Terrace **IV** elevates 9 m. It is a fossiliferous coral-rich limestone perforated by the effect of carbonate-feeding marine organisms. The most notable feature of this terrace is the presence of a marine notch in which beach deposits of various compositions were deposited. Its surface is abraded and covered with recent alluvial sand and occasionally covered by 0.5 m thick beach gravels.
- Terrace **V** varies in elevation between 22-25 m. The terrace is associated with beach conglomerates and laminated calcareous sandstone that may represent either an older sandy beach or coastal aeolianite phase at wadi Sharm El Bahri south of El Quseir.
- Terrace **VI** represents discontinuous coral reef fragments affected by tilting and faulting at an elevation of 30 m.
- Terrace **VII** attains about 32 m at wadis Guesses and Abu Safi. It is in the form of a patch reef overlaying a staircase alluvial gravel terraces.
- Terrace **VIII** is represented by the deposits of Shagra formation. In wadi El Quseir El Qadiem the lower member of the terrace is represented by a fossiliferous

calcareous sandstone bed of variable thickness. However, the upper member exhibits three stratigraphic successions; they are from top to bottom: Vermetid reef (fossiliferous coralline limestone), dark yellow to yellowish brown fossiliferous sandy limestone, and Clypeaster-Laganum bed.

El Moursi et al. (1994) argued that these eight terraces were laid down in three distinct cycles of reef formation separated by intervals of emergence and weathering or continental deposition of gravel fans (Fig. 6-16).

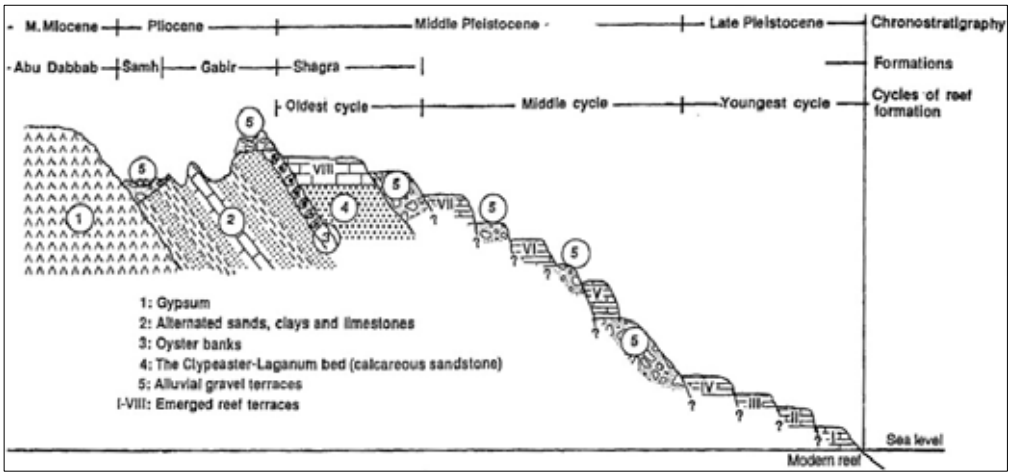

Fig. 6-16: *Generalized cross-section showing the stratigraphic relations, major facies, and the suggested age of the post-gypsum sequence of the Red Sea coastal plain, Egypt.* *(Source: El Moursi et al. 1994)*

- The Oldest Cycle.

The oldest cycle is represented by the deposits of Shagra formation that forms terrace **VIII** that varies in elevation between 9 and 35 m above msl. The suggested age of the formation is either Pliocene or Plio-Pleistocene (Said, 1990). Deposits of Shagra formation are nearly horizontal marking the angular unconformity of the Red Sea coastal plain. Thus in accordance with the relative rise of the global sea level during the Pleistocene times. Therefore, the deposits of this cycle may represent the successive high water condition phase of the Pleistocene sea. The top of the formation is represented by distinctly identified vermetid reef. The terraces are unconformably overlain by alluvial gravel terraces, which are made up of several fining upward cycles indicating deposition by shallow meandering streams that followed during regressive sea conditions in response to probable irregular precipitation.

El Moursi et al. (1994) assumed that this oldest cycle corresponds to terrace 5 from the Jordanian coast of the Gulf of Aqaba, which was determined by Al Rifaiy and Cherif (1988), and to the older terrace described by Gvirtzman and Friedman (1977) from Sinai coast, from which a U/Th age is older than 250 ka BP. It may also in accordance with Ophira terrace **I** in Southern Sinai that was dated between 290-330 ka BP (Gvirtzman et al. 1992), and to terrace **I** recorded along the Egyptian Gulf of Aqaba that gives an uranium series age between 280-300 ka (El-Asmar, 1997). According to El Moursi et al. (1994), this cycle was formed during Oxygen Isotope Stage 9 (300-330 ka BP), and the present-day altitudes of its terraces are the product of eustatic sea level fluctuations and differential tectonic uplift.

- The Middle Cycle.

The middle cycle of reef formation comprises terraces **V, VI,** and **VII**. They are fossil coral terraces overlying a sequence of alluvial gravel terraces that in turn overlie the deposits of Shagra formation. Terraces of this cycle correspond to the older reef sequence (R1-R4) described by Conchon et al. (1988) from the southern Egyptian Red Sea coast at elevations of 24, 31, and 35m above msl respectively. They may also correspond to terraces 6 and 7 recognized in the Jordanian coast of the Gulf of Aqaba at elevations of 25 and 30 m above msl respectively (Al Rifaiy & Cherif, 1988), and to the middle fossil coral reef terrace recognized in Sinai coast from which U/Th ages ranging between 200.000 and 250.000 yr BP (Gvirtzman & Friedman, 1977). It may also correspond to Mureikha terraces **II** and/or **III** in Southern Sinai, which were dated between 170-215 ka BP (Gvirtzman et al. 1992), and to Terrace **III** of Umm Sid and Ras Mohammed in southern Sinai that range in age between 202.5 ±10.20 and 303.4 ±35.40 ka (El-Asmar, 1997). El Moursi et al. (1994) demonstrated that terraces of this cycle are considered to have been formed during Oxygen Isotope Stage 7 (170-230 ka BP).

- The Youngest Cycle.

This cycle is represented by terraces **I, II, III,** and **IV** that are nearly continuous along the coastline. The elevation of the upper surface of this cycle is about 9 m above msl equivalents with other terraces recorded along the Red Sea coast and the Gulf of Aqaba. However, they are equivalent to those described from the Jordanian coast up to 9.5 m above msl (Al Rifaiy & Cherif, 1988), and the lower terrace system along

Sinai coast from which a U/Th age range from 108 to 140 ka BP (Gvirtzman & Friedman, 1977). They are also equivalent to those described from the Sudanese Red Sea coast at 2-8 m above msl from which a $^{230}Th/^{234}U$ age of 91 ±5 ka BP was recorded (Berry et al. 1966).

However, terraces of this cycle were described along the Egyptian Red Sea coast by many authors. Terrace **I** is estimated to be of Holocene age by Conchon et al. (1988). Terrace **II** is dated to 120 ±10 ka BP (Aïssaoui, 1985). Terraces **III** is the same as R 5, 5-7 m above msl, which was considered to represent the last interglacial stage (Conchon et al. 1988). Terraces **IV** is equivalent to the youngest coral terrace recognized at 6-8 m above msl at Hurghada and Zabargad Island that represent the last interglacial stage 125 ka BP (Hoang & Taviani, 1991). It is also corresponding to the coral terraces at elevation 15 m at Jabal Zeit, which have an average U/Th and ESR age of 125 ka BP and tectonic uplift of 5-10 m (Andreas & Radtke, 1988). Terraces of this cycle may be also equivalent to Na'ama terraces **II** and/or **III** in southern Sinai, which dated between 81-141 ka BP, and to Umm Sid terraces **IV**, which dated between 2.5-6.5 ka BP (Gvirtzman et al. 1992). El Moursi et al. (1994) demonstrated that the three lowermost terraces (**I-III**) give $^{230}Th/^{234}U$ ages distributed in three ranges i.e. 72.1 ±2.5 - 87.6 ±2.2; 112.1 ±3.3 - 113.2 ±4.1; and 123.6 ±4.7 - 131.2 ±4.4 ka BP. These age ranges coincide with the last interglacial cycle but their correlation with the Oxygen Isotope Substages 5a, 5c, and 5e, respectively, is not evident. Therefore, these three terraces, combined with terrace **IV**, were mostly built during the maximum high sea level stand of the last interglacial cycle (Oxygen Isotope Substage 5e ~120-130 ka yr BP).

References:

Aïssaou, D. M. (1985) Botryoidal aragonite and its diagenesis. *Sedimentology, Vol. 32-3, pp. 345 -361.*

Andres, W. & Radtke, U. (1988) Quartäre Strandterrassen an der Küste des Gebel Zeit (Golf von Suez, Ägypten). *Erdkunde, 42, 7-16.*

Arvidson, R., Becker, R., Shanabrook, A., Luo, W., Sturchio, N., Sultan, M., Lotfy, Z., Mahmood, A., & El Alfy, Z. (1994) Climatic, eustatic and tectonic controls on Quaternary deposits and landforms, Red Sea, Egypt. *Journal of Geophysical Research, Vol. 99, No. B6, pp. 12,175-12,190.*

Bemert, G. (1987) Red Sea coral reef. *Kegan Paul International Ltd. London UK. 192 P.*

Braithwaite, C. J. R. (1982) Pattern of accretion of reefs in the Sudanese Red Sea. *Marine Geology, 45, 297-325.*

Braithwaite, C. J. R. (1984) Geology and paleography of the Red Sea region. In: Edwards, A. J. & Head, S. M. (Ed.) Red Sea, *Pergamon Press, Oxford, pp. 22-44*

Choukri, A., Reyss, J-L., Hakam, O-K., & Plaziat, J-C (2002) A statistical study of ^{238}U and $^{234}U/^{238}U$ distributions in coral samples from the Egyptian shoreline of the northwestern Red Sea and fossil mollusc shells from the Atlantic coast of High Atlas in Morocco: Implications for $^{230}Th/^{234}U$ dating. *Radiochim, Acta, Vol. 90, pp. 329-336.*

El Moursi, M., Hoang, C. T., El Fayoumy, I. F., Hegab, O., & Faure, H. (1994) Pleistocene evolution of the Red Sea coastal plain, Egypt: Evidence from uranium-series dating of emerged reef terraces. *Quaternary Science Reviews, Vol. 13, pp. 345-359.*

El-Asmer, H. M. (1997) Quaternary isotope stratigraphy and paleoclimate of coral reef terraces, Gulf of Aqaba, South Sinai, Egypt. *Quaternary Science Reviews, Vol. 16, pp. 911-924.*

Fricke, H. W. (1983) On the origin of Red Sea submarine canyons. *Naturwissenschaften, 70, pp. 195-197.*

Gornitz, V. (2007) Sea level, after the ice melted and today. *http://www.giss.nasa.gov/research /briefs/gornitz_09/ (Accessed 15 October 2007).*

Guilcher, A. (1988) A heretofore neglected type of coral reef: the ridge reef, Morphology and origin. *Online Summary available at: http://www.reefbase.org/resourcecenter/publication/icrs.aspx (Accessed 13. Juni. 2007).*

Gvirtzman G., Buchbinder B., Sneh A., Nir Y. & Friedman G.M. (1977) Morphology of the Red Sea fringing reefs: a result of the erosional pattern of the last-glacial low-stand sea level and the following Holocene recolonization. *Memoires Bureau Recherches Geologiques Minieres, 89, pp. 480-491.*

Gvirtzman, G. (1994) Fluctuations of sea level during the past 400.000 years: the record of Sinai, Egypt (northern Red Sea). *Coral Reefs, Vol. 13, pp. 203-214*.

Gvirtzman, G., Kronfeld, J. & Buchbinder, B. (1992) Dated coral reefs of southern Sinai (Red Sea) and their implication to late Quaternary sea levels. *Marine Geology, 108, pp. 29-37.*

Head, S. M. (1987) Corals and coral reefs of the Red Sea. In: Edwards, A. J. & Head, S. M. (ed.) Red Sea. pp. 128-151, *Pergamon Press, Oxford.*

Hoang, C. T. & Taviani, M. (1991) Stratigraphic and tectonic implications of uranium series-dated coral reefs from uplifted Red Sea islands. *Quaternary Research, Vol. 35, Issue 2, pp. 264-273.*

Hoegh-Guldberg, O. (2000) Climate change, coral bleaching and the future of the world's coral reefs. *Mar. Freshwater Res.*,*Vol. 50, pp. 839-866.*

Jones, D. A., Ghamrawy, M. & Wahbeh, M. I. (1987) Littoral and shallow subtidal environments. In: Edwards, A. J. & Head, S. M. (Ed.) Red Sea. pp. 169-193, *Pergamon Press, Oxford.*

Kleypas, J. A., McManus, J. W. and Meñez, L. A. B. (1999b) Environmental limits to coral reef development: where do we draw the line? *American Zoologist, vol. 39 (1): pp. 146-159.*

Moawad, M. B. (2003) The geomorphology of the coastal zone between Ras Abu Girab and Ras Alam El-Roum, The NW coast of Egypt. *Unpublished M.Sc. (In Arabic), Department of Geography, Faculty of Arts, Ain Shams University, Cairo, 273 p.*

Mohamed, E. E. E. (1988) Circulation patterns and hydrographic structure of the southern Red Sea and Gulf of Aden. *Ph. D. Thesis, Alex. Univ., 220 p.*

Nasr, A. H. (1955) Ecological observations on the marine algae of Ghardaqa (Red Sea). *Hydrobiologia, Springer Netherlands, Vol. 7. No. 3, pp. 245-255.*

Newman, A. C. and McGill, D. A. (1962) Circulation of the Red Sea in early summer. *Deep-Sea Res., Vol. 8: pp. 223-235. Pergamon Press Ltd. Great Britain.*

Orszag-Sperber, F., Plaziat, J.-C., Baltzer, F., & Purser, B. H. (2001) Gypsum salina-coral reef relationships during the Last Interglacial (Marine Isotope Stage 5e) on the Egyptian Red Sea coast: a Quaternary analogue for Neogene marginal evaporates? *Sedimentary Geology, Vol. 140, pp. 61-85.*

Perillo, G. M. E. (1995) Geomorphology and sedimentology of estuaries: an introduction. *In: Perillo, G. M. E. (ed.) geomorphology and sedimentology of estuaries, pp. 1-16, Elsevier Sci; New York.*

Plaziat, J-C., Baltzer, F., Choukri, A., Conchon, O., Freytet, P., Orszag-Sperber, F., Purser, B., Raguideau, A. & Reyss, J-L. (1995) Quaternary changes in the Egyptian

shoreline of the northwestern Red Sea and Gulf of Suez. *Quaternary International, Vol. 29/30, pp. 11-22.*

Por, F. D. (1972) Hydrological notes on the high-salinity waters of the Sinai Peninsula. *Marine Biology, Vol. 14, pp. 111-119.*

Radwan, G. El-D. M. (2001) Impact of human activities on coral reef sedimentary environment in Mabahiss bay, north to Hurghada city – Red Sea. *Unpub. M. Sc. Thesis. Geol. Dept. Fac. Sci. Cairo University, 132 p.*

Reaches, Z., Erez, J. & Garfunkel, Z. (1987) Sedimentary and tectonic features in the north eastern Gulf of Elat, Israel. *Tectonophysics, Vol. 141, pp. 169-180.*

Reiss, Z. & Hottinger L. (1984) The gulf of Aqaba: ecological micropaleontology. *Ecological Studies. vol. 50. Springer Verlag, Berlin, 354 pp.*

Roberts, H. H. & Murray, S. P. (1984) Developing carbonate platforms: southern Gulf of Suez, Northern Red Sea. *Marine Geology, Vol. 59, pp. 165-185.*

Said, R. (ed.) (1990) The geology of Egypt. *A.A. Balkema Rotterdam, Netherlands, 734p.*

Schick, A. P. (1958) Marine terraces on Tiran Island, Northern Red Sea. G*eografiska Annaler, V. 40, No. 1, pp. 63-66.*

Scholz, D. (2005) U-series dating of diagenetically altered fossil reef corals and the application for sea level reconstructions. *Ph.D. thesis, Combined Faculties for the Natural Sciences and for Mathematics of the Ruperto - Carola University of Heidelberg, Germany, 172 p.*

Spencer, T. & Viles, H. (2002) Bioconstruction, bioerosion and disturbance on tropical coasts: coral reefs and rocky limestone shores. *Geomorphology, vol. 48(1-3):pp. 23-50.*

Talling, P. J. (1998) How and where do incised valleys form if sea level remains above the shelf edge? *Geology, Vol. 26, No. 1, pp. 87–90.*

Tomczak, M. (1996-2000) Oceanogr. *www.es.flinders.ed.au (Accessed on 05 September 2007).*

Vandersträte, T. (2006-2007) The use of remote sensing for coral reef mapping in support of integrated coastal zone management: a case study in the NW Red Sea. *Ph.D. Universiteit of GENT Faculteit Wetenschappen, Vakgroep Geografie, Belgium. 426 p.*

Yentsch, C. S., Yentsch, C. M., Cullen, J. J., Lapointe, B., Phinney, D. A. and Yentsch, S. W. (2002) Sunlight and water transparency: cornerstones in coral research. *Journal of Experimental Marine Biology and Ecology*, *vol. 268 (2): pp.171-183.*

Conclusions

The study area is divided into four morphological units they are: coastal zone and coastal plain, tablelands, Red Sea Terrain, and drainage basins. Every effort has been made to reveal the main climatic, geologic, and geomorphologic characteristics of the study area. The foremost conclusions are summarized as follows:

- ***Climate and aridity indices.***

1. The highest values of mean maximum temperature occur in June, July, and August and the absolute maximum temperatures exceed 40˚ C.
2. The lowest minimum temperatures take place in winter and the mean minimum temperatures vary greatly from 6.7˚ C to 13.8˚ C.
3. The mean monthly of temperature ranges between 13.2˚ C and 34.4˚ C and the diurnal variation of temperature exceeds 20˚ C during the period from April to November owing to the passage of Khamasin depressions.
4. The absolute diurnal of temperature ranges between 25.2˚ C and 24.2˚ C and shores of the Red Sea experience diurnal wind changes usually reaching its maximum strength in early or mid-afternoon.
5. Northern and north-westerly winds are prevailing throughout the year and the mean annual wind speed is relatively high along the coastline varying between 12.3 and 8.9 knots in Hurghada and El Quseir respectively. In spite of that, the wind has minor influences on the physical landscape, which is restricted to dispersed patches of Nebkas and sand sheets along the coastal plain.
6. Scarcity and irregularity of rainfall are the most significant characteristics of the study area where the annual rainfall is less than 5 mm/yr generally.
7. The mean daily evaporation varies greatly from winter to summer between 9.6 mm and 22.3 mm respectively.
8. Implementation of aridity indices after Köppen (1931), De Martonne (1926) and Thornthwaite (1933) revealed that the area under study is considerably arid. Hyper-arid condition is expressed after Emberger (1955) and by using the graphical representation of the mean monthly precipitation versus the mean monthly temperature after Walter & Lieth (1967). On the other hand, ratio drought index is applied to the ETM image revealing that vegetation cover is almost absent as a result of rain scarcity.

- ***Coastal environment.***

9. The probable wave height ranges between 0.6 - 1.5 m in Hurghada and El Quseir respectively and capillary waves (≤ 0.6 m) are the most common wave types. However, wave height is about ±1 m and infrequently exceeds 3 and/or 5 m during gale winds, which mostly occur in winter and spring.
10. Generally, NW waves are predominant during winter and the NE direction is prevailing during summer.
11. Fringing coral reefs act as line of breaker and lie in the vicinity of the coastline (100-500 m) leading the approaching waves to incline at various angles relative to the coastline.

12. Wave celerity varies between 2.21-3.3 m/sec in the shallow water ±1 m bsl behind the line of breaker.
13. The study area experienced semi-diurnal micro-tide (≤0.5 m) where time difference between two successive high waters or low waters is approximately 12 hours with amplitude 0.6 m.
14. Two sets of longshore currents are deduced, one is of high velocity that exists where sea cliffs overlook the sea ranging in velocity between 50-60 cm/sec. The second set characterizes beach profiles of low angles (2˚-4˚) varying in velocity from 20-30 cm/sec.

- ***Cultural manifestations.***

15. Settled population confined to few places along or near the coastline where phosphates are mined or modern tourist centres are constructed.
16. The annual growth rate of population during the period 1986-1996 varies between 7.9 % for Safaga, 0.7 % for Hamraween, and 0.07 % for El Quseir.
17. Great changes have been occurred in the economic activities during the period 1986-1996 from mining to tourism and trade activities that constitute the present-day backbone of the economic activities in Safaga and El Quseir cities.

- ***Geology and structure geomorphology using digital image processing.***

18. The Precambrian rocks constitute about 78% of the study area, which are mainly crystalline in character.
19. Correlation coefficient of the ETM image bands indicates a direct relationship between each two pair of bands. Therefore, contrast stretching is essentially applied to expand the narrow range of image brightness.
20. Using convolution filter is valuable to change the spatial frequency of the image and exaggerate the local contrast of the original image for portraying linear features and edges between the image features. The study deduced that a detailed geological map can be obtained using convolution filter 3x3 edge enhancements, while regional or generalized geological map can be obtained using low pass filter.
21. Although the Optimum Index Factor (OIF) is necessary for synthesizing the image for better visual interpretation, it is not implied that it creates the best colour composite because this depends greatly on the purpose of the study. Accordingly, it has been observed that band combination 7 red, 4 green, 2 blue is being the best band combination for discriminating the major rock units and clarifying the intrusive dykes.
22. Numerous compound band ratioing (CBR) were examined of which the hydrothermal band ratio (7/5 red, 3/1 green, 4/3 blue) gives the best output for determining and separating the main rock units. The ratios 3/1 and 4/3 would enhance the small contribution of iron minerals by giving pixels of iron-bearing rocks a higher value than those composed of pure quartz. The ratio 7/5 manifest clay-rich rocks as high reflectance of all minerals is found in band 5 and the Al-OH and Mg-OH rational effects associated with clays and other hydroxylated minerals result in absorptions within band 7.

23. Multispectral supervised classification is carried out using the maximum likelihood algorithm and assembling convenient of 303 areas of interest (AOI) to include tonal, texture, shadow, and pattern differentiations. The output classes are visually verified where most of the output histograms are of normal distribution. However, contingency matrix clarifies that the accuracy assessment ranges between 89.56 % for ms class (gneisses and migmatites) and 99.96 % for sea water and the overall accuracy of the classification is about 93.26 %. The study concluded that the supervised classification is one of the best image processing methods for distinguishing the main rock units and; therefore, the classified geological map represents a well base map for the forward landforms analysis.
24. The study area has been long-term subjected to tectonic processes that contributed distinctive landforms. Analysis of the regional structure revealed two main fault directions NW and NE. The first direction is the most widespread adhering to the major Red Sea axe and known as Erythrean or African faulting. The second direction is corresponding to the Gulf of Aqaba and known as Aualitic faults. Steep faults are common and more conspicuous along the Qena-El Quseir highway where the basement rocks are faulted against the Nubian Sandstone that is in turn faulted against the Eocene strata of Jabal Duwi.
25. Regarding to characteristics of the remotely sensed data, a lineament is defined as a series of pixels that have similar digital values and presuming geologic and geomorphologic origin (i.e. faults, folds, dykes, joints).
26. Edge detection technique is widely applied to band 4 for reducing data distortion and edge detections. The first derivative edge enhancement (directional filter) is used to reveal the main lineaments from the following directions N-S, NE-SW, E-W, and NW-SE. The sum of the kernel is zero and the results are areas with uniform pixel values, which are zeroed in the output image and those that are variable are presented as bright edges.
27. Laplacian filter (non-directional) or the 2^{nd} derivative edge enhancement is used to enhance edges regardless of edge direction. The kernel composed of a high center value surrounded by positive values from the west and the corners are of zero values.
28. Shaded and painted relief maps depicting small features that could not be effectively shown using the original image data. They are one of the most appropriate terrain models for feature recognitions.
29. The study compiled the lineament map that contains a total of 7329 linear features of a total length of 5212 km. The azimuth frequency diagrams clarify three dominate directions with three peaks they are: N-S, NE-SW and NW-SE representing 9.5%, 7.6% and 7.5% of the total count and 10.8%, 8.4% and 8.26% of the total length respectively. However, peaks more than 7% of the total length are considered as anomalies, which may reflect significant regional and/or local trends.
30. Spatial concentration analysis of the lineament clarifies different dispersed epicentres that are confined to plutonic intrusions of the younger granite and Dokhan volcanic (e.g. Jabals Barud and Naqarah). The study concluded that lineaments are lithologically controlled in spite of that no particular orientation can be given to distinguish specific rock units.
31. The study area is dominated by two large linked normal fault systems, they are: the coastal fault system and the border fault system including domino-style fault blocks. The coastal fault system dominantly trends NW and delineates the main exposure syn-rift strata along the Red Sea. It induces

abrupt topographic discontinuities of landforms and a major steep coastal fault scarp. On the other hand, the border system is more complex bounding a series of WNW and NW half graben.

32. The study points out a method for studying warped landforms by defining rock outcrops and dip identification from satellite images in comparison with the field data. The results are greatly approximate.
33. The study concluded that the general terrain of the study area comprises half graben separates between two huge uplifted faulted mountains (horsts). Two distinctive depressions are recognized as the coastal depression and the inland depression. The inland depression comprises elongated trench trends NW-SE generally. It is restricted to latitude of Jabal Rabah in the north and extends about 115 km southwest. This depression is a distinctive form characterizes the central Eastern Desert of Egypt for preserving the Cretaceous-Tertiary rocks.
34. Warped landforms along the coast reveal a simple monocline or flexure dipping uniformly eastward with angles vary from 5˚ to 20˚ and constituting a series of tabular mesas and outliers. They are probably remnants of a larger plateau that has been subjected to severe erosion.
35. The inland depressions constitute generally oval and/or elongation shaped hollows occupied by low hills. The depressions are semi-closed since they connect to each other through incised narrow wadis.
36. The general structure of the inland depressions demonstrates markedly normal faults of different trends manifesting the whole depressions as faulted basins or graben flanked by the basement rocks.
37. The preserved sedimentary rocks within the inland depressions incline west-east generally, with the exception of Jabal Duwi, revealing either cuestas or tabular remnants. The cuestas are considerably detached by strike-slip faults and incised wadis.
38. The northern block of Jabal Duwi is seemingly an overturned fault block as it is reversed to the major axe of Jabal Duwi. On the other hand, the southern block specifically forms a bold white cliff rises considerably along a strike fault and inclines seaward or eastward.
39. Jabal Duwi, as a whole, exposes distinctive solutional landforms of which Sodmein cave is well developed in the lower part of a 100 m high cliff and looks over the 200 m wide wadi Sodmein. Moeyersons et al. (2002) denoted to different wet periods in the cave at 6.320 - 7.470 and ±25.000 yr BP and at ±115.000 yr BP. In addition, a blade core of limestone flakes is founded 60 cm below the floor of the cave that is likely belonging to middle Palaeolithic time. However, preservation of sheep and goats droppings (±1 m) suggests the idea that during the middle and upper Palaeolithic there was a wealthy wild-life in the Eastern Desert of Egypt where the climate was probably semi-arid.
40. Exhumed and buried old erosion surfaces are recognized in the study area. The exhumed one has mostly regional extensions and characterized by a flat surface with low relief, truncation of different rock types and general accordant levels of its interstream areas and mountain summits. The buried erosion surfaces constitute the unconformities of stratigraphic geology and are noted in small-scale exposures in Jabal Naqarah.
41. The study suggests two cycles of peneplanation the first one was probably synchronous with the early stage of Hammamat sedimentation during the upper Proterozoic and the second one is mostly

occurred during the upper Tertiary since the Tertiary rocks are partially and/or completely eroded elsewhere.

42. Diapiric plutons are abundant in the Eastern Desert of Egypt constituting ring-like structures. They area composed primarily of the younger granite (lower Paleozoic) that is intruded by dykes of different types, orientations, and ages. The plutons comprise high mountains generally with rugged relief (e.g. Jabals Barud, Kab Amiri, Umm Oradah, and Umm Had). They underwent normal vertical and lateral offsets especially along the contact zones.
43. Dykes are widely established in the study area comprising narrow, steeply dipping bodies of a few meters thick and several kilometres long. They are considerably controlled by the geometric characteristics of rock fractures and fault systems. Significantly, they are perpendicular to the Red Sea trend (northwest) and less significantly parallel to this trend. As they differ greatly in their composition, they form markedly positive or negative landforms. Quartz veins are also common and notably intrude Jabal Umm Oradah and are well exploited in wadi Sodmein.
44. Tectonic joints are well investigated from satellite images since they are relatively long, wide-spaced and convoying no notable offset.

- ***Hydrological modelling and drainage basin analysis.***

45. Concept of hydrological modelling is widely applied within the present study for representing a digital simulation of drainage basins depending on the analysis of the DEM. The model delineates stream networks and executes stream orders, watershed delineation and quantifying the most important morphometric measurements of basin analysis. The study deduced that 10 cell threshold is suitable for automatic stream delineation using the SRTM image and; therefore, the model extracts drainages ≥ 900 m in length.
46. It has been observed that the model orders each reach as a separate stream segment, so that stream numbers differ greatly and do not fulfil law of stream numbers versus stream orders. To overcome this problem, each stream order is extracted separately, the intersected nodes of the other stream orders are removed and stream lines are dissolved.
47. Validity of the hydrological model is tested using variable and variance analyses. The study revealed a great similarity between the data extracted from the SRTM image and the topographic map of scale 1:50.000 generally. The study permits the conclusion that the SRTM image is suitable for modelling small-scale drainage basins as well.
48. The dominating stream patterns are mostly dendritic, sub-dendritic, parallel, and sub-parallel, revealing litho and structure controls.
49. Drainage basins are poorly drained (<8 km/km2) as a result of scarce annual rain, relief, and rock resistance. Surface textures range from coarse (<4 miles) to fine texture (> 10 miles).
50. The study spots a method for computing and representing the hypsometric analysis in quantitative terms based on the analysis of the DEM. Shapes of the hypsometric curves are either convex, S-shape, and concave indicating significantly the geomorphological stage. The curves reveal that large portions of drainage area lie at low elevations because the basins have been mostly subjected to peneplanation for long-time specifically where the older granite dominates the drainage area.

51. The study suggests that antecedent drainages (e.g. Sodmein, Mohamed Rabah) were synchronized to the orogenic process that is postdated at late Oligocene – early Miocene. They were probably synchronized to the Gilf System assumed by Issawi & McCauley (1993) as the major Oligocene drainage system in Egypt. During the late Miocene, fluvial erosion was extremely active eliminating the fractured sedimentary rocks which covered the present-day Red Sea Terrain and the drainages are being superimposed-like on the basement rocks adhering to major structures.
52. On the other hand, the coastal drainages are relatively smaller and mostly postdated at Plio-Pleistocene as they drain principally the coastal tablelands that are composed of middle Miocene and Pliocene rocks.
53. The coastal plain of the Egyptian Red Sea is primarily a result of coalescing deltas alternating with reefal plain. Deltas are considerably irregular shaped and characterized by wide and straight fronts or toes in the vicinity of the sea.
54. The study distinguishes six alluvial terraces along the lower courses of the drainages at heights 1-1.5, 2.5-3, 4.5-6, 10-12, 15-16, and ≥20 m above the wadi floors generally.
55. Terraces of wadi al-Ambagi are dated relatively as follows:
    - Terrace 1-1.5 m is likely corresponding to the present-day climate where the Holocene high sea-level was developed around 4.000 to 7.300 yr BP during the Holocene climatic optimum (5.000-9.000 yr BP) after the Flandrian Transgression.
    - Terrace 4.5-5 m is probably equivalent to the last interglacial climatic substage 5e (Emian: Riss-Würm) between 115.000 - 130.000 yr BP approximately.
    - Terrace 10-12 m is mostly corresponding to the middle Pleistocene (Holstein interglacial period: Mindel-Riss) between 200.000 - 300.000/380.000 yr BP.
    - Terrace 20-21 might be correlated to istope stage 11 (older than 300.000 yr BP) where the sea-level was about 13-20 m above its present-day level.

- ***Flood Hazard.***

56. Under very specific conditions the Red Sea coast is vulnerable to thunderstorms especially during October and November owing to movements of the Sudanese monsoon depression towards the north. This condition is accompanied by a pronounced quasi-stationary upper-level disturbance.
57. Analysis of the daily weather reports revealed that the study area is ordinary influenced by exceptional torrential rainfall causing unusual ephemeral runoff and flash floods. Rain intensity varies from 12.10 and 17 mm/hr generally and reached about 30 mm/hr near El Quseir during a flash-flood event on 14th November 1996.
58. Peak discharge represents poorly drained watersheds and shallow soil covers of the impermeable basement rocks. Peak discharge of the drainage basins varies from <10 to +100 m^3/sec generally. In addition, time concentration varies greatly from 0.69 to 11.29 hr.
59. Probability of annual occurrence of the torrential rain is high 92.3 % where the rainfall is about 10 mm and it is estimated to be occurred every 1.3 yr. On the other hand, probability of annual occurrence is very low 2.9 % where the rainfall attains about 75 mm and this may occur every 34 yr.

60. The study concluded that wadis el Barud and al Ambagi are of high flood magnitude as a result of high flood potentiality, high peak discharge, and human interferences.

- ***Coastal forms and coral reefs.***

61. Coastal cliffs are the most widespread erosional forms along the coastline. They composed primarily of reef limestone 1-4 m thick overlain by alluvial deposits ±1 m thick.
62. Estuaries markedly characterize the coastline as a result of rising sea level during the last 4.000-5.000 yr BP.
63. Four types of coral reefs are distinguished in the study area as: fringing reefs, barrier reefs, atolls, patch, and coral carpets.
64. Coastal lagoons are distinguished as non-reef lagoons, reef barriers lagoons, and inter-reef lagoons.
65. Mangrove trees are a part of the coastal habitat, which inhabit protected areas from high energy wave action.
66. The study distinguishes three submarine terraces at levels 20, 50, and 100 m bsl. Numerous submarine canyons are denoted at different levels below sea level, as well. They represent mostly either tectonic troughs or sea-level fall below the shelf edge canyons.
67. Reef terraces above the present-day sea level are laid down in three distinct cycles of reef formation separated by intervals of emergence and weathering or continental deposition of gravel fans (El Moursi, et al. 1994). The oldest cycle was probably formed during Oxygen Isotope Stage 9 (300 - 330 ka BP). The middle cycle is considered to have been formed during Oxygen Isotope Stage 7 (170 - 230 ka BP). Finally, the youngest cycle was mostly formed during the maximum high sea level stand of the last interglacial cycle (Oxygen Isotope Substage 5e).

- ***Geological - geomorphological evolution and climate changes.***

Geological and geomorphological evolution of the study area is very complicated rather than simplified. On behalf of simply understanding landscape evolution in the study area, particular interests have been given to rock units, tectonic events, alluvial deposits, reef terraces, and sea level and climate changes. The study concludes that the area may have been developed according to the following statements:

- ***Orogenic Cycles (Precambrian).***

68. The earliest event in the geological evolution of the basement rocks was the deposition of a succession of sediments, which later gave rise to a group of metasedimentary gneisses or paragneisses.
69. ***The first orogeny*** in the Precambrian took place between 900-600 Ma yr (Beniamin, et al. 2005) and the mentioned sediments were ultimately metamorphosed and associated with minor basic intrusions (Akaad & El-Ramly, 1960 b).
70. The old surface is widely eroded resulting in the deposition of a thick succession of fine clastic geosynclinal like-fold sediments. These sediments were deposited on the old surface, grading into an interbedded polymictic conglomerate with pebbles of granite, greywacke, mudstone, and slates as well as metamorphosed felsites, basalt, andesites, and quartz-porphyry.

71. Before the final phase of the filling of the geosynclines, a period of volcanic activity occurred and lavas of considerable thickness were extruded and intruded at shallow depths in the associated sediments. Accordingly, ultrabasic sills and dykes apparently intruded the sediments. Akkad & El-Ramly (1960 b) denoted that these intrusions appeared in the on coming second orogeny and are most conspicuous in the basement complex rocks.
72. During ***the second orogeny*** (600-540 Ma yr) (Beniamin, et al. 2005) the older rocks were bent and converted or altered into the metasediments that are widely distributed as schist, mudstone, and greywacke series. At the same time, the associated volcanics were converted into the old series of metavolcanics and this was the last regional metamorphism affecting the basement rocks where the later rocks are unmetamorphosed (Akaad & El-Ramly, 1960 b).
73. During this orogeny, the intrusion of gabbro-diorite rocks occurred and has followed by another intrusion of the grey granite. As well, a new eruption of volcanics occurred, composed mainly of a variety of purple coloured porphyry of Dokhan Volcanics.
74. Dokhan Volcanics were followed by a period of erosion and deposition that is apparently purple-red hematite and conglomerate of Hammamat group, which was derived mainly from the Dokhan Volcanics. This represents ***the early stage of peneplanation*** (680-640 Ma yr) where significant volumes of igneous rocks were vigorously eroded and the Hammamat group was deposited in a major river system of a continental-scale (Wild & Youssef, 2002).
75. A period of activation ***(1st period of activation)*** took place and performed folding and faulting the basement rocks. At the same time, the younger granite, which forms the diapiric plutons within the study area (e.g. Jabals Ras Barud and Umm Oradah) was emplaced (620-570 Ma yr) (Hassan & Hashad, 1990) and followed by a number of intrusive dykes that are known as post-granite dykes (650-550 Ma yr) (Abdel-Rahman, 1995).
76. During the late Paleozoic a relatively long period of stability mostly occurred and extended to the upper Mesozoic (late Cretaceous) where the Nubia group was deposited.

- ***Platform Stage.***

77. The Cretaceous-Eocene sediments (pre-rift sediments) were deposited generally in the troughs of the synclinal-like folds within the crystalline mountain ranges (Beniamin, et al. 2005). The fundamental complex of ancient crystalline rocks with its overlaying Cretaceous-Eocene sediments were widely subjected to intense deformation or compression which started mostly at the end of the Cretaceous epoch and known as ***the 2nd period of activation***. The compression was probably related to the late Cretaceous-Early Tertiary oblique convergence between Africa and Eurasia (Zaky, 1999) and resulting in a series of highly tilted fault blocks running north or northwest (e.g. Jabals Duwi, Rabah, and Wasif). On the other hand, a variety of dykes intruded the older basement rocks owing to this period of activation that was mostly continued until the Paleogene time. The dykes are of granite porphyry and felsite porphyry dykes, trachyte, microsyenite and bostonite, and dolerite and diorite porphyrite dykes.

78. During upper Eocene-Oligocene epochs, the land must have undergone uplifting since the upper Eocene-Oligocene sediments are absent (Beniamin, et al. 2005) or widely eroded as a result of folding, faulting and intense denudation in the eastern Egypt (Ball, 1939).
79. During late Oligocene-Miocene epochs the process of the Red Sea formation mostly occurred associated with gradual uplifting of the Red Sea Mountains (Beniamin, et al. 2005). As well, the area was subjected to northeast movement as a result of divergent movement between Africa and Arabia caused right-lateral displacement along NE trend (Zaky, 1999). Geological and palaeontologic data from the Sahara suggest a wet equatorial climate in the lower Eocene that is shifted in the Oligocene towards a Sudano-Guinean type of savanna (Le Houérou, 1997). These events resulted in the wadi system in the study area, which was probably simultaneous with the Gilf River System assumed by Issawi & McCauley (1993) as the end Oligocene epoch (24 Ma yr) drainage system in Egypt that has developed due to the uplift of the southern corner of Egypt and the Red Sea Mountain Ranges. During the middle Miocene, the climate turned towards tropical wet climatic conditions, which caused the emergence of the ancestral wadi Qena (Early Qena River ~16 Ma yr). Wadis of the study area most likely have been developed during the same period.
80. In the late Miocene, the climate was mostly hot and arid and the Mediterranean sea-level was about 4.000 m below its present-day level. During this period the Eonile drained primarily most of the wadis of the Eastern Desert to attain its base-level (Said, 1993).
81. Probably, ***the second stage of peneplanation*** took place during the upper Tertiary, where most of the Tertiary rocks were partly or fully eroded elsewhere and different rock types of the basement complex rocks were truncated and characterized by general accordant levels of the interstream areas or mountainous summits.
82. During the Pliocene time, a short pluvial period occurred in which the clastic rocks and carbonates of Samah formation were deposited and followed by Gabber formation that is rich in Indo-Pacific fossils. This was after the invasion of the Indo-pacific water through Bab el-Mandab strait[1] (Said, 1990). This is followed by a period of aridity between the Pliocene and Pleistocene (Le Houérou, 1997).

- ***Pleistocene-Holocene Changes.***

83. During the Pleistocene and Holocene epochs dramatic climate and sea-level changes occurred and resulted in the formation of the present-day physical landscape. The Red Sea experienced greatly eustatic changes resulting in a sequence of raised coral terraces and submerged forms. Three cycles of coral terraces were deposited around the middle Pleistocene. The older cycle is mostly corresponding to Oxygen Isotope stage 9 and the maximum insolation (300-330 ka yr BP), (Holstein or Mindel-Riss interglacial 200 – 300/380 Ka yr BP). This is in accordance with the relative rise of global sea level during the Pleistocene time. Deposits of this cycle may represent the successive high water condition phase of the Pleistocene Sea.

[1] *Said (1990) denoted that it is not certain weather the transgression was the result of global rise of sea level or of a tectonic movements.*

84. This is followed by a drop in sea level, regression of the shoreline and the onset of the deposition of the alluvial terraces (El Moursi, et al. 1994). The middle cycle of coral formation is formed mostly during the Oxygen Isotope stage 7 (170-230 ka yr BP) during the late middle Pleistocene. The youngest cycle was deposited during the maximum high sea level of the last interglacial cycle, Oxygen Isotope Substage 5e (~120-130 ka yr BP) (Eemian or Riss-Würm 110 – 130 Ka yr BP) where the global sea level was about 2-6 m above its present day level. It is worthy mentioning that the peripheral parts of the Red Sea rift were mostly inactive during 150-120 ka yr BP.
85. During the last glacial maximum, sea-level was dramatically jumped down about 120-100 m bsl that is resulting in the submarine terraces of 100, 50 and 20 bsl. Terrace -100 m may be in corresponding to the last glacial maximum (LGM) in the age range of meltwater pulse (MWP) 1A0 and 1A (~19.000-16.000 yr BP). Terrace -50 m is probably in accordance to the meltwater pulse-1B (11.500-11.000 yr BP). Terrace -20 m is mostly formed during the fourth meltwater pulse 1C (8.200-7.600 yr BP) (Gornitz, 2007) that is in accordance with the Flandrian Transgression. Most of the submarine canyons were probably formed during those intervals of sea-level rising.
86. Sea-level remained at or around its present-day level during the last 4-5 ka yr BP owing to the Holocene high sea level. Formation of the present-day estuaries may be also in accordance to this period.
87. Evidences from Sodmein cave and the discovered implements from the wadi gravel terraces lead to the conclusion that during early and middle Palaeolithic age (~120-30 ka yr BP) the climate was probably semi-arid and favoured wild-life and grazing of sheep and goats better than today. Another dry period took place between 24-18 ka yr BP during the last glacial maximum (L.G.M) (Würm or Weichsel 20.000 yr BP) followed by an optimum pluvial period during the Neolithic (10-4 ka yr BP). The present-day hyperarid conditions occurred mostly from 3.000 yr BP forth (Le Houérou, 1997).

References:

Abdel-Rahman, A-F. M. (1995) Tectonic -magmatic stages of shield evolution: the Pan- African belt in northeastern Egypt. *Tectonophysics, Vol. 242, pp. 223-240.*

Akaad, M. K. & El-Ramly, M. F. (1960b) Geological history and classification of the- basement rocks of the Central-Eastern Desert of Egypt. *Geological Survey of Egypt, Cairo, Paper No. 9, 24 p.*

Ball, J. (1939) Contributions to the geography of Egypt. *Egypt Survey Dept., Cairo, 300 p.*

Beniamin, N. Y., Youssef, M. M., Azzam, H. M., Mahmoud, M. H., Salama, A. M. & Abd El Migid, A. (2005) On the main tectonic features of the central and northern Eastern Desert, Egypt. *Ministry of Petroleum, Egyptian Mineral Resources Authority, Regional Geology Department, 77 p.*

Bradley, R. S. (1999) Paleoclimatology: reconstructing climates of the Quaternary, *2nd ed. Academic Press, London, 416 p.*

Burroughs, W. J. (2005) Climatic change in Prehistory: the end of the reign of chaos, *Cambridge University Press, 356 p.*

E.G.S.M.A. (1984) Metallogenic map of the Qena quadrangle, Egypt: Scale 1:500.000.

E.G.S.M.A. (1987) Basement rocks of Safajah quadrangle, Egypt: Scale 1:100.000.

E.G.S.M.A. (1988) Basement rocks of Al Qusayr quadrangle, Egypt: Scale 1:100.000.

El Moursi, M., Hoang, C. T., El Fayoumy, I. F., Hegab, O., & Faure, H. (1994) Pleistocene evolution of the Red Sea coastal plain, Egypt: Evidence from uranium-series dating of emerged reef terraces. *Quaternary Science Reviews, Vol. 13, pp. 345-359.*

Gornitz, V. (2007) Sea level, after the ice melted and today. http://www.giss.nasa.gov/research /briefs/gornitz_09/ (Accessed 15 October 2007).

Goudie, A. S. (2005) The drainage of Africa since the Cretaceous, *Geomorphology, Vol. 67. pp. 437-456.*

Hassan, M. A. & Hashad, A. H. (1990) Precambrian of Egypt. In: Said, R. (ed.), The Geology of Egypt. *Balkema, Rotterdam, pp. 201-245.*

Issawi, B. & McCauley, J. (1993) The Cenozoic landscape of Egypt and its river system. *Annals. Geol. Survey of Egypt, v.19, pp. 357-384.*

Le Houérou, H. N. (1997) Climate, flora and fauna changes in the Sahara over the past 500 million years. *Journal of Arid Environments, Vol. 37, pp. 619-647.*

Moeyersons. J. Vermeersch. P.M. & Van Peer, P. (2002) Dry cave deposits and their palaeoenvironmental significance during the last 115 ka, Sodmein Cave, Red Sea Mountains, Egypt. *Quaternary Science Reviews, Vol. 21, pp.837–851.*

Oliver, J. E. (ed.) (2005) Encyclopedia of world climatology. *Springer, 854 p.*

Said, R. (ed.) (1990) The geology of Egypt. *A.A. Balkema Rotterdam, Netherlands, 734p.*

Said, R. (1993) The River Nile: geology, hydrology and utilization. *(In Arabic), 2ed edition, Dar El Hilal, Cairo, 342 p.*

Wilde, S.A. & Youssef, Kh. (2002) A re-evaluation of the origin and setting of the Late Precambrian Hammamat Group based on SHRIMP U-Pb dating of detrital zircons from Gebel Umm Tawat, North Eastern Desert, Egypt. *Journal of the Geological Society, 159, 595-604.*

Zaky, Kh. S. (1999) Structural studies on rift geometry of south Safaga- Quseir tilted blocks. Northwestern part of the Red Sea, Egypt. *The first International Conference on the Geology of Africa. Vol. 1, pp. 313-330.*